# The State and Evolution of Isolated Dense Molecular Cores

**Promotion**

zur

Erlangung des Doktorgrades (Dr. rer. nat.)

der

Mathematisch-Naturwissenschaftlichen Fakultät

der

Rheinischen Friedrich-Wilhelms-Universität Bonn

vorgelegt von

Jens Kauffmann

aus

Remscheid

Bonn 2006

Angefertigt mit Genehmigung der Mathematisch-Naturwissenschaftlichen Fakultät der Rheinischen Friedrich-Wilhelms-Universität Bonn

*Für Thushara, in tiefer Liebe.*

# Abstract

This work presents studies of nearby ($\leq 500$ pc) dense molecular cloud cores, the sites of low-mass star formation. The sample includes starless and protostellar cores and allows to compare their properties in a homogenous manner. All of the projects presented here are related to an extensive dust thermal continuum emission imaging survey at 1.2 mm wavelength that probes the mass distribution of dense cores. Many of them are also related to the Spitzer Legacy Project "From Molecular Cores to Planet Forming Disks" (c2d) that stimulated the dust emission survey and provided a general framework for my thesis. The main body of this work discusses the dust emission survey and the properties and nature of an unusually faint ($\approx 0.1\ L_\odot$) source apparently embedded in one of the dense cores surveyed.

The data from the dust emission survey is used to study the physical state and evolution of starless cores, "normal" protostars, and of the recently discovered Very Low Luminosity Objects (VeLLOs). This is the first study probing VeLLO dense core properties homogeneously for a larger sample of 4 sources. Given that this survey covers both starless and protostellar cores, it is well suited to perform comparative studies. The aim is to understand how the mass distribution in dense cores controls the presence or absence of active star formation. As part of this effort I infer conditions that are necessary (but not sufficient) for active star formation to be possible. These can be understood as a consequence of the quasistatic evolution of a dense core, but do not conclusively imply the latter. Most VeLLO cores fulfil these conditions, questioning the notion that some VeLLOs form in cores that are not sufficiently evolved to form stars. I suggest a revision of the criteria used to identify "evolved" cores. Class 0 and class I protostars covered by my survey cannot be uniquely discriminated, suggesting also a revision of criteria used to assign infrared classes.

Furthermore, I report the discovery of L1148-IRS, a candidate Very Low Luminosity Object (VeLLO; $L \leq 0.1\ L_\odot$) in the nearby ($\approx 325$ pc) L1148 dense core. The global spectral energy distribution, the morphology of nebulosity detected at $\approx 1\ \mu$m wavelength, the inferred density profile of the dense core, and the tentative detection of inward motions towards L1148-IRS are consistent with the source being an embedded protostar. It is unlikely that L1148-IRS is a galaxy by chance projected onto the L1148 dense core. I do, however, not detect hallmarks of active star formation like molecular outflows or clear bipolar nebulosity proving a protostellar nature of L1148-IRS. This is consistent with our present view of VeLLOs.

If L1148-IRS is a VeLLO, then it is a very interesting one. Its present mass would be substellar, and its immediate envelope has a mass of only $\approx 0.15\ M_\odot$. Thus, L1148-IRS would be the first protostar to definitely have a significantly sub-solar final mass. The collapse of the natal dense core could not be understood in the framework of quasistatically evolving cores. This would make L1148 the first dense core in which non-quasistatic evolution plays a significant role.

# Curriculum Vitae

Please refer to the printed edition for a full reference.

| | |
|---|---|
| name: | Jens Kauffmann |
| nationality: | german |
| gender: | male |
| email: | jkauffmann@cfa.harvard.edu |
| present office address: | Harvard-Smithsonian Center for Astrophysics |
| | 60 Garden Street |
| | Cambridge, MA 02138, USA |

# Contents

# Chapter 1

# Introduction

I here present an introduction to my thesis. Starting with a summary of the present state of star formation research (Sec. 1.1), followed by an overview of the immediate aim and methods of this work. An introduction would, however, be incomplete without having discussed the layout of my thesis project, which would not have been possible without an intensive collaboration within a larger international research project (Sec. 1.3). The structure of this document is summarised in Sec. 1.4.

## 1.1 An Introduction to contemporary Star Formation Research

### 1.1.1 Molecular Cloud Structure and Star Formation

In the first decades of the 20$^{\text{th}}$ century photographs of star fields revealed "dark markings" (Barnard 1919) in the sky, where no or fewer stars were seen compared with an average position in the sky. Although early on it was thought that these dark markings could be due to clouds of "dark" matter that screen the stars, this was not always the commonly accepted explanation (Barnard 1919). Further observations substantiated evidence for the existence of an interstellar gaseous medium (Trumpler 1930a,b) and eventually the dark markings were considered a compact component of this interstellar gas.

In the following decades further investigations of the dark clouds were limited by the fact that their internal structure could not be studied at optical wavelength. Eventually line emission from molecules was discovered and became the major probe of their interior structure and composition. At this point "molecular cloud" became a synonym for what was earlier called dark cloud. The sizes and masses of molecular clouds known today span across many orders of magnitude, ranging from tiny solar mass structures to over $10^5 M_\odot$ massive and up to 100 pc large giant molecular cloud complexes (e.g. Clemens & Barvainis 1988, Blitz 1993).

A leap forward in our understanding of giant molecular clouds complexes were the first complete maps at millimetre wavelength (Kutner et al. 1977, Blitz & Thaddeus 1980). First it appeared that the observed structure was best interpreted as an ensemble of discrete clumps (Blitz & Stark 1986), some of which harbour dense cores (Myers et al. 1983), which appeared to be the sites of star formation in a molecular cloud. Later it was argued that this hierarchy from clumps to cores might also be explained within a fractal (i.e., self-similar scale free) picture for the morphology of the dense gas (Bazell & Desert 1988, Scalo 1990, Falgarone et al. 1991). However, star formation is commonly observed in discrete and isolated regions within giant molecular clouds, indicating that gas here has become unstable and collapses at a size-scale small compared with the overall cloud size. Thus, qualitative differences must exist between regions that form stars and others that do not.

Bertoldi & McKee (1992; see also Williams et al. 2000) argued that the existence of such a characteristic scale of dense structures in GMCs implies a departure from self-similarity. This characteristic scale is given by the growing importance of self-gravity relative to other energy density (pressure) components. Structures for which

self-gravity is strong have an "individual identity", the gas they contain is no longer part of the continuous flow of matter between all scales. Self-gravitating structures are partially decoupled from their parental cloud, and their characteristics are determined by the physical state of the gas, such as its temperature, turbulence, magnetic field, heating or ionisation. They are not unstructured lumps of gas, but evolve into objects with density increasing inwards in which gravitational forces are approximately balanced by pressure gradients. The pressure in molecular clouds is due to thermal motions, bulk "turbulent" gas motions, and due to the effect of magnetic fields.

Williams et al. (2000) defined clumps as "coherent regions in $lbv$ space" (i.e., in spatial coordinates and radial velocity), star-forming clumps as "the massive clumps out of which stellar clusters form", and cores as "regions out of which single stars (or multiple systems) form". I shall adopt these definitions. Some dense cores are starless, i.e. they do not actively form stars at present. Others contain protostars, i.e. young stars that have not grown to their final mass yet, which accrete from the surrounding dense core. Those cores that are not forming stars yet, but are expected to do so in future, are sometimes said to be in the prestellar phase.

Dense cores are believed to start forming protostars when they become unstable to gravitational collapse (e.g., Larson 1969). The core is thought to collapse approximately in free-fall (Shu 1977) while the infalling matter accretes onto the central protostar, thereby increasing its mass. I shall further detail protostellar evolution in Sec. 1.1.3.

Small clouds in relative isolation comparable to those in the sample of Clemens & Barvainis (1988, mass $< 10^2 \, M_\odot$) can be regions of isolated star formation, where stars do not form as part of larger groups. Among such clouds we find the Bok globules discovered as dark patches in early optical photographs (Bok & Reilly 1947). If such clouds form part of larger cloud complexes (mass $\lesssim 10^4 M_\odot$; e.g., Taurus) one also speaks of a distributed mode of star formation. In recent years it was, however, found that such lower mass molecular clouds do not contribute much to the overall star formation activity in the Galaxy (Magnani et al. 1995). Most stars form via some clustered mode of star formation (for recent reviews see Pudritz [2002] and Ward-Thompson [2002]), in which most stars are born as part of larger clusters. This mode occurs almost exclusively in the massive giant molecular clouds.

On smaller scales these differences in the star formation modes are due to differences in the properties of the star-forming dense cores. These stand in relative isolation in regions of isolated or distributed star formation, while they form part of tight groups in regions of clustered star formation. This is illustrated in Fig. 1.1 by a direct comparison of isolated and clustered dense cores imaged using the same instrument.

It has become custom also to distinguish between low-mass star formation (Ward-Thompson 2002) and high-mass star formation (Walmsley 2003). While low-mass stars appear to form via both the isolated and the clustered mode of star formation, massive stars (i.e. masses $> 7 \, M_\odot$) seem to form only in massive clusters along with hundreds or thousands of low-mass stars (Ward-Thompson 2002, Pudritz 2002). One suspects that high-mass stars might form via processes rather different from those responsible for the formation of low-mass stars. I will not expand this issue, and in the following I shall only be concerned with the isolated formation of low-mass stars in low-mass isolated molecular cores.

## 1.1.2   Isolated Dense Starless Cores: Ideal Laboratories for Star Formation Studies

Dense starless cores are objects where low-mass stars are suspected to form in the future. The physical and chemical properties of such cores describe the necessary conditions for star formation. We need to study such objects to gain insights to the conditions of star formation. However, two issues make it difficult to study the fundamental physics of star formation in cluster-forming environments (for both see, e.g., Motte et al. 1998). First, cores can be confused in crowded regions; it becomes difficult to identify and study individual cores. Second, cores might interact in crowded regions; more parameters than relevant in isolated cores influence the evolution of dense cores. These problems can be avoided if studying dense cores in relative isolation instead of cores hosted in larger (up to $\gtrsim 100$ pc) complexes of dense and massive molecular clouds. In this respect isolated dense cores are "ideal" laboratories for star formation studies: their simple structure and evolution allows to acquire a basic understanding of the physics shaping dense cores. One should, however, also keep in mind that their structure and evolution is probably too simple to reflect the properties of dense cores in crowded regions dominating the galactic
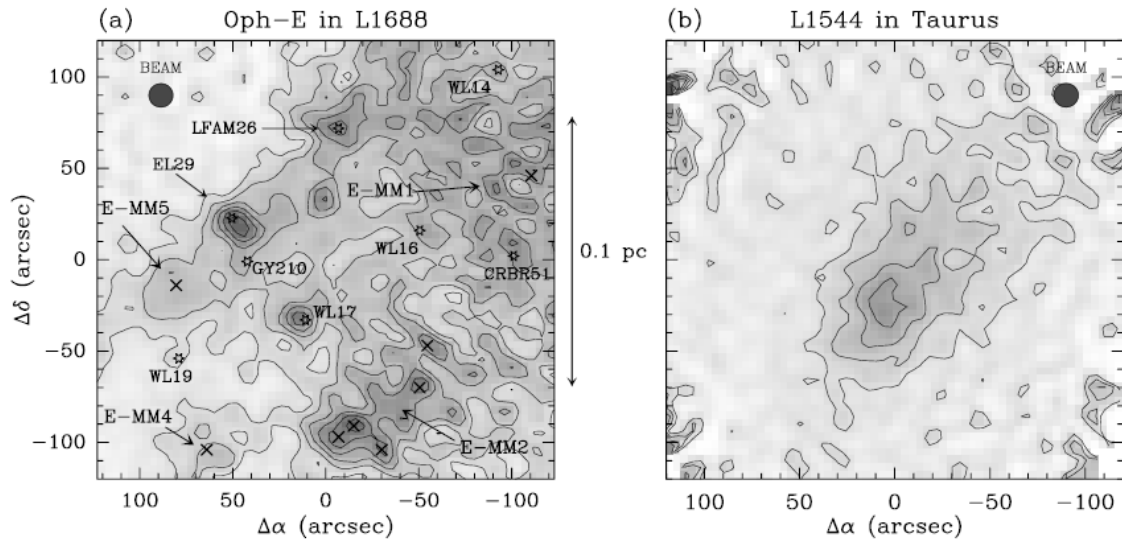
**Figure 1.1:** Comparison of clustered (*panel a*; clump 'E' in the ϱ Ophiuchi star-forming complex) and isolated (*panel b*; L1544 in the Taurus molecular cloud) dense cores. *Crosses and stars* in panel a) mark starless and protostellar cores, respectively. Both 1.2 mm dust continuum images are taken at the same resolution with the IRAM 30m-telescope, and both regions are at approximately the same distance to the sun. The cluster-forming ϱ Ophiuchi clump shows far more substructure than the more isolated Taurus core at the same linear scale. Clustered cores are thus likely to be more perturbed and harder to disentangle than isolated ones. (Reproduction of Fig. 5 of Ward-Thompson et al. [2007], which is based on Motte et al. [1998] and Ward-Thompson et al. [1999].)

star formation activity.

For these reasons, in the past years isolated dense molecular cores have become a prime target for detailed studies of the initial conditions of star formation. In particular, such studies focused on nearby ($\lesssim$ 500 pc) cores, which are, again, probably not typical for the average galactic star formation sites, but can be easily studied in detail. Their receivable radiation intensity is stronger and the spatial resolution is finer than for their more distant counterparts. Cores with and without ongoing star formation have been studied in order to learn how dense cores evolve towards the onset of star formation, and finally make stars.

Two sets of dense core properties are investigated. First, their physical state — e.g., velocity dispersions, rotation speeds, densities, density gradients, total mass, magnetic field strengths, and size — is derived from analysis of molecular emission lines and thermal continuum emission from the dust mixed with a dense cores' gas, and by analysing the dimming of background stars by the intervening dust. Second, their chemical state — i.e., relative abundances of molecules — is probed by spectroscopy of molecules and a combination of such analysis with information on the mass distribution.

An early observational result was that the density increases toward the core center but becomes constant near the center (Ward-Thompson et al. 1994). Typical hydrogen particle densities of the observed cores are $n(H_2) \approx$ $10^5$ to $10^6$ cm$^{-3}$, and their masses are 0.5 to 2 $M_\odot$, depending also on the observers' definition of the boundary. Their typical sizes are of order 0.1 pc and the dust temperatures are around 10 K. There is evidence that the dust temperature decreases toward the core center (Shirley et al. 2000, Langer & Willacy 2001). The hydrogen column densities on the central line-of-sight can reach up to $N(H_2) \approx 10^{23}$ cm$^{-2}$, corresponding to about 100 magnitudes of visual extinction.

Studies of the velocity fields of dense cores revealed that the linewidth-size correlation, as first inferred by Larson (1981) for large molecular clouds, also holds for some smaller cores (Barranco & Goodman 1998). In some cores the observed velocity dispersions approach the thermal velocity dispersion in the densest parts (Hotzel et al. 2002), in other cases no clear trend between the observed velocity dispersion and the observed scale could be found (Caselli et al. 2002a). Thus the role of such "turbulence" in cores seems to be a complicated, not yet well understood process. Goodman et al. (1998) found, however, that the non-thermal line width in cores (i.e., after removal of the thermal linewidth) is smaller than the thermal hydrogen velocity dispersion. Thus turbulent pressure in dense cores does not appear to be larger than thermal pressure. For typical gas temperatures of the order of 10 K this limits the total linewidth at half maximum to $\Delta v = 0.6$ km s$^{-1}$.

Other studies searched for evidence of inward motions in starless cores. Motions with an amplitude of 0.1 km s$^{-1}$ were first seen in the core L1544 (Tafalla et al. 1998), where they prevail across an area of 0.2 pc diameter. These motions are thought not to be related to the actual gravitational collapse of a dense core into a star, but to the evolution of a core towards the onset of the runaway gravitational collapse. They are thought to be a hallmark of cores in late stages of their evolution (Crapsi et al. 2005a). Nowadays a handful of good candidate cores with inward motions are known (Lee et al. 1999, 2001, 2004a).

Recent studies of the dense core chemistry provide a new way to gauge the evolutionary state of dense cores. At high densities carbon-bearing molecules appear to freeze out onto dust grains with increasing core age (e.g., Tafalla et al. 2002). To give examples, dense core maps in optically thin lines of the $C^{18}O$ molecule sometimes exhibit a "hole" in the intensity distribution at the position where the total gas column density peaks. At the same time the deuterium fractionation of the molecules remaining in the gas phase increases (Crapsi et al. 2005a). Despite the galactic deuterium abundance of order $10^{-5}$ (Neufeld et al. 2006) the $N_2D^+$-to-$N_2H^+$ abundance ratio is found to be of order 0.2 in some cores (Crapsi et al. 2005a). Both allows to derive "chemical ages" from observed molecular abundances. In this respect most known cores appear to be chemically evolved. Only very recently cores without significant CO-depletion by freeze-out were identified (Tafalla & Santiago 2004; see Sec. 4.2.2 for my identification of a second such core).

The measurement of magnetic field strengths in cores present a difficult observational challenge. In a recent review Crutcher (1999) analysed 27 observations of the Zeeman effect to measure magnetic field strengths. Only for 13 regions of high-mass star formation or large molecular cloud complexes and for 2 regions of low-mass star formation the Zeeman effect was detected; towards 11 regions of low-mass star formation only upper limits were

reported. This is in part due to the lack of suitable molecular tracers. In a recent effort Uchida et al. (2001) and Levin et al. (2001) tried CCS as a new probe of the Zeeman effect towards low-mass star forming cores. They failed to detect it but derived limits for the average magnetic field strength parallel to the line of sight of $B_{\text{l.o.s.}} < 100\,\mu\text{G}$.

A suitable alternative approach to estimate magnetic field strengths may be polarised emission from dust grains that align with the magnetic field, which yield a determination of the field geometry. First results show that for some cores the magnetic field is well ordered across the face of a core (Ward-Thompson et al. 2000), while for other cores the situation remains ambiguous (Henning et al. 2001). For three sources one can infer field strengths below $100\,\mu\text{G}$ (Henning et al. 2001).

### 1.1.3   Early Stellar Evolution

Early stellar evolution can be roughly divided into two main phases. Young stars first enter the obscured phase of star formation, in which the star is deeply embedded in and obscured by its natal dense core from which it accretes mass. The conservation of angular momentum forces this accretion to proceed via a disk. Such sources are called protostars. This phase is believed to last for about $10^5$ years (Barsony & Kenyon 1992, Greene et al. 1994, Kenyon & Hartmann 1995). From then on the part of the natal dense core immediately surrounding the star is often called the envelope. Young stars then enter the revealed phase of star formation, in which the natal dense core disperses and the young star is left with a disk that decreases in mass with time. From this phase on there is only weak accretion onto the star from the remaining disk. Such sources are called pre main sequence stars. Once accretion ceases completely the star adjusts its internal structure and finally enters the main sequence phase; it is now a mature star.

Research during the past 20 years has lead to subdivisions of the above evolutionary scheme. Very young stars in the obscured phase are called class 0 sources (Andre et al. 1993). They are conceptually defined to have yet accreted less than half of their final mass. They are observationally identified by comparing the stellar mass estimated from the stellar luminosity to the fraction of the mass of the natal dense core that still can be accreted. Later stages were initially assigned based on the observed spectral index between about 2 and 20 $\mu$m wavelength, $\alpha = \text{d}(\nu F_\nu)/\,\text{d}\nu$, where $\nu$ and $F_\nu$ are frequency and flux density. This spectral index measures the amount of mass in the protostellar envelope and disk; it generally decreases with decreasing circumstellar mass. One thus defined the infrared classes I to III in order of decreasing spectral index, respectively circumstellar mass (Lada 1987; $0 \leq \alpha$ for class I, $-1.5 \leq \alpha < 0$ for class II, and $\alpha < -1.5$ for class III). Class 0 sources are thus thought evolve into class I sources, which are still part of the obscured star formation phase. Later on the stars become class II and III sources, which were found to be largely identical with the disk-dominated T Tauri variable stars known from previous research. This scheme of protostellar evolution is summarised in Fig. 1.2.

It was later shown that this sequence can also be parameterised by the bolometric temperature, which measures the mean frequency of the spectral energy distribution (SEDs; Chen et al. 1995, 1997). This employs the fact that the SEDs of very young protostars are dominated by the long-wavelength ($\geq 100\,\mu$m, low bolometric temperatures) emission of their envelope, while in evolved protostars the short-wavelength ($\leq 10\,\mu$m, high temperatures) stellar photospheric emission dominates. Both class assignment methods are, however, not fully consistent. I discuss my research on this issue in Sec. 2.6.4.

Envelopes of class 0 and class I sources are found to have density profiles similar to $\varrho \propto r^{-2}$, where $r$ is the radial distance from the protostar (Motte & André 2001). This is consistent with theoretical predictions (Shu 1977). Infall related to the protostellar collapse is observed in such envelopes (Mardones et al. 1997). Class 0 and class I sources do, however, also drive molecular outflows with typical velocities of order 5 km s$^{-1}$ (Bontemps et al. 1996). In these a fraction of the infalling matter is ejected from the protostar-core system. Outflows are therefore hallmarks of ongoing star formation. Before our research on *Very Low Luminosity Objects* (VeLLOs; Kauffmann et al. 2005), which are unusually faint sources of apparently protostellar nature, it was actually thought that all class 0 and class I sources drive such outflows (see Sec. 3.3.4 for details).
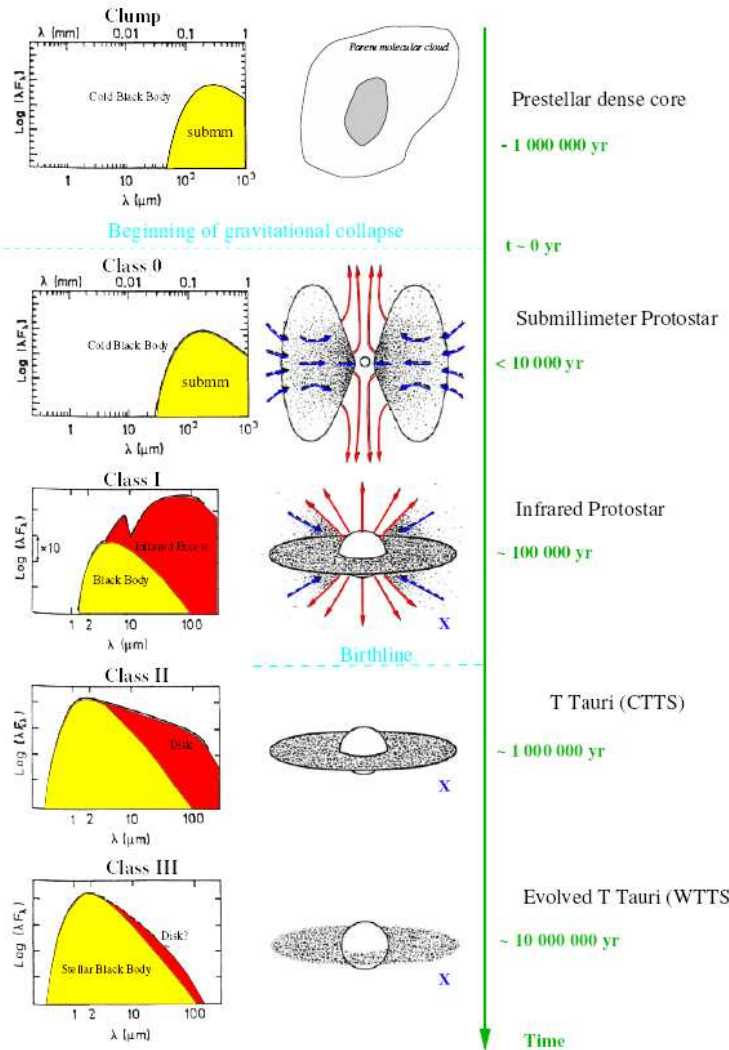
**Figure 1.2:** Summary of star formation stages in order of advancing age (*top to bottom*). The *left panels* summarise the characteristic spectral energy distributions (SEDs) of the respective stages and list the corresponding infrared class, the *right panels* sketch the physical structure (not drawn to a common scale), and the *right labels* give a descriptive type of the core-star system (not adopted for this thesis) and an approximate age with respect to the onset of gravitational collapse (positive time after collapse). The amount of circumstellar matter decreases with time, while the SED maximum wavelength decreases. The latter implies that the spectral index between about 2 and 20 $\mu$m wavelength decreases with time, while the bolometric temperature increases. (Adopted from N. Grosso, Laboratoire d'Astrophysique de Grenoble. Based on Lada [1987] and Andre et al. [1993].)

## 1.2    Aim and Methods of the Thesis

### 1.2.1    Scientific Aim

Though the above summary might read as if most questions in star formation research are settled, this is by far not the case. Even very basic questions are still unanswered. Some of them are addressed in my thesis. An incomplete list of such questions is given below.

One of the fundamental riddles of star formation research is why some dense cores do actively form stars while others do not. This problem could be resolved partially by the research presented here. Section 2.6.3.2 derives necessary conditions for active star formation to be initiated: dense core properties need to exceed certain critical values. These conditions are, however, not sufficient for star formation to occur; starless and protostellar dense cores have similar properties. This indicates that the mass distribution probed by our observations is not the only parameter controlling the star formation ability of dense cores. The critical values for active star formation to be possible are about identical to the critical values for hydrostatic equilibria supported by pure thermal pressure that are on the verge of gravitational instability. If starless dense cores evolve quasistatically, it is possible to understand — and actually derive — the existence of such necessary but not sufficient conditions for active star formation to occur: the critical values for gravitational collapse depend on the turbulent and magnetic pressure prevailing in a particular core. This results in a spectrum of critical values for a sample of dense cores. The assumption of quasistatic evolution is, however, not needed to derive the above conditions observationally. We do not claim that dense cores are hydrostatic equilibria.

A new puzzle is the nature of *Very Low Luminosity Objects*, apparent protostars of a new kind that we discovered in some nearby dense cores (VeLLOs; Young et al. 2004, Kauffmann et al. 2005). Their unusually low internal luminosities (i.e., after subtraction of the power from interstellar heating) of order $\leq 0.1 \, L_\odot$ suggests that they are class 0 sources of substellar present mass ($\leq 0.08 \, M_\odot$; see Sec. 3.6.1 for a critical discussion of VeLLO mass estimates). It is, however, not clear what their final mass will be. If they continue to accrete strongly they grow to stellar final masses. Still, some VeLLOs might be the first candidate proto-brown-dwarfs known.

A larger VeLLO sample is needed to study their general properties. My main role in this part of our VeLLO research was to establish the infrared star L1148-IRS as a candidate VeLLO (Chapter 3). It is not possible to fully rule out that L1148-IRS actually is a background galaxy that is by chance projected onto a dense core. No hallmark of ongoing star formation, like a molecular outflow or clear bipolar nebulosity, was found. However, the probability for L1148-IRS to be a galaxy is low and the overall properties of L1148-IRS are consistent with a VeLLO.

The actual formation of some VeLLOs might pose a challenge and test to star formation theories. Some of them form in dense cores previously thought not to be dense and evolved enough to be able to actively form stars. Most of the cores studied by us, however, do fulfil the conditions for ongoing star formation introduced above (Sec. 2.6.5). It appears that most VeLLO cores are dense and evolved, as predicted by star formation theory, but that existing criteria to identify such cores are biased such that they select only a fraction of such cores (Sec. 2.6.6).

Finally, there is an ongoing debate on whether dense cores evolve quasistatically, or significantly depart from hydrostatic equilibrium (e.g., Alves et al. 2001, Ballesteros-Paredes et al. 2003). The important underlying question is whether the dense core structure is entirely determined by the equations of state relating pressure and density, as required for quasistatic evolution. This debate will be further fueled if L1148-IRS turns out to be a VeLLO. The overall structure of its natal core then implies that gravitational collapse is possible for a dense core in which only $\approx 0.1 \, M_\odot$ is concentrated in the central 4 000 AU radius area; this could not be understood in the framework of the hydrostatic evolution of dense cores (Sec. 3.6.2.1). Non-quasistatic evolution appears to play a significant role in some cores.

### 1.2.2    Dust Emission: A reliable Probe of Mass Distributions

A large fraction of the work presented here is based on the analysis of maps of thermal dust continuum emission. It is appropriate to briefly introduce dust emission as a tracer of the mass distribution of dense cores.

### DSS Image at Visual Wavelength

### MAMBO 1.2 mm Dust Emission Image
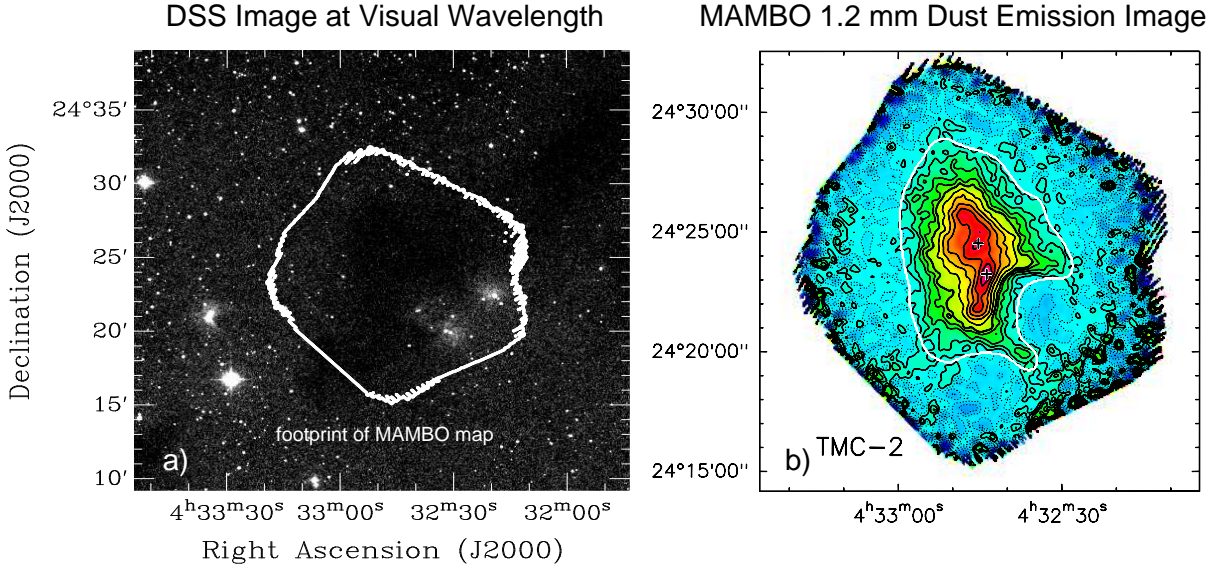


**Figure 1.3:** Thermal continuum emission from dust at ≈ 10 K (*right panel*; 1.2 mm MAMBO map from our sample) is a reliable tracer of the interstellar matter in TMC-2, which is also detected via its screening of background stars (*left panel*; image from the Digitized Sky Survey). The *contour in panel a)* marks the dust emission map boundary. *Black contours in panel b)* indicate the intensity levels. The *white contours* and the *crosses* indicate the boundaries and positions of "subcores" and "peaks" identified in the map; see Fig. 2.2 for more details on the dust emission map. The dust continuum emission traces the distribution of interstellar matter intuitively derived from the distribution of the "dark clouds" at visual wavelengths. This demonstrates the use of dust emission as a probe of dense core mass distributions.

Assuming the far-infrared to mm dust emission to be optically thin and that the dust is well mixed with the gas, the dust emission intensity, $I_\nu$, traces the hydrogen column density, $N(\mathrm{H_2})$:

$$I_\nu \propto N(\mathrm{H_2})\,\kappa_\nu\,B(\nu, T_{\mathrm{dust}})\,, \tag{1.1}$$

where $B$, $\kappa$, $\nu$, and $T_{\mathrm{dust}}$ are the Planck function, the opacity (i.e., the absorption cross section), the frequency, and the dust temperature, respectively. At about 1 mm wavelength, where most of the present bolometers operate, and temperatures ≈ 10 K, which are observed to prevail in dense cores and are not found to have significant spatial gradients, the Planck function has an approximate linear dependence on the temperature. Also, the dust opacity is commonly assumed to be spatially constant, though this is not well constrained. Dust emission intensity gradients across cores are thus dominated by gradients in the column density. Appendix A provides a detailed discussion of dust emission properties. Figure 1.3 shows an example of how dust continuum emission traces interstellar matter.

To probe the cloud density structure through the dust continuum emission has two advantages compared with molecular line observations:

- Most dense molecular gas is optically thin to thermal dust continuum emission, which is not the case for most molecular tracers.

- The specific thermal dust emission is nearly independent of the gas density. (The dust absorption coefficient depends weakly on the particle density, due to enhanced grain coagulation at high densities [e.g., André et al. 2000].) The excitation of molecular tracers on the other hand is density-dependent, and so are the molecular abundances, due to chemistry and depletion onto dust grains.

Dust emission observations are today performed with bolometers operated at the IRAM 30m-telescope (the MAMBO bolometers), the James Clerk Maxwell Telescope (JCMT; the SCUBA bolometer), the CSO (SHARC and SHARC II), the HHT, and until recently at the SEST (SIMBA).

## 1.3   Thesis Background

### 1.3.1   Course of the Thesis

My involvement in the field of dense core structure and evolution began with my diploma thesis. During its course I developed a model of hydrostatic dense starless cores in which self-gravity is balanced by a mix of thermal, turbulent, and magnetic pressure components. Comparison of the model predictions with published observations of dense cores suggested that a significant fraction of these must either be supported by significant non-thermal pressure or must be in a state of collapse. A detailed analysis of a dense core sample in the framework of these models was a logical continuation of this research — a work indeed presented in Sec. 2.6.3.

Fortunately the supervisor of my diploma thesis, Frank Bertoldi, had just embarked on such a study, which then was handed over to me and became the foundation of the thesis project presented here. This dust continuum emission imaging study at 1.2 mm wavelength using the Max-Planck Bolometer (MAMBO) arrays at the IRAM 30m-telescope near Granada (Spain) is the c2d MAMBO survey discussed in Chapter 2.

This survey is actually just one element of a larger international collaboration ($\approx$ 50 members), a so-called legacy program on the Spitzer Space Telescope (SST). It was triggered by the recent launch of the SST in 2003. This observatory provides imaging capabilities in the 3 to 160 $\mu$m wavelength range. The unprecedented combination of high spatial resolution and sensitivity at these wavelengths promised new insights into star formation research, if used in a systematic fashion. To guarantee the latter the Spitzer Legacy Program "From Molecular Cores to Planet Forming Disks" (AKA. "Cores to Disks" or "c2d"; Evans et al. 2003) was initiated years before the actual launch of the telescope. It imaged about 90 nearby ($\leq$ 500 pc) isolated dense cores and 5 nearby clouds as part of its agenda. The demand for complementary data raised by this project is a main driver of our survey. Such data is needed to, e.g., put the properties of the stellar content probed by Spitzer in context with dense core properties like density and mass; the latter can usually not be derived from Spitzer data. Our dense core survey is one of 4 new dust continuum emission surveys carried out in the c2d framework (Table 2.1).

The c2d collaboration allowed me to play a role in a discovery presented as one of Spitzers highlights: the discovery of the VeLLO L1014-IRS (Young et al. 2004). The data from the c2d MAMBO survey allowed a quick and reliable check of the association between the L1014 dense core and the embedded VeLLO. The MAMBO data was crucial to gauge the mass distribution of the dense core.

This collaboration also granted me preferred access to data products derived from the c2d Spitzer observations. On 2004 August 25 this allowed me to discover another VeLLO candidate in one of the c2d MAMBO cores, L1148-IRS. From then on I was increasingly drawn into VeLLO research. This lead to the research on L1148-IRS presented in Chapter 3, but also to collaboration on sources like L1521F-IRS (Bourke et al., in prep.).

I also conducted a dedicated dust emission study of the Chamaeleon II cloud for the c2d collaboration. Because of exceptionally bad raw data, this project produced only very meager results that were not suited to warrant a separate publication or thesis chapter (Young et al. 2005). A brief summary of the results is presented in Sec. 4.1.1.

To fully exploit the dust emission data from the c2d MAMBO survey we launched several extensive complementary surveys of molecular line emission from c2d MAMBO cores. As part of these surveys we found a chemically unevolved dense core without significant CO-depletion. This is only the second such core known. Cores like this one are thought to represent the earliest stages in the formation of dense cores. We also found a chemically strongly evolved starless core with an unusual velocity field. This core appears to be similar to the prototypical evolved cores L1544 and L1521F and can thus serve as a testbed for further studies of dense core chemistry. We hope that this core might also be a test case for star formation studies: despite its extreme chemical and physical state (high densities) this core does not actively form stars. We finally conducted an extensive CCS mapping study of several c2d MAMBO cores. Some cores exhibit systematic intensity gradients across their face, possibly hinting an interaction of the cores with their surrounding. These projects are still ongoing and are summarised in Secs. 4.2.2, 4.2.3, and 4.2.4.

I finally had the pleasure to get involved in a study using dust emission maps derived between 450 and 1 200 $\mu$m wavelength to infer the dust temperature distribution within a dense core covered also by the c2d MAMBO survey.

Though I did not perform the final analysis, I contributed to the data and with expertise on problems of bolometer imaging; for completeness I provide a summary of this work in Sec. 4.1.2.

### 1.3.2 Collaboration within c2d: Who are "We"?

This thesis is a collaborative effort in the sense that at every point there was intensive communication about and coordination of all ongoing c2d research projects. To give examples, essentially all observing proposals submitted during the course of my thesis were written in collaboration with c2d and other authors. The practical work necessary was, however, always executed by me alone.

With the exception of the datasets listed below, all data presented in this thesis has been collected, reduced, analysed, and written down in this text by myself without any immediate contributions from others. This only excludes the images and source catalogues based on data acquired with Spitzer (provided by the c2d collaboration) and FLAMINGOS (provided by Tracy Huard, Harvard-Smithsonian Center for Astrophysics), where I skipped the first step of data reduction. All other outside input to this thesis was only via the usual feedback received during scientific discussions, but never, e.g., in the form of partial or complete data analysis by others, nor in the form of complete texts or text fragments.

This thesis was conducted by myself and reflects work done by myself. The "we" is used to formally indicate that my research was carried out in a framework designed and executed by a group that includes me. It also indicates that input from discussions with colleagues often changed the way I analysed or finally interpreted the data. The help of these people is acknowledged at the end of this thesis.

## 1.4 The Structure of this Thesis

Chapters 2 and 3 are extended versions of two papers in preparation for publication in scientific journals. They were designed to be independent, and they might thus not harmonise as much as possible if directly written to be part of a larger research thesis. Such formal inconsistencies were mitigated as much as possible.

Chapter 2 discusses a dust emission survey of nearby isolated dense cores. The introduction to this particular project (Sec. 2.1) is followed by several sections on data acquisition and reduction, and details of the numerical data analysis (Secs. 2.2 through 2.5); the latter sections are of a rather technical nature. In Sec. 2.6 the results are interpreted in the framework of our present knowledge of star formation, which brings new insights to some of its aspects. Section 2.7 summarises this chapter.

Chapter 3 presents research on the VeLLO candidate L1148-IRS. The related introduction (Sec. 3.1) is followed by a short section on data acquisition (Sec. 3.2). Sections 3.3 through 3.5 address the different aspects of this VeLLO: the general properties of the infrared star (Sec. 3.3), its spectral energy distribution (Sec. 3.4), and the properties of the natal dense core (Sec. 3.5). These elements are combined in Sec. 3.6 in order to infer the nature of L1148-IRS and to derive implications for star formation theory. Sections of rather technical or scientific nature cannot be separated in this chapter: conclusions are drawn here from the data at every point. Section 3.7 provides a summary of the work on L1148-IRS.

Chapter 4 summarises the thesis and gives an outlook to future research. It first outlines two projects finished during my thesis that were, however, not suited to be included here in detail (Sec. 4.1). Ongoing projects that were not finished during my thesis are presented in Sec. 4.2. These projects also sketch the steps for future research after the end of my thesis project. Section 4.3 provides a final summary of the whole thesis project and tries to put its results into a broader context.

Appendix A details aspects of the treatment of dust emission properties. It is followed by Acknowledgements.

# Chapter 2

# A MAMBO Dust Emission Survey for the c2d Spitzer Legacy Programme

We present results from a comprehensive imaging study of thermal dust emission from 38 nearby ($\leq$ 500 pc) isolated dense molecular cores at 1.2 mm wavelength. An innovative data reduction strategy allows us to reliably trace also faint ($\lesssim$ 10 mJy beam$^{-1}$) extended ($\gtrsim$ 5$'$) emission from the starless and protostellar cores probed by our study. The survey is designed to complement Spitzer imaging observations by the c2d Spitzer Legacy Project, but it also constitutes an independent dataset well worth a separate study.

The data is used to study the physical state and evolution of starless cores, "usual" protostars, and of the recently discovered Very Low Luminosity Objects (VeLLOs). This is the first study probing VeLLO dense core properties homogeneously for a larger sample of 4 sources. Given that this survey covers both starless and protostellar cores, it is well suited to perform comparative studies. The aim is to understand how the mass distribution in dense cores controls the presence or absence of active star formation. As part of this effort we infer conditions that are necessary (but not sufficient) for ongoing star formation to be possible. These can be understood as a consequence of the quasistatic evolution of a dense core, but do not imply the latter. Most VeLLO cores fulfil these conditions, questioning the notion that some VeLLOs form in cores that are not sufficiently evolved to form stars. We suggest a revision of criteria used to identify "evolved" cores. Class 0 and class I protostars covered by our survey cannot be uniquely discriminated, suggesting also a revision of criteria to assign infrared classes.

## 2.1 Introduction

### 2.1.1 The Need for a new Dust Emission Survey

Stars form from dense gas. Such gas is, e.g., found in discrete nearby ($\lesssim$ 500 pc) cold ($\approx$ 10 K) small-scale ($\lesssim$ 0.1 pc) condensations referred to as dense cores (Myers et al. 1983). These are thought to be the sites were low-mass stars form (Myers & Benson 1983). Their properties provide the initial conditions for star formation. It is thus necessary to understand the physical state of dense cores in order to be able to understand the star formation process in detail.

Some of the many physical parameters of dense cores are their sizes, masses, and densities. Given that thermal dust continuum emission at $\approx$ 1 mm wavelength is a better mass tracer than molecular emission lines (e.g., Tafalla et al. 2002), and that modern bolometer cameras allow to acquire complete maps of the dust emission from dense cores within a short time, dust emission maps are a prime tool to study the above parameters. Dust emission surveys thus allow to systematically acquire overviews of dense core properties.

In recent years several surveys studied dense cores in large (up to several 10 pc) and massive (up to several $10^3 \, M_\odot$) complexes of molecular clouds (Motte et al. 1998, Johnstone et al. 2000, 2001, 2004, 2006, Hatchell et al.

11

**Table 2.1:** Major dust emission imaging surveys towards isolated dense cores at ≈ 1 mm wavelength. For every survey the instrument used is listed (bracketed telescope is given for unnamed facility receivers) together with the adopted observational strategy ('scan' if the map is reconstructed combining data across several chop throws, 'jiggle' otherwise). We finally list the types of cores covered ('pr.' for protostellar cores, 's.l.' for starless ones) and their number. Only 5 cores are listed for Ward-Thompson et al. (1994) as the remaining ones in their sample were not imaged.

| | | | Objects | |
| --- | --- | --- | --- | --- |
| Reference | Instrument | Strategy | Type | Number |
| *focused on isolated protostellar cores:* | | | | |
| Walker et al. (1990) | (NRAO 12m) | jiggle | pr. | 12 |
| Ladd et al. (1991a,b) | UKT14 | scan | pr. | 10 |
| Chandler et al. (1998) | UKT14 | jiggle | pr. | 3 |
| Shirley et al. (2000) | SCUBA | jiggle | pr., s.l. | 21 |
| Motte & André (2001) | (IRAM 30m) | scan | pr., s.l. | 49 |
| *focused on isolated starless cores:* | | | | |
| Ward-Thompson et al. (1994) | UKT14 | jiggle | s.l. | 5 |
| Ward-Thompson et al. (1999) | (IRAM 30m) | scan | s.l. | 8 |
| Visser et al. (2001, 2002) | SCUBA | jiggle, scan | pr., s.l. | 42 |
| Tafalla et al. (2002) | MAMBO | scan | s.l. | 5 |
| Kirk et al. (2005) | SCUBA | jiggle | s.l. | 52 |
| *c2d surveys:* | | | | |
| Brede et al. (in prep.) | SIMBA | scan | pr., s.l. | 149 |
| Wu et al. (in prep.) | SHARC II | scan | pr., s.l. | 53 |
| Young et al. (in press) | SCUBA | scan | pr., s.l. | 38 |
| ***present work*** | MAMBO | scan | pr., s.l. | 38 |

2005, Enoch et al. 2006, Young et al. 2006, Stanke et al. 2006). Although it is believed that most stars in the galaxy form in such environments (Magnani et al. 1995), two issues make it difficult to study the fundamental physics of star formation in such environments (see, e.g., Motte et al. 1998; see also Sec. 1.1.2 for illustrative examples). First, cores can be confused in crowded regions; it becomes difficult to identify and study individual cores. Second, cores might interact in crowded regions; more parameters than relevant in isolated cores influence the evolution of dense cores. These problems can be avoided if studying dense cores in relative isolation (Clemens & Barvainis 1988) instead of cores hosted in larger (up to ≳ 100 pc) complexes of giant molecular clouds (Blitz 1993).

Several surveys of cores with and without active star formation have been conducted in the past ≈ 15 years. The major dust emission imaging surveys at ≈ 1 mm wavelength from this period are summarised in Table 2.1. They have covered a large number of dense cores in a broad variety of physical states. While these surveys in principle should yield a comprehensive database on the properties of dense cores, this is in fact true only to a limited extent. Instruments for dust emission studies only recently became sensitive and stable (w.r.t. time) enough to allow to detect faint and extended emission; state-of-the-art dust emission cameras allow to reliably image faint large-scale (≳ 5′) extensions of sources initially — if at all — only detected in their brightest intensity peaks. To be more precise, many maps from the studies listed in Table 2.1 suffer from extended artifacts due to instrumental instabilities. They arise from if combining differential "chopped" intensity measurements across several chop throws (i.e., length for the differential intensity measurement) into 'scan maps'. Others suffer from incomplete mapping of scales larger than one or a few chop throws (≪ 5′), if only using differential intensity measurements between two positions separated by one chop throw to derive 'jiggle maps' or employing small

scan maps, respectively. A few are affected by both. (See Sec. 2.3.1 for a comprehensive discussion of map reconstruction problems.)

Today, state-of-the-art bolometer cameras allow to image the dust emission of dense cores with lesser instrumental biases than those affecting previous studies. This urged us to conduct a new comprehensive dust emission survey towards isolated dense cores at $\approx$ 1 mm wavelength. In particular, the research presented here is the first such census covering $\geq$ 10 starless dense cores that uses the Max-Planck Millimetre Bolometer (MAMBO) bolometer arrays (Kreysa et al. 1999) at the IRAM 30m-telescope.

A further motivation of our survey is the demand for complementary data on dense cores for the recent Spitzer Space Telescope imaging surveys of dense cores. Such data is needed to, e.g., put the properties of the stellar content probed by Spitzer in context with dense core properties like density and mass; the latter can usually not be derived from the Spitzer data. In particular the Spitzer Legacy Program "From Molecular Cores to Planet Forming Disks" (AKA. "Cores to Disks" or "c2d"; Evans et al. 2003), which imaged about 90 nearby ($\leq$ 500 pc) isolated dense cores as part of its agenda, stimulated a number of coordinated core surveys covering many spectral windows. Our core survey — the c2d MAMBO survey — is one of four new dust continuum emission surveys carried out in the c2d framework (Table 2.1).

## 2.1.2 Aim of the c2d MAMBO Survey

Dust emission data can be used to address a number of open issues in star formation research. In general, stars are thought to aggregate from very dense molecular cores ($H_2$ densities $\gg 10^5$ cm$^{-3}$). In particular, the spatial mass distribution is thought to govern the stability of dense cores against gravitational collapse (e.g., McKee & Holliman 1999). One might thus hope to derive criteria to be fulfilled to allow star formation in dense cores by comparing the mass distributions of starless cores with those of cores actively forming stars. This could lead to a better understanding of the underlying star formation physics. The c2d MAMBO survey is ideally suited for such comparative studies as it probes the mass distribution in cores with and without ongoing star formation at high sensitivity (see Sec. 2.6.3 for details).

Also, the evolution of protostars, i.e., stars that are surrounded by significant amounts of the matter from which they did or do form, can be studied with dust continuum emission data. They allow to investigate the relation between the broadband spectral properties and the structure of the circumstellar envelope (see Sec. 2.6.4 for details).

Our sample includes four candidate *Very Low Luminosity Objects* (VeLLOs; Kauffmann et al. 2005), enigmatic objects of apparent protostellar nature that were recently discovered by c2d (Young et al. 2004; cf. André et al. 1999). They are defined as objects with internal luminosities (i.e., not including the dense core luminosity from interstellar heating due to, e.g., the interstellar radiation field) $\leq 0.1\,L_{\odot}$ that are embedded in dense cores. Some of these objects have been interpreted as very young ($\lesssim 10^4$ years; André et al. 1999) protostars of stellar final mass (i.e., $\geq 0.08\,M_{\odot}$). Based on their low accretion rates, others are thought to be young objects in the process of growing to substellar final mass (Young et al. 2004; Bourke et al. 2005). The c2d MAMBO survey is the first study with a sensitive and homogenous dataset on several starless, protostellar, and VeLLO natal cores. This allows comparative studies between these core types to better understand how VeLLO natal cores differ from others (see Sec. 2.6.5 for details).

## 2.1.3 Structure of the present Study

In Sec. 2.2 we begin with an introduction to our sample and a summary of the observations. Section 2.3 details our data reduction. This includes a description of a new iterative data reduction scheme designed to mitigate problems affecting the reconstruction of maps of weak extended emission. Section 2.4 provides a first discussion of the source properties and an overview of the source identification and quantification strategies. Protostellar properties from supplemental data are derived in Sec. 2.5. The main scientific discussion of the data follows in Sec. 2.6. We summarise our findings in Sec. 2.7. Appendix A defines the standard dust emission properties adopted by the c2d collaboration to derive the mass distribution from observed dust emission maps.

## 2.2 Sample and Observations

### 2.2.1 Sample Selection

Our sample of 38 cores is drawn from the initial target list of the c2d Spitzer survey of isolated dense cores (Evans et al. 2003). This list contains dense cores within about 400 pc from the sun that are smaller than $\approx 5'$ and were mapped in dense gas tracers before the start of the c2d surveys. These cores are nearby enough to allow for the detection of intrinsically faint embedded sources. Their small apparent size allows to map them in a reasonable time. This sample was drawn from the compilations and surveys of Jijina et al. (1999, for $NH_3$ maps), Lee et al. (2001, for CS and $N_2H^+$ maps), and Caselli et al. (2002a, for $N_2H^+$ maps), and completed by adding individual cores. Due to time constraints not all sources of the initial c2d target list were observed by Spitzer.

The initial c2d target list contains about 150 cores. MAMBO is the most efficient bolometer camera available for sensitive mapping of large fields. Therefore, those cores in this list that were expected or known to have faint or extended dust continuum emission, or both, were mapped by MAMBO. The other cores were observed in other surveys with SCUBA (Young et al., in press) on the JCMT, SHARC II (Wu et al., in prep.) on the CSO, and with SIMBA on the SEST (Brede et al., in prep.). We obtained usable MAMBO data for 38 cores, which are listed in Table 2.2. Of these cores 21 are starless to our present knowledge, 4 contain VeLLOs, and 13 contain protostars (see Sec. 2.5.1 for a discussion of the association between protostars and dense cores.) Spitzer data is or will be available for 26 cores (i.e., 2/3) of the MAMBO sample. The MAMBO sample thus covers roughly 1/4 of the $\approx 90$ c2d cores probed by Spitzer. However, only 6 out of the 13 protostellar cores were so far targeted by Spitzer.

The observed cores reside in very different environments, ranging from regions of isolated low-mass star formation, like Taurus, over more turbulent regions, like the Cyg OB7 molecular cloud complex and the Cepheus Flare, to the high-mass star-forming site of Orion. In this respect the c2d MAMBO sample does not constitute a homogenous sample, but a cross section of the different star-forming clouds in the solar neighbourhood. Correspondingly our sample includes cores from near ($\approx 100$ pc) to intermediate ($\approx 400$ pc) distances.

### 2.2.2 Observations

Continuum observations of the 1.2 mm thermal dust emission were done with the IRAM 30m-telescope on Pico Veleta (Spain) using the 37-channel MAMBO-1 and 117-channel MAMBO-2 bolometer cameras of the MPIfR (Kreysa et al. 1999). A total of 122 usable maps was taken between the summer of 2002 and the winter of 2003/2004 in the framework of a flexible observing pool (Table 2.3). Only 6 maps were acquired using the MAMBO-1 array. The weather conditions were good, with zenith optical depths between 0.1 and 0.3 for most of the time, and above this for $\approx 20\%$ of the time. Some of the maps were affected by clouds. All but 13 maps (i.e., 11%) were taken at an elevation above $40°$. This yields typical line-of-sight optical depths much below 0.5. Two maps are affected by strong anomalous refraction (Altenhoff et al. 1987; one map on the southern part of L1041-2, one map on L1148).

The beam size on the sky was $11''$, and the effective frequency 250 GHz with half sensitivity limits at 210 and 290 GHz. Pointing and focus position were usually checked before and after each map. The pointing and focus corrections were usually below $3''$ and 0.3 mm, respectively. The zenith optical depth was typically measured with a skydip at least once within an hour from start or end of a map. The sources were observed with the standard on-the-fly technique, where the telescope secondary was chopping by $\approx 40''$ to $\approx 70''$ at a rate of 2 Hz parallel to the scanning direction of the telescope. The telescope was scanning in azimuth at a speed of 6 to $8'' \, s^{-1}$, except for one map of L1521B-2 for which the telescope moved in azimuth and elevation (then using the "rotated" chopping secondary). Where possible, each source was mapped with varying scanning directions (in equatorial coordinates) and chop throws. Several times per week Mars and Uranus were observed for absolute flux calibration. "Secondary" calibrators of constant but not a priori known flux density were observed every few hours.

Part of the data were already presented by Crapsi et al. (2004, for L1521F), Crapsi et al. (2005a, for TMC-2 and L492), and Young et al. (2004, for L1014). The raw data for these sources are included in this thesis and are partially complemented by additional maps.

**Table 2.2:** Dense cores covered by the c2d MAMBO survey. The table lists, from left to right, the core name adopted within the c2d collaboration, names of the core adopted by other authors, the core distance, the type of the core (i.e., starless or protostellar), the approximate galactic environment of the dense core, and whether Spitzer data is available for the core. The last column gives a rough description of the morphology of the subcores (i.e., extended substructures; see Sec. 2.4.2) within each core using the c2d standard morphology keywords (Young et al., in press; see Sec. 2.4.3 for a description).

| c2d Name | Other Names | Distance[a] pc | Type[b] | Region[c] | Spitzer Data[d] | Morphology Keywords[e] |
|---|---|---|---|---|---|---|
| L1355 | | $200 \pm 50$ | s.l. | Cepheus Flare | c2d | elongated, extended |
| L1521B-2 | | $140 \pm 10$ | s.l. | Taurus | c2d | multiple, elongated, extended |
| L1521F | | $140 \pm 10$ | Ve. | Taurus | c2d | elongated, extended |
| L1521-2 | | $140 \pm 10$ | s.l. | Taurus | c2d | round, extended |
| L1524-4 | | $140 \pm 10$ | s.l. | Taurus | c2d | multiple, round to elongated, extended |
| B18-1 | TMC-2A | $140 \pm 10$ | s.l. | Taurus | c2d | multiple, round to elongated, extended |
| TMC-2 | L1529 | $140 \pm 10$ | s.l. | Taurus | c2d | multiple, elongated, extended |
| B18-2 | | $140 \pm 10$ | s.l. | Taurus | c2d | multiple, elongated, extended |
| B18-4 | | $140 \pm 10$ | pr. | Taurus | GO 3584 | multiple, elongated, extended |
| B18-5 | | $140 \pm 10$ | s.l. | Taurus | c2d | multiple, elongated, extended |
| TMC-1C | | $140 \pm 10$ | s.l. | Taurus | c2d | multiple, elongated, extended |
| TMC-1 | L1534 | $140 \pm 10$ | s.l. | Taurus | c2d | multiple, elongated, extended |
| L1507A | | $140 \pm 10$ | s.l. | Taurus | c2d | multiple, round to elongated, extended |
| L1582A | | $400 \pm 40$ | | $\lambda$ Orionis | | multiple, elongated, extended |
| IRAS05413 | HH212-mm | $450 \pm 50$ | pr. | Orion B | | multiple, round to elongated, extended |
| L1622A | | $450 \pm 50$ | s.l. | Orion East | | multiple, elongated, extended |
| L183 | L134N | $110 \pm 10$ | s.l. | north of Ophiuchus | | multiple, round to elongated, extended |
| L438 | | $270 \pm 50$ | s.l. | Aquila Rift | c2d | round, extended |
| L492 | | $270 \pm 50$ | s.l. | Aquila Rift | c2d | elongated, extended |
| CB188 | L673-1 | $300 \pm 100$ | pr. | Aquila Rift, Cloud B | c2d | elongated, extended |
| L673-7 | | $300 \pm 100$ | Ve. | Aquila Rift, Cloud B | c2d | multiple, round to elongated, extended |
| L675 | | $300 \pm 100$ | s.l. | Aquila Rift, Cloud B | c2d | elongated, weak |
| L1100 | CB224 | $400 \pm 50$ | pr. | northern Cyg OB7 | | elongated, extended |
| L1041-2 | | $400 \pm 50$ | pr. | northern Cyg OB7 | | multiple, round to elongated, extended |
| L1148 | | $325 \pm 25$ | Ve. | Cepheus Flare | c2d | multiple, elongated, extended |
| L1155E | | $325 \pm 25$ | s.l. | Cepheus Flare | c2d | multiple, elongated, extended |
| L1082C-2 | | $400 \pm 50$ | s.l. | Cyg OB7 | | elongated, extended |
| L1082C | | $400 \pm 50$ | pr. | Cyg OB7 | | elongated, extended |
| L1082A | | $400 \pm 50$ | pr. | Cyg OB7 | | multiple, round to elongated, extended |
| L1228 | | $200 \pm 50$ | pr. | Cepheus Flare | c2d | round, extended |
| Bern48 | | $200 \pm 50$ | pr. | Cepheus Flare | c2d | round, extended |
| L1172A | | $288 \pm 25$ | pr. | Cepheus Flare | | multiple, round, extended |
| L1177 | CB230 | $288 \pm 25$ | pr. | Cepheus Flare | | round, extended |
| L1021 | | $250 \pm 50$ | s.l. | Cyg OB7 | c2d | elongated, extended |
| L1014 | | $250 \pm 50$ | Ve. | Cyg OB7 | c2d | elongated, extended |
| L1103-2 | | $250 \pm 50$ | s.l. | Cyg OB7 | | elongated, extended |
| L1251A | | $300 \pm 50$ | pr. | Cepheus Flare | c2d | multiple, round to elongated, extended |
| L1197 | | $300 \pm 50$ | s.l. | Cepheus Flare | c2d | elongated, extended |

Notes:

a) Standard c2d distances collected from the literature (Bourke, priv. comm.). These are mostly derived through star-counts. In some cases the probable association to a nearby core (e.g., inferred from similar radial velocities) with know distance is used.

b) The abbreviations mark starless cores ('s.l.'; these have no known star within the core boundaries defined in Sec. 2.4.2), protostellar cores ('pr.'; protostars within the core boundaries), and VeLLO cores ('Ve.'; VeLLOs within the core boundaries). The cores L1521-2, B18-1, TMC-1, and L1622A were excluded from the protostellar category, as the protostars are off the main core body. See Sec. 2.5.1 for a discussion of the association between protostars and dense cores.

c) The designation of regions roughly follows Dame et al. (1987), Maddalena et al. (1986), Yonekura et al. (1997), and Dobashi et al. (1994).

d) Cores with Spitzer data from the c2d project are labeled 'c2d'. For B18-4 data is only available from the general observer program 3584.

e) The s2d standard keywords are adopted from the c2d SCUBA survey by Young et al. (in press). See Sec. 2.4.3 for a description.

**Table 2.3:** MAMBO map details. For each core the products 'number of maps' × 'array type' list how often a core was observed with which array ('37' for MAMBO-1 and '117' for MAMBO-2). Several products are given if a dense core was observed with both arrays. The last column lists the minimum noise level in a map after smoothing to 20″ resolution.

| c2d Name | MAMBO Maps | Minimum Noise Level mJy per 11″ beam |
|---|---|---|
| L1355 | $2 \times 117$ | 1.6 |
| L1521B-2 | $5 \times 117$ | 1.1 |
| L1521F | $2 \times 117$ | 2.0 |
| L1521-2 | $4 \times 117$ | 1.3 |
| L1524-4 | $2 \times 117$ | 1.4 |
| B18-1 | $4 \times 117$ | 1.1 |
| TMC-2 | $4 \times 117$ | 0.9 |
| B18-2 | $2 \times 117$ | 1.3 |
| B18-4 | $3 \times 117^{a}$ | 1.1 |
| B18-5 | $3 \times 117^{a}$ | 1.1 |
| TMC-1C | $6 \times 117$ | 1.2 |
| TMC-1 | $6 \times 117$ | 1.7 |
| L1507A | $5 \times 117$ | 1.6 |
| L1582A | $3 \times 117$ | 1.3 |
| IRAS05413 | $3 \times 117$ | 1.2 |
| L1622A | $7 \times 117$ | 1.1 |
| L183 | $4 \times 117$ | 1.4 |
| L438 | $2 \times 117$ | 1.2 |
| L492 | $3 \times 117$ | 0.8 |
| CB188 | $1 \times 37, 2 \times 117$ | 0.8 |
| L673-7 | $2 \times 117$ | 1.3 |
| L675 | $1 \times 37, 2 \times 117$ | 0.9 |
| L1100 | $1 \times 37, 2 \times 117$ | 1.3 |
| L1041-2 | $4 \times 117$ | 1.4 |
| L1148 | $5 \times 117$ | 1.1 |
| L1155E | $2 \times 117$ | 1.5 |
| L1082C-2 | $2 \times 117$ | 1.8 |
| L1082C | $2 \times 117$ | 1.5 |
| L1082A | $4 \times 117$ | 1.1 |
| L1228 | $3 \times 117$ | 1.3 |
| Bern48 | $1 \times 37, 1 \times 117$ | 1.0 |
| L1172A | $2 \times 117$ | 1.5 |
| L1177 | $1 \times 117$ | 1.3 |
| L1021 | $3 \times 117$ | 1.0 |
| L1014 | $2 \times 37$ | 1.3 |
| L1103-2 | $3 \times 117$ | 1.4 |
| L1251A | $3 \times 117$ | 1.2 |
| L1197 | $6 \times 117$ | 0.9 |

Notes: a) B18-4 and B18-5 were observed together in one field.

## 2.3 Data Reduction

For the data reduction of bolometer maps of weak and extended emission we face several difficulties.

- Skynoise, i.e., the rapid fluctuation of the sky brightness, must be subtracted to reveal the faint emission of our sources. The skynoise signal is estimated as a weighted average of the signals within the bolometer array. *Thereby one tends to filter out the source itself* when the emission scale is comparable to or larger than the array diameter.

- Restoration algorithms for chopped on-the-fly maps assume that in scanning direction map boundaries are free of emission.*Too small maps lead to artifacts* (intensity offsets) if this is not the case.

We developed an iterative scheme to overcome both limitations partially. Using source models derived from smoothed maps of previous iterations, sources significantly larger than the array pattern for which the intensity does not vanish at one boundary in scanning direction can be reconstructed.

### 2.3.1 Limitations of Chopped Bolometer Maps

Bolometer mapping with a chopping secondary mirror (subreflector) yields maps of intensity differences between positions spaced by one chop throw. Spatially constant intensity backgrounds are removed by a high-pass filtering of the data in the time domain. The measured signals thus mainly reflect the spatial intensity variation in the celestial background and the spatial and temporal intensity variations in the atmospheric foreground. It is important to keep this differential nature of chopped bolometer data in mind when reducing and interpreting the data. The series of measurements can be represented in the spatial domain (e.g., to make maps) and in the temporal domain (e.g., to analyse noise properties).

The following discussion is general to all bolometer arrays observing with a chopping secondary. This includes MAMBO and SCUBA. Arrays like SIMBA, SCUBA II, SHARC II, and Bolocam employ different observing techniques. For them the following discussion of skynoise removal applies partially, while the one on source reconstruction does not apply. The bolometers for the APEX telescope will be able to operate with and without chopping.

#### 2.3.1.1 Skynoise Subtraction

The temporal atmospheric intensity variations are known as skynoise. Variations on timescales shorter than about the chopping period are fully transmitted by the high-pass filtering through the bolometer electronics. They thereby constitute a source of noise.

For every array receiver the atmospheric intensity variations can be divided into a correlated part, which produces similar signals for several or all pixels of the array, and an uncorrelated part. The correlated intensity fluctuations for a given receiver and time can be estimated from the signals in the neighbouring receivers by calculating their weighted average signal. The weights are determined by quantifying the correlation between the array pixels. The weighted average is then subtracted from the signal in the receiver considered.

This subtracted average can be "contaminated" by the signal from spatial intensity variations in the celestial background. To give an example, if the source intensity is equal between two neighbouring receivers, then here the signal of the celestial background cannot be distinguished from correlated atmospheric intensity fluctuations. If this neighbourhood is used to estimate the correlated intensity fluctuations, then the signal due to the celestial background — which is actually to be measured — is completely removed.

To mitigate this problem one can for the correlated noise estimate of a given pixel signal exclude all receivers within some sky-projected radius, $f/2$, from the neighbourhood used to estimate the correlated intensity fluctuations. In the following we refer to $f/2$ as the correlation exclusion radius. Then, for circular sources with a diameter $s < f/2$ the neighbourhood of on-source pixels is free of source emission. For $s < f$ this neighbourhood contains at least some off-source pixels, but for $s \geq f$ all neighbourhood pixels are on-source too.

Therefore, the straight-forward skynoise subtraction method outlined above will not properly reproduce sources with $s \geq f/2$, where $s$ is the maximum extent of the source along any axis.

### 2.3.1.2   Reconstruction of Extended Sources

The potential problems in the reconstruction of bolometer maps with emission at the beginning or end of a map (seen in scanning direction) can be understood by considering in detail the reconstruction of intensity maps from chopped on-the-fly mapping data.

Let $\vec{c}$ be the direction and amplitude of the chop throw, $\vec{v}$ be the telescope scanning velocity, and $\vec{x}$ be a position on the sky. Then for every receiver an ideal chopped on-the-fly observation yields a map of intensity differences between two positions spaced by $\vec{c}$:

$$\Delta I(\vec{x}, \vec{c}) = I(\vec{x} + \vec{c}) - I(\vec{x}). \tag{2.1}$$

If the telescope scanning and chopping directions are parallel, $\vec{c} \parallel \vec{v}$, and the spatial sampling of the intensity differences is sufficient, then the intensity difference between two positions spaced by an integer multiple of $\vec{c}$ can be calculated as

$$I(\vec{x} + n\vec{c}) - I(\vec{x}) = \sum_{i=1}^{n} \Delta I(\vec{x} + (i-1)\vec{c}, \vec{c}), \tag{2.2}$$

where $n \in \mathbb{Z}$. If the intensity at some position $\vec{x}_0$ in the map is known, Eq. (2.2) can be used to calculate the intensity at the positions $\vec{x}_0 + n\vec{c}$:

$$I(\vec{x}_0 + n\vec{c}) = I(\vec{x}_0) + \sum_{i=1}^{n} \Delta I(\vec{x}_0 + (i-1)\vec{c}, \vec{c}). \tag{2.3}$$

From this Emerson et al. (1979) concluded that when the intensity is zero at the start and stop position of a restorated telescope scan lag, $\vec{x}_{\text{start}}$ and $\vec{x}_{\text{stop}}$, respectively, and if furthermore $\vec{x} - \vec{x}_{\text{stop}} = n_{\text{stop}}\vec{c}$ and $\vec{x} - \vec{x}_{\text{start}} = n_{\text{start}}\vec{c}$ with $n_{\text{start}}, n_{\text{stop}} \in \mathbb{Z}$, then

$$I_{\text{EKH}}^{\text{start}}(\vec{x}) = \sum_{i=1}^{n_{\text{start}}} \Delta I(\vec{x}_{\text{start}} + (i-1)\vec{c}, \vec{c}) \quad \text{and} \tag{2.4}$$

$$I_{\text{EKH}}^{\text{stop}}(\vec{x}) = \sum_{i=1}^{n_{\text{stop}}} \Delta I(\vec{x}_{\text{stop}} + (i-1)\vec{c}, \vec{c}) \tag{2.5}$$

give the intensity at the position $\vec{x}$. If the spatial sampling of the data is fine enough, the intensity for any position along the scan path of an individual receiver can be found by changing the start and end positions for the restoration. In practice

$$I_{\text{EKH}}(\vec{x}) = [I_{\text{EKH}}^{\text{start}}(\vec{x}) + I_{\text{EKH}}^{\text{stop}}(\vec{x})]/2 \tag{2.6}$$

is adopted to derive independent intensity maps from maps of intensity differences for each receiver of an array. The start and end positions are placed as close as possible to the map boundaries, i.e. $\left| \vec{x}_{\text{start}} - \vec{x}_{\text{stop}} \right|$ is made as large as possible. The intensity distribution can thus be derived from the observed intensity differences, as long as $I(\vec{x}_{\text{start}}) = I(\vec{x}_{\text{stop}}) = 0$ for every receiver. This approach to map reconstruction is known as EKH restoration.

More generally, however,

$$I_{\text{EKH}}(\vec{x}) = I(\vec{x}) - [I(\vec{x}_{\text{start}}) + I(\vec{x}_{\text{stop}})]/2. \tag{2.7}$$

Thus the intensity distribution reconstructed using Eq. (2.6) can differ from the actual one if there is emission at the start or end position of the restoration. To avoid this the extent of the source in scan direction, $s$, must be smaller than $\left| \vec{x}_{\text{start}} - \vec{x}_{\text{stop}} \right|$ for all paths along which the data is reconstructed. The maximum possible length of such a path is $\approx \ell + c$, where $\ell$ is the length of the telescope scan path (the "scan length" in IRAM terminology), and $c = \left| \vec{c} \right|$; the relation $\left| \vec{x}_{\text{start}} - \vec{x}_{\text{stop}} \right|_{\text{max}} = \ell + c$ only holds if $\ell/c \in \mathbb{N}$. The minimum length of an independent reconstruction path is $\left| \vec{x}_{\text{start}} - \vec{x}_{\text{stop}} \right| \approx \ell - c$, as only reconstructions along the telescope scan path with start positions (same for

stop positions) spaced by $r\vec{c}$ are independent, where $r \in \mathbb{R}$ and $0 < |r| < 1$. Therefore, $s < \ell - c$ is a necessary condition for Eq. (2.6) to give the actual intensity.

These considerations holds for the reconstruction of the intensity distribution for a single receiver of a bolometer camera. Yet present bolometer arrays have several pixels which are roughly grouped in a hexagonal pattern of diameter $a$. The reconstruction paths for the individual receivers are thus displaced by up to $a$. All reconstruction start and stop positions for all receivers of an array can be free of emission only if

$$s < \ell - c - a, \tag{2.8}$$

which is, thus, the necessary requirement for Eq. (2.6) to yield the true intensity. This is a sufficient condition only if the map is centered on the source. More generally, the emission must be confined to the centre of each scan lag to obtain correct reconstructions, i.e.,

$$\left| (\vec{x} - \vec{x}_{\text{centre}}) \cdot \vec{c}/c \right| < (\ell - c - a)/2 \tag{2.9}$$

for all positions of non-vanishing intensity, $\vec{x}$, where $\vec{x}_{\text{centre}}$ is the map centre.

Yet it is possible to reconstruct the intensity distribution for sources with $s \geq \ell - c - a$. If some receiver moves off the emission during the observation, this receiver's signal can be used as reference for all other receivers. Then the reconstruction is not possible using EKH restoration; below we will devise an alternative method for this case. However, if no receiver moves off the source, then restoration is not possible. This is the case when

$$s \geq \ell + c + a. \tag{2.10}$$

### 2.3.1.3 Summary of Reconstruction Problems

Figure 2.1 summarises the problems with the reconstruction of, and skynoise subtraction in, bolometer maps of extended sources. The main parameters of this problem are the reduced mapsize, $\ell_{\text{red}} = \ell - c$, the source diameter, $s$, the array diameter, $a$, and the diameter of the region excluded from the neighbourhood used to estimate the correlated intensity variations, $f$. In practice latter is usually chosen to be as large as possible, and therefore $f \approx a$ is assumed for Fig. 2.1. The mapping restrictions because of skynoise removal hold for all bolometer arrays, independent of the specific observing mode; correlated signals always have to be estimated by averaging the signals across the array. The restrictions because of map reconstruction hold for chopped observations, but similar constraints hold for all bolometer array observations; independent of the observing mode (e.g., chopped observations or total power) a position in the mapped area must be assumed to have a zero intensity.

The limitations for bolometer mapping are not fundamental, but hard to overcome. The mapping restrictions for extended emission because of skynoise removal are fixed for a given bolometer camera. One way to overcome these limitations is to not subtract skynoise in the data reduction, but to reduce the noise level by observing the source for a longer time. The mapping restrictions from map reconstruction can be overcome by making the maps large enough. Both approaches would, however, make bolometer observations very inefficient under usual observing conditions. Skipping skynoise removal requires a longer integration time. Dropping small maps from the data analysis also increases the total integration time and, given the limited prior knowledge on the source extent, it is not always possible to choose an optimum map layout. The maximum possible map size is furthermore limited by instabilities of the receivers or amplifiers, which occur on longer timescales. It is thus desirable to be able to remove skynoise and use small maps for observations of extended sources.

Many effects not discussed here can further deteriorate the quality of the reconstructed maps. One example are drifts in the signals with time, e.g. from the electronic noise, which can be removed by subtracting polynomial fits to the time sequence data. Artifacts from such noise, or from data correction to remove such drifts, can veil signals from the celestial emission. A discussion of these effects, which are not immediately related to the map reconstruction, is beyond the scope of this paper.
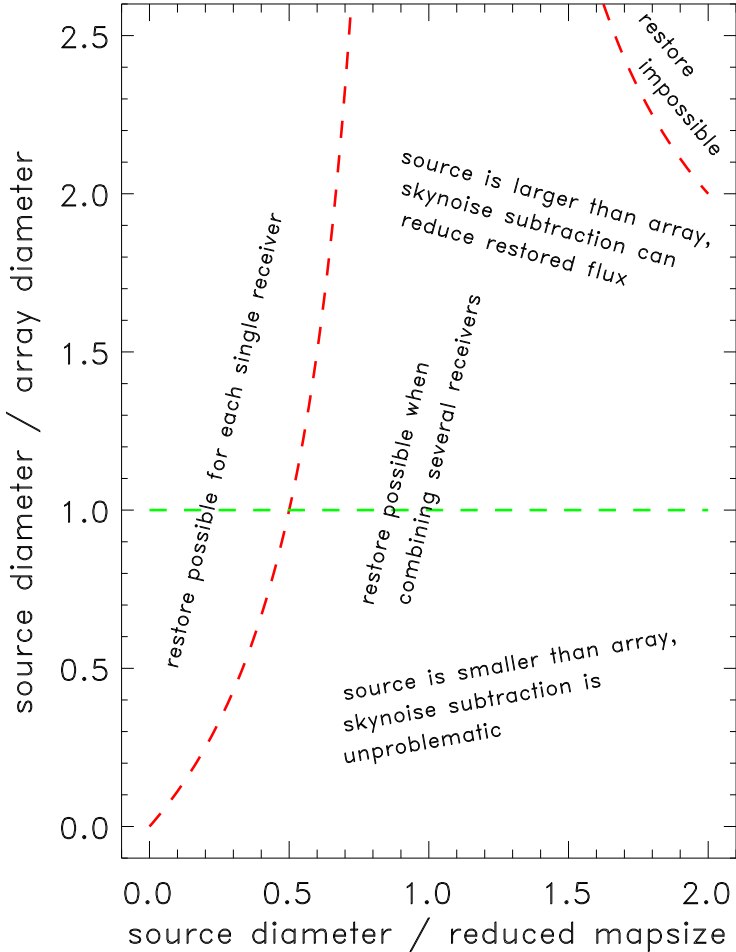
**Figure 2.1:** Summary of data reconstruction problems. The basic parameters of the problem are the source and bolometer array diameters, and the reduced mapsize, given by the difference between the length of the scan path and the chop throw. For sources large compared with the array diameter skynoise subtraction is difficult: source flux might be removed from the data when subtracting the weighted mean of the signals across the array thought to measure the skynoise. The *horizontal dashed line* (labeled by *horizontal text*) separates sources smaller than the array (for which skynoise removal is less problematic) from those larger (for which the removal is problematic). For sources large compared to the map size the map reconstruction is problematic: it is difficult to define the zero intensity level in a map from the differentially measured bolometer data if only few or no array receivers (i.e., pixels) move off the emission. For simplicity we here assume maps centered on a circular sources of diameter $s$. When increasing the source-to-map size ratio all receivers do then move off the emission when $s < \ell - c - a$ (reconstruction simple), only a few do if $\ell - c - a \leq s < \ell + c + a$ (reconstruction possible when combining several receivers), and finally none do for $s \geq \ell + c + a$ (no reconstruction possible; all indicated by *vertical lines and labels*).

### 2.3.2 Iterative Restoration and Skynoise Removal

The mentioned problems with the restoration of bolometer maps can be mitigated. A significant fraction of extended celestial emission can be preserved even with skynoise removal when subtracting an estimate of its signals from the data before estimating the correlated signals. Furthermore, information from receivers that move off the source during mapping can be used to reconstruct maps of receivers that do not move off the emission.

These techniques are implemented using iterative methods. Initially the data are reduced without skynoise removal and by using classical EKH restoration. From this an estimate of the the celestial emission is derived and used for the second iteration. The estimate of the celestial emission, the source model, is then improved in further iterations.

#### 2.3.2.1 Iterative Skynoise Removal

The subtraction of the simulated celestial emission signal (i.e., the intensity difference map calculated for a given source model) from the raw data reduces the bias by celestial emission in the correlation across the array. After skynoise subtraction the reconstruction of this data will thus ideally be the difference between the source model and the actual celestial intensity distribution. However, because the bias in the skynoise subtraction decreases with decreasing difference between the actual and model source emission (the latter might also suffer from reconstruction artifacts that are reduced when iterating), several iterations are usually required to reach convergence. Since the bias in the correlation decreases when increasing the correlation exclusion radius, a large correlation exclusion radius is still desirable for iterative skynoise removal at the price of a less accurate skynoise removal.

#### 2.3.2.2 Iterative Map Reconstruction

As shown above, EKH restoration does not yield the actual intensity received from a given position on the sky if the start or stop positions used for the reconstruction are not free of emission (Eq. 2.7). It is, however, possible to remove the intensity offsets partially, or even completely.

Consider a single receiver. Let

$$I_{\mathrm{diff}} = \left| I(\vec{x}_{\mathrm{start}}) - I(\vec{x}_{\mathrm{stop}}) \right| \tag{2.11}$$

and

$$I_{\mathrm{off}} = [I(\vec{x}_{\mathrm{start}}) + I(\vec{x}_{\mathrm{stop}}) - I_{\mathrm{diff}}]/2 \,, \tag{2.12}$$

with $I_{\mathrm{diff}} \geq 0$ and $I_{\mathrm{off}} \geq 0$ (as negative intensities are not physical). Then the result of EKH restoration reads

$$I_{\mathrm{EKH}}(\vec{x}) = I(\vec{x}) - I_{\mathrm{off}} - I_{\mathrm{diff}}/2 \,. \tag{2.13}$$

In an iterative reconstruction scheme this can be taken as a first reconstruction of the actual intensity distribution, $I_{\mathrm{rec}}^{(1)}$. These results can be used to create a model of the actual intensity distribution to be used in the second iteration, $I_{\mathrm{model}}^{(2)}$. As negative intensities are unphysical, they are truncated:

$$I_{\mathrm{model}}^{(2)}(\vec{x}) = \begin{cases} I(\vec{x}) - I_{\mathrm{off}} - I_{\mathrm{diff}}/2 & \text{where } I_{\mathrm{rec}}^{(1)}(\vec{x}) \geq 0 \\ 0 & \text{otherwise} \,. \end{cases} \tag{2.14}$$

For the further steps let $\Delta_{\vec{c}}$ be the operator that yields the intensity difference map for the chop throw $\vec{c}$, i.e. $(\Delta_{\vec{c}}I)(\vec{x}) = \Delta I(\vec{x}, \vec{c})$ (see Eq. 2.1), and let $[\ldots]_{\mathrm{EKH}}$ be the operator to perform EKH restoration on a given intensity difference map, i.e. $[\Delta_{\vec{c}}I]_{\mathrm{EKH}}(\vec{x}) = I_{\mathrm{EKH}}(\vec{x})$. We also define that for $n$ iterations

$$I_{\mathrm{rec}}^{(n)}(\vec{x}) = I_{\mathrm{model}}^{(n)}(\vec{x}) + \left[ \Delta_{\vec{c}}(I - I_{\mathrm{model}}^{(n)}) \right]_{\mathrm{EKH}}(\vec{x}) \tag{2.15}$$

with

$$I_{\mathrm{model}}^{(n)}(\vec{x}) = \begin{cases} I_{\mathrm{rec}}^{(n-1)}(\vec{x}) & \text{where } I_{\mathrm{rec}}^{(n-1)}(\vec{x}) \geq 0 \\ 0 & \text{otherwise} \,. \end{cases} \tag{2.16}$$

Then

$$I_{\text{rec}}^{(n)}(\vec{x}) = I(\vec{x}) - I_{\text{off}} - I_{\text{diff}}/2^n \,, \tag{2.17}$$

as is now shown by induction. In other words, the difference between the actual intensity and the reconstructed one, $\left|I(\vec{x}) - I_{\text{rec}}^{(n)}(\vec{x})\right| = I_{\text{off}} + I_{\text{diff}}/2^n$, decreases with every iteration if $I_{\text{diff}} > 0$.

The case $n = 1$ treated above forms the base of our proof. For larger $n$ the induction hypothesis implies

$$I_{\text{model}}^{(n+1)}(\vec{x}) = \begin{cases} I(\vec{x}) - I_{\text{off}} - I_{\text{diff}}/2^n & \text{where } I_{\text{rec}}^{n}(\vec{x}) \geq 0 \\ 0 & \text{otherwise} \end{cases} \tag{2.18}$$

for the source model. Then

$$\left[\Delta_{\vec{c}} I_{\text{model}}^{(n+1)}\right]_{\text{EKH}} (\vec{x}) = I_{\text{model}}^{(n+1)}(\vec{x}) - I_{\text{diff}}(1/2 - 1/2^{n+1}) \,, \tag{2.19}$$

where we have made use of Eq. (2.7), while substitution yields $I_{\text{model}}^{(n+1)}(\vec{x}_{\text{start}}) + I_{\text{model}}^{(n+1)}(\vec{x}_{\text{stop}}) = I_{\text{diff}}(1 - 1/2^n)$. Furthermore, as only sums are involved, $(\Delta_{\vec{c}} a)(\vec{x}) + (\Delta_{\vec{c}} b)(\vec{x}) = (\Delta_{\vec{c}}[a + b])(\vec{x})$ and $[a]_{\text{EKH}}(\vec{x}) + [b]_{\text{EKH}}(\vec{x}) = [a + b]_{\text{EKH}}(\vec{x})$, where $a$ and $b$ are arbitrary functions. Thus,

$$\begin{aligned} \left[\Delta_{\vec{c}}(I - I_{\text{model}}^{(n+1)})\right]_{\text{EKH}} (\vec{x}) \\ &= \left[\Delta_{\vec{c}} I\right]_{\text{EKH}} (\vec{x}) - \left[\Delta_{\vec{c}} I_{\text{model}}^{(n+1)}\right]_{\text{EKH}} (\vec{x}) \\ &= I(\vec{x}) - I_{\text{model}}^{(n+1)}(\vec{x}) - I_{\text{off}} - I_{\text{diff}}/2^{n+1} \,, \end{aligned} \tag{2.20}$$

which is the reconstruction of the difference in the intensity difference maps for the observed actual intensity distribution and the model intensity distribution. This reconstruction is a biased residual between the actual intensity and the source model. The sum of this residual and the source model thus gives an improved estimate of the actual intensity distribution:

$$\begin{aligned} I_{\text{rec}}^{(n+1)}(\vec{x}) &= I_{\text{model}}^{(n+1)}(\vec{x}) + \left[\Delta_{\vec{c}}(I - I_{\text{model}}^{(n+1)})\right]_{\text{EKH}} (\vec{x}) \\ &= I(\vec{x}) - I_{\text{off}} - I_{\text{diff}}/2^{n+1} \,. \end{aligned} \tag{2.21}$$

The induction hypothesis is thus proven, as Eq. (2.21) follows from Eq. (2.17).

In summary, for a single receiver the difference between the actual and the reconstructed intensity depends on the number of iterations and the intensity offset,

$$\left|I(\vec{x}) - I_{\text{rec}}^{(n)}(\vec{x})\right| = I_{\text{off}} + I_{\text{diff}}/2^n \,. \tag{2.22}$$

For a sufficiently large number of iterations the actual and reconstructed intensity differ only by the intensity offset: $\left|I(\vec{x}) - I_{\text{rec}}^{(n)}(\vec{x})\right| \rightarrow I_{\text{off}}$ for $n \rightarrow \infty$. In practice usually the start or the stop position is free of emission, $I(\vec{x}_{\text{start}}) = 0$ or $I(\vec{x}_{\text{start}}) = 0$, as — at least for our sample — problems with sources not well centered in a map are more common than source sizes exceeding the length of a map. Then $I_{\text{off}} = 0$ and thus $I_{\text{rec}}^{(n)}(\vec{x}) \rightarrow I(\vec{x})$ for $n \rightarrow \infty$. Therefore, in practice it is possible to obtain a bias-free reconstruction of the intensity distribution from the data of a single receiver, even if condition (2.9) is violated.

When co-adding intensity maps, e.g., from different receivers or scans, the convergence of the reconstruction depends on the average intensity offsets, $\langle I_{\text{off}} \rangle$, and differences, $\langle I_{\text{diff}} \rangle$, respectively, of the different map reconstructions:

$$\left|I(\vec{x}) - I_{\text{rec}}^{(n)}(\vec{x})\right| = \langle I_{\text{off}} \rangle + \langle I_{\text{diff}} \rangle /2^n \,. \tag{2.23}$$

Again, in practice usually $\langle I_{\text{off}} \rangle = 0$, and thus $\left|I(\vec{x}) - I_{\text{rec}}^{(n)}(\vec{x})\right| = \langle I_{\text{diff}} \rangle /2^n$. As the average intensity difference is smaller than or equal to the maximum intensity in the map, $\langle I_{\text{diff}} \rangle \leq I_{\text{max}}$, the maximum signal-to-artifact intensity ratio in the map, $I_{\text{max}}/\left|I(\vec{x}) - I_{\text{rec}}^{(n)}(\vec{x})\right|$, is larger than $2^n$. The ratio is, e.g., larger than 100 for $n \geq 7$, and larger than 1000 for $n \geq 10$.

**2.3.2.3 Discussion of the Iterative Reconstruction Scheme**

The scheme outlined above allows to derive correct source reconstructions for map and source parameters for which this was previously impossible. With the old scheme only sources that are smaller than the array and a limited source size comparable to the map size can be reconstructed (lower left corner in Fig. 2.1). Iterative skynoise removal now allows the reconstruction maps of sources more extended than the array (area above the horizontal line in Fig. 2.1). The iterative map reconstruction allows an unbiased source reconstruction as long as a small fraction of the receivers move off source (all area except for the upper right corner in Fig. 2.1). In summary, the parameter space for which an unbiased source reconstruction is possible is largely increased when using iterative methods.

## 2.3.3 Implementation

The iterative data reduction scheme discussed above is implemented using the MOPSI and MOPSIC software packages, which were developed and are maintained by R. Zylka. These packages provide subroutines to estimate and remove the correlated skynoise, to calculate EKH restored maps, to calculate chopped intensity difference maps for given source models, and many other tools. These routines are combined to carry out our iterative data reduction scheme.

During the first iteration no skynoise is removed. The intensity maps derived for each observation using EKH restoration are co-added. In the resulting map the area with emission is then marked by hand. The intensity for the area outside the area with emission is set to zero, as is done for all pixels with negative intensity inside the area with emission. The modified intensity map is then smoothed to an effective resolution of $20''$, except for hand-marked area with strong emission, where the data is smoothed to $14''$ resolution. This smoothing increases the signal-to-noise ratio for emission more extended than the beam. This "cleaned" intensity map is then taken as the source model for the second iteration.

In the further iterations the chopped intensity difference map for the source model is first subtracted from the raw data for every single observation. Then the correlated skynoise is estimated and subtracted. We use a correlation exclusion radius of $50''$ for all sources with data from the 37 receiver MAMBO-1 camera, and $100''$ for MAMBO-2. A constant is then subtracted from each receiver signal for every scan lag (i.e., a subscan in IRAM terminology). A co-added intensity map including all observations is then derived using EKH restoration. This map is then added to the source model, and a source model for the next iteration is derived as done above. In total 10 iterations are performed, increasing the signal-to-artifact intensity ratio to more than 1000 in ideal cases.

The use of smoothed source models does to first order not affect the effective resolution reached in the final map derived using the above scheme. A too extended source in the source model would yield non-vanishing residuals between the reconstruction of the observed intensity differences and those calculated for the source model, $\left[\Delta_{\vec{c}}(I - I_{\text{model}}^{(n)})\right]_{\text{EKH}}(\vec{x})$, which are the negative artifacts due to smoothing, plus a bias (Eq. 2.20). When summing the source model and the residuals these artifacts are thus removed from the reconstruction, provided the bias is zero.

The final maps presented here are usually smoothed to an effective resolution of $20''$, though they are available for resolutions down to $11''$. This smoothing improves the signal-to-noise level for emission more extended than the beam. In order to facilitate comparison with maps of different resolutions the data is calibrated in mJy per $11''$ beam. Further weight maps give the variation of the effective integration time per pixel across the map. They are calculated during the data reduction and used to calculate noise maps. Due to a decreasing exposure towards the map boundaries the noise increases with increasing distance from the map center.

## 2.4   Results

### 2.4.1   Maps

Figure 2.2 presents the intensity maps of the molecular cores covered by our MAMBO observations. The minimum noise level in the maps ranges from 0.8 to 2.0 mJy per 11″ beam and is listed for each source in Table 2.3. To facilitate comparison, all maps are drawn with the same contouring levels and to the same angular scale.

In most sources the maps reveal extended emission on scales of several arc-minutes, and in many fields the presence of compact emission with a full width at half maximum of only a few beams. Compared with many other bolometer surveys that often detect only the most prominent intensity peaks, our MAMBO maps are very rich in structure.

In spite of our careful data reduction, some maps are still affected by artifacts such as stripes in scanning direction and extended areas of negative intensities. Sources significantly affected by this are given lesser weight in our analysis (see below).

### 2.4.2   Source Identification and Quantification

The MAMBO maps reveal extended emission and compact emission peaks with no direct correspondence between these. We therefore separately identify and quantify extended features ('subcores'), emission peaks in these subcores, and additional 'significant peaks' that fulfil some significance criterion and are not necessarily located within the subcore boundaries.

For some properties it is not possible to derive their uncertainties by Gaussian error propagation. In these cases we compute Monte-Carlo simulations with artificial noise to estimate the uncertainties. For this we take the observed map, add artificial Gaussian noise with a spatially varying amplitude (i.e., root of the mean squared intensity) identical to the one in the observed noise maps, and then extract source properties from the resulting maps in the same way as done for the observed maps. This allows to estimate, e.g., how much the position of an intensity peak can vary due to noise. The uncertainty for a given property is estimated as the standard deviation derived from several Monte-Carlo experiments with different seeds for the artificial noise. These estimates are biased, because the noise is not removed from the input maps for the Monte-Carlo experiments, but they reflect the order of uncertainty to be expected.

To reduce the noise level for the extended emission, all quantities derived for the cores and peaks are derived from maps smoothed to 20″ resolution.

#### 2.4.2.1   Extended Structures

**Identification**   Our source identification method aims at a formal definition of what a human investigator would intuitively identify as a source. Our criteria are therefore not mathematically exact, but adopted from a series of trial-and-error experiments.

To identify sources we generate signal-to-noise (SNR) maps for a beamsize of 20″, which are then smoothed to a spatial resolution of 60″. Regions above an SNR of 2 in these maps are taken as source candidates. Obvious artifacts at the rim of the maps are excluded. The remaining area above an SNR of 2 is then hand-divided into 'subcores'. For this we search the maps for saddle points and draw core boundaries by following the gradient. This scheme is conceptually similar to, but not identical with, the "Clumpfind" algorithm by Williams et al. (1994). Our scheme thus assigns all emission above an SNR of 2 to some 'subcore'.

**Quantification**   Table 2.4 lists general information on the identified subcores. For each subcore we list the centroid position. It is derived by finding the "center of gravity" of the geometrical shape. Our calculation does not take the intensity distribution into account, i.e. the core elements are not weighted by their intensity. For each field mapped the subcores are labeled by a 'C', followed by a number in order of increasing right ascension. A star marks those cores associated with a protostar (see below). Cores with uncertain properties due to an unreliable
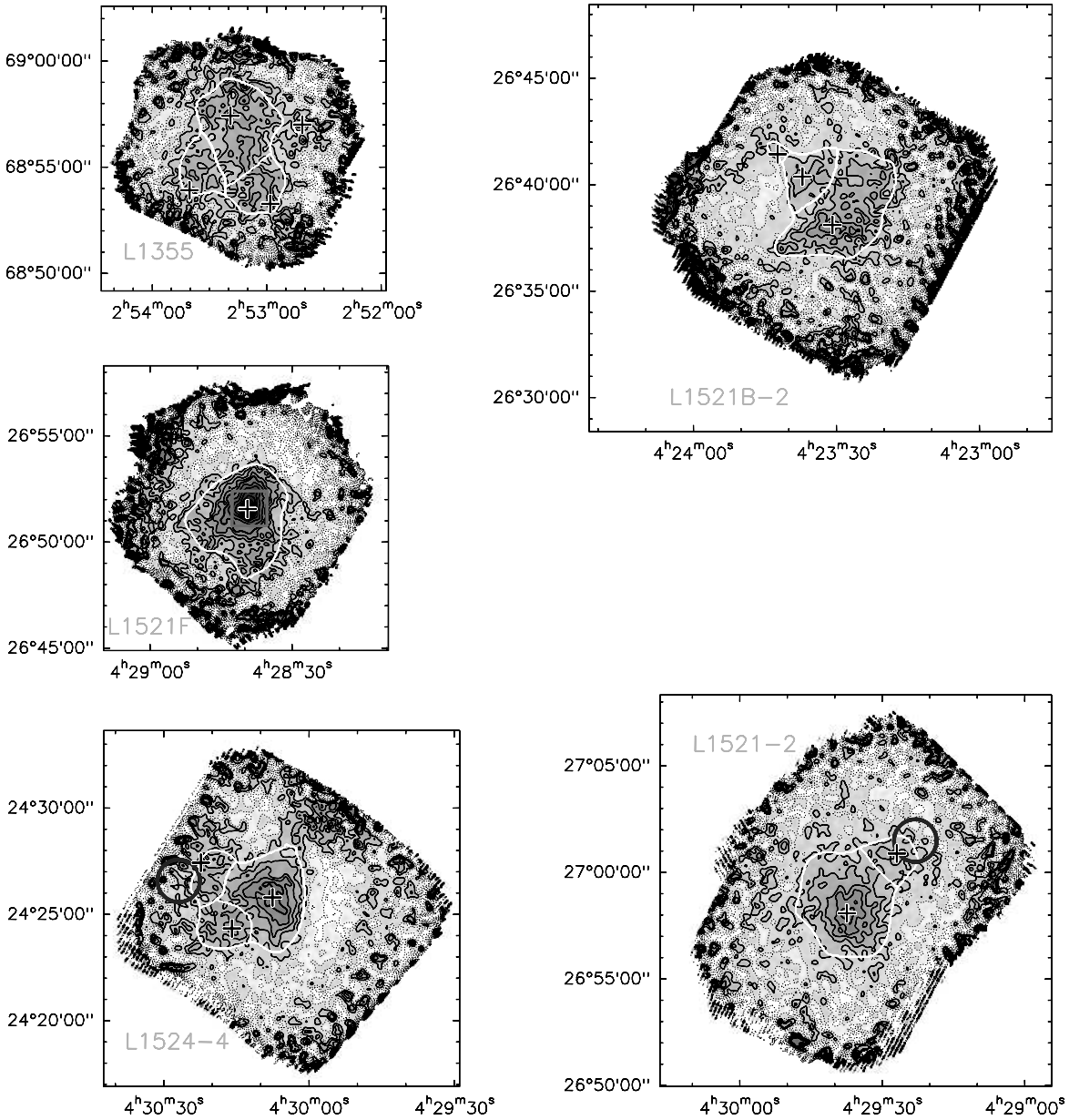
**Figure 2.2:** Maps of the sources in the c2d MAMBO survey after smoothing to 20″ resolution. *Coordinates* are given for J2000.0. The sources are roughly ordered in sequence of increasing right ascension. *Solid and dotted black contours* are drawn for positive intensities and intensities $\leq 0$ mJy beam$^{-1}$, respectively. Contours start at zero intensity and are spaced by $\pm 3$ mJy per 11″ beam; this corresponds to the noise level in the map center times a factor $\approx 2$ to 3 (Table 2.3). Above 15 mJy beam$^{-1}$, indicated by a *thick solid contour*, the contour spacing is 5 mJy beam$^{-1}$. *Gray shading* also reflects these intensity variations. *White contours* indicate subcore boundaries, while *crosses* indicate dust emission peak positions. *Circles and squares* mark the positions of IRAS and Spitzer detected infrared stars, respectively. If detected by several missions, IRAS Point Source Catalogue (PSC) positions are used instead of those from the Faint Source Catalogue (FSC), and Spitzer positions are used instead of those listed from IRAS. The IRAS PSC source 20410+6710 in L1148 is not marked, as missing Spitzer counterparts indicate that this source is an artifact.
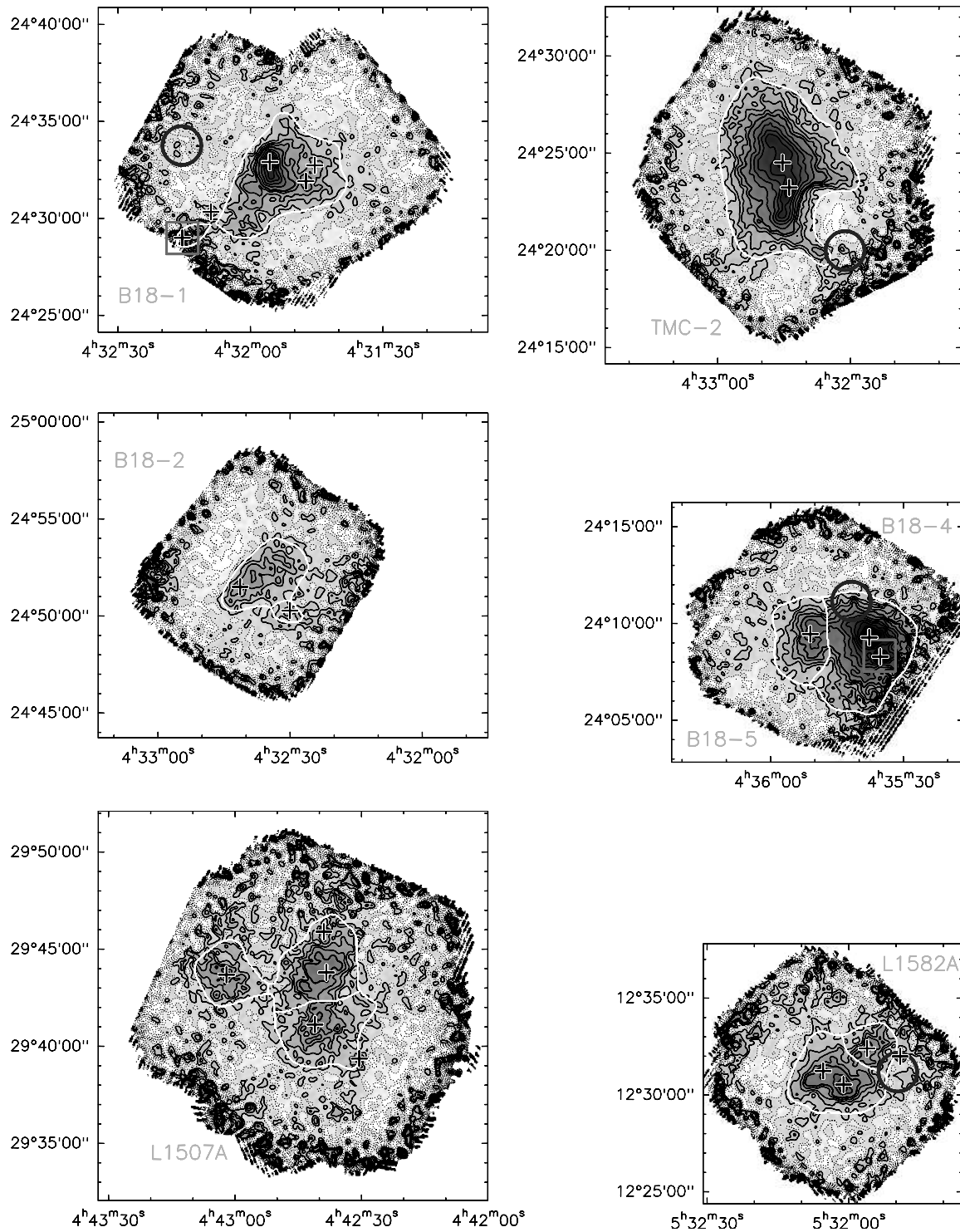
**Figure 2.2:** continued.
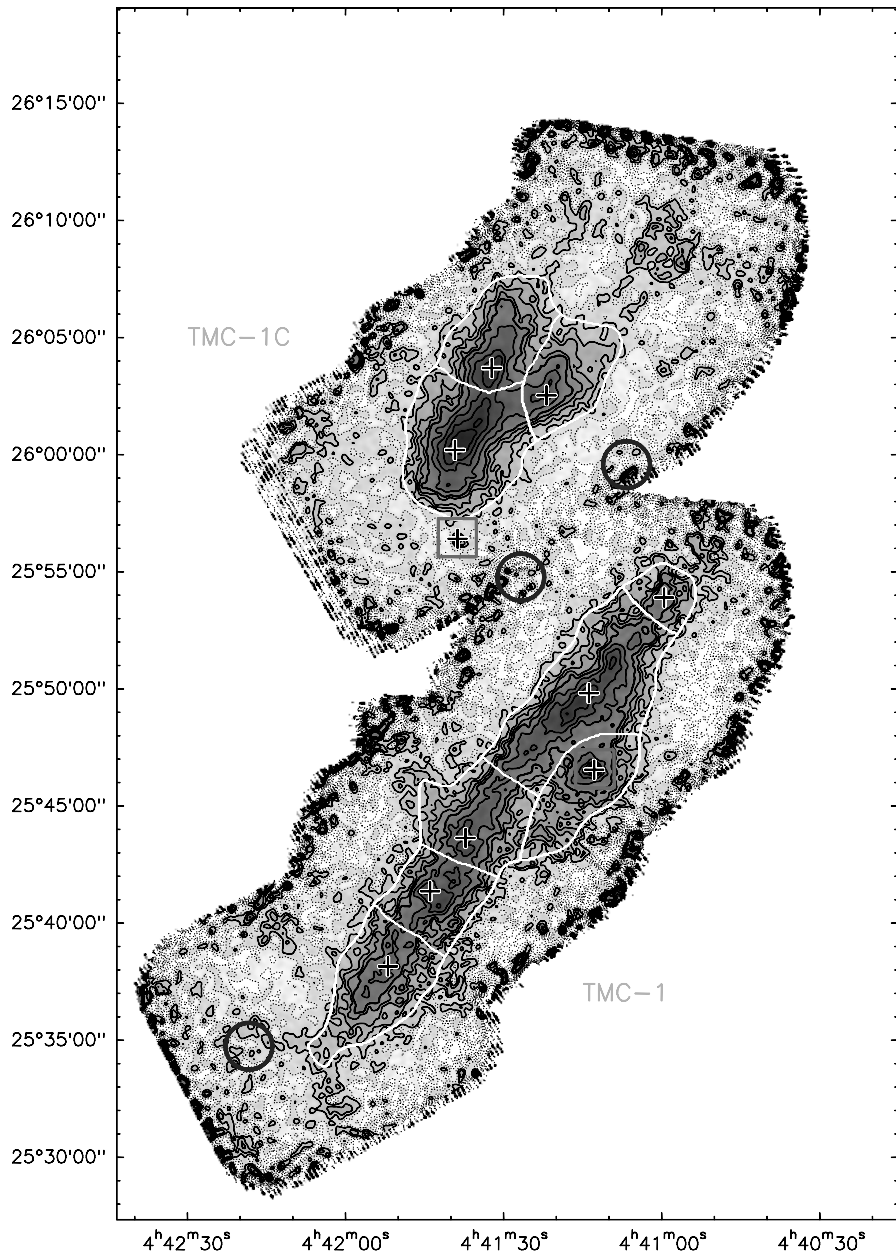
**Figure 2.2:** continued.
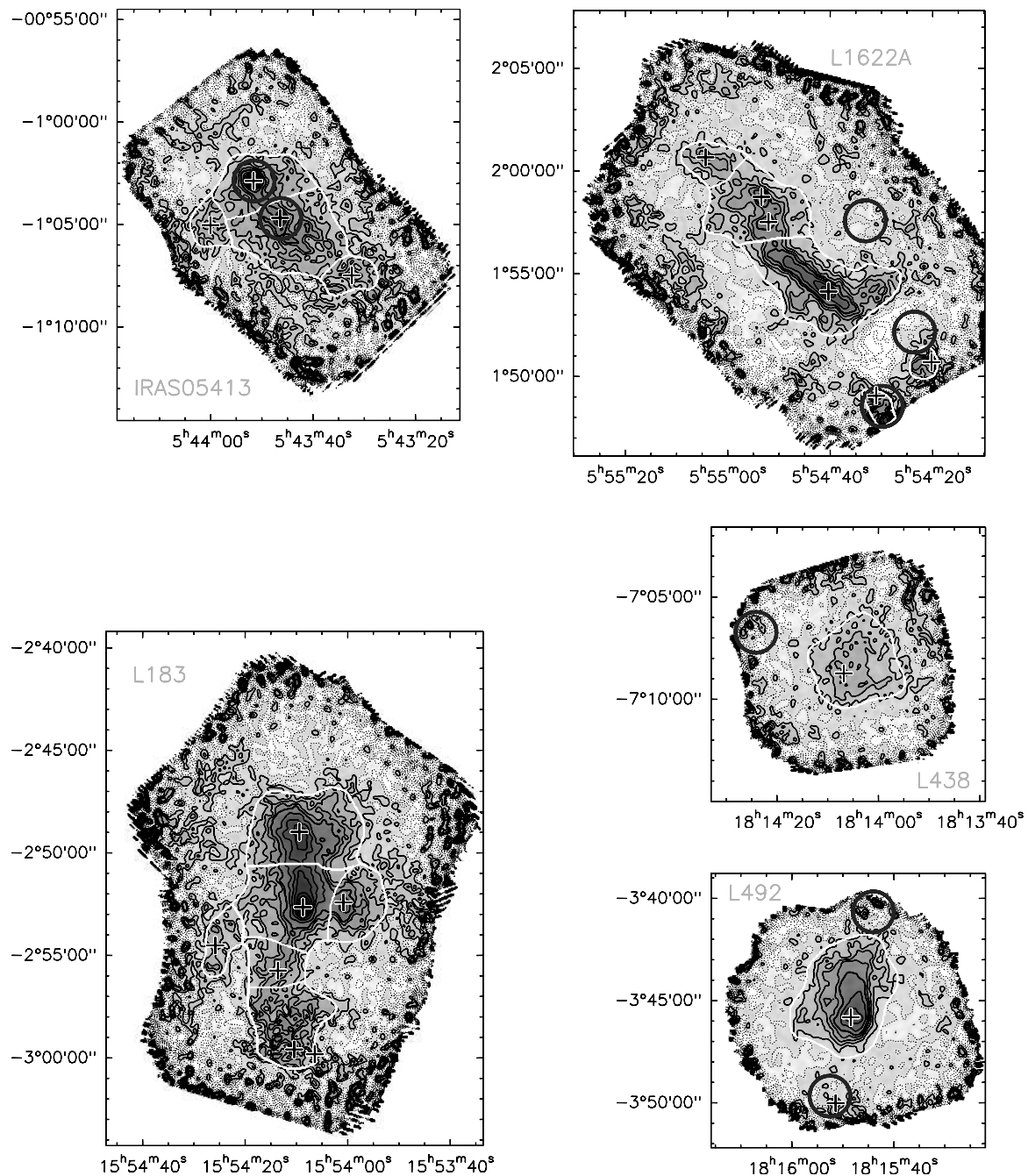
**Figure 2.2:** continued.
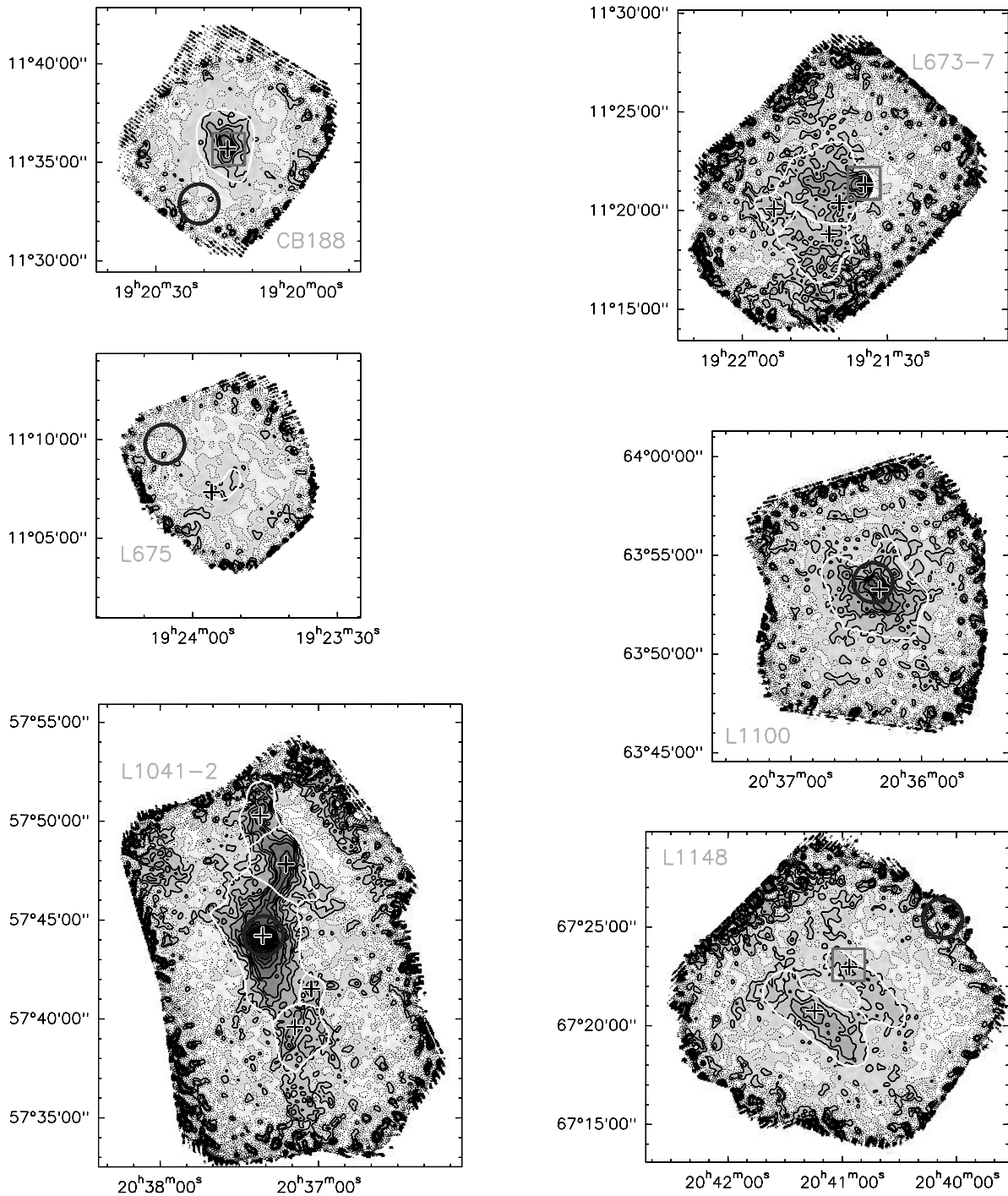
**Figure 2.2:** continued.
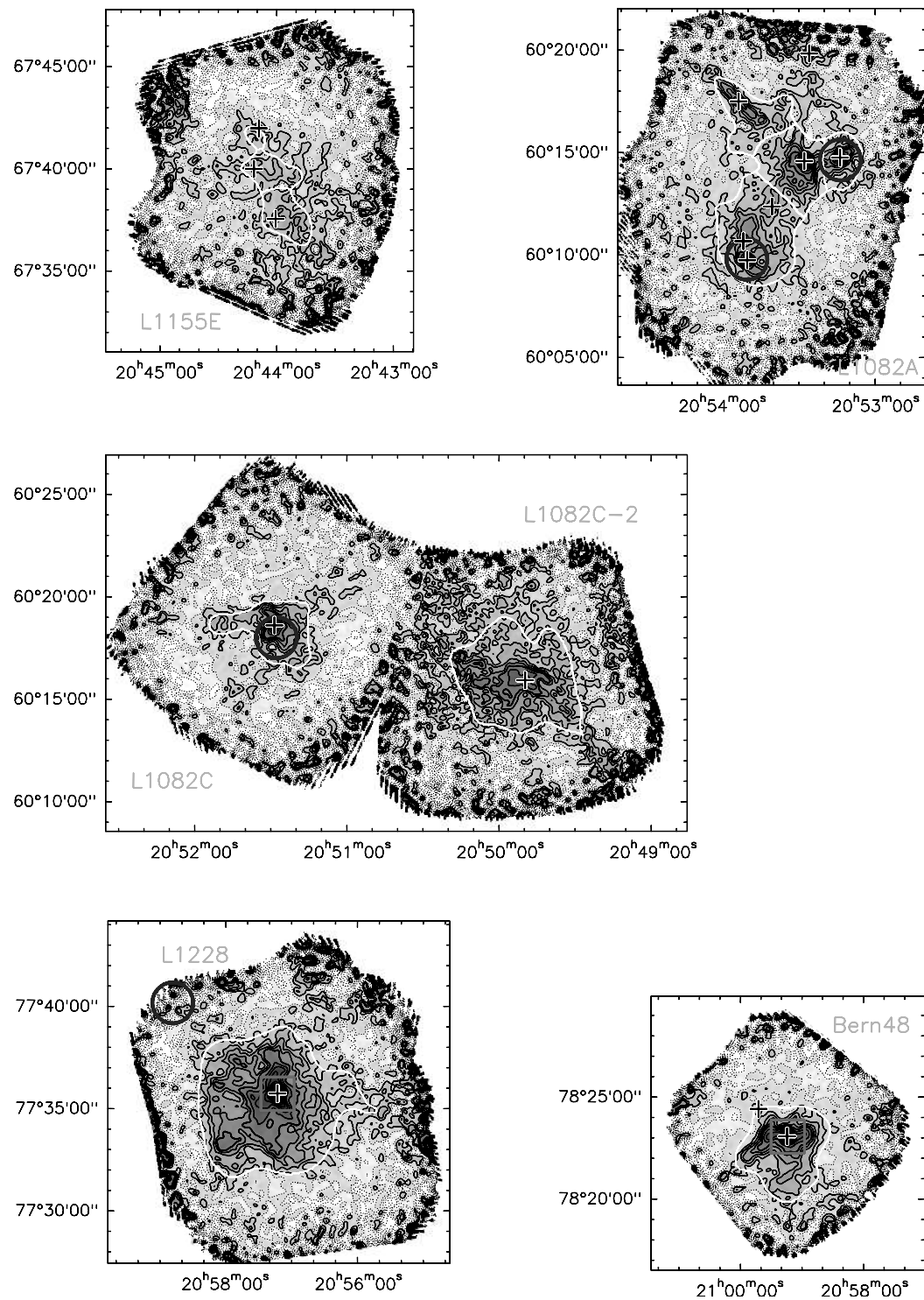
**Figure 2.2:** continued.
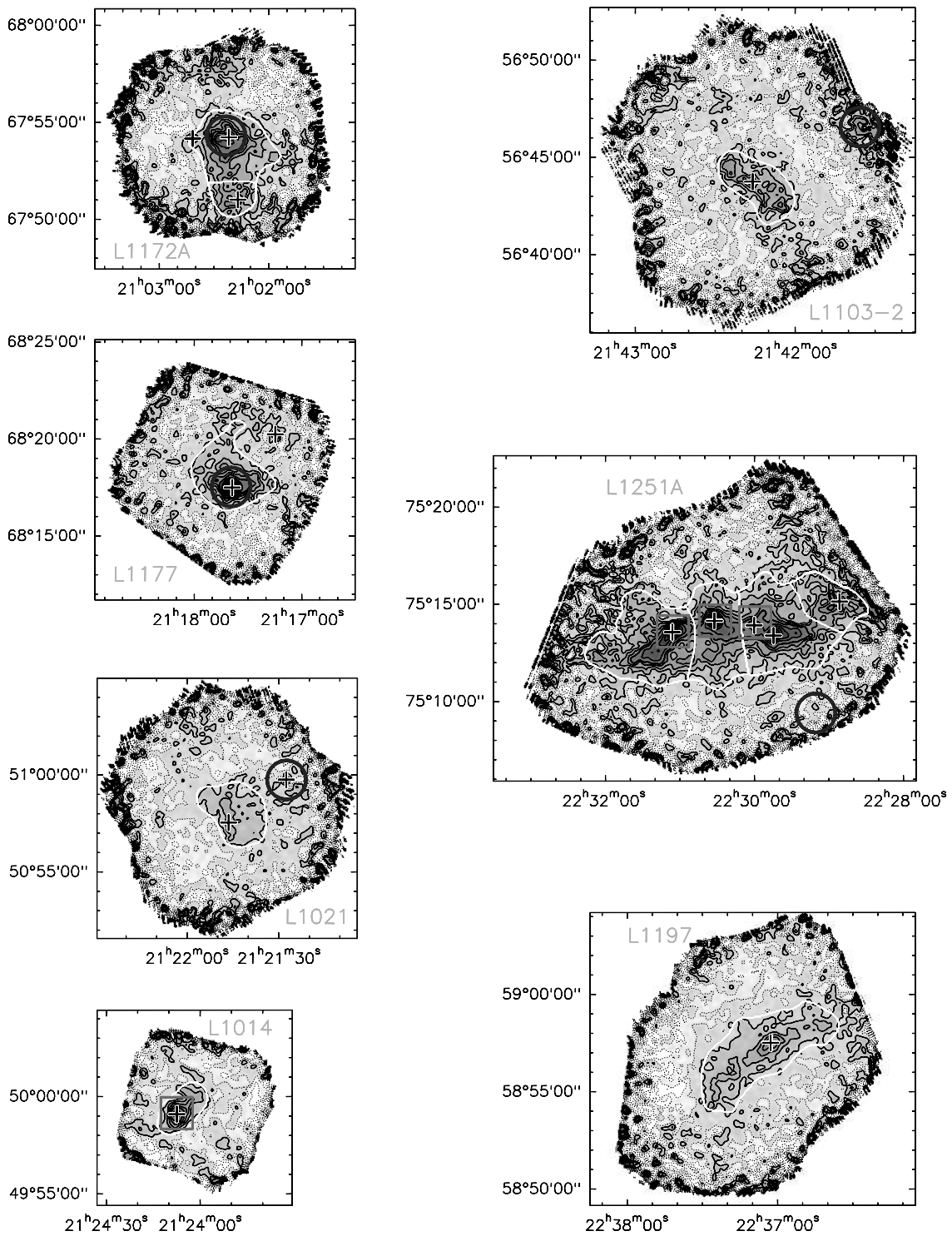
**Figure 2.2:** continued.

reconstruction are marked by square brackets. These are subcores with obvious scanning stripes in their boundaries (i.e., L183 C4), i.e., series of intensity peaks in scanning direction separated by the chop throw, those located at map boundaries (e.g., L183 C6), or with a low intensity contrast to the surrounding at the subcore boundary (e.g., L1082C-2 C1).

We then list the area assigned to the subcore, $A$, and the corresponding effective radius,

$$r_{\text{eff}} = (A/\pi)^{1/2}. \tag{2.24}$$

Furthermore, we derive the flux densities, $F$, and the corresponding masses, $M$, for the total subcore's area (subscripts 'tot') and for the area above 50% of the peak intensity for the respective subcore (subscripts '50%'). The masses are derived from the flux densities as described in Sec. 2.4.2.3. Finally, Table 2.4 lists the maximum SNR for each subcore, $S_{\text{max}}^{\text{beam}}$. The uncertainties of $F_{\text{tot}}$ and $M_{\text{tot}}$ are derived by Gaussian error propagation of the measured noise level. For $F_{50\%}$ and $M_{50\%}$ the uncertainties are estimated by the Monte-Carlo experiments described above.

Table 2.5 lists geometrical information on the identified cores. On one hand this is done by fitting ellipsoids to the area above 50% of the peak intensity for the respective core (no weighting by intensity is applied)[1]. We give the major and minor axis, $a$ and $b$, their ratio, and the position angle (east of north). The filling factor, $f$, gives the fraction of the fitted ellipse filled with emission above 50% peak intensity. Low filling factors for a few sources indicate that sometimes ellipses provide are a bad fit to the observed intensity distributions. We also list the effective diameter for the area above 70% of the peak intensity, $r_{70\%}$.

### 2.4.2.2 Peaks

**Identification**   In order to quantify all intensity peaks in our maps we study the peak position of every identified subcore. In addition we search each map manually for 'significant peaks'. These have an SNR of at least 4 and can be spatially separated from already identified peaks. To identify them we search the map for local intensity peaks with an SNR $\geq 4$ and find the surrounding contour at an SNR smaller than the peak's value by a number 3. Such a peak is taken to be significant if no brighter peak is situated in this contour. In the area outside identified cores we also require that there is also no fainter local peak within the contour. This additional restriction excludes most artifacts.

**Quantification**   Peak properties are listed in Table 2.6. For each mapped field peaks are labeled by a 'P', followed by a number in order of increasing right ascension. Uncertain peaks, which are not well reconstructed, are marked by square brackets. These were identified by searching the maps for peaks close to map boundaries, and those affected by scanning stripes.

Besides the peak position we give the subcore to which the peak belongs, if applicable. The peak intensity, $F_{\text{max}}^{\text{beam}}$, is listed besides the corresponding peak $H_2$ colum density and visual extinction, $N(H_2)$ and $A_V$. These are derived using the c2d standard assumptions on dust properties, as outlined in Appendix A, but only listed for starless cores for which there is no radiative heating. In protostellar cores the dust temperature exceeds 10 K and needs to be calculated separately for each source (Sec. 2.4.2.3). Also given are the flux density and the corresponding mass within an aperture of 4 200 AU radius, $F_{4200\text{AU}}$ and $M_{4200\text{AU}}$, as derived in Sec. 2.4.2.3. We finally list the flux density for the c2d standard apertures of 20″, 40″, 80″, 120″ diameter. In deviation to most other parts of the thesis the flux densities for the apertures are derived from unsmoothed maps, as the smoothed maps sometimes have a resolution comparable to the aperture size.

---

[1]This is implemented by using the IDL routine FitEllipse by David Fanning.

**Table 2.4:** General data on subcores. Bracketed and starred subcore designations indicate subcores with uncertain properties due to artifacts and subcores with associated protostars or VeLLOs, respectively. For every subcore the table lists the position of its "center of gravity", the subcore area and effective radius, and the integrated flux density and mass for the whole subcore and its area above 50% of its peak intensity.

| Core | | $\alpha$ J2000.0 | $\delta$ J2000.0 | $A$ arcmin$^2$ | $r_{eff}$ arcsec | AU | $F_{tot}$ Jy | $M_{tot}$ $M_\odot$ | $F_{50\%}$ Jy | $M_{50\%}$ $M_\odot$ | $S_{max}^{beam}$ |
|---|---|---|---|---|---|---|---|---|---|---|---|
| L1355 | [C1] | 02 52 43.2 | +68 56 54.0 | 0.2 | 14.6 | 2929 | 0.04 ± 0.01 | 0.08 ± 0.02 | 0.04 ± 0.00 | 0.07 ± 0.01 | 4 |
| | [C2] | 02 53 02.8 | +68 53 54.7 | 5.0 | 76.1 | 15214 | 0.98 ± 0.05 | 1.84 ± 0.09 | 0.70 ± 0.11 | 1.32 ± 0.20 | 7 |
| | [C3] | 02 53 14.9 | +68 57 03.4 | 13.1 | 122.4 | 24473 | 2.45 ± 0.07 | 4.60 ± 0.13 | 1.50 ± 0.19 | 2.82 ± 0.37 | 8 |
| | [C4] | 02 53 35.5 | +68 54 46.5 | 4.4 | 71.3 | 14261 | 0.73 ± 0.04 | 1.38 ± 0.08 | 0.49 ± 0.07 | 0.92 ± 0.14 | 5 |
| L1521B-2 | C1 | 04 23 28.0 | +26 38 27.0 | 17.6 | 142.1 | 19897 | 3.09 ± 0.07 | 2.85 ± 0.06 | 1.42 ± 0.21 | 1.31 ± 0.19 | 11 |
| | C2 | 04 23 35.5 | +26 40 19.5 | 5.5 | 79.3 | 11100 | 0.74 ± 0.03 | 0.68 ± 0.02 | 0.52 ± 0.08 | 0.48 ± 0.08 | 8 |
| | [C3] | 04 23 42.4 | +26 41 38.8 | 0.6 | 26.0 | 3647 | 0.07 ± 0.01 | 0.07 ± 0.01 | 0.06 ± 0.01 | 0.06 ± 0.01 | 5 |
| L1521F | C1$\star$ | 04 28 39.3 | +26 51 38.2 | 17.1 | 140.1 | 19609 | 5.78 ± 0.09 | 4.60 ± 0.07 | 0.92 ± 0.09 | 0.73 ± 0.07 | 33 |
| L1521-2 | C1$\star$ | 04 29 27.7 | +27 00 42.2 | 3.9 | 66.8 | 9346 | 0.50 ± 0.03 | 0.46 ± 0.03 | 0.38 ± 0.05 | 0.35 ± 0.05 | 5 |
| | C2 | 04 29 36.7 | +26 58 06.0 | 18.4 | 145.0 | 20304 | 3.47 ± 0.06 | 3.19 ± 0.05 | 1.35 ± 0.16 | 1.25 ± 0.15 | 14 |
| L1524-4 | C1 | 04 30 07.9 | +24 25 44.5 | 13.5 | 124.5 | 17430 | 3.11 ± 0.05 | 2.87 ± 0.05 | 1.60 ± 0.19 | 1.47 ± 0.18 | 13 |
| | [C2] | 04 30 17.3 | +24 24 34.1 | 4.7 | 73.4 | 10281 | 0.89 ± 0.04 | 0.82 ± 0.03 | 0.72 ± 0.06 | 0.67 ± 0.05 | 7 |
| | [C3] | 04 30 20.1 | +24 26 49.4 | 3.6 | 64.1 | 8975 | 0.58 ± 0.04 | 0.54 ± 0.03 | 0.45 ± 0.06 | 0.41 ± 0.05 | 5 |
| B18-1 | C1 | 04 31 55.4 | +24 32 33.7 | 25.2 | 170.0 | 23797 | 6.47 ± 0.06 | 5.96 ± 0.06 | 1.29 ± 0.04 | 1.18 ± 0.04 | 40 |
| | [C2$\star$] | 04 32 15.5 | +24 28 59.5 | 1.5 | 40.9 | 5719 | 0.55 ± 0.05 | 0.27 ± 0.03 | 0.15 ± 0.01 | 0.06 ± 0.00 | 13 |
| B18-2 | C1 | 04 32 29.8 | +24 50 11.4 | 1.4 | 40.0 | 5605 | 0.17 ± 0.02 | 0.16 ± 0.02 | 0.11 ± 0.03 | 0.10 ± 0.03 | 5 |
| | C2 | 04 32 36.9 | +24 52 05.1 | 11.1 | 112.9 | 15804 | 1.96 ± 0.05 | 1.81 ± 0.04 | 1.14 ± 0.13 | 1.05 ± 0.12 | 10 |
| TMC-2 | C1 | 04 32 45.9 | +24 24 08.0 | 46.4 | 230.6 | 32291 | 17.48 ± 0.08 | 16.11 ± 0.07 | 8.44 ± 0.19 | 7.77 ± 0.18 | 43 |
| B18-4 | C1$\star$ | 04 35 36.7 | +24 09 05.0 | 24.1 | 166.1 | 23260 | 12.54 ± 0.11 | 7.10 ± 0.49 | 4.03 ± 0.22 | 2.28 ± 0.16 | 42 |
| B18-5 | C1 | 04 35 50.4 | +24 09 20.6 | 11.1 | 112.6 | 15768 | 2.92 ± 0.04 | 2.69 ± 0.04 | 1.63 ± 0.09 | 1.51 ± 0.08 | 22 |
| TMC-1C | C1 | 04 41 21.5 | +26 02 55.2 | 14.3 | 128.0 | 17921 | 4.19 ± 0.05 | 3.86 ± 0.04 | 2.38 ± 0.07 | 2.19 ± 0.07 | 22 |
| | C2 | 04 41 31.7 | +26 04 06.5 | 16.9 | 139.4 | 19511 | 6.33 ± 0.06 | 5.84 ± 0.05 | 3.06 ± 0.16 | 2.82 ± 0.15 | 28 |
| | C3 | 04 41 35.9 | +26 00 54.1 | 26.7 | 175.0 | 24505 | 11.63 ± 0.07 | 10.71 ± 0.07 | 7.00 ± 0.20 | 6.45 ± 0.19 | 28 |
| TMC-1 | C1 | 04 40 59.6 | +25 53 46.7 | 5.9 | 82.0 | 11479 | 1.64 ± 0.05 | 1.51 ± 0.05 | 0.95 ± 0.08 | 0.88 ± 0.07 | 10 |
| | C2$\star$ | 04 41 13.3 | +25 46 31.7 | 14.5 | 128.9 | 18046 | 5.05 ± 0.09 | 2.77 ± 0.05 | 0.51 ± 0.09 | 0.28 ± 0.05 | 25 |
| | C3 | 04 41 16.0 | +25 49 11.6 | 32.7 | 193.5 | 27092 | 13.82 ± 0.11 | 12.73 ± 0.10 | 7.77 ± 0.61 | 7.16 ± 0.57 | 21 |
| | C4 | 04 41 34.9 | +25 44 20.7 | 17.2 | 140.2 | 19634 | 6.40 ± 0.09 | 5.90 ± 0.09 | 3.85 ± 0.36 | 3.55 ± 0.33 | 13 |
| | C5 | 04 41 42.3 | +25 41 17.4 | 13.3 | 123.6 | 17302 | 5.72 ± 0.10 | 5.27 ± 0.09 | 3.83 ± 0.35 | 3.53 ± 0.32 | 12 |
| | C6 | 04 41 52.6 | +25 38 00.2 | 19.6 | 149.8 | 20976 | 5.81 ± 0.09 | 5.35 ± 0.09 | 3.26 ± 0.27 | 3.00 ± 0.25 | 12 |
| L1507A | C1 | 04 42 39.3 | +29 43 56.6 | 16.0 | 135.2 | 18933 | 3.86 ± 0.07 | 3.55 ± 0.06 | 2.24 ± 0.20 | 2.07 ± 0.18 | 12 |
| | C2 | 04 42 39.6 | +29 41 06.2 | 14.3 | 128.0 | 17916 | 2.83 ± 0.06 | 2.60 ± 0.06 | 1.28 ± 0.16 | 1.18 ± 0.15 | 11 |

**Table 2.4:** continued.

| Core | | $\alpha$ J2000.0 | $\delta$ J2000.0 | $A$ arcmin$^2$ | $r_{\text{eff}}$ arcsec | AU | $F_{\text{tot}}$ Jy | $M_{\text{tot}}$ $M_\odot$ | $F_{50\%}$ Jy | $M_{50\%}$ $M_\odot$ | $S_{\text{max}}^{\text{beam}}$ |
|---|---|---|---|---|---|---|---|---|---|---|---|
| | C3 | 04 43 03.1 | +29 43 35.4 | 8.7 | 99.6 | 13944 | 1.75 ± 0.06 | 1.61 ± 0.05 | 0.88 ± 0.11 | 0.81 ± 0.10 | 8 |
| L1582A | C1 | 05 31 55.3 | +12 32 24.2 | 5.1 | 76.7 | 30683 | 1.16 ± 0.04 | 8.71 ± 0.30 | 0.74 ± 0.08 | 5.59 ± 0.61 | 11 |
| | C2 | 05 32 03.1 | +12 30 43.2 | 15.1 | 131.4 | 52554 | 3.97 ± 0.05 | 29.86 ± 0.40 | 1.48 ± 0.12 | 11.16 ± 0.92 | 22 |
| IRAS05413 | C1 | 05 43 32.7 | −01 07 27.6 | 4.0 | 67.3 | 30278 | 0.76 ± 0.05 | 7.23 ± 0.49 | 0.39 ± 0.05 | 3.72 ± 0.49 | 6 |
| | C2⋆ | 05 43 46.4 | −01 04 49.4 | 17.2 | 140.2 | 63097 | 4.08 ± 0.07 | 18.09 ± 6.47 | 0.27 ± 0.04 | 1.24 ± 0.37 | 32 |
| | C3⋆ | 05 43 51.6 | −01 02 51.2 | 10.6 | 110.4 | 49690 | 3.11 ± 0.04 | 12.21 ± 0.17 | 0.39 ± 0.01 | 0.74 ± 0.01 | 94 |
| | C4 | 05 44 00.1 | −01 05 00.3 | 3.5 | 63.7 | 28656 | 0.59 ± 0.03 | 5.64 ± 0.28 | 0.43 ± 0.05 | 4.09 ± 0.51 | 8 |
| L1622A | [C1] | 05 54 21.3 | +01 50 34.0 | 1.8 | 45.4 | 20418 | 0.52 ± 0.04 | 4.90 ± 0.36 | 0.37 ± 0.05 | 3.51 ± 0.50 | 6 |
| | [C2⋆] | 05 54 29.8 | +01 47 29.5 | 2.0 | 48.2 | 21694 | 0.78 ± 0.07 | 7.46 ± 0.63 | 0.07 ± 0.02 | 0.62 ± 0.16 | 6 |
| | C3 | 05 54 42.6 | +01 54 31.4 | 21.3 | 156.0 | 70222 | 5.49 ± 0.06 | 52.27 ± 0.59 | 1.43 ± 0.11 | 13.62 ± 1.04 | 28 |
| | C4 | 05 54 52.6 | +01 57 49.3 | 15.1 | 131.3 | 59097 | 3.05 ± 0.05 | 29.00 ± 0.46 | 1.19 ± 0.15 | 11.32 ± 1.46 | 17 |
| | C5 | 05 55 02.9 | +02 00 24.6 | 4.7 | 73.2 | 32926 | 0.77 ± 0.03 | 7.30 ± 0.30 | 0.43 ± 0.06 | 4.09 ± 0.54 | 8 |
| L183 | C1 | 15 54 00.5 | −02 52 28.6 | 8.1 | 96.3 | 10597 | 2.09 ± 0.05 | 1.19 ± 0.03 | 0.85 ± 0.12 | 0.48 ± 0.07 | 16 |
| | C2 | 15 54 08.6 | −02 52 03.3 | 17.0 | 139.7 | 15362 | 6.75 ± 0.06 | 3.84 ± 0.03 | 1.92 ± 0.14 | 1.09 ± 0.08 | 38 |
| | C3 | 15 54 09.1 | −02 49 17.8 | 19.0 | 147.7 | 16252 | 6.89 ± 0.08 | 3.92 ± 0.05 | 3.43 ± 0.24 | 1.95 ± 0.14 | 18 |
| | [C4] | 15 54 12.2 | −02 58 22.1 | 13.1 | 122.3 | 13458 | 3.04 ± 0.07 | 1.73 ± 0.04 | 1.77 ± 0.31 | 1.00 ± 0.17 | 8 |
| | C5 | 15 54 13.5 | −02 55 25.5 | 6.1 | 83.6 | 9195 | 1.27 ± 0.04 | 0.72 ± 0.02 | 0.75 ± 0.09 | 0.43 ± 0.05 | 10 |
| | [C6] | 15 54 25.2 | −02 54 28.4 | 4.5 | 72.0 | 7922 | 0.70 ± 0.04 | 0.40 ± 0.02 | 0.42 ± 0.06 | 0.24 ± 0.04 | 6 |
| L438 | C1 | 18 14 04.7 | −07 08 22.8 | 15.6 | 133.9 | 36145 | 2.21 ± 0.05 | 7.56 ± 0.17 | 1.32 ± 0.15 | 4.53 ± 0.51 | 9 |
| L492 | C1 | 18 15 48.1 | −03 45 11.6 | 22.6 | 161.1 | 43494 | 5.36 ± 0.05 | 18.35 ± 0.17 | 2.13 ± 0.07 | 7.31 ± 0.23 | 34 |
| CB188 | C1⋆ | 19 20 15.1 | +11 35 50.3 | 8.7 | 99.9 | 29956 | 1.33 ± 0.03 | 2.61 ± 0.09 | 0.20 ± 0.02 | 0.38 ± 0.01 | 40 |
| L673-7 | C1⋆ | 19 21 35.5 | +11 21 19.7 | 14.0 | 126.8 | 38029 | 2.31 ± 0.05 | 8.81 ± 0.63 | 0.20 ± 0.04 | 0.76 ± 0.05 | 17 |
| | [C2] | 19 21 44.0 | +11 17 58.1 | 8.7 | 100.0 | 29991 | 1.09 ± 0.05 | 4.62 ± 0.20 | 0.46 ± 0.10 | 1.96 ± 0.44 | 7 |
| | [C3] | 19 21 53.7 | +11 20 05.9 | 2.7 | 55.4 | 16629 | 0.30 ± 0.02 | 1.25 ± 0.11 | 0.15 ± 0.02 | 0.63 ± 0.10 | 7 |
| L675 | C1 | 19 23 53.0 | +11 07 43.0 | 1.5 | 42.1 | 12622 | 0.12 ± 0.01 | 0.51 ± 0.05 | 0.10 ± 0.01 | 0.42 ± 0.06 | 5 |
| L1100 | C1⋆ | 20 36 19.6 | +63 53 12.6 | 18.3 | 144.6 | 57849 | 3.53 ± 0.06 | 12.94 ± 1.04 | 0.31 ± 0.03 | 1.12 ± 0.09 | 32 |
| L1041-2 | [C1] | 20 37 02.3 | +57 41 21.7 | 1.7 | 44.1 | 17644 | 0.26 ± 0.02 | 1.93 ± 0.15 | 0.16 ± 0.02 | 1.17 ± 0.17 | 6 |
| | [C2] | 20 37 08.3 | +57 39 27.6 | 6.9 | 88.7 | 35491 | 1.12 ± 0.04 | 8.44 ± 0.30 | 0.54 ± 0.12 | 4.07 ± 0.87 | 8 |
| | C3 | 20 37 13.5 | +57 47 50.5 | 8.5 | 98.9 | 39564 | 2.42 ± 0.05 | 18.23 ± 0.35 | 1.15 ± 0.08 | 8.67 ± 0.57 | 17 |
| | C4⋆ | 20 37 21.0 | +57 44 08.3 | 22.1 | 159.0 | 63612 | 8.27 ± 0.07 | 22.34 ± 1.22 | 0.95 ± 0.02 | 2.75 ± −0.03 | 72 |
| | [C5] | 20 37 22.0 | +57 50 32.1 | 4.6 | 72.8 | 29118 | 1.19 ± 0.05 | 8.91 ± 0.36 | 0.79 ± 0.10 | 5.91 ± 0.71 | 9 |
| L1148 | C1⋆ | 20 40 48.0 | +67 22 07.6 | 7.2 | 90.6 | 29430 | 0.77 ± 0.03 | 3.12 ± 0.13 | 0.34 ± 0.08 | 1.36 ± 0.33 | 7 |
| | C2 | 20 41 08.7 | +67 20 01.4 | 12.9 | 121.6 | 39514 | 1.74 ± 0.04 | 8.65 ± 0.21 | 0.87 ± 0.09 | 4.32 ± 0.43 | 10 |

**Table 2.4:** continued.

| Core | | $\alpha$ J2000.0 | $\delta$ J2000.0 | $A$ arcmin$^2$ | $r_{\mathrm{eff}}$ arcsec | AU | $F_{\mathrm{tot}}$ Jy | $M_{\mathrm{tot}}$ $M_\odot$ | $F_{50\%}$ Jy | $M_{50\%}$ $M_\odot$ | $S_{\max}^{\mathrm{beam}}$ |
|---|---|---|---|---|---|---|---|---|---|---|---|
| L1155E | [C1] | 20 43 54.7 | +67 37 31.5 | 4.8 | 74.3 | 24132 | 0.77 ± 0.04 | 3.82 ± 0.18 | 0.40 ± 0.08 | 1.97 ± 0.42 | 7 |
| | [C2] | 20 44 01.9 | +67 39 49.6 | 3.9 | 66.5 | 21602 | 0.51 ± 0.03 | 2.55 ± 0.15 | 0.40 ± 0.05 | 1.96 ± 0.25 | 5 |
| | [C3] | 20 44 09.4 | +67 41 38.0 | 0.8 | 30.5 | 9901 | 0.10 ± 0.01 | 0.51 ± 0.07 | 0.05 ± 0.02 | 0.23 ± 0.08 | 6 |
| L1082C-2 | [C1] | 20 49 55.0 | +60 15 49.7 | 26.0 | 172.7 | 69072 | 6.43 ± 0.11 | 48.35 ± 0.80 | 1.98 ± 0.31 | 14.90 ± 2.33 | 13 |
| L1082C | C1⋆ | 20 51 28.3 | +60 18 34.7 | 10.0 | 107.2 | 42893 | 2.34 ± 0.06 | 10.19 ± 1.92 | 0.41 ± 0.04 | 1.79 ± 0.34 | 21 |
| L1082A | C1⋆ | 20 53 13.7 | +60 14 45.0 | 4.4 | 71.0 | 28402 | 0.99 ± 0.03 | 3.67 ± 0.46 | 0.24 ± 0.01 | 0.89 ± 0.11 | 26 |
| | C2 | 20 53 27.9 | +60 14 33.8 | 10.2 | 108.3 | 43328 | 2.47 ± 0.04 | 18.56 ± 0.29 | 0.28 ± 0.00 | 2.09 ± 0.03 | 63 |
| | C3⋆ | 20 53 50.4 | +60 09 45.1 | 16.7 | 138.2 | 55279 | 3.14 ± 0.05 | 12.70 ± 0.83 | 0.18 ± 0.01 | 0.75 ± 0.05 | 29 |
| | C4 | 20 53 51.9 | +60 17 17.9 | 8.2 | 97.0 | 38808 | 1.23 ± 0.04 | 9.24 ± 0.28 | 0.40 ± 0.04 | 3.05 ± 0.29 | 13 |
| L1228 | C1⋆ | 20 57 13.2 | +77 35 44.0 | 43.3 | 222.7 | 44545 | 13.24 ± 0.10 | 10.95 ± 0.08 | 0.56 ± 0.01 | 0.39 ± 0.01 | 107 |
| Bern48 | C1⋆ | 20 59 13.9 | +78 23 04.4 | 15.5 | 133.4 | 26689 | 4.17 ± 0.05 | 2.32 ± 0.03 | 0.43 ± 0.01 | 0.10 ± 0.00 | 159 |
| L1172A | C1 | 21 02 20.5 | +67 51 08.8 | 3.8 | 65.6 | 18905 | 0.82 ± 0.05 | 3.21 ± 0.18 | 0.51 ± 0.09 | 2.01 ± 0.33 | 7 |
| | C2⋆ | 21 02 22.8 | +67 54 03.1 | 12.4 | 119.0 | 34269 | 3.04 ± 0.06 | 7.57 ± 0.38 | 0.77 ± 0.10 | 1.92 ± 0.10 | 21 |
| L1177 | C1⋆ | 21 17 39.0 | +68 17 30.3 | 11.5 | 114.8 | 33063 | 2.93 ± 0.05 | 4.70 ± 0.26 | 0.47 ± 0.01 | 0.68 ± 0.08 | 104 |
| L1021 | C1 | 21 21 44.5 | +50 57 51.5 | 8.8 | 100.5 | 25114 | 1.02 ± 0.03 | 2.98 ± 0.09 | 0.64 ± 0.08 | 1.87 ± 0.22 | 8 |
| L1014 | C1⋆ | 21 24 07.2 | +49 59 05.0 | 4.7 | 73.3 | 18326 | 0.85 ± 0.03 | 1.93 ± 0.07 | 0.29 ± 0.03 | 0.66 ± 0.08 | 16 |
| L1103-2 | C1 | 21 42 14.2 | +56 43 34.1 | 8.9 | 101.0 | 25254 | 1.53 ± 0.04 | 4.48 ± 0.13 | 0.92 ± 0.10 | 2.70 ± 0.29 | 8 |
| L1251A | [C1] | 22 28 53.5 | +75 14 56.6 | 7.2 | 90.9 | 27270 | 1.66 ± 0.06 | 7.03 ± 0.26 | 0.77 ± 0.15 | 3.27 ± 0.63 | 8 |
| | C2⋆ | 22 29 42.7 | +75 13 32.2 | 18.0 | 143.7 | 43099 | 4.85 ± 0.06 | 14.98 ± 1.31 | 0.96 ± 0.11 | 2.96 ± 0.26 | 30 |
| | C3⋆ | 22 30 32.1 | +75 14 07.9 | 13.0 | 122.2 | 36667 | 3.62 ± 0.05 | 13.20 ± 1.42 | 0.36 ± 0.01 | 1.32 ± 0.14 | 52 |
| | C4⋆ | 22 31 11.7 | +75 13 06.8 | 19.0 | 147.7 | 44319 | 4.96 ± 0.07 | 18.40 ± 1.50 | 0.98 ± 0.08 | 3.65 ± 0.30 | 34 |
| L1197 | C1 | 22 37 02.9 | +58 57 20.8 | 20.8 | 154.4 | 46325 | 2.58 ± 0.05 | 10.93 ± 0.20 | 0.38 ± 0.10 | 1.60 ± 0.42 | 17 |

**Table 2.5:** Geometry data of subcores. See Table 2.4 for an explanation of the subcore designations. For every subcore the table lists the major and minor axis at the 50% peak intensity level and their ratio, the position angle of the major axis (east of north), and the effective radius at the 70% peak intensity level.

| Core | | $a$ | | $b$ | | $a/b$ | P.A. | $f$ | $r_{70\%}$ | |
| --- | --- | --- | --- | --- | --- | --- | --- | --- | --- | --- |
| | | arcsec | AU | arcsec | AU | | deg | | arcsec | AU |
| L1355 | [C1] | 30 ± 1 | 5942 ± 297 | 23 ± 4 | 4615 ± 709 | 1.3 ± 0.3 | 63 ± 35 | 0.98 ± 0.05 | 11.0 ± 1.5 | 2199 ± 292 |
| | [C2] | 157 ± 11 | 31456 ± 2140 | 121 ± 8 | 24211 ± 1543 | 1.3 ± 0.1 | 138 ± 28 | 0.67 ± 0.11 | 32.0 ± 7.1 | 6393 ± 1417 |
| | [C3] | 267 ± 11 | 53495 ± 2275 | 163 ± 15 | 32665 ± 2968 | 1.6 ± 0.2 | 14 ± 5 | 0.57 ± 0.09 | 35.8 ± 7.5 | 7153 ± 1500 |
| | [C4] | 140 ± 15 | 28097 ± 2946 | 111 ± 14 | 22116 ± 2895 | 1.3 ± 0.2 | 6 ± 75 | 0.64 ± 0.09 | 24.5 ± 5.8 | 4901 ± 1161 |
| L1521B-2 | C1 | 304 ± 25 | 42574 ± 3452 | 148 ± 12 | 20669 ± 1655 | 2.1 ± 0.2 | 131 ± 5 | 0.47 ± 0.06 | 36.5 ± 5.4 | 5113 ± 753 |
| | C2 | 151 ± 13 | 21160 ± 1821 | 105 ± 12 | 14649 ± 1689 | 1.4 ± 0.2 | 124 ± 7 | 0.79 ± 0.07 | 34.1 ± 5.8 | 4772 ± 816 |
| | [C3] | 61 ± 11 | 8493 ± 1493 | 34 ± 5 | 4769 ± 696 | 1.8 ± 0.5 | 45 ± 14 | 0.90 ± 0.13 | 17.1 ± 3.0 | 2394 ± 424 |
| L1521F | C1* | 69 ± 8 | 9715 ± 1058 | 51 ± 3 | 7186 ± 477 | 1.4 ± 0.2 | 172 ± 50 | 0.91 ± 0.03 | 17.1 ± 0.7 | 2394 ± 103 |
| L1521-2 | C1* | 130 ± 9 | 18267 ± 1307 | 117 ± 15 | 16322 ± 2161 | 1.1 ± 0.2 | 95 ± 47 | 0.66 ± 0.08 | 36.5 ± 5.4 | 5113 ± 750 |
| | C2 | 152 ± 14 | 21276 ± 1913 | 127 ± 15 | 17817 ± 2035 | 1.2 ± 0.1 | 8 ± 59 | 0.87 ± 0.04 | 34.1 ± 7.6 | 4772 ± 1062 |
| L1524-4 | C1 | 176 ± 11 | 24656 ± 1603 | 129 ± 16 | 18127 ± 2254 | 1.4 ± 0.1 | 45 ± 11 | 0.79 ± 0.04 | 42.3 ± 8.7 | 5916 ± 1214 |
| | [C2] | 139 ± 6 | 19441 ± 814 | 123 ± 8 | 17275 ± 1144 | 1.1 ± 0.1 | 81 ± 35 | 0.81 ± 0.07 | 40.8 ± 4.1 | 5713 ± 568 |
| | [C3] | 154 ± 17 | 21623 ± 2404 | 97 ± 6 | 13585 ± 818 | 1.6 ± 0.2 | 157 ± 30 | 0.64 ± 0.11 | 28.7 ± 4.7 | 4016 ± 654 |
| B18-1 | C1 | 109 ± 2 | 15321 ± 300 | 60 ± 2 | 8362 ± 287 | 1.8 ± 0.1 | 8 ± 2 | 0.92 ± 0.02 | 24.3 ± 1.0 | 3408 ± 136 |
| | [C2*] | 24 ± 5 | 3412 ± 660 | 22 ± 1 | 3016 ± 163 | 1.1 ± 0.3 | 180 ± 60 | 1.00 ± 0.04 | 8.4 ± 0.3 | 1173 ± 40 |
| B18-2 | C1 | 87 ± 20 | 12197 ± 2849 | 39 ± 10 | 5512 ± 1331 | 2.2 ± 0.3 | 61 ± 24 | 0.82 ± 0.12 | 18.1 ± 4.2 | 2534 ± 587 |
| | C2 | 243 ± 13 | 34010 ± 1855 | 96 ± 9 | 13484 ± 1267 | 2.5 ± 0.1 | 124 ± 3 | 0.79 ± 0.06 | 42.5 ± 5.8 | 5955 ± 808 |
| TMC-2 | C1 | 309 ± 4 | 43306 ± 630 | 155 ± 3 | 21764 ± 485 | 2.0 ± 0.0 | 10 ± 1 | 0.84 ± 0.01 | 75.6 ± 2.3 | 10581 ± 327 |
| B18-4 | C1* | 147 ± 4 | 20536 ± 629 | 102 ± 4 | 14268 ± 609 | 1.4 ± 0.1 | 37 ± 4 | 0.91 ± 0.03 | 31.7 ± 1.8 | 4432 ± 259 |
| B18-5 | C1 | 152 ± 7 | 21256 ± 922 | 101 ± 4 | 14074 ± 625 | 1.5 ± 0.1 | 180 ± 87 | 0.92 ± 0.02 | 44.8 ± 2.8 | 6268 ± 390 |
| TMC-1C | C1 | 174 ± 3 | 24379 ± 457 | 122 ± 4 | 17116 ± 585 | 1.4 ± 0.1 | 148 ± 4 | 0.90 ± 0.02 | 50.6 ± 2.7 | 7081 ± 384 |
| | C2 | 211 ± 9 | 29494 ± 1221 | 112 ± 6 | 15654 ± 817 | 1.9 ± 0.1 | 158 ± 2 | 0.80 ± 0.03 | 43.6 ± 2.7 | 6107 ± 374 |
| | C3 | 335 ± 6 | 46903 ± 820 | 144 ± 4 | 20221 ± 528 | 2.3 ± 0.1 | 143 ± 1 | 0.80 ± 0.02 | 64.1 ± 2.8 | 8971 ± 397 |
| TMC-1 | C1 | 134 ± 9 | 18765 ± 1322 | 92 ± 10 | 12926 ± 1438 | 1.5 ± 0.2 | 158 ± 15 | 0.76 ± 0.08 | 34.8 ± 3.0 | 4875 ± 426 |
| | C2* | 58 ± 9 | 8144 ± 1304 | 44 ± 9 | 6120 ± 1201 | 1.3 ± 0.2 | 94 ± 22 | 0.91 ± 0.07 | 13.4 ± 0.6 | 1875 ± 86 |
| | C3 | 475 ± 15 | 66492 ± 2117 | 134 ± 10 | 18734 ± 1391 | 3.5 ± 0.2 | 133 ± 1 | 0.76 ± 0.03 | 66.4 ± 7.1 | 9297 ± 996 |
| | C4 | 284 ± 6 | 39699 ± 859 | 120 ± 14 | 16804 ± 1983 | 2.4 ± 0.3 | 149 ± 1 | 0.82 ± 0.03 | 55.9 ± 9.4 | 7829 ± 1313 |
| | C5 | 244 ± 10 | 34105 ± 1405 | 127 ± 12 | 17728 ± 1622 | 1.9 ± 0.2 | 135 ± 3 | 0.87 ± 0.04 | 57.1 ± 6.9 | 7988 ± 959 |
| | C6 | 270 ± 10 | 37819 ± 1389 | 126 ± 12 | 17662 ± 1617 | 2.1 ± 0.2 | 147 ± 3 | 0.85 ± 0.04 | 63.9 ± 7.6 | 8950 ± 1066 |
| L1507A | C1 | 221 ± 15 | 30936 ± 2122 | 134 ± 7 | 18783 ± 984 | 1.6 ± 0.1 | 153 ± 5 | 0.81 ± 0.04 | 52.5 ± 5.9 | 7356 ± 832 |
| | C2 | 160 ± 12 | 22420 ± 1672 | 145 ± 17 | 20248 ± 2432 | 1.1 ± 0.1 | 166 ± 56 | 0.71 ± 0.06 | 39.8 ± 7.7 | 5577 ± 1081 |
| | C3 | 158 ± 12 | 22079 ± 1690 | 106 ± 14 | 14891 ± 1993 | 1.5 ± 0.2 | 55 ± 34 | 0.69 ± 0.06 | 27.9 ± 4.6 | 3910 ± 646 |

**Table 2.5:** continued.

| Core | | $a$ arcsec | $a$ AU | $b$ arcsec | $b$ AU | $a/b$ | P.A. deg | $f$ | $r_{70\%}$ arcsec | $r_{70\%}$ AU |
|---|---|---|---|---|---|---|---|---|---|---|
| L1582A | C1 | 139 ± 14 | 55663 ± 5515 | 84 ± 8 | 33637 ± 3343 | 1.7 ± 0.2 | 144 ± 7 | 0.76 ± 0.06 | 34.7 ± 4.7 | 13885 ± 1871 |
| | C2 | 170 ± 9 | 67871 ± 3470 | 85 ± 6 | 33838 ± 2478 | 2.0 ± 0.2 | 73 ± 4 | 0.81 ± 0.04 | 26.4 ± 3.5 | 10568 ± 1398 |
| IRAS05413 | C1 | 162 ± 11 | 73042 ± 4916 | 95 ± 10 | 42641 ± 4293 | 1.7 ± 0.2 | 114 ± 10 | 0.41 ± 0.06 | 18.5 ± 3.9 | 8336 ± 1773 |
| | C2★ | 67 ± 19 | 30110 ± 8642 | 36 ± 2 | 16175 ± 929 | 1.9 ± 0.5 | 13 ± 67 | 0.66 ± 0.18 | 11.7 ± 0.3 | 5257 ± 150 |
| | C3★ | 28 ± 0 | 12508 ± 113 | 26 ± 1 | 11595 ± 265 | 1.1 ± 0.0 | 119 ± 25 | 0.98 ± 0.01 | 9.3 ± 0.1 | 4168 ± 41 |
| | C4 | 119 ± 8 | 53594 ± 3587 | 103 ± 10 | 46547 ± 4339 | 1.2 ± 0.1 | 170 ± 68 | 0.67 ± 0.09 | 30.8 ± 5.4 | 13852 ± 2428 |
| L1622A | [C1] | 82 ± 7 | 37112 ± 3135 | 73 ± 10 | 32685 ± 4597 | 1.1 ± 0.3 | 121 ± 23 | 0.71 ± 0.09 | 20.1 ± 3.4 | 9062 ± 1516 |
| | [C2★] | 18 ± 8 | 8323 ± 3632 | 7 ± 2 | 3179 ± 1024 | 2.6 ± 0.5 | 122 ± 8 | 1.00 ± 0.12 | 3.9 ± 0.2 | 1777 ± 73 |
| | C3 | 269 ± 12 | 121133 ± 5582 | 40 ± 2 | 18114 ± 963 | 6.7 ± 0.3 | 53 ± 1 | 0.87 ± 0.03 | 21.9 ± 2.0 | 9855 ± 879 |
| | C4 | 177 ± 11 | 79819 ± 5046 | 97 ± 14 | 43660 ± 6231 | 1.8 ± 0.2 | 17 ± 7 | 0.74 ± 0.05 | 29.7 ± 5.1 | 13359 ± 2285 |
| | C5 | 158 ± 16 | 71105 ± 7025 | 65 ± 11 | 29159 ± 5133 | 2.4 ± 0.4 | 66 ± 5 | 0.71 ± 0.07 | 29.8 ± 4.2 | 13388 ± 1881 |
| L183 | C1 | 112 ± 11 | 12294 ± 1188 | 84 ± 12 | 9187 ± 1330 | 1.3 ± 0.1 | 177 ± 72 | 0.82 ± 0.06 | 25.7 ± 3.5 | 2832 ± 386 |
| | C2 | 151 ± 9 | 16650 ± 1007 | 60 ± 3 | 6603 ± 378 | 2.5 ± 0.2 | 180 ± 89 | 0.92 ± 0.03 | 22.8 ± 1.1 | 2505 ± 120 |
| | C3 | 177 ± 10 | 19468 ± 1099 | 143 ± 9 | 15775 ± 1003 | 1.2 ± 0.1 | 50 ± 13 | 0.87 ± 0.04 | 51.5 ± 4.7 | 5664 ± 521 |
| | [C4] | 238 ± 13 | 26193 ± 1395 | 177 ± 17 | 19499 ± 1890 | 1.3 ± 0.1 | 11 ± 70 | 0.54 ± 0.09 | 38.5 ± 9.5 | 4240 ± 1045 |
| | C5 | 140 ± 7 | 15415 ± 812 | 90 ± 13 | 9932 ± 1435 | 1.6 ± 0.2 | 144 ± 13 | 0.85 ± 0.06 | 31.8 ± 5.6 | 3502 ± 612 |
| | [C6] | 205 ± 19 | 22556 ± 2125 | 85 ± 7 | 9362 ± 765 | 2.4 ± 0.3 | 167 ± 4 | 0.49 ± 0.08 | 25.2 ± 4.2 | 2773 ± 461 |
| L438 | C1 | 221 ± 10 | 59549 ± 2827 | 188 ± 16 | 50816 ± 4339 | 1.2 ± 0.1 | 5 ± 78 | 0.69 ± 0.05 | 51.9 ± 9.2 | 14025 ± 2493 |
| L492 | C1 | 198 ± 8 | 53555 ± 2220 | 94 ± 3 | 25379 ± 858 | 2.1 ± 0.1 | 179 ± 79 | 0.89 ± 0.02 | 41.5 ± 2.3 | 11196 ± 624 |
| CB188 | C1★ | 51 ± 5 | 15441 ± 1486 | 28 ± 1 | 8456 ± 334 | 1.8 ± 0.2 | 16 ± 6 | 0.88 ± 0.04 | 11.0 ± 0.3 | 3298 ± 94 |
| L673-7 | C1★ | 56 ± 53 | 16829 ± 15837 | 36 ± 10 | 10784 ± 3015 | 1.6 ± 1.2 | 90 ± 23 | 0.88 ± 0.25 | 12.0 ± 0.8 | 3603 ± 233 |
| | [C2] | 188 ± 19 | 56491 ± 5636 | 166 ± 19 | 49780 ± 5808 | 1.1 ± 0.1 | 50 ± 56 | 0.33 ± 0.08 | 22.7 ± 5.5 | 6806 ± 1660 |
| | [C3] | 110 ± 18 | 32885 ± 5323 | 52 ± 8 | 15454 ± 2332 | 2.1 ± 0.4 | 56 ± 15 | 0.55 ± 0.09 | 17.7 ± 3.1 | 5299 ± 917 |
| L675 | C1 | 131 ± 9 | 39235 ± 2645 | 60 ± 6 | 18001 ± 1706 | 2.2 ± 0.3 | 125 ± 7 | 0.62 ± 0.11 | 24.8 ± 3.8 | 7446 ± 1153 |
| L1100 | C1★ | 64 ± 10 | 25760 ± 4157 | 34 ± 2 | 13414 ± 756 | 1.9 ± 0.3 | 31 ± 6 | 0.71 ± 0.09 | 11.5 ± 0.3 | 4606 ± 106 |
| L1041-2 | [C1] | 88 ± 7 | 35159 ± 2693 | 51 ± 9 | 20267 ± 3664 | 1.7 ± 0.3 | 8 ± 60 | 0.72 ± 0.11 | 17.8 ± 3.3 | 7109 ± 1320 |
| | [C2] | 166 ± 19 | 66259 ± 7743 | 134 ± 18 | 53597 ± 7243 | 1.2 ± 0.2 | 166 ± 34 | 0.40 ± 0.07 | 25.8 ± 6.3 | 10329 ± 2539 |
| | C3 | 164 ± 6 | 65597 ± 2552 | 69 ± 7 | 27482 ± 2934 | 2.4 ± 0.2 | 177 ± 89 | 0.78 ± 0.06 | 27.9 ± 2.9 | 11170 ± 1170 |
| | C4★ | 49 ± 1 | 19422 ± 508 | 41 ± 1 | 16585 ± 391 | 1.2 ± 0.0 | 57 ± 7 | 0.98 ± 0.01 | 14.2 ± 0.2 | 5696 ± 90 |
| | [C5] | 188 ± 10 | 75020 ± 3837 | 69 ± 10 | 27555 ± 4084 | 2.7 ± 0.4 | 175 ± 39 | 0.72 ± 0.07 | 32.9 ± 5.5 | 13170 ± 2204 |
| L1148 | C1★ | 334 ± 25 | 108709 ± 8181 | 71 ± 9 | 23023 ± 2989 | 4.7 ± 0.6 | 45 ± 2 | 0.39 ± 0.09 | 15.2 ± 7.7 | 4930 ± 2516 |
| | C2 | 291 ± 33 | 94458 ± 10791 | 82 ± 7 | 26700 ± 2432 | 3.5 ± 0.4 | 50 ± 2 | 0.70 ± 0.08 | 38.0 ± 4.6 | 12345 ± 1509 |
| L1155E | [C1] | 158 ± 19 | 51375 ± 6150 | 97 ± 10 | 31363 ± 3167 | 1.6 ± 0.2 | 47 ± 12 | 0.45 ± 0.09 | 21.5 ± 4.8 | 6971 ± 1575 |

**Table 2.5:** continued.

| Core | | $a$ arcsec | $a$ AU | $b$ arcsec | $b$ AU | $a/b$ | P.A. deg | $f$ | $r_{70\%}$ arcsec | $r_{70\%}$ AU |
|---|---|---|---|---|---|---|---|---|---|---|
| | [C2] | 172 ± 18 | 55813 ± 5812 | 86 ± 12 | 27996 ± 3932 | 2.0 ± 0.5 | 80 ± 4 | 0.67 ± 0.09 | 33.5 ± 4.6 | 10891 ± 1505 |
| | [C3] | 80 ± 10 | 26095 ± 3262 | 38 ± 10 | 12208 ± 3183 | 2.1 ± 0.6 | 33 ± 11 | 0.33 ± 0.15 | 8.4 ± 3.4 | 2723 ± 1121 |
| L1082C-2 | [C1] | 238 ± 27 | 95163 ± 10900 | 120 ± 12 | 48085 ± 4824 | 2.0 ± 0.2 | 84 ± 5 | 0.59 ± 0.06 | 36.0 ± 5.0 | 14414 ± 1995 |
| L1082C | C1⋆ | 58 ± 6 | 23283 ± 2327 | 42 ± 3 | 16778 ± 1263 | 1.4 ± 0.1 | 167 ± 50 | 0.95 ± 0.03 | 16.0 ± 1.0 | 6417 ± 417 |
| L1082A | C1⋆ | 48 ± 4 | 19277 ± 1528 | 30 ± 2 | 12141 ± 693 | 1.6 ± 0.2 | 122 ± 4 | 0.98 ± 0.02 | 11.7 ± 0.4 | 4673 ± 150 |
| | C2 | 30 ± 0 | 12066 ± 176 | 25 ± 1 | 10070 ± 207 | 1.2 ± 0.0 | 32 ± 5 | 0.99 ± 0.01 | 9.7 ± 0.2 | 3870 ± 88 |
| | C3⋆ | 33 ± 2 | 13355 ± 695 | 28 ± 1 | 11360 ± 363 | 1.2 ± 0.1 | 37 ± 15 | 1.00 ± 0.02 | 9.7 ± 0.3 | 3870 ± 113 |
| | C4 | 182 ± 19 | 72704 ± 7587 | 32 ± 22 | 12831 ± 8607 | 5.7 ± 1.3 | 46 ± 5 | 0.85 ± 0.20 | 21.6 ± 2.9 | 8653 ± 1155 |
| L1228 | C1⋆ | 32 ± 0 | 6350 ± 99 | 27 ± 1 | 5497 ± 139 | 1.2 ± 0.0 | 13 ± 5 | 1.00 ± 0.01 | 10.1 ± 0.0 | 2014 ± 9 |
| Bern48 | C1⋆ | 25 ± 0 | 4961 ± 55 | 23 ± 1 | 4500 ± 119 | 1.1 ± 0.0 | 180 ± 68 | 1.00 ± 0.01 | 8.4 ± 0.0 | 1676 ± 0 |
| L1172A | C1 | 107 ± 9 | 30875 ± 2696 | 100 ± 15 | 28762 ± 4438 | 1.1 ± 0.2 | 119 ± 43 | 0.70 ± 0.09 | 21.3 ± 4.6 | 6125 ± 1313 |
| | C2⋆ | 90 ± 9 | 25969 ± 2469 | 74 ± 9 | 21361 ± 2486 | 1.2 ± 0.1 | 70 ± 32 | 0.82 ± 0.06 | 21.8 ± 2.7 | 6282 ± 776 |
| L1177 | C1⋆ | 28 ± 0 | 8142 ± 131 | 26 ± 1 | 7457 ± 160 | 1.1 ± 0.0 | 105 ± 8 | 0.96 ± 0.01 | 9.7 ± 0.1 | 2786 ± 35 |
| L1021 | C1 | 216 ± 14 | 54043 ± 3562 | 115 ± 10 | 28869 ± 2564 | 1.9 ± 0.2 | 42 ± 8 | 0.69 ± 0.07 | 35.6 ± 5.4 | 8900 ± 1338 |
| L1014 | C1⋆ | 62 ± 19 | 15519 ± 4737 | 49 ± 3 | 12255 ± 787 | 1.3 ± 0.4 | 160 ± 13 | 0.92 ± 0.12 | 18.2 ± 1.2 | 4551 ± 304 |
| L1103-2 | C1 | 273 ± 9 | 68328 ± 2239 | 81 ± 11 | 20275 ± 2872 | 3.4 ± 0.5 | 56 ± 2 | 0.69 ± 0.06 | 36.0 ± 5.8 | 8995 ± 1456 |
| L1251A | [C1] | 173 ± 16 | 51784 ± 4885 | 98 ± 16 | 29293 ± 4857 | 1.8 ± 0.3 | 103 ± 11 | 0.54 ± 0.10 | 26.7 ± 7.2 | 8014 ± 2149 |
| | C2⋆ | 147 ± 13 | 44246 ± 4007 | 56 ± 3 | 16868 ± 869 | 2.6 ± 0.3 | 81 ± 2 | 0.59 ± 0.05 | 19.7 ± 1.4 | 5924 ± 416 |
| | C3⋆ | 37 ± 1 | 10998 ± 355 | 35 ± 1 | 10459 ± 356 | 1.1 ± 0.1 | 71 ± 22 | 1.00 ± 0.01 | 11.8 ± 0.2 | 3554 ± 71 |
| | C4⋆ | 158 ± 9 | 47291 ± 2804 | 41 ± 2 | 12350 ± 638 | 3.8 ± 0.2 | 135 ± 1 | 0.80 ± 0.04 | 18.1 ± 1.2 | 5429 ± 349 |
| L1197 | C1 | 200 ± 63 | 59945 ± 18875 | 59 ± 12 | 17669 ± 3683 | 3.4 ± 0.9 | 127 ± 5 | 0.48 ± 0.05 | 25.0 ± 2.5 | 7493 ± 748 |

**Table 2.6:** Data on dust emission peaks. Bracketed and starred peak designations indicate peaks with uncertain properties due to artifacts and peaks with associated protostars or VeLLOs, respectively. For every peak the table lists the peak position, the associated subcore, if applicable, the peak flux density per 11″ beam (after smoothing to 20″ resolution) and the related column density and extinction, the flux density and radius for an aperture of 4 200 AU radius, and the flux densities for the c2d standard apertures between 20″ and 120″ diameter.

| Core | $\alpha$ J2000.0 | $\delta$ J2000.0 | Asso. | $F_{max}^{beam}$ mJy beam$^{-1}$ | $N(H_2)$ $10^{22}$ cm$^{-2}$ | $A_V$ mag | $F_{4200AU}$ mJy | $M_{4200AU}$ $M_\odot$ | $F_{20''}$ mJy | $F_{40''}$ mJy | $F_{80''}$ mJy | $F_{120''}$ mJy |
|---|---|---|---|---|---|---|---|---|---|---|---|---|
| L1355 | [P1] | 02 52 41.2 | +68 57 01.0 | [C1] | 11 ± 2 | 0.72 ± 0.16 | 7.6 ± 1.7 | 83 ± 14 | 0.16 ± 0.03 | 31 ± 7 | 79 ± 14 | 198 ± 28 | 337 ± 44 |
| | [P2] | 02 52 58.1 | +68 53 17.0 | [C2] | 13 ± 2 | 0.87 ± 0.16 | 9.3 ± 1.7 | 102 ± 14 | 0.19 ± 0.03 | 36 ± 7 | 91 ± 13 | 241 ± 27 | 528 ± 42 |
| | [P3] | 02 53 18.9 | +68 57 25.5 | [C3] | 14 ± 2 | 0.95 ± 0.12 | 10.1 ± 1.3 | 115 ± 11 | 0.22 ± 0.02 | 40 ± 5 | 110 ± 10 | 334 ± 21 | 695 ± 31 |
| | [P4] | 02 53 40.3 | +68 53 55.5 | [C4] | 11 ± 2 | 0.76 ± 0.16 | 8.1 ± 1.7 | 84 ± 15 | 0.16 ± 0.03 | 28 ± 7 | 84 ± 14 | 246 ± 29 | 449 ± 45 |
| L1521B-2 | P1 | 04 23 30.8 | +26 38 07.0 | C1 | 15 ± 1 | 1.00 ± 0.09 | 10.6 ± 0.9 | 259 ± 11 | 0.24 ± 0.01 | 38 ± 4 | 120 ± 8 | 438 ± 16 | 832 ± 23 |
| | P2 | 04 23 37.1 | +26 40 23.5 | C2 | 9 ± 1 | 0.62 ± 0.07 | 6.6 ± 0.8 | 153 ± 10 | 0.14 ± 0.01 | 24 ± 3 | 73 ± 6 | 256 ± 13 | 473 ± 19 |
| | [P3] | 04 23 42.3 | +26 41 26.5 | [C3] | 6 ± 1 | 0.43 ± 0.09 | 4.6 ± 1.0 | 78 ± 12 | 0.07 ± 0.01 | 17 ± 4 | 46 ± 8 | 113 ± 16 | 249 ± 25 |
| L1521F | P1* | 04 28 39.4 | +26 51 34.0 | C1* | 66 ± 2 | 4.42 ± 0.13 | 47.0 ± 1.4 | 972 ± 17 | 0.77 ± 0.01 | 173 ± 6 | 537 ± 11 | 1476 ± 23 | 2471 ± 34 |
| L1521-2 | P1 | 04 29 26.9 | +27 00 53.5 | C1* | 8 ± 1 | 0.51 ± 0.10 | 5.4 ± 1.0 | 135 ± 12 | 0.12 ± 0.01 | 21 ± 4 | 59 ± 8 | 216 ± 17 | 416 ± 25 |
| | P2 | 04 29 37.4 | +26 58 05.5 | C2 | 19 ± 1 | 1.26 ± 0.09 | 13.4 ± 0.9 | 331 ± 11 | 0.30 ± 0.01 | 50 ± 4 | 161 ± 7 | 556 ± 15 | 1124 ± 22 |
| L1524-4 | P1 | 04 30 07.5 | +24 25 48.0 | C1 | 19 ± 1 | 1.30 ± 0.09 | 13.9 ± 1.0 | 343 ± 12 | 0.32 ± 0.01 | 50 ± 4 | 164 ± 8 | 605 ± 16 | 1190 ± 25 |
| | [P2] | 04 30 15.9 | +24 24 20.5 | [C2] | 11 ± 2 | 0.76 ± 0.10 | 8.1 ± 1.1 | 204 ± 13 | 0.19 ± 0.01 | 30 ± 4 | 98 ± 9 | 324 ± 18 | 634 ± 27 |
| | [P3] | 04 30 22.3 | +24 27 26.0 | [C3] | 10 ± 2 | 0.70 ± 0.16 | 7.4 ± 1.7 | 115 ± 21 | 0.11 ± 0.02 | 31 ± 7 | 61 ± 14 | 206 ± 29 | 468 ± 45 |
| B18-1 | P1 | 04 31 45.4 | +24 32 44.5 | C1 | 13 ± 1 | 0.89 ± 0.07 | 9.5 ± 0.8 | 219 ± 9 | 0.20 ± 0.01 | 37 ± 3 | 104 ± 6 | 349 ± 12 | 704 ± 19 |
| | P2 | 04 31 47.4 | +24 31 55.5 | C1 | 15 ± 1 | 1.01 ± 0.07 | 10.7 ± 0.8 | 274 ± 9 | 0.25 ± 0.01 | 41 ± 3 | 128 ± 6 | 446 ± 13 | 945 ± 19 |
| | P3 | 04 31 55.6 | +24 32 55.0 | C1 | 49 ± 1 | 3.30 ± 0.08 | 35.1 ± 0.8 | 808 ± 10 | 0.74 ± 0.01 | 124 ± 3 | 421 ± 7 | 1200 ± 13 | 1992 ± 20 |
| | P4 | 04 32 08.9 | +24 30 21.0 | | 9 ± 2 | 0.59 ± 0.12 | 6.3 ± 1.3 | 61 ± 94 | 0.06 ± 0.01 | 23 ± 5 | 53 ± 10 | 90 ± 21 | 210 ± 32 |
| | [P5*] | 04 32 15.4 | +24 29 00.5 | [C2*] | 65 ± 5 | | | > 360 ± 50 | > 0.18 ± 0.00 | 204 ± 14 | > 293 ± 30 | > 480 ± 85 | > 584 ± 473 |
| B18-2 | P1 | 04 32 30.0 | +24 50 17.0 | C1 | 9 ± 2 | 0.58 ± 0.11 | 6.2 ± 1.2 | 116 ± 15 | 0.11 ± 0.01 | 26 ± 5 | 56 ± 10 | 172 ± 20 | 334 ± 30 |
| | [P2] | 04 32 41.3 | +24 51 30.5 | C2 | 14 ± 1 | 0.91 ± 0.09 | 9.7 ± 1.0 | 223 ± 12 | 0.21 ± 0.01 | 35 ± 4 | 112 ± 8 | 369 ± 16 | 641 ± 24 |
| TMC-2 | P1 | 04 32 43.8 | +24 23 14.5 | C1 | 45 ± 1 | 2.98 ± 0.07 | 31.7 ± 0.7 | 835 ± 9 | 0.77 ± 0.01 | 111 ± 3 | 402 ± 6 | 1388 ± 11 | 2694 ± 17 |
| | P2 | 04 32 45.3 | +24 24 31.5 | C1 | 41 ± 1 | 2.73 ± 0.07 | 29.1 ± 0.7 | 849 ± 9 | 0.78 ± 0.01 | 101 ± 3 | 379 ± 6 | 1488 ± 11 | 3130 ± 17 |
| B18-4 | P1* | 04 35 35.2 | +24 08 17.5 | C1* | 71 ± 2 | | | 974 ± 19 | 0.55 ± 0.04 | 195 ± 6 | 524 ± 13 | 1557 ± 27 | 3126 ± 41 |
| | P2 | 04 35 37.7 | +24 09 17.0 | C1* | 71 ± 2 | 4.75 ± 0.11 | 50.5 ± 1.2 | 1282 ± 14 | 1.18 ± 0.01 | 172 ± 5 | 643 ± 9 | 2068 ± 19 | 3841 ± 29 |
| B18-5 | P1 | 04 35 51.0 | +24 09 27.5 | C1 | 25 ± 1 | 1.68 ± 0.08 | 17.9 ± 0.8 | 462 ± 10 | 0.43 ± 0.01 | 64 ± 3 | 217 ± 6 | 809 ± 13 | 1566 ± 19 |
| TMC-1C | P1 | 04 41 21.8 | +26 02 32.5 | C1 | 27 ± 1 | 1.78 ± 0.08 | 18.9 ± 0.9 | 525 ± 10 | 0.48 ± 0.01 | 63 ± 3 | 245 ± 7 | 885 ± 14 | 1740 ± 21 |
| | P2 | 04 41 32.2 | +26 03 42.5 | C2 | 36 ± 1 | 2.42 ± 0.09 | 25.8 ± 0.9 | 705 ± 11 | 0.65 ± 0.01 | 89 ± 4 | 328 ± 7 | 1197 ± 15 | 2306 ± 22 |
| | P3* | 04 41 38.7 | +25 56 25.0 | | 12 ± 2 | | | 71 ± 17 | 0.04 ± 0.00 | 38 ± 5 | 58 ± 11 | 58 ± 23 | 76 ± 35 |
| | P4 | 04 41 39.2 | +26 00 12.5 | C3 | 39 ± 1 | 2.63 ± 0.09 | 28.0 ± 1.0 | 794 ± 12 | 0.73 ± 0.01 | 97 ± 4 | 356 ± 8 | 1350 ± 16 | 2659 ± 24 |
| TMC-1 | P1 | 04 40 59.5 | +25 53 54.5 | C1 | 21 ± 2 | 1.40 ± 0.15 | 14.9 ± 1.6 | 406 ± 19 | 0.37 ± 0.02 | 55 ± 6 | 174 ± 12 | 613 ± 25 | 1164 ± 38 |
| | P2* | 04 41 12.8 | +25 46 33.5 | C2* | 52 ± 2 | | | 684 ± 18 | 0.37 ± 0.01 | 143 ± 6 | 366 ± 12 | 1053 ± 25 | 1900 ± 37 |
| | P3 | 04 41 13.8 | +25 49 49.5 | C3 | 36 ± 2 | 2.39 ± 0.11 | 25.4 ± 1.2 | 668 ± 15 | 0.62 ± 0.01 | 91 ± 5 | 307 ± 10 | 1147 ± 20 | 2246 ± 29 |
| | P4 | 04 41 37.2 | +25 43 38.5 | C4 | 30 ± 2 | 2.00 ± 0.16 | 21.3 ± 1.7 | 569 ± 20 | 0.52 ± 0.02 | 80 ± 7 | 256 ± 13 | 999 ± 27 | 1960 ± 41 |
| | P5 | 04 41 43.9 | +25 41 22.0 | C5 | 31 ± 3 | 2.08 ± 0.18 | 22.2 ± 1.9 | 605 ± 23 | 0.56 ± 0.02 | 83 ± 7 | 277 ± 15 | 986 ± 30 | 1997 ± 45 |
| | P6 | 04 41 51.9 | +25 38 09.5 | C6 | 24 ± 2 | 1.63 ± 0.14 | 17.3 ± 1.5 | 460 ± 18 | 0.42 ± 0.02 | 65 ± 6 | 199 ± 12 | 766 ± 24 | 1553 ± 36 |
| L1507A | P1 | 04 42 30.5 | +29 39 22.5 | C2 | 10 ± 2 | 0.69 ± 0.12 | 7.4 ± 1.3 | 116 ± 15 | 0.11 ± 0.01 | 31 ± 5 | 66 ± 10 | 143 ± 21 | 256 ± 31 |
| | P2 | 04 42 38.3 | +29 43 48.5 | C1 | 20 ± 2 | 1.35 ± 0.11 | 14.4 ± 1.1 | 369 ± 14 | 0.34 ± 0.01 | 50 ± 5 | 168 ± 9 | 653 ± 19 | 1335 ± 28 |
| | P3 | 04 42 38.9 | +29 45 54.5 | C1 | 15 ± 2 | 1.03 ± 0.13 | 11.0 ± 1.4 | 173 ± 17 | 0.16 ± 0.02 | 43 ± 5 | 111 ± 11 | 296 ± 23 | 576 ± 34 |
| | P4 | 04 42 41.0 | +29 41 07.5 | C2 | 18 ± 2 | 1.20 ± 0.11 | 12.8 ± 1.1 | 308 ± 14 | 0.28 ± 0.01 | 48 ± 4 | 140 ± 9 | 507 ± 18 | 1030 ± 27 |

**Table 2.6:** continued.

| Core | | $\alpha$ J2000.0 | $\delta$ J2000.0 | Asso. | $F_{\mathrm{max}}^{\mathrm{beam}}$ mJy beam$^{-1}$ | $N(\mathrm{H_2})$ $10^{22}$ cm$^{-2}$ | $A_V$ mag | $F_{4200\,\mathrm{AU}}$ mJy | $M_{4200\,\mathrm{AU}}$ $M_\odot$ | $F_{20''}$ mJy | $F_{40''}$ mJy | $F_{80''}$ mJy | $F_{120''}$ mJy |
|---|---|---|---|---|---|---|---|---|---|---|---|---|---|
| | P5 | 04 43 02.0 | +29 43 41.5 | C3 | 17 ± 2 | 1.14 ± 0.13 | 12.2 ± 1.4 | 289 ± 17 | 0.27 ± 0.02 | 47 ± 6 | 146 ± 11 | 470 ± 23 | 863 ± 34 |
| L1582A | P1 | 05 31 49.1 | +12 32 00.0 | | 14 ± 2 | 0.92 ± 0.14 | 9.7 ± 1.5 | 43 ± 6 | 0.32 ± 0.05 | 40 ± 6 | 61 ± 12 | 125 ± 25 | 302 ± 40 |
| | P2 | 05 31 56.1 | +12 32 24.5 | C1 | 17 ± 2 | 1.16 ± 0.11 | 12.3 ± 1.1 | 48 ± 5 | 0.36 ± 0.03 | 44 ± 4 | 141 ± 9 | 493 ± 18 | 904 ± 28 |
| | P3 | 05 32 01.1 | +12 30 32.5 | C2 | 30 ± 1 | 2.01 ± 0.09 | 21.3 ± 0.9 | 82 ± 4 | 0.61 ± 0.03 | 76 ± 4 | 260 ± 7 | 837 ± 15 | 1477 ± 23 |
| | P4 | 05 32 05.4 | +12 31 14.5 | C2 | 22 ± 1 | 1.44 ± 0.09 | 15.3 ± 0.9 | 58 ± 4 | 0.44 ± 0.03 | 54 ± 4 | 188 ± 7 | 632 ± 15 | 1283 ± 23 |
| IRAS05413 | P1 | 05 43 32.4 | −01 07 28.5 | C1 | 15 ± 3 | 0.98 ± 0.17 | 10.5 ± 1.8 | 37 ± 6 | 0.36 ± 0.06 | 38 ± 7 | 108 ± 14 | 289 ± 29 | 597 ± 44 |
| | P2⋆ | 05 43 46.4 | −01 04 40.5 | C2⋆ | 39 ± 1 | | | 99 ± 3 | 0.37 ± 0.23 | 109 ± 3 | 263 ± 7 | 704 ± 14 | 1288 ± 22 |
| | P3⋆ | 05 43 51.6 | −01 02 52.0 | C3⋆ | 124 ± 1 | | | 337 ± 3 | 0.39 ± 0.00 | 369 ± 4 | 694 ± 7 | 1242 ± 15 | 1734 ± 23 |
| | P4 | 05 43 60.0 | −01 05 01.5 | C4 | 11 ± 1 | 0.73 ± 0.10 | 7.7 ± 1.1 | 25 ± 4 | 0.24 ± 0.04 | 30 ± 4 | 90 ± 8 | 297 ± 18 | 575 ± 27 |
| L1622A | [P1] | 05 54 20.2 | +01 50 42.0 | [C1] | 19 ± 3 | 1.28 ± 0.19 | 13.6 ± 2.1 | 45 ± 7 | 0.42 ± 0.07 | 50 ± 8 | 139 ± 16 | 376 ± 35 | 654 ± 57 |
| | [P2] | 05 54 31.0 | +01 49 04.0 | [C2⋆] | 15 ± 3 | 1.02 ± 0.17 | 10.9 ± 1.8 | 31 ± 7 | 0.30 ± 0.06 | 35 ± 7 | 133 ± 14 | 308 ± 31 | 536 ± 48 |
| | P3 | 05 54 40.3 | +01 54 08.5 | C3 | 37 ± 1 | 2.45 ± 0.08 | 26.1 ± 0.9 | 81 ± 3 | 0.77 ± 0.03 | 96 ± 4 | 299 ± 7 | 865 ± 15 | 1464 ± 22 |
| | P4 | 05 54 52.0 | +01 57 31.5 | C4 | 19 ± 1 | 1.28 ± 0.08 | 13.7 ± 0.8 | 42 ± 3 | 0.40 ± 0.03 | 48 ± 3 | 172 ± 7 | 564 ± 13 | 1119 ± 20 |
| | P5 | 05 54 53.4 | +01 58 45.0 | C4 | 22 ± 1 | 1.45 ± 0.08 | 15.5 ± 0.9 | 47 ± 3 | 0.45 ± 0.03 | 54 ± 4 | 187 ± 7 | 498 ± 14 | 889 ± 22 |
| | P6 | 05 55 04.3 | +02 00 40.5 | C5 | 12 ± 1 | 0.83 ± 0.10 | 8.8 ± 1.0 | 26 ± 4 | 0.25 ± 0.04 | 31 ± 4 | 105 ± 8 | 291 ± 17 | 524 ± 26 |
| L183 | P1 | 15 54 00.8 | −02 52 24.5 | C1 | 25 ± 2 | 1.69 ± 0.10 | 18.0 ± 1.1 | 637 ± 17 | 0.36 ± 0.01 | 64 ± 4 | 207 ± 9 | 705 ± 18 | 1376 ± 27 |
| | [P2] | 15 54 06.4 | −02 59 49.0 | [C4] | 14 ± 2 | 0.95 ± 0.14 | 10.1 ± 1.5 | 154 ± 24 | 0.09 ± 0.01 | 45 ± 6 | 66 ± 12 | 177 ± 25 | 460 ± 38 |
| | P3 | 15 54 08.7 | −02 52 38.5 | C2 | 56 ± 1 | 3.76 ± 0.09 | 40.1 ± 1.0 | 1316 ± 15 | 0.75 ± 0.01 | 142 ± 4 | 483 ± 8 | 1426 ± 16 | 2419 ± 24 |
| | P4 | 15 54 09.4 | −02 48 58.0 | C3 | 34 ± 2 | 2.29 ± 0.12 | 24.3 ± 1.3 | 1021 ± 20 | 0.58 ± 0.01 | 85 ± 5 | 310 ± 10 | 1133 ± 21 | 2217 ± 32 |
| | [P5] | 15 54 10.4 | −02 59 35.0 | [C4] | 18 ± 2 | 1.19 ± 0.14 | 12.7 ± 1.5 | 337 ± 23 | 0.19 ± 0.01 | 49 ± 6 | 124 ± 12 | 371 ± 25 | 809 ± 37 |
| | P6 | 15 54 13.6 | −02 55 44.0 | C5 | 16 ± 2 | 1.08 ± 0.10 | 11.5 ± 1.1 | 394 ± 17 | 0.22 ± 0.01 | 42 ± 4 | 124 ± 9 | 432 ± 18 | 854 ± 27 |
| | [P7] | 15 54 25.8 | −02 54 30.5 | [C6] | 11 ± 2 | 0.76 ± 0.13 | 8.1 ± 1.4 | 194 ± 21 | 0.11 ± 0.01 | 33 ± 5 | 64 ± 11 | 219 ± 23 | 471 ± 35 |
| L438 | P1 | 18 14 06.8 | −07 08 43.5 | C1 | 10 ± 1 | 0.69 ± 0.08 | 7.4 ± 0.8 | 57 ± 5 | 0.20 ± 0.02 | 28 ± 3 | 82 ± 7 | 323 ± 13 | 644 ± 20 |
| L492 | P1 | 18 15 48.4 | −03 45 48.5 | C1 | 29 ± 1 | 1.94 ± 0.06 | 20.7 ± 0.6 | 164 ± 4 | 0.56 ± 0.01 | 72 ± 2 | 263 ± 5 | 949 ± 10 | 1723 ± 15 |
| | [P2] | 18 15 51.4 | −03 50 00.5 | | 10 ± 2 | 0.69 ± 0.15 | 7.4 ± 1.5 | 47 ± 10 | 0.16 ± 0.03 | 31 ± 6 | 53 ± 13 | 118 ± 28 | 179 ± 51 |
| CB188 | P1⋆ | 19 20 15.1 | +11 35 42.5 | C1⋆ | 35 ± 1 | | | 142 ± 3 | 0.21 ± 0.02 | 100 ± 2 | 218 ± 5 | 540 ± 10 | 842 ± 15 |
| L673-7 | P1⋆ | 19 21 34.6 | +11 21 19.5 | C1⋆ | 26 ± 2 | 1.72 ± 0.10 | 18.3 ± 1.1 | 106 ± 6 | 0.41 ± 0.03 | 73 ± 4 | 174 ± 9 | 374 ± 18 | 482 ± 26 |
| | P2 | 19 21 39.9 | +11 20 23.5 | C1⋆ | 12 ± 1 | 0.80 ± 0.09 | 8.5 ± 1.0 | 52 ± 5 | 0.22 ± 0.02 | 34 ± 4 | 80 ± 8 | 252 ± 16 | 563 ± 24 |
| | [P3] | 19 21 42.0 | +11 18 49.0 | [C2] | 11 ± 1 | 0.72 ± 0.10 | 7.7 ± 1.1 | 39 ± 6 | 0.16 ± 0.02 | 30 ± 4 | 65 ± 8 | 205 ± 17 | 428 ± 26 |
| | [P4] | 19 21 53.4 | +11 20 06.0 | [C3] | 10 ± 2 | 0.68 ± 0.10 | 7.3 ± 1.1 | 43 ± 6 | 0.18 ± 0.02 | 30 ± 4 | 76 ± 9 | 186 ± 18 | 343 ± 27 |
| L675 | P1 | 19 23 56.0 | +11 07 20.5 | C1 | 5 ± 1 | 0.30 ± 0.07 | 3.2 ± 0.7 | 19 ± 4 | 0.08 ± 0.02 | 13 ± 3 | 35 ± 6 | 92 ± 11 | 154 ± 17 |
| L1100 | P1⋆ | 20 36 19.2 | +63 53 16.5 | C1⋆ | 44 ± 1 | | | 130 ± 4 | 0.42 ± 0.10 | 125 ± 4 | 294 ± 7 | 761 ± 15 | 1265 ± 22 |
| L1041-2 | [P1] | 20 37 02.7 | +57 41 32.0 | [C1] | 11 ± 2 | 0.72 ± 0.10 | 7.7 ± 1.1 | 34 ± 4 | 0.26 ± 0.03 | 33 ± 4 | 76 ± 9 | 223 ± 18 | 407 ± 26 |
| | [P2] | 20 37 08.9 | +57 39 36.5 | [C2] | 13 ± 2 | 0.90 ± 0.10 | 9.6 ± 1.1 | 41 ± 4 | 0.31 ± 0.03 | 38 ± 4 | 100 ± 9 | 327 ± 17 | 616 ± 26 |
| | P3 | 20 37 12.3 | +57 47 50.0 | C3 | 29 ± 2 | 1.97 ± 0.11 | 20.9 ± 1.1 | 84 ± 5 | 0.63 ± 0.04 | 79 ± 4 | 235 ± 9 | 751 ± 18 | 1337 ± 27 |
| | P4⋆ | 20 37 21.1 | +57 44 13.0 | C4⋆ | 114 ± 1 | | | 334 ± 4 | 0.52 ± 0.05 | 309 ± 4 | 850 ± 8 | 2086 ± 17 | 3364 ± 25 |
| | [P5] | 20 37 22.0 | +57 50 17.0 | [C5] | 18 ± 2 | 1.22 ± 0.13 | 13.0 ± 1.4 | 47 ± 6 | 0.35 ± 0.04 | 45 ± 5 | 149 ± 11 | 494 ± 23 | 867 ± 35 |
| L1148 | P1⋆ | 20 40 56.2 | +67 22 58.5 | C1⋆ | 9 ± 1 | 0.59 ± 0.08 | 6.3 ± 0.8 | 35 ± 4 | 0.14 ± 0.02 | 26 ± 3 | 59 ± 7 | 172 ± 14 | 296 ± 20 |
| | P2 | 20 41 14.4 | +67 20 45.5 | C2 | 12 ± 1 | 0.79 ± 0.08 | 8.4 ± 0.8 | 48 ± 4 | 0.24 ± 0.02 | 30 ± 3 | 93 ± 6 | 335 ± 13 | 543 ± 20 |
| L1155E | [P1] | 20 44 00.5 | +67 37 33.5 | [C1] | 12 ± 2 | 0.83 ± 0.11 | 8.8 ± 1.1 | 49 ± 6 | 0.24 ± 0.03 | 37 ± 4 | 79 ± 9 | 285 ± 18 | 466 ± 27 |
| | [P2] | 20 44 09.1 | +67 41 59.5 | [C2] | 10 ± 2 | 0.67 ± 0.10 | 7.2 ± 1.1 | 42 ± 6 | 0.21 ± 0.03 | 29 ± 4 | 60 ± 9 | 144 ± 18 | 242 ± 27 |
| | [P3] | 20 44 11.6 | +67 40 00.5 | [C3] | 9 ± 2 | 0.58 ± 0.10 | 6.2 ± 1.1 | 38 ± 6 | 0.19 ± 0.03 | 26 ± 4 | 57 ± 9 | 187 ± 17 | 363 ± 26 |

**Table 2.6:** continued.

| Core | | $\alpha$ J2000.0 | $\delta$ J2000.0 | Asso. | $F_{max}^{beam}$ mJy beam$^{-1}$ | $N(H_2)$ $10^{22}$ cm$^{-2}$ | $A_V$ mag | $F_{4200\ AU}$ mJy | $M_{4200\ AU}$ $M_\odot$ | $F_{20''}$ mJy | $F_{40''}$ mJy | $F_{80''}$ mJy | $F_{120''}$ mJy |
|---|---|---|---|---|---|---|---|---|---|---|---|---|---|
| L1082C-2 | [P1] | 20 49 49.7 | +60 15 56.0 | [C1] | 27 ± 2 | 1.80 ± 0.13 | 19.1 ± 1.4 | 74 ± 6 | 0.56 ± 0.04 | 69 ± 5 | 226 ± 11 | 813 ± 22 | 1477 ± 33 |
| L1082C | P1$^\star$ | 20 51 28.5 | +60 18 37.0 | C1$^\star$ | 40 ± 2 | | | 111 ± 5 | 0.44 ± 0.14 | 105 ± 5 | 317 ± 10 | 795 ± 21 | 1264 ± 32 |
| L1082A | P1$^\star$ | 20 53 13.7 | +60 14 46.0 | C1$^\star$ | 40 ± 1 | | | 118 ± 4 | 0.38 ± 0.11 | 111 ± 4 | 270 ± 8 | 607 ± 17 | 921 ± 25 |
| | [P2] | 20 53 25.9 | +60 19 50.5 | | 14 ± 3 | 0.97 ± 0.18 | 10.3 ± 1.9 | 49 ± 8 | 0.37 ± 0.06 | 45 ± 8 | 93 ± 16 | 157 ± 33 | 320 ± 52 |
| | P3 | 20 53 27.8 | +60 14 35.5 | C2 | 83 ± 1 | 5.58 ± 0.08 | 59.4 ± 0.9 | 256 ± 4 | 1.93 ± 0.03 | 246 ± 3 | 474 ± 7 | 933 ± 14 | 1420 ± 21 |
| | P4 | 20 53 40.5 | +60 12 22.5 | C3$^\star$ | 13 ± 1 | 0.88 ± 0.07 | 9.3 ± 0.8 | 38 ± 3 | 0.29 ± 0.02 | 35 ± 3 | 108 ± 6 | 326 ± 13 | 590 ± 19 |
| | P5$^\star$ | 20 53 50.3 | +60 09 45.0 | C3$^\star$ | 46 ± 1 | | | 140 ± 4 | 0.53 ± 0.07 | 134 ± 4 | 284 ± 8 | 593 ± 17 | 995 ± 26 |
| | P6 | 20 53 51.8 | +60 10 41.0 | C3$^\star$ | 16 ± 1 | 1.08 ± 0.09 | 11.5 ± 0.9 | 47 ± 4 | 0.35 ± 0.03 | 45 ± 4 | 131 ± 7 | 456 ± 15 | 997 ± 23 |
| | P7 | 20 53 53.7 | +60 17 30.5 | C4 | 19 ± 1 | 1.24 ± 0.09 | 13.2 ± 0.9 | 53 ± 4 | 0.40 ± 0.03 | 51 ± 4 | 132 ± 7 | 325 ± 15 | 498 ± 23 |
| L1228 | P1$^\star$ | 20 57 12.7 | +77 35 44.9 | C1$^\star$ | 151 ± 1 | | | 931 ± 8 | 0.54 ± 0.00 | 444 ± 4 | 889 ± 8 | 1834 ± 16 | 2925 ± 24 |
| Bern48 | P1$^\star$ | 20 59 14.4 | +78 23 05.0 | C1$^\star$ | 170 ± 1 | | | 877 ± 6 | 0.20 ± 0.00 | 523 ± 3 | 851 ± 6 | 1445 ± 12 | 2153 ± 18 |
| | [P2] | 20 59 42.3 | +78 24 25.5 | C1$^\star$ | 6 ± 1 | 0.41 ± 0.07 | 4.4 ± 0.8 | 41 ± 6 | 0.08 ± 0.01 | 18 ± 3 | 40 ± 6 | 94 ± 12 | 219 ± 19 |
| L1172A | P1 | 21 02 16.9 | +67 51 01.5 | C1 | 16 ± 2 | 1.05 ± 0.16 | 11.2 ± 1.7 | 73 ± 10 | 0.29 ± 0.04 | 43 ± 7 | 116 ± 13 | 375 ± 28 | 727 ± 43 |
| | P2$^\star$ | 21 02 21.8 | +67 54 14.0 | C2$^\star$ | 32 ± 2 | | | 154 ± 6 | 0.38 ± 0.02 | 86 ± 4 | 237 ± 9 | 791 ± 18 | 1403 ± 26 |
| | P3 | 21 02 41.6 | +67 54 10.5 | C2$^\star$ | 10 ± 2 | 0.68 ± 0.10 | 7.2 ± 1.1 | 48 ± 6 | 0.19 ± 0.03 | 29 ± 4 | 69 ± 9 | 139 ± 18 | 251 ± 27 |
| L1177 | [P1] | 21 17 14.7 | +68 20 15.0 | | 10 ± 2 | 0.68 ± 0.14 | 7.3 ± 1.5 | 50 ± 9 | 0.20 ± 0.04 | 31 ± 6 | 66 ± 12 | 89 ± 25 | 216 ± 39 |
| | P2$^\star$ | 21 17 38.8 | +68 17 30.5 | C1$^\star$ | 146 ± 1 | | | 657 ± 6 | 0.69 ± 0.08 | 433 ± 4 | 837 ± 8 | 1377 ± 16 | 1796 ± 24 |
| L1021 | P1$^\star$ | 21 21 27.5 | +50 59 46.0 | | 11 ± 2 | | | 42 ± 8 | 0.01 ± 0.00 | 35 ± 5 | 39 ± 9 | 89 ± 19 | 137 ± 29 |
| | P2 | 21 21 46.4 | +50 57 33.0 | C1 | 8 ± 1 | 0.57 ± 0.07 | 6.0 ± 0.7 | 48 ± 5 | 0.14 ± 0.01 | 22 ± 3 | 64 ± 6 | 219 ± 12 | 385 ± 17 |
| L1014 | P1$^\star$ | 21 24 07.4 | +49 59 06.0 | C1$^\star$ | 23 ± 1 | 1.56 ± 0.09 | 16.5 ± 1.0 | 141 ± 6 | 0.32 ± 0.01 | 59 ± 4 | 199 ± 8 | 487 ± 16 | 623 ± 23 |
| L1103-2 | P1 | 21 42 15.9 | +56 43 45.5 | C1 | 14 ± 1 | 0.91 ± 0.10 | 9.7 ± 1.0 | 86 ± 7 | 0.25 ± 0.02 | 34 ± 4 | 111 ± 8 | 321 ± 17 | 593 ± 25 |
| L1251A | [P1] | 22 28 51.4 | +75 15 09.0 | [C1] | 17 ± 2 | 1.17 ± 0.16 | 12.4 ± 1.7 | 78 ± 9 | 0.33 ± 0.04 | 49 ± 7 | 131 ± 13 | 470 ± 28 | 846 ± 43 |
| | P2 | 22 29 44.6 | +75 13 24.0 | C2$^\star$ | 43 ± 1 | 2.88 ± 0.09 | 30.6 ± 1.0 | 190 ± 5 | 0.80 ± 0.02 | 110 ± 4 | 353 ± 8 | 996 ± 16 | 1715 ± 24 |
| | P3$^\star$ | 22 30 00.1 | +75 13 55.5 | C2$^\star$ | 26 ± 1 | | | 114 ± 5 | 0.35 ± 0.03 | 66 ± 4 | 214 ± 8 | 713 ± 15 | 1413 ± 23 |
| | P4$^\star$ | 22 30 32.2 | +75 14 09.5 | C3$^\star$ | 67 ± 1 | | | 282 ± 5 | 1.03 ± 0.11 | 185 ± 3 | 456 ± 7 | 1020 ± 14 | 1636 ± 22 |
| | P5$^\star$ | 22 31 06.0 | +75 13 34.5 | C4$^\star$ | 45 ± 1 | | | 198 ± 5 | 0.73 ± 0.06 | 117 ± 4 | 359 ± 7 | 925 ± 15 | 1490 ± 22 |
| L1197 | P1 | 22 37 02.7 | +58 57 31.5 | C1 | 15 ± 1 | 1.02 ± 0.06 | 10.9 ± 0.6 | 68 ± 3 | 0.29 ± 0.01 | 39 ± 2 | 133 ± 5 | 386 ± 10 | 637 ± 15 |

### 2.4.2.3 Mass Estimates

Mass and column density estimates are derived from the observed flux densities assuming the c2d standard dust emission properties, i.e., a dust temperature of 10 K and an opacity of 0.0102 cm$^2$ g$^{-1}$ (per gram of ISM) at MAMBO's effective observing wavelength. Appendix A presents a detailed discussion of the conversion between mass and dust emission. Dust near protostars is, however, heated by the protostellar radiation, and for later protostellar stages likely to be more coagulated than interstellar dust. Therefore, we adopted higher dust temperatures and opacities when deriving masses for protostellar cores.

The dust temperature near protostars can be estimated from analytic models of temperature profiles for protostellar envelopes cooling by dust emission. For opacities with power-law dependence on wavelength, $\kappa \propto \lambda^{-\beta}$, where $\beta$ is the emissivity spectral index, the dust temperature profile in a protostellar envelope only heated radiatively by the star is

$$T_{\rm d}^{\rm rad}(r) = 38.4 \text{ K} \left(\frac{r}{100 \text{ AU}}\right)^{-q} \left(\frac{L}{L_\odot}\right)^{q/2},\qquad(2.25)$$

where $q = 2/(4 + \beta)$, $L$ is the luminosity, and $r$ is the distance from the star (Terebey et al. 1993). Rearrangement allows to estimate the radius with a particular dust temperature,

$$r^{\rm rad}(T_{\rm d}) = 2890 \text{ AU} \left(\frac{T_{\rm d}}{10 \text{ K}}\right)^{-1/q} \left(\frac{L}{L_\odot}\right)^{1/2}.\qquad(2.26)$$

However, the interstellar dust and gas is also heated by cosmic rays and by the interstellar radiation field, which produces a typical equilibrium temperature of order 10 K (e.g., Goldsmith 2001). The dust temperature can not drop below this value, so that

$$T_{\rm d}(r) = \max(10 \text{ K}, T_{\rm d}^{\rm rad}[r]).\qquad(2.27)$$

For this temperature profile Belloche et al. (2006) derive the mass-averaged dust temperature. For this we assume the density profile in a column density peak to be roughly described by a power-law, i.e. $\varrho \propto r^{-p}$, where $\varrho$ is the density and $r$ is the distance from peak center. Then the mass-averaged dust temperature within an aperture of radius $R$ is

$$\langle T_{\rm d}\rangle = \begin{cases} \frac{3-p}{3-q-p} T_{\rm d}^{\rm rad}(R), & \text{if } T_{\rm d}^{\rm rad}(R) \geq 10 \text{ K}, \\ \left(\frac{q}{3-p-q}\left[\frac{r^{\rm rad}(10 \text{ K})}{R}\right]^{3-p} + 1\right) 10 \text{ K}, & \text{otherwise}. \end{cases}\qquad(2.28)$$

For protostellar peaks and subcores we use this average temperature to derive masses from the flux densities of the whole subcore, of the area above 50% peak intensity, and of an aperture of 4 200 AU radius. In these cases the aperture radius $R$ is set to be the effective core radius of the whole core, or the geometric mean of the major and minor axis at 50% peak intensity, or 4 200 AU, respectively. We assume power-law exponents of $q = 0.4$ (Belloche et al. 2006) and $p = 2$ (i.e., profile for a singular isothermal sphere; Shu 1977). The mean dust temperatures are thus overestimated for density profiles shallower than $\varrho \propto r^{-2}$. The protostellar luminosities are taken to be identical to the bolometric luminosities derived in Sec. 2.5.2. For the VeLLO candidates associated with L1521F P1, L1148 P1, and L1014 P1, however, we use the better constrained "internal luminosities" derived by Bourke et al. (in prep.), Kauffmann et al. (in prep.) and Young et al. (2004).

For the dust in the envelopes of class II protostars we adopt an opacity of 0.02 cm$^2$ g$^{-1}$ because of an expected enhanced coagulation (Motte & André 2001, Ossenkopf & Henning 1994). For the other protostellar and starless cores we adopt the c2d opacities.

Circumstellar disks might also contribute to the millimetre continuum emission. Their contribution to apertures with radii $\geq 4\,200$ AU is estimated to be $\lesssim 10\%$ (Motte & André 2001). The emission from the disks does therefore not significantly bias our envelope mass estimates.

### 2.4.3 Overview of Source Properties

In order to compare the dense core morphologies revealed by our maps with those shown by other c2d bolometer surveys we use the morphology keywords adopted by Enoch et al. (2006) to describe our maps, as summarised in Table 2.2.

All dense cores that were observed are also detected in our maps, i.e., the maximum SNR in the map is at least 4. Only for one source 'weak' emission is detected, meaning a peak SNR equal to or below 5; all other sources are brighter. In total 21 cores (55% of all cores) have at least two peaks separated by less than 3′, and we consider them to be 'multiple'. All cores are 'extended', as they contain at least one subcore with an equivalent radius exceeding 30″. We take all subcores with a major-to-minor axis ratio exceeding 1.2 to be 'elongated', and the others to be 'round'. Then 6 cores (16%) only contain round subcores, 21 cores (55%) only contain elongated subcores, and 9 cores (24%) contain both round and elongated subcores.

Figure 2.3 gives an overview over the sizes, masses, column densities, and ellipticities of well reconstructed subcores. These have typical values in the range (1 to 6) $\cdot$ $10^4$ AU = 0.05 to 0.30 pc for the effective radius, 0.5 to 20 $M_\odot$ for the subcore masses, 0.1 to 1.0 $M_\odot$ for the mass within 4 200 AU from the peak, and major-to-minor axes ratios at 50% peak intensity ranging from 1 to about 4. Implications from these properties for the physical state and evolution of dense cores are discussed in Sec. 2.6.1.

## 2.5 Supplemental Protostellar Data

For the c2d MAMBO survey to be fully exploited, it needs to be complemented with information on the protostars covered by the maps. All embedded sources need to be identified to distinguish between starless cores, protostellar cores, and those containing VeLLOs. Furthermore, the protostellar properties are a prerequisite to derive masses for dense cores heated from within by embedded stars, and to relate the state of the dense cores to the embedded protostars.

Since less than half of the protostellar cores in the c2d MAMBO sample are targeted by Spitzer (i.e., 6 out of 13), most of our analysis is based on data from IRAS and 2MASS. However, we use Spitzer data where available.

### 2.5.1 Associated IRAS, 2MASS, and Spitzer Sources

Table 2.7 lists sources from the IRAS Point Source Catalogue (PSC) and IRAS Faint Source Catalogue (FSC) not associated with intensity peaks in the MAMBO maps, and Table 2.8 lists those that are associated. The sources are considered to be associated with subcores and peaks detected by MAMBO if the separation between an IRAS source and a MAMBO source is lesser than the uncertainty of the separation at the $2\sigma$ level (i.e., the IRAS uncertainty ellipse plus the MAMBO pointing error). These sources are most likely physically associated with the dense cores and are assumed to be young stars.

The criterion of association is relaxed for three sources. For L1100 and L1082C the FSC lists one source each that appears to be the counterpart of a PSC source, given that the flux densities are identical within the uncertainties. The positions of the PSC and FSC sources are, however, discrepant at more than the $2\sigma$ level. This suggests an erroneous pointing reconstruction. Unusually compact ($\leq$ 15″ at 70% peak intensity) and bright ($\geq$ 40 mJy beam$^{-1}$) dust emission peaks, which are usually associated with protostars, are separated by less than 1′ from these IRAS sources. Given the apparent IRAS pointing errors we thus consider these IRAS and MAMBO sources to be associated. For IRAS05413 the PSC and FSC positions and flux densities are consistent for one IRAS source pair near IRAS05413 P2, but the FSC position is not consistent with the one of the MAMBO peak. Because the MAMBO peak is unusually compact (5″ at 70% peak intensity) and bright (39 mJy beam$^{-1}$), and IRAS pointing errors are known from other sources, we tentatively associate the IRAS and MAMBO sources.

For IRAS 20410+6710, which is projected onto L1148 C2, our more sensitive Spitzer maps show no corresponding source in the MIPS bands. We therefore consider this IRAS source to be an artifact.

**Table 2.7:** IRAS sources not detected as MAMBO emission peaks. For every core in the c2d MAMBO survey the table lists sources from the IRAS Point Source Catalogue and the IRAS Faint Source Catalogue (preceeded by an 'F'), and the subcores in which the IRAS sources are located, if applicable. Objects from the IRAS Point Source and Faint Source catalogues present in both catalogues are connected. The last column gives the spectral index between 12 and 25 $\mu$m wavelength.

| Core | IRAS Source | Asso. | $\alpha^{25\ \mu\mathrm{m}}_{12\ \mu\mathrm{m}}$ |
|------|-------------|-------|------|
| L1521-2 | F04262+2654 | C1 | $0.27 \pm 0.43$ |
| L1524-4 | 04274+2420 | | $-0.85 \pm 0.27$ |
| | ⌊ F04274+2420 | | $-0.83 \pm 0.19$ |
| B18-1 | 04292+2427 | | $< -1.5$ |
| | ⌊ F04291+2427 | | $< -1.9$ |
| TMC-2 | 04294+2413 | | $-0.9 \pm 0.15$ |
| | ⌊ F04294+2413 | | $-0.89 \pm 0.11$ |
| B18-4 | 04326+2405 | C1 | $< -1.68$ |
| | ⌊ F04326+2405 | | $< -0.75$ |
| TMC-1C | 04380+2553 | | $-0.51 \pm 0.15$ |
| | ⌊ F04380+2553 | | $-0.76 \pm 0.12$ |
| TMC-1 | F04383+2549 | | $< -1.12$ |
| | 04392+2529 | | |
| L1582A | F05290+1229 | | $-0.51 \pm 0.17$ |
| L1622A | 05517+0151 | | $-2.14 \pm 0.16$ |
| | ⌊ F05517+0151 | | $-2.25 \pm 0.15$ |
| | 05519+0148 | [C2] | |
| | 05519+0157 | | |
| L438 | 18116−0707 | | $< -1.33$ |
| L492 | 18130−0341 | | |
| | 18132−0350 | | $-1.82 \pm 0.15$ |
| CB188 | 19180+1127 | | $< -1.31$ |
| L675 | 19217+1103 | | $-1.81 \pm 0.25$ |
| L1148 | 20395+6714 | | |
| | 20410+6710[a] | C2 | |
| L1228 | F20598+7728 | | $-0.26 \pm 0.34$ |
| L1103-2 | 21399+5632 | | $> -1.47$ |
| L1251A | F22282+7454 | | $< -2.54$ |

Notes: a) Probably an artifact as no corresponding Spitzer source exists.

**Table 2.8:** Properties of MAMBO-detected IRAS sources. For every core in the c2d MAMBO survey the table lists dust emission peaks and, if applicable, the related subcore associated with an IRAS source ( Sec. 2.5.1 discusses the identification of associated sources; FSC sources are preceeded by an 'F'). Associated 2MASS sources are listed too. The table further lists the spectral index between 12 and 25 $\mu$m wavelength, the bolometric temperature and luminosity, the submillimetre-to-bolometric luminosity ratio, the mass within a peak-centered aperture of 4 200 AU radius, and the infrared SED class.

| Core | Asso. | IRAS Source | 2MASS Source | $\alpha^{25\,\mu m}_{12\,\mu m}$ | $T^{IRAS}_{bol}$ K | $L^{IRAS}_{bol}$ $L_\odot$ | $L^{IRAS}_{submm}/L^{IRAS}_{bol}$ | $M^{YSO}_{4200AU}$ $M_\odot$ | Class |
|---|---|---|---|---|---|---|---|---|---|
| B18-1 | [C2], [P5] | 04292+2422 & F04292+2422 | 04321540+2428597 | 0.84 ± 0.13 | < 588 | > 1.11 | > 0.016 | > 0.179 | I |
| B18-4 | C1, P1 | 04325+2402 & F04325+2402 | 04353539+2408194 | > 3.76 | < 78 | 0.42 to 0.85 | 0.057 to 0.115 | 0.513 to 0.589 | I |
| TMC-1C | P3 | 04385+2550 & F04385+2550 | 04413882+2556267 | 0.41 ± 0.13 | > 585 | 0.23 to 0.48 | 0.008 to 0.018 | 0.042 to 0.047 | I |
| TMC-1 | C2, P2 | 04381+2540 & F04381+2540 | 04411267+2546354 | 1.52 ± 0.14 | 125 | 0.71 ± 0.21 | 0.047 ± 0.014 | 0.375 ± 0.01 | I |
| IRAS05413 | C2, P2 | 05412-0105 & F05411-0106 | 05434630-0104439 | > 0.25 | > 64 | 0.52 to 7.79 | 0.01 to 0.15 | 0.142 to 0.597 | I |
|  | C3, P3 | 05413-0104 | none | > −0.7 | < 53 | > 11.21 | < 0.02 | < 0.393 | 0 |
| CB188 | C1, P1 | 19179+1129 | 19201494+1135400 | > 0.88 | < 236 | 1.74 to 2.26 | 0.018 to 0.023 | 0.193 to 0.229 | I |
| L1100 | C1, P1 | 20355+6343 & F20355+6343 | none | 0.7 ± 0.18 | < 98 | 1.22 to 2.25 | 0.026 to 0.049 | 0.316 to 0.515 | I |
| L1041-2 | C4, P4 | 20361+5733 & F20361+5733 | none | > 3.12 | < 57 | 3.91 to 5.44 | 0.029 to 0.04 | 0.468 to 0.571 | 0 |
| L1148 | C1, P1 | F20404+6712 | 20405664+6723047 | > −0.07 | > 103 | 0.06 to 0.43 | 0.027 to 0.203 | 0.114 to 0.146 | I |
| L1082C | C1, P1 | 20503+6006 & F20503+6007 | none | > 1.05 | > 59 | 0.32 to 1.89 | 0.029 to 0.174 | 0.303 to 0.576 | I |
| L1082A | C1, P1 | 20520+6003 | 20531346+6014425 | 0.39 ± 0.2 | 191 | 1.00 to 2.60 | 0.02 to 0.053 | 0.262 to 0.491 | I |
|  | C3, P5 | 20526+5958 | none |  | < 112 | 0.84 to 1.46 | 0.041 to 0.072 | 0.452 to 0.602 | 0 |
| L1228 | C1, P1 | 20582+7724 & F20582+7724 | 20571294+7735437 | 0.35 ± 0.11 | 293 | 2.39 ± 0.39 | 0.039 ± 0.006 | 0.543 ± 0.005 | I |
| Bern48 | C1, P1 | 21004+7811 & F21004+7811 | 20591408+7823040 | −0.17 ± 0.1 | 615 | 11.3 ± 0.6 | 0.009 ± 0.001 | 0.201 ± 0.001 | I |
| L1172A | C2, P2 | 21017+6742 & F21017+6742 | 21022122+6754202 | > −0.13 | < 94 | 0.37 to 0.64 | 0.052 to 0.09 | 0.364 to 0.403 | I |
| L1177 | C1, P2 | 21169+6804 & F21168+6804 | 21173862+6817340 | 1.26 ± 0.27 | < 118 | 2.5 to 3.61 | 0.042 to 0.06 | 0.613 to 0.772 | I |
| L1021 | P1 | 21197+5046 | 21212751+5059475 | −0.82 ± 0.13 | > 980 | 4.09 to 6.98 | 0.001 to 0.003 | 0.01 to 0.014 | II |
| L1251A | C2, P3 | 22290+7458 & F22290+7458 | 22300004+7513578 | > 0.68 | > 82 | 0.12 to 0.82 | 0.037 to 0.262 | 0.279 to 0.38 | I |

Notes: a) there are several 2MASS sources within 10″ from the peak position; b) 2MASS photometry might be affected by confusion

For those IRAS sources associated with dust emission peaks it is possible to significantly improve the accuracy of their position by adopting the position of the MAMBO peak. This then also allows to search for 2MASS counterparts of these sources. We do so by searching for 2MASS sources less than $10''$ away from the MAMBO peak. If several 2MASS sources are found we assume the one closest to the MAMBO peak to be the counterpart. The identified counterparts are listed in Table 2.8. If no counterpart is found, 2MASS upper limits are taken to be similar to those of nearby 2MASS sources with upper limits in some bands.

This combined data yields a spectral coverage with data near $1\,\mu$m wavelength (from 2MASS), a well sampled range from 12 to $100\,\mu$m (from IRAS), and information at $1\,200\,\mu$m (from MAMBO). For consistency with previous work (e.g., André et al. 1999), and to avoid problems of distance bias, we use dust emission flux densities for the $4\,200$ AU aperture to study the spectral energy distributions.

In Table 2.9 we also present a preliminary list of associations between MAMBO dust emission peaks and Spitzer point sources. This is only a fraction of the list of candidate Spitzer protostars within the dense cores covered by the c2d MAMBO survey. The contaminating extragalactic background sources have not been fully removed from the source catalogue, and not all stars likely to be young are identified by present selection algorithms. We therefore abstain from using the Spitzer catalogue of protostellar objects in the present work.

We search for Spitzer sources that are detected as point sources at $70\,\mu$m wavelength with an offset of less than $1'$ from a dust emission peak. The restriction to sources with emission at $70\,\mu$m constrains the selected Spitzer sources to those apparently having emission at infrared wavelength in excess of the photospheric emission. (This criterion actually makes use of the low source luminosities and detection thresholds involved.) The spatial proximity criterion selects sources that have a high probability to be physically associated with the studied dense cores.

The data on the selected sources is complemented by 2MASS data where possible. Given the nominal positional uncertainties, 2MASS sources within $2''$ from Spitzer sources are assumed to be counterparts of these. For Spitzer sources without 2MASS counterparts upper limits to their flux densities in the 2MASS bands are derived from upper limits for nearby 2MASS sources not detected in all filters. The source emission is thus probed in the 1 to $24\,\mu$m wavelength range (by 2MASS and IRAS; Spitzer source extraction at $70\,\mu$m wavelength is pending and no Spitzer data is available at $160\,\mu$m) and at $1\,200\,\mu$m (from MAMBO for the $4\,200$ AU aperture).

### 2.5.2  Protostar Properties

Below we characterise the sources associated with dust emission peaks. All our target cores were covered by the extensive but insensitive IRAS and 2MASS surveys. This data thus allows a homogenous quantification of all sources in our survey that are brighter than a few times $0.1\,L_\odot$. Fainter sources could only be detected by Spitzer, from which data exists only for a fraction of our dense cores.

Given the differences in the spectral bands probed by these instruments, it is difficult to compare a source only detected by 2MASS and IRAS to one only detected by 2MASS and Spitzer. In order to explore and suppress related biases in estimates of source properties, we therefore analyse the Spitzer and IRAS data separately. To better distinguish results from the different approaches, in the following properties are labeled by the data source used to derive them (superscripts 'IRAS' and 'SST', the latter for Spitzer Space Telescope).

#### 2.5.2.1  Estimates from IRAS and 2MASS Data

Following Lada (1987), the spectral properties of young stars can be characterised by the spectral index between 12 and $25\,\mu$m wavelength,

$$\alpha^{25\,\mu\mathrm{m}}_{12\,\mu\mathrm{m}} = \frac{\log(12\,\mu\mathrm{m}\cdot F_{25\,\mu\mathrm{m}}/[25\,\mu\mathrm{m}\cdot F_{12\,\mu\mathrm{m}}])}{\log(25\,\mu\mathrm{m}/12\,\mu\mathrm{m})}\,. \tag{2.29}$$

Spectral indices are listed in Tables 2.7 and 2.8 for all IRAS sources in the MAMBO maps, if detected in these bands. They roughly probe whether the spectral energy distribution (SED) is dominated by photospheric or enve-

**Table 2.9:** Properties of MAMBO detected Spitzer sources. Like Table 2.8, but now listing sources from Spitzer point source catalogues and giving the spectral index between 3.6 and 24 $\mu$m wavelength. VeLLO candidates bear a mark in the class designation.

| Field | Asso. | Spitzer Source | 2MASS Source | $\alpha_{3.6\,\mu m}^{24\,\mu m}$ | $T_{\mathrm{bol}}^{\mathrm{SST}}$ K | $L_{\mathrm{bol}}^{\mathrm{SST}}$ $L_\odot$ | $L_{\mathrm{submm}}^{\mathrm{SST}}/L_{\mathrm{bol}}^{\mathrm{SST}}$ | $M_{4200\mathrm{AU}}^{\mathrm{YSO}}$ $M_\odot$ | Class |
|---|---|---|---|---|---|---|---|---|---|
| L1521F | C1, P1 | SSTc2d J042839.0+265135 | none | $1.56 \pm 0.08$ | < 34 | 0.002 to 0.112 | > 0.506 | 0.708 to 0.867 | 0, VeLLO |
| B18-1 | [C2], [P5] | SSTc2d J043215.4+242859 | 04321540+2428597 | $-0.25 \pm 0.06$ | no IRAC data available | | | | |
| B18-4 | C1, P1 | no Spitzer source catalogue available | | | | | | | |
| TMC1-1C | P3 | SSTc2d J044138.8+255627 | 04413882+2556267 | $-0.04 \pm 0.05$ | 692 | $0.361 \pm 0.054$ | $0.014 \pm 0.002$ | $0.022 \pm 0.001$ | II |
| TMC-1 | C2, P2 | SSTc2d J044112.7+254635 | 04411267+2546354 | $0.96 \pm 0.06$ | no IRAC data available | | | | |
| CB188 | C1, P1 | SSTc2d J192014.9+113540 | 19201494+1135400 | $0.25 \pm 0.05$ | 417 | $1.142 \pm 0.171$ | $0.041 \pm 0.006$ | $0.211 \pm 0.018$ | I |
| L673-7 | C1, P1 | SSTc2d J192134.8+112123 | none | $0.97 \pm 0.08$ | < 52 | 0.002 to 0.059 | > 0.486 | 0.378 to 0.435 | 0, VeLLO |
| L1148 | C1, P1 | SSTc2d J204056.7+672305 | 20405664+6723047 | $0.73 \pm 0.05$ | < 140 | 0.026 to 0.094 | > 0.135 | 0.139 to 0.154 | I, VeLLO |
| L1228 | C1, P1 | SSTc2d J205712.9+773544 | 20571294+7735437 | $0.14 \pm 0.05$ | 376 | $1.832 \pm 0.275$ | $0.071 \pm 0.011$ | $0.542 \pm 0.004$ | I |
| Bern48 | C1, P1 | SSTc2d J205914.0+782304 | 20591408+7823040 | $-0.42 \pm 0.10$ | 741 | $8.273 \pm 1.241$ | $0.016 \pm 0.002$ | $0.100 \pm 0.001$ | II |
| L1014 | C1, P1 | SSTc2d J212407.5+495909 | none | $0.33 \pm 0.07$ | < 150 | 0.020 to 0.156 | > 0.187 | 0.315 to 0.374 | I, VeLLO |
| L1251A | C2, P3 | SSTc2d J222959.5+751404 | 22295953+7514044 | $0.51 \pm 0.05$ | < 225 | 0.108 to 0.390 | > 0.092 | 0.321 to 0.383 | I |
| | C3, P4 | SSTc2d J223031.8+751409 | none | $0.57 \pm 0.08$ | < 47 | 0.004 to 0.143 | > 0.525 | 0.918 to 1.140 | 0 |
| | C4, P5 | SSTc2d J223105.6+751337 | none | $-0.23 \pm 0.07$ | < 46 | 0.005 to 0.093 | > 0.556 | 0.673 to 0.793 | 0 |

lope emission and are sometimes used to classify observed protostellar SEDs within evolutionary schemes (Lada 1987).

For the IRAS sources associated with MAMBO peaks and for which 2MASS data is available, we calculate the bolometric temperature defined by Myers & Ladd (1993),

$$T_{\text{bol}} = \frac{\zeta(4)}{4\zeta(5)} \frac{h\langle \nu \rangle}{k_{\text{B}}}, \quad (2.30)$$

where $\langle \nu \rangle = \int_0^\infty \nu F_\nu \, d\nu \big/ \int_0^\infty F_\nu \, d\nu$ is the flux-weighted mean frequency, $\zeta$ is the Riemann zeta function, and $h$ and $k_{\text{B}}$ are Planck's and Boltzmann's constant. We integrate across the SED by interpolation between observed 2MASS and IRAS bands. For this we use piecewise power laws matching the flux densities. At 500 $\mu$m wavelength these connect to a flux density distribution $\propto \lambda^{-4}$ extending to infinite wavelength and matching the MAMBO observation, assuming a modified blackbody of opacity $\propto \lambda^{-2}$ and more than 10 K temperature. The integration extends from the 2MASS bands at $\approx 1$ $\mu$m to infinity. Unlike Myers & Ladd we treat all flux density upper limits like actual detections. Therefore, the derived bolometric temperatures must be interpreted with some caution, if a source is not detected in some of the bands. In these cases lower and upper limits are assigned to the bolometric temperature, depending on whether adopting flux densities below the upper limits would increase or decrease the calculated mean frequency, respectively.

Based on the derived bolometric temperature the protostars are separated into four infrared classes. Following Chen et al. (1995, 1997) all stars with an inferred temperature < 70 K are considered to be class 0 sources. Those with temperatures $70 \le T_{\text{bol}}/\text{K} < 650$ belong to class I, for $650 \le T_{\text{bol}}/\text{K} < 2880$ they belong to class II, and class III sources have $T_{\text{bol}} \ge 2880$ K. Sources in a given class are believed to be in a similar evolutionary stage (Chen et al. 1995, 1997). In their evolution from a deeply embedded object to a star surrounded by a remnant dust disk, protostars are though to pass through these phases in that order. Thus class 0 objects would represent the youngest protostars and class III objects would be in a stage just prior to the main sequence. Almost all of the MAMBO-detected stars covered by the present survey are in classes 0 and I; only one class II and no class III object are among them.

When upper and lower limits to the bolometric temperature do not indicate the infrared SED class we assign the class through an individual inspection of the SED. Class 0 sources have single-peaked SEDs steeply dropping for wavelengths shortwards of 100 $\mu$m (i.e., by several orders of magnitude per magnitude in wavelength; Andre et al. 2000). Given the detection thresholds of 2MASS and IRAS and the luminosities of the objects in our sample, none the stars detected by 2MASS can thus be class 0 sources. Furthermore, the star associated with L1100 P1 can not be a class 0 source as $\nu F_\nu$ drops by less than a factor 10 from 10 to 100 $\mu$m. The SED for the star associated with L1082A P5 is, however, consistent with a class o source.

From the interpolated SED we derive an estimate for the bolometric luminosity,

$$L_{\text{bol}} = 4\pi d \int_0^\infty F_\nu \, d\nu, \quad (2.31)$$

for IRAS sources associated with MAMBO dust emission peaks. If the source is detected in a few bands only an upper limit to the bolometric luminosity is calculated by integrating across the flux density upper limits, while a lower limit is given by the sum of the maximum 2MASS and IRAS "monochromatic luminosities", $\nu F_\nu$, in the bands with a detection. In a similar fashion we derive the luminosity in the submillimetre wavelength range,

$$L_{\text{submm}} = 4\pi d \int_0^{c/350 \, \mu\text{m}} F_\nu \, d\nu, \quad (2.32)$$

where $c$ is the speed of light. The luminosities are also used to derive estimates of the mass within 4 200 AU from the dust emission peak, which need to be corrected for protostellar heating (Sec. 2.4.2.3).

The derived bolometric luminosities are dominated by the power of the embedded source, and not by the heating processes in the interstellar medium (like interaction with cosmic rays or absorption of the interstellar

radiation field). The latter contribution can be estimated for the material within 4 200 AU from the density peak. A heating power $0.16 L_\odot \cdot (M_{4200\mathrm{AU}}/M_\odot)$ is required to heat the matter to a temperature of 10 K that is typical in the dense interstellar medium. For $M_{4200\mathrm{AU}} = 0.4 M_\odot$, which is typical for the protostellar cores in our sample (Sec. 2.6.1.3), this power is $0.06 L_\odot$. This is much smaller than the bolometric luminosities derived, with the exception of the limits for the protostars associated with L1148 P1 and L1251A P3. We turn to these again in the next section.

### 2.5.2.2 Estimates from Spitzer and 2MASS Data

The protostellar properties derived from Spitzer and 2MASS data (Table 2.9) are calculated using methods similar to those adopted for the combined IRAS and 2MASS data. The spectral sampling is, however, much worse than for the combined 2MASS and IRAS dataset, resulting in more uncertain estimates.

The spectral index for the Spitzer bands, $\alpha_{3.6\,\mu\mathrm{m}}^{24\,\mu\mathrm{m}}$, is derived by fitting the monochromatic luminosities in the 3.6 to 24 $\mu$m wavelength range by a power law. It is, thus, not directly comparable to the spectral index derived from IRAS data.

We estimate the bolometric luminosity by integrating over the SED. Where necessary, we interpolate across Spitzer bands without detected emission. A lower limit to the luminosity is given by the maximum monochromatic luminosity in the 2MASS and Spitzer bands with a detection. Also, the bolometric temperature is calculated using these interpolations of the SED.

In some sources the derived bolometric luminosity is dominated by the power due to interstellar heating processes. For dust temperatures of at least 10 K this power exceeds the inferred bolometric luminosities of the protostars in L1521F P1, L673-7 P1, and L1251A P4 and P5, also demonstrating that our method to derive $L_{\mathrm{bol}}$ can miss part of the actual radiative power. This is also reflected in these sources' unusually large submillimetre-to-bolometric luminosity ratios. In such cases the bolometric luminosity is not a good measure of the power input by the young star. This leads to uncertain heating correction in mass estimates of protostellar envelopes (Sec. 2.4.2.3). The related uncertainties in the mass estimates are, however, not significant, given that the low derived luminosities imply small corrections.

Some stars are detected by IRAS and Spitzer. These are estimated to be significantly hotter and fainter when relying on Spitzer data instead of IRAS data. This is because the Spitzer long wavelength cutoff in the spectral sampling significantly falls short of the one for IRAS (24 $\mu$m vs. 100 $\mu$m with the present Spitzer source catalogues). In the present sample this results in that the Spitzer estimates for luminosities at wavelength > 24 $\mu$m are smaller than those derived using IRAS fluxes. Therefore, higher temperatures and lower total luminosities are found when relying on Spitzer.

Four stars in our sample might qualify as VeLLOs, given that they appear to be embedded in dense cores and have luminosities likely below 0.1 $L_\odot$. This group includes the sources associated with L1521F P1, L1148 P1, and L1014 P1, which have been subject to detailed studies (Bourke et al., in prep.; Kauffmann et al., in prep.; Young et al. 2004; see also Chapter 3). These studies confirm the spectral properties found here. Given the evidence for protostellar outflows from scattered light nebulosity and outflows seen in CO, the stars in L1521F P1, L1014 P1, and L673-7 P1 are indeed proven VeLLOs (Dunham et al., in prep., for L673-7). The stars in L1251A P4 and P5, for which our above analysis suggests low luminosities, are apparently not VeLLOs. Preliminary photometry at 70 $\mu$m indicates monochromatic luminosities of 0.15 $L_\odot$ and 0.09 $L_\odot$, respectively, and, thus, luminosities in excess of the set limit for VeLLOs.

### 2.5.2.3 Properties chosen for the Analysis

The above analysis yields two different sets of properties, one based on Spitzer data, one based on IRAS. For the bright sources of a few 0.1 $L_\odot$, the temperatures and luminosities estimated from IRAS data are used for the further protostar analysis. This is the preferred option because IRAS data is available for all our cores, and because — as shown above — Spitzer fails to detect a significant fraction of the protostellar emission, leading to biased estimates.

Fainter sources are usually only detected by Spitzer. Thus, Spitzer data is used for the study of the sources in L673-7 P1, and L1251A P4 and P5. For L1521F P1, L1148 P1, and L1014 P1 results from the more involved Spitzer data analysis by Bourke et al. (in prep.), Kauffmann et al. (in prep.) and Young et al. (2004) are used.

## 2.6 Analysis

In this section we exploit the survey data in order to better understand the state and evolution of starless and protostellar dense cores. We discuss the general core properties before we turn to the discussion of specific issues. Throughout the following discussion we exclude starless cores with uncertain properties, unless noted otherwise.

### 2.6.1 General Core Properties

Figure 2.3 shows the frequency distributions of some properties of well reconstructed dense cores. Some conclusions about the physical state of individual cores and of dense cores in general, can be derived from these distributions.

#### 2.6.1.1 Radius

The sizes of protostellar cores are on average larger than those of starless and VeLLO cores. This could to some extend be an observational bias. Only one protostellar subcore in our sample is at a distance below 200 pc, while two dozen starless cores are within this distance. Because confusion increases with distance, the subcores identified in the more distant protostellar cores are thus likely biased towards larger sizes.

At small radii the size distribution of starless cores is limited by the beam size; their number steeply drops to zero at the resolution limit. We might miss a population of small subcores.

#### 2.6.1.2 Total Mass

The mass of the subcore L1622A C3 exceeds the mass of all other subcores by a factor 1.8 and more. Given that L1622A is one out of only 3 dense cores located in the Orion star forming complex, in which special environmental conditions prevail, it might be that L1622A C3 has, e.g., a mass much larger than for the other cores in our sample. However, the extreme mass contrast to all other cores does cast some doubt on this.

It might be that L1622A is warmer than most other cores. By adopting a dust temperature of 10 K one would then overestimate the true mass. Furthermore, substructure easily disentangled in more nearby cores may be confused in L1622A, the core with the largest distance in our sample (450 pc). Then the subcore area, and therefore the mass, would be biased towards higher values. This is supported by the fact that L1622A C3 has the largest effective radius of all subcores. Also, L1582A C2 and L1622A C4, which are second to L1622A C3 in mass and are also located in Orion, are second to L1622A C3 in the effective radius. This may hint that mass and size estimates of cores are indeed biased for larger distances.

Thus data on distant cores must be interpreted with some caution. Properties of nearby and distant cores are not necessarily directly comparable.

#### 2.6.1.3 Mass within 4 200 AU

For L1082A P3 the mass $M_{4200AU}$ exceeds those of all other peaks by a factor 1.7 and more. This large aperture mass contrast may hint on a biased mass estimate. The dust in L1082A P3 might be significantly warmer than 10 K, if this core is heated by an undetected embedded star. Following Myers et al. (1987), the failure of IRAS to detect a point source in this peak implies (for a distance of 400 pc) implies an upper limit to the bolometric luminosity of $\approx 0.8\,L_\odot$ to any embedded source. In this case the average dust temperature could be underestimated and, thus, the mass be overestimated by us by up to a factor of 2. Then $M_{4200AU}$ would not be unusual for a protostellar core. Though this evidence is not conclusive, we, thus, suspect the presence of a heating protostellar source in L1082A
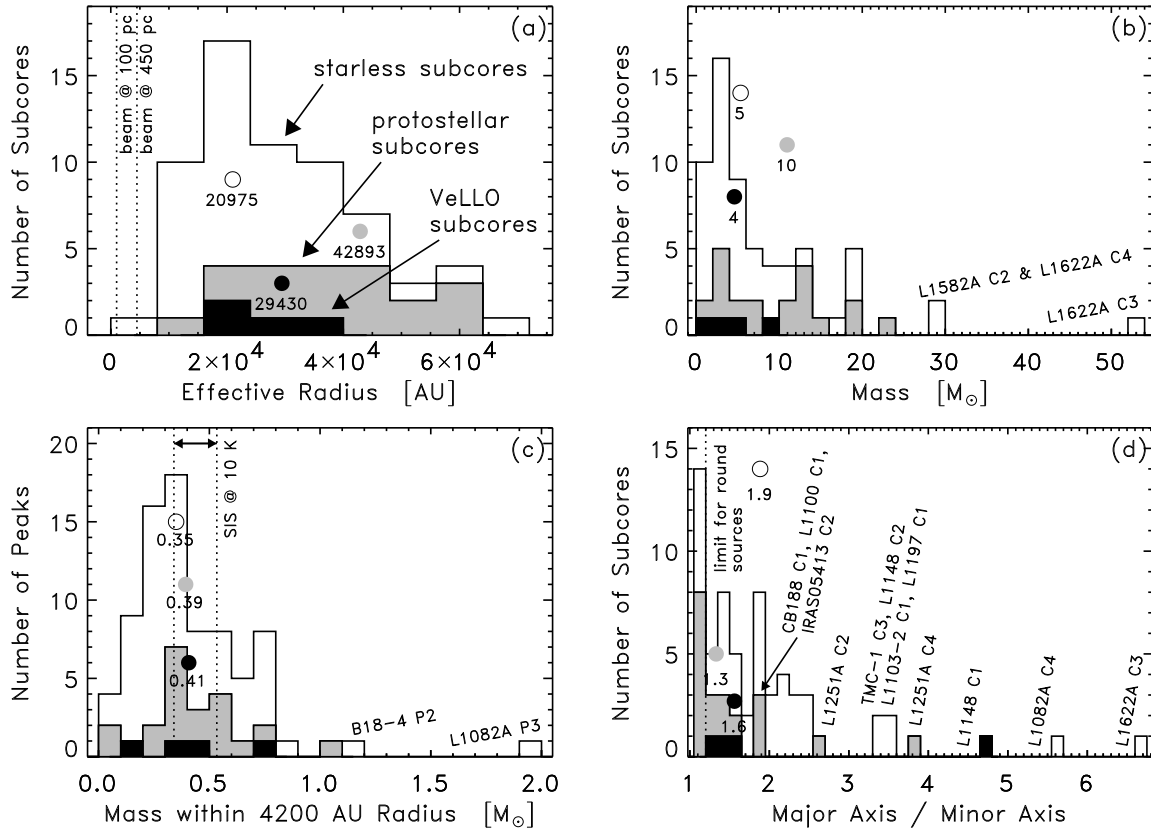
**Figure 2.3:** Overview of the dense core properties, excluding subcores and peaks with uncertain properties due to artifacts. The *white area* represents the properties of starless peaks and subcores, while the *grey and black areas* hold for protostellar and VeLLO cores, respectively. *Bullets* of the same colours give the respective median values of the distributions. *Vertical lines in panel a)* give the beam radius at distances of 100 pc and 450 pc, respectively. The *vertical lines in panel c)* show the range of masses within a 4 200 AU aperture for truncated singular isothermal spheres of 10 K temperature. The *vertical line in panel d)* marks the boundary between round and elongated sources.

P3 that is too faint to be detected by IRAS. Unfortunately, no Spitzer data is available for this region to confirm this.

In the $M_{\mathrm{4200AU}}$ distribution the peak B18-4 P2 is separated from the other starless subcores. As Spitzer images show no point sources associated with this peak internal heating cannot explain the unusual value of $M_{\mathrm{4200AU}}$. A protostar of $\approx 0.5\,L_{\odot}$ resides in B18-4 P1, which is separated from B18-4 P2 by 10000 AU = 0.05 pc. At this distance a protostar of this low luminosity is unlikely to provide significant external heating to the peak P2. Thus the high value of $M_{\mathrm{4200AU}}$ in B18-4 P2 is likely to be real.

The $M_{\mathrm{4200AU}}$ distributions for all types of subcores peak at a mass of $\approx 0.35\,M_{\odot}$. The median aperture mass is of the same order. As this is typical value for all kinds of subcores, the underlying physical process shaping the distributions must be fundamental. Interestingly, this mass is similar to the mass within 4 200 AU for a (truncated) singular hydrostatic equilibrium isothermal sphere (SIS) of 10 K gas temperature,

$$M_{\mathrm{4200AU}} = 0.34\,M_{\odot}\,\varepsilon\,(T_{\mathrm{g}}/10\,\mathrm{K})\,. \tag{2.33}$$

Here $T_{\mathrm{g}}$ is the gas temperature and the factor $\varepsilon$ depends on the density distribution outside a radius of 4 200 AU; it is 1 if the density drops to zero outside 4 200 AU and becomes $\pi/2 \approx 1.57$ if it continues out to infinity. The mass for a singular equilibrium constitutes a critical value for dense cores: no hydrostatic equilibrium solutions exist for higher values of $M_{\mathrm{4200AU}}$. Cores exceeding this limit can, thus, not be supported against gravitational collapse by isothermal pressure. (Note, however, that equilibria below this limit can be gravitationally unstable against perturbations.) The aperture mass for singular isothermal hydrostatic equilibrium spheres therefore appears to be a characteristic value of the aperture mass distribution. It thus appears that a critical state manifests in characteristic values of dense core properties.

If this is true it has two interesting implications. First, dense cores appear to preferentially exist in a close-to-critical physical state. We speculate that this might be because subcritical cores can easily disperse while supercritical ones will collapse to form stars. Only critical cores could then exist for a longer period. Second, the total pressure in the core, $P$, appears to be comparable to the thermal pressure. Contributions to the total pressure from the effect of turbulent gas motions or magnetic fields can not much exceed the thermal pressure. Otherwise the critical mass in the 4 200 AU aperture would be much larger, as one would need to replace the gas temperature with some higher effective one, $T_{\mathrm{g}} \to T_{\mathrm{eff}} = 2.33\,P m_{\mathrm{H}}/(\varrho k_{\mathrm{B}}) > T_{\mathrm{g}}$, where $m_{\mathrm{H}}$ is the hydrogen mass and the factor 2.33 holds for a gas mixture at cosmic abundance with most hydrogen in molecular form.

Densities can be derived from the aperture masses when assuming specific density profiles. For spherically symmetric density distributions with a constant density $\varrho_{\mathrm{flat}}$ within a radius $r_{\mathrm{flat}}$ (i.e., a "flat" density profile), a continuously connecting density profile $\varrho \propto r^{-2}$ for radii $r_{\mathrm{flat}} < r \le r_{\mathrm{out}}$, where $r_{\mathrm{out}}$ is the outer core radius, and $\varrho = 0$ for $r \ge r_{\mathrm{out}}$, the $H_2$ particle density and aperture mass are related by

$$n_{\mathrm{flat}}(H_2) = (0.7 \text{ to } 5.1) \cdot 10^5\,\mathrm{cm}^{-3}\,(M_{\mathrm{4200AU}}/M_{\odot})\,; \tag{2.34}$$

the conversion factor decreases when increasing $r_{\mathrm{flat}}$ from 2 000 AU to 10 000 AU (as adopted here; see below). To derive this we adopt the c2d standard $H_2$-to-gas mass conversion factors documented in Appendix A and $r_{\mathrm{out}} \gtrsim$ 15 000 AU (from observed effective subcore radii). The value of $r_{\mathrm{flat}}$ can, e.g., be roughly estimated from the effective radius at the 70% peak intensity level. For peaks with a width comparable to that of pure power law density profiles the observed width is approximately given by the geometric sum of $r_{\mathrm{flat}}$ and the half width of a pure $\varrho \propto r^{-2}$ density profile ($10\rlap{.}''7$ at 70% of the peak after smoothing to a 20$''$ beam). Thus $r_{\mathrm{flat}}$ can be as small as $\approx 2\,000$ AU (e.g., for L1521F C1), as also seen in Fig. 2.6. For other cores it can be of order of several 1 000 AU; we thus adopt the range in $r_{\mathrm{flat}}$ given above. Similar figures were derived by Tafalla et al. (2002), Crapsi et al. (2004), and Kirk et al. (2005). For typical inner radii $4\,000 \le r_{\mathrm{flat}}/\mathrm{AU} \le 10\,000$ the typical mass in a peak-centered aperture of 4 200 AU radius of $\approx 0.35\,M_{\odot}$ corresponds to a central $H_2$ particle density of 3 to $6 \cdot 10^4\,\mathrm{cm}^{-3}$. Adopting $r_{\mathrm{flat}} \le 2\,000$ AU for L1521F C1 we, however, also derive central densities of up to $\ge 4 \cdot 10^5\,\mathrm{cm}^{-3}$ in our sample.

#### 2.6.1.4 Elongation

Only 14% and 44% our of all starless and protostellar subcores, respectively, have major-to-minor axis ratios ≤ 1.2 and can be considered round; most subcores are not round. Unless these subcores are shaped by magnetic fields, which provide a non-isotropic supporting pressure, they can hardly on the whole be in a state of hydrostatic equilibrium.

The axis ratio distribution is continuous up to ratios of 2.0 and 2.5 for protostellar and starless subcores, respectively. Several subcores have much larger axis ratios. Subcores with larger axis ratios might be physically elongated to an unusual extent. However, they might also exhibit smaller and less elongated substructure, which is not disentangled into subcores because of insufficient resolution or signal-to-noise level, or both. Interestingly, two of the most distant subcores have the largest elongations (L1082A C4 and L1622A C3 at distances ≥ 400 pc). This suggests that some cores appear elongated due to confusion, as confusion on average increases with distance.

The median axis ratio of protostellar subcores is smaller than that of starless and VeLLO cores. This could be because the protostellar heating leads to an intensity peak of small physical size, which is blurred into a close-to-round structure because of beam smearing. On the other hand stars are expected to form in close-to-spherical density enhancements, which in projection show a low elongation (Shu 1977). Then, protostellar cores would be less elongated than the starless cores with their complex shapes at lower intensity contours. A more detailed analysis is needed to separate these effects.

The protostellar subcores CB188 C1, IRAS05413 C2, L1100 C1, L1251A C2, and L1251A C4 are well separated from the other protostellar cores in the elongation distribution. For IRAS05413 C2, however, the axis ratio and the orientation of the major axis are very uncertain ($1.9 \pm 0.5$ and $13° \pm 58°$, respectively). The observed elongation is likely to be an observational artifact. In L1251A, where the major axis exceeds the beam size by a factor of several, this elongation likely reflects the morphology of the dense core from that the embedded star formed. For CB188 and L1100, however, where the major axis exceeds the beam size by a factor 3.2 and less, this elongation should reflect the morphology of the immediate density peak from that the young star accretes. This region could be shaped by the interaction with outflows from the central star. An outflow has indeed been detected toward CB188 (Yun & Clemens 1994) and for L1100 there is some evidence for an outflow from broad line wings (De Vries et al. 2002). For CB188 the position of the outflow axis derived by Yun & Clemens (1994) and the major axis of the dust emission intensity distribution are neither aligned nor perpendicular (position angles of $\approx 75°$ and $16° \pm 5°$, respectively). If the elongated structure towards CB188 seen in the MAMBO maps is indeed related to the outflows, then the dust emission feature is likely to trace the wall of an outflow cavity. If it would trace the jet or a protostellar disk, the axes are expected to be parallel or perpendicular. While these observations do not prove the interaction between jets and the dense core, they motivate dedicated studies on this issue. A more detailed analysis of the dust emission maps might yield more candidates for jet-core interactions.

### 2.6.2 Relations between Core Properties

Figure 2.4 shows the relations between masses, radii, and column densities for the subcores within our sample. While some interesting trends appear biases in our source selection and quantification must be noted.

There is a clear correlation between the mass and the size of a subcore. Mass and effective radius are roughly related by $M \propto r_{\mathrm{eff}}^2$, as indicated by the line drawn in Fig. 2.4. The mean column densities across the dense cores are proportional to $M/r_{\mathrm{eff}}^2$ and appear constant across the sample. This is at least partially due to a selection bias: for a given total mass the effective radius can not be above a certain value. Else the the subcore would be too faint to be detected. To see this, consider that because of the selection criteria given in Sec. 2.4.2 the dust emission intensity within a subcore, $I$, must be larger than about twice the local RMS, $I_{\mathrm{RMS}}$. Using the relations from Appendix A this noise level can be converted into a column density, $N_{\mathrm{RMS}}(\mathrm{H}_2)$. Integration of the column density across a subcore of effective radius $r_{\mathrm{eff}}$ then yields a lower limit to the mass of the subcore, and thus $M \geq \pi N_{\mathrm{RMS}}(\mathrm{H}_2) r_{\mathrm{eff}}^2$. This reads $r_{\mathrm{eff}} \leq \{M/[\pi N_{\mathrm{RMS}}(\mathrm{H}_2)]\}^{1/2}$ after rearrangement and thus shows that for given noise level there is a maximum radius for a subcore of given mass. The limit shown in Fig. 2.4 is calculated adopting a noise level of 2 mJy beam$^{-1}$ typical for our survey.
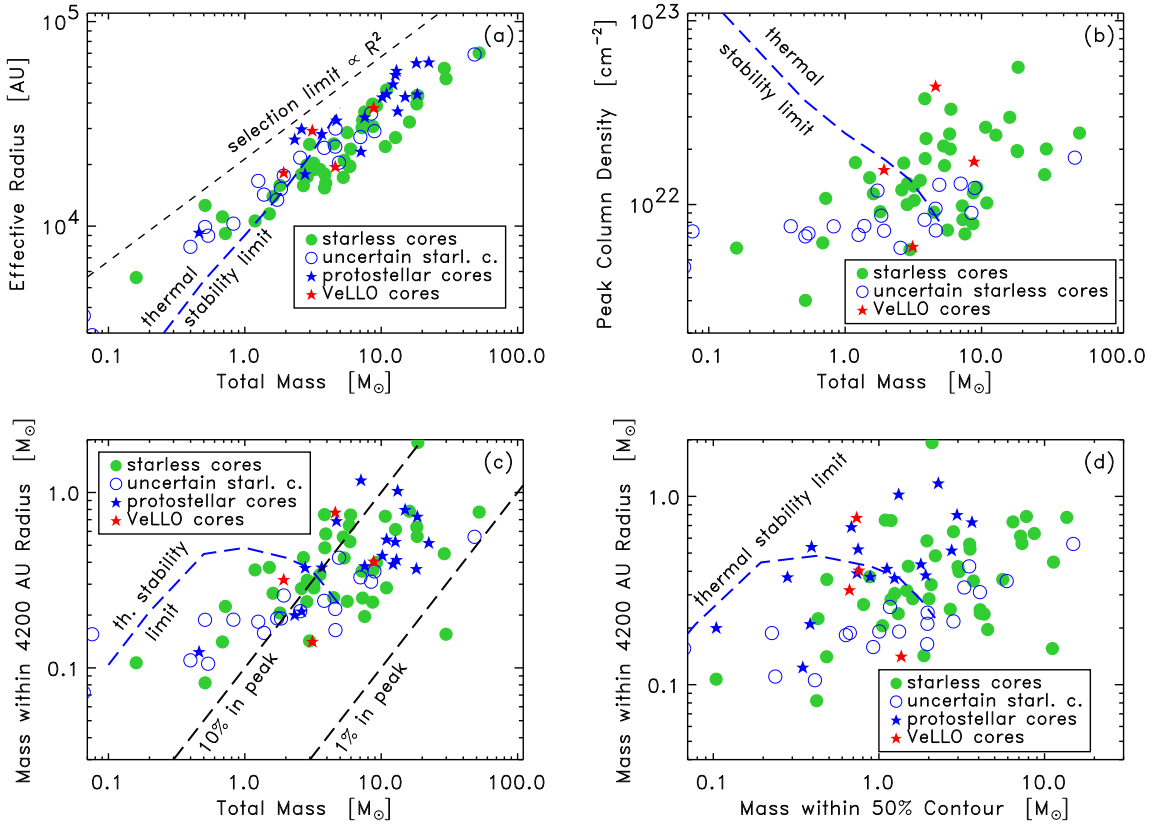
**Figure 2.4:** Necessary conditions for active star formation from relations between dense core properties. *Filled and empty circles* give the properties of subcores with well determined and uncertain properties due to artifacts, respectively. *Blue and red stars* are used for subcores hosting protostars and VeLLOs, respectively. The *black diagonal dashed line in panel a)* indicates a selection limit; for given total mass all subcores larger than this limit would be too faint to be identified in our maps. The *black diagonal dashed lines in panel c)* mark where $M = 0.1 \, M_{4200AU}$ and $M = 0.01 \, M_{4200AU}$: only a fraction of the dense core mass is available to form stars from a column density peak. The *blue dashed lines* show the critical stability limits for hydrostatic equilibria with pure thermal pressure. For given total mass, or mass within the half intensity contour, all subcores with pure thermal pressure and with radii smaller than the critical one — respectively column density or aperture mass exceeding the critical one — are unstable. These stability limits manifest in the data as necessary conditions for active star formation; most dense cores presently forming stars exceed these limits. However, these limits do not give sufficient conditions for ongoing star formation. Many starless cores have properties exceeding the critical values.

It is thus not likely that the correlation between mass and radius apparent in our data reflects actual properties of dense cores.

A correlation is also apparent between the peak column density and the total mass. It is not possible to place protostellar cores in this diagram because it is technically difficult to correct the observed intensities for the heating by the embedded protostar. Observational biases are at least partially responsible for the apparent correlation.

The limited size of our maps sets upper limits to the total mass of a subcore of given peak column density, $N_{\mathrm{max}}(\mathrm{H}_2)$. For given effective radius of the map, $r_{\mathrm{map}}$, it follows that $M \leq \pi N_{\mathrm{max}}(\mathrm{H}_2) r_{\mathrm{map}}^2$. Our survey thus can not detect massive subcores ($M \gg 10\,M_\odot$) of low peak column density ($N(\mathrm{H}_2) \leq 10^{22}$ cm$^{-2}$).

Beam smearing does not allow to infer accurate peak column densities for peaks smaller than the 20″ beam, i.e., a radius of 1 000 to 4 500 AU for distances of 100 to 450 pc. Since the effective radius is observed to increase with mass we can not exclude that the observed increase of the maximum peak column density with increasing total mass is partially an observational artifact.

The apparent deficiency of subcores with peak column densities below $\approx 5 \cdot 10^{21}$ cm$^{-2}$ is a direct result of the limited sensitivity of our observations. Cores with lower column density are usually too faint to be detected.

An increase of the mass within a 4 200 AU radius aperture is seen for increasing total mass, and the mass above half peak intensity. This again results from the limited size of the maps; the mass within a 4 200 AU radius aperture can be interpreted as an aperture-averaged column density and, thus, the argument given above applies. Similarly, the apparent deficiency of subcores with aperture masses below 0.1 $M_\odot$ results from the limited sensitivity.

The deficiency of cores with aperture masses exceeding the total mass, or the mass above the half intensity contour, is a combined effect of the source properties and the source identification scheme. To give an example, a very particular, though possible, source morphology is required in order to derive an aperture mass larger than the total mass.

For a given aperture mass, protostellar cores appear to have a lower mass within the half intensity contour than starless cores do. This is because for a given density structure a protostellar core with internal heating has a steeper intensity profile than a starless one (e.g., Motte & André 2001). Thus, for a given density structure the area above the half peak intensity contour and, thus, the derived mass, is smaller for protostellar cores.

Some 2% to 20% of the total mass of a dense core is concentrated in its brightest peak, which is quantified by the mass within an aperture of 4 200 AU radius. This is about the mass available for a star to accrete if the column density peak forms a star: the radius of the infalling part of a protostellar envelope increases at about the thermal sound speed during the collapse (Shu 1977) and thus becomes 4 200 AU for a gas temperature of 10 K at the end of the main accretion phase thought to last for about $10^5$ yr (Barsony & Kenyon 1992; Greene et al. 1994; Kenyon & Hartmann 1995). This scenario has several implications.

The observed aperture-to-total mass ratio can be taken as a rough estimate of the star formation efficiency of dense cores, i.e., the ratio of the stellar mass produced by a dense core to the total core mass. Then every star finally only contains a small fraction of the mass of the parental core. This would mean that dense cores contain enough mass to be able to form several stars. This would then question the fundamental rule "one dense core produces one star" often adopted when discussing the evolution of dense cores (e.g., Motte et al. 1998).

Finally, such a low star formation efficiency would suggest that the final mass of a star does not directly reflect the mass of the dense core from that it formed. Then the initial mass function of newborn stars would not be directly related to the mass function of the dense cores from that these stars form. This would question some current ideas on the origin of the initial stellar mass function (Motte et al. 1998).

### 2.6.3  Star Formation Ability

The masses, radii, and column densities presented in Fig. 2.4 provide insights on the densities and pressures within the dense cores. These in turn determine whether a dense core is stable against gravitational collapse. Thus a detailed analysis of the observed properties of dense cores allows to study their stability — and therefore their ability to form stars through gravitational collapse. We do so for our sample by interpreting the observations in the framework of a model of the structure and stability of dense cores.

### 2.6.3.1 Structure and Stability of Starless Dense Cores

Kauffmann & Bertoldi (in prep.) develop a theoretical model for the structure and stability of isolated dense cores. They assume them to be in hydrostatic equilibrium, i.e. to be supported against self-gravity by gradients of an isotropic pressure. These equilibria are idealized to be spherical. The total pressure, $P$, is calculated as the sum of thermal, $P_{th}$, turbulent wave, $P_w$, and magnetic pressure components, $P_m$. The thermal pressure is derived through a detailed thermal equilibrium calculation, while the turbulent and magnetic pressures are assumed to obey a polytropic equation of state. The equilibria are assumed to be embedded in some extended envelope that attenuates the interstellar radiation field.

Whether a given hydrostatic equilibrium is gravitationally stable depends on its response to perturbations in pressure or density. To evaluate the pressure response the thermal equilibrium calculation is solved for the perturbed state and polytropic relations are adopted to infer the pressure perturbations for the turbulent and magnetic pressure. A hydrostatic equilibrium is stable against spontaneous contraction or expansion when at every point in the cloud the pressure increases during a compression or decreases during an expansion, i.e. $\delta P/\delta r < 0$, where $r$ is the radius from the equilibrium center.

This analysis yields critical properties for dense cores. To give an example, when keeping the total mass and the central values of $P_w/P_{th}$ and $P_m/P_{th}$ fixed, there is a critical value for the column density on the central line of sight such that all dense cores with higher than critical column densities are unstable, while those with lower are stable. Furthermore, cores with thermal pressure only set *general* limits for several properties of stable cores. For example, for given mass the critical column density for cores with additional non-thermal pressure exceeds that of cores with pure thermal pressure.

Critical values for equilibria with pure thermal pressure can thus be used to limit ranges in observable properties for which stable equilibria exist for any boundary condition (i.e., ratio between non-thermal and thermal pressure components), from those where they exist only for special conditions, or not at all. However, many processes not taken into account in the above model might influence a cores' fate. For example starless cores may not evolve quasistatically and it is not clear how a cores' density structure evolves after the onset of collapse. The fundamental nature of this limit does, however, suggest that it *somehow* manifests in the properties of dense cores.

### 2.6.3.2 Necessary Conditions for Star Formation

The limits for the parameters of stable hydrostatic cores with pure thermal pressure are shown in Fig. 2.4. Somewhat different from the observational definition, the mass above the half peak intensity contour for the model is approximated by the mass within the half peak column density contour. The boundaries can only be calculated for total masses $\leq 5\,M_\odot$, as gas cooling rates are not available for $H_2$ densities $\leq 1\,000\,cm^{-2}$ that occur in more massive cores with pure thermal support. For given total mass, or mass within the half intensity contour, all subcores with pure thermal pressure and with radii smaller than the critical one — respectively column density or aperture mass exceeding the critical one — are unstable.

Comparison with the properties of protostellar cores and those containing VeLLOs reveals that most protostars in our sample do not fall within the zone containing stable equilibria with pure thermal pressure. Their envelopes are gravitationally unstable, unless supported by significant non-thermal pressure.

A careful analysis requires to take the limited spatial resolution and the significant deviations of core shapes from spherical symmetry into account. We therefore study the relation between the peak column density and the mass of a core through three slightly different approaches.

One way is to analyse the relation between the peak column density and the total mass (Fig. 2.4 b)). This has the advantage that the derived column densities are free of a distance bias, as the core distance does not enter in their calculation. They are, however, biased by the telescope resolution; only a lower limit to the peak column density can be derived for peaks smaller than the beam. It is also technically challenging to take the effect of protostellar heating into account when calculating the column densities of protostellar cores.

It is therefore helpful to substitute the peak column density by the mass within an aperture of $4\,200$ AU radius (Fig. 2.4 c)). This quantity is not biased by insufficient resolution, as we use the $11''$ resolution data, for which

the aperture is resolved for all our target cores, to calculate the aperture masses. Also, protostellar heating can be easily taken into account when deriving this mass (Sec. 2.4.2.3). The subcore masses can, however, include contributions from an extended envelope. It is questionable whether an extended envelope of some 10 000 AU radius can be considered to be the outer part of a smaller scale column density peak of some 1 000 AU radius, or is physically decoupled. Thus the total mass might not be a good parameter to compare models with observations.

One might therefore use the mass within the half peak intensity contour instead of the total mass, as this excludes some possibly unrelated emission. Combination with the mass within an 4 200 AU radius aperture yields a diagnostic diagram of core properties that is free of many biases (Fig. 2.4 d)).

Most protostellar and VeLLO subcores avoid the zone where stable equilibria with pure thermal pressure reside. Given typical uncertainties in the derived properties of a factor two, only for four such subcores their location within this zone is significant.

For one of the protostellar subcores in this region, L1521-2 C1, the protostellar nature is highly questionable. The association is only based on the fact that an IRAS source is projected onto the core. This source does not manifest as a dust emission peak, which makes the association uncertain. One further protostellar subcore, B18-1 C2, is not well mapped and has very uncertain properties. Furthermore, this protostar has a high bolometric temperature of 636 K, suggesting an evolutionary state much more advanced than the initial states of star-forming cores contemplated in the Kauffmann & Bertoldi model. In the case of the VeLLO candidate subcore L1148 C1 the nature of the object is not ultimately clarified. If it is a young protostar, then it must have formed by non-quasistatic evolution, as it would otherwise not have become unstable for the low column densities observed (Kauffmann et al., in prep.). Thus L1148 C1 might be a true exception from the rule that protostars in early evolutionary stages do not reside in the zone where stable equilibria with pure thermal pressure exist. As this is a VeLLO, this source might however not reflect the evolution of most protostars.

The subcore CB188 C1 is definitely such an exception. Its bolometric temperature is below about 250 K, and it can thus not be much evolved. However, as discussed in Sec. 2.6.1.4, it does drive an outflow that is possibly interacting with the parental dense core. In this case one would expect that the parental dense core is disrupted and reduced in mass via this interaction. It might thus be that CB188 C1 is an unusual case, not suited to study general properties of star-forming cores.

Thus, all protostars of our sample that are in an early evolutionary stage (i.e., $T_{\mathrm{bol}} \lesssim 300$ K), which furthermore from their general properties appear to reflect the majority of protostars (i.e., no core-outflow interactions, not a VeLLO), do not reside in the parameter space where stable equilibria exist for pure thermal pressure. Thus physical properties (e.g., masses and column densities) exceeding those for stable hydrostatic cores with pure thermal pressure appear to be a necessary condition for star formation to occur in a given dense core. This is not a sufficient condition, as also the properties of many starless cores without active star formation exceed the hydrostatic stability limits for pure thermal pressure. Similarly, it is not possible to separate starless and protostellar cores using the properties analysed above.

If dense cores evolve quasistatically, and feature levels of non-thermal pressure varying between cores, the nature of this necessary condition can be understood in the framework of the model of hydrostatic cores introduced above. Cores not exceeding the limits for stable hydrostatic cores with pure thermal pressure support are then stable against collapse. They are therefore starless. Cores need to exceed these limits in order to be able to form stars. Thus, protostars form only beyond the limits and stay there for a longer time as their envelope evolves slowly while collapsing. For sufficiently high non-thermal pressure the same parameter space contains, however, also stable hydrostatic cores that stay starless. This would in this interpretation be the reason why there is no sufficient condition for star formation to occur; no general stability limit exists as stability depends on the amplitude of non-thermal pressure in a given dense core. Protostellar cores finally evolve by reducing their masses and their column density. In these later stages they can then also appear in the parameter space where hydrostatic cores with pure thermal pressure reside.

Quasistatic evolution of dense cores would explain the necessary condition for stars to form. Though it helps to interprete the data, we cannot conclude that our observations uniquely show that dense cores are in hydrostatic equilibria.
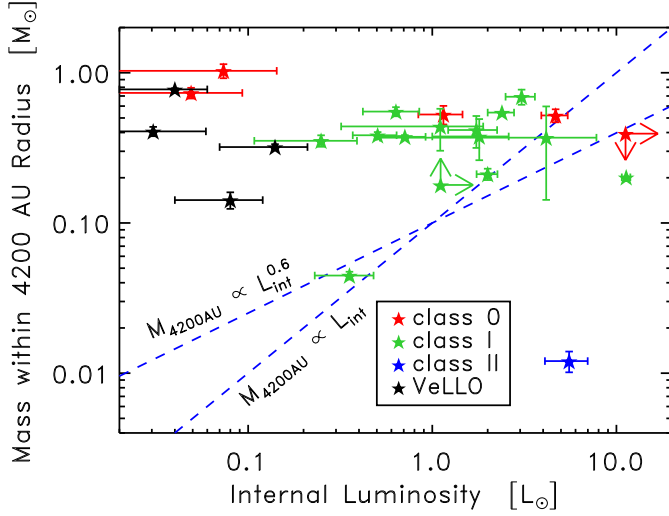
**Figure 2.5:** The relation between the internal luminosity and the mass within a peak-centered 4 200 AU radius aperture for protostellar cores. The internal luminosity is the radiation due to the embedded star, i.e., the bolometric luminosity minus the power from interstellar heating. *Stars of different colours* give properties for protostars belonging to different infrared SED classes assigned on basis of their bolometric temperature and luminosity (see legend). The *dashed lines* indicate the conceptual boundary between class 0 sources and objects in later evolutionary stages for a spectrum of stellar mass-luminosity relations, $M_{4200AU} \approx 0.1 \, M_{\odot} \, (L/L_{\odot})^{0.6 \text{ to } 1.0}$. Interestingly, class 0 and class I sources covered by the c2d MAMBO survey are not separated by the conceptual class boundaries.

## 2.6.4 Evolution of Protostars

Protostars are expected to evolve in luminosity and envelope properties during the star formation process. Three basic properties to characterise a protostar are its age, as roughly measured by the bolometric temperature or the infrared class, the luminosity, and the amount of matter surrounding the star. The two latter should depend on the age, as the accretion of envelope mass onto the forming star affects the amount of matter near the protostar, while the stellar luminosity from accretion, e.g., depends on the stellar mass and radius, which evolve with time. Figure 2.5 shows the relation between luminosities and envelope masses.

To better characterise the central star we use the internal luminosity, $L_{int}$, that is due to the protostar instead of the bolometric luminosity, i.e., the total radiative power minus that due to interstellar heating. This luminosity is taken to be identical to the bolometric one, except for some VeLLOs for which detailed estimates exist from other studies (Bourke et al., in prep.; Kauffmann et al., in prep.; Young et al. 2004).

Except for the significant decrease in $M_{4200AU}$ towards the class II phase, no clear evolutionary trends exist in our data; the crowding of VeLLO candidates at low luminosities is due to their definition. In particular it is not possible to identify an evolutionary sequence that has young class 0 sources at one end and old class II or III sources at its other. This is surprising, considering that previous studies identify such sequences in the $L_{int}$–$M_{4200AU}$ parameter space (e.g., Motte & André 2001).

Motte & André (2001) analyse the luminosities and envelope masses for protostars in Taurus and the $\varrho$ Ophiuchi region. Their data is consistent with protostars being born as class 0 sources with low luminosities and high envelope masses that then evolve towards the class I stage by increasing their luminosity and reducing their envelope mass via accretion. Once the envelope is sufficiently dispersed and accretion ceases, the stars become class II or III sources with luminosities and envelope masses smaller than what they had in the class I stage.

Motte & André also give a limit in the $L_{int}$–$M_{4200AU}$ space that separates class 0 sources from the later stages.

This boundary is thought to reflect the conceptual definition of class 0 sources, i.e., they have accreted less than half of their final mass (Andre et al. 1993). This requires that the envelope mass approximated by $M_{4200AU}$ exceeds the stellar mass. Depending on the exact form of the protostellar mass-luminosity relation, Motte & André suggest this boundary to be at $M_{4200AU} \approx 0.1\, M_\odot\, (L/L_\odot)^{0.6\ \text{to}\ 1.0}$ (see Andre & Montmerle 1994 and Andre et al. 2000 for further details). More massive objects should be in their class 0 stage, i.e. their main accretion phase. For accretion rates proportional to the envelope mass $M_{4200AU}$, which decreases in mass via accretion, the $M_{4200AU} = 0.1\, M_\odot\, (L/L_\odot)^{0.6}$ limit is furthermore the position of maximum luminosity along protostellar evolutionary tracks (Motte & André 2001). Protostars first evolve at about constant envelope mass from the start of the collapse, where the luminosity is zero, to this curve. Then they evolve towards lower luminosities and envelope masses (with masses being below the limit for class 0 sources). In particular models with such or similar accretion rates provide a good fit to the protostar data of Motte & André.

Our data is not fully consistent with such scenarios. Our class 0 and class I sources have similar properties, i.e., they occupy the same parameter range in the $L_{int}$–$M_{4200AU}$ space. This is different for the stars studied by Motte & André: for given aperture mass, or luminosity, their class 0 objects have lower luminosities, respectively higher aperture masses, than all their class I sources. Second, not all class 0 sources in our sample are well above the luminosity-dependent theoretical mass limit thought to separate class 0 from class I sources. No such behaviour is seen in the samples of Motte & André. Third, essentially all class I objects in our sample are in the parameter range thought to be only occupied by sources having envelope masses exceeding their stellar mass, i.e., occupied by class 0 sources. This is also the case for the Taurus class I sources studied by Motte & André. Their class I objects in the $\varrho$ Ophiuchi region, however, do all fall short of the luminosity-dependent limiting aperture mass, i.e., these have masses and luminosities expected for stars beyond the class 0 stage.

.

The discrepancies betweenexpectations and observations in our sample can, in principle, be caused by different biases in the aperture mass estimates for class 0 and class I sources. These biases would need to affect both classes of sources, as not all class 0 and I sources would satisfy the conceptual class definition. The biases would need to be different for each class, as otherwise class 0 and class I aperture masses would still be similar for given luminosity. This would, however, require errors in the mass estimates of order of a factor 5 for both classes of objects, and a systematical bias between mass estimates of class 0 and class I sources of order of a factor 2 (see Fig. 2.5). However, systematic biases of this order, and in particular a differential bias of such a large magnitude between two similar types of sources, are not consistent with the expected uncertainties of our mass estimates. We thus discard biases in our mass estimates as an explanation for the above deviations between observations and expectations. Systematic errors in the luminosity estimates can be excluded, given that they can be observed directly.

If the placement of the protostellar cores in the $L_{int}$–$M_{4200AU}$ space are correct, then the class assignments for our sample are incorrect. Otherwise class 0 sources and later stages are not separated by the conceptual limit. As the classification is based on the bolometric temperature, this would imply that the derived temperatures are wrong. Such wrong assignments are, however, unlikely: for the three class 0 sources with internal luminosities $\gtrsim 1\, L_\odot$ the IRAS data alone indicates that the SED maximum, and thereby the flux-weighted mean wavelength, lies longwards of 100 $\mu$m wavelength, so that $T_{bol} \leq 70$ K, implying a class 0 sources. Given the good 2MASS-to-IRAS spectral coverage of bolometric temperatures of hotter sources are beyond doubt.

It thus appears that either the concept of infrared classes, respectively their assignment via the bolometric temperature, or our general understanding of protostellar evolution as a linear sequence of states in the $L_{int}$–$M_{4200AU}$ parameter space, needs some modifications. That similar studies of different regions find different relations between protostellar and envelope properties suggests that the environment influences these relations. The resolution of these issues is beyond the scope of our work. It might be that the analysis of additional stellar properties, such as outflow energetics (Bontemps et al. 1996), can help to better understand the relation between evolutionary trends and class assignment. It has been speculated that actual class I sources have SEDs like class 0 sources if the circumstellar disk-envelope structure is seen edge-on (e.g., Whitney et al. 2003b for an overview). This could explain why we find class 0 sources that have envelope properties typical of class I objects. Interestingly, the class 0 source

in IRAS05413 P3 appears to have such a particular geometry; here the outflow has an estimated inclination of $\gtrsim 85°$ with respect to the line of sight, suggesting that a protostellar disk, is seen nearly edge-on (Claussen et al. 1998). No information on outflow inclinations is available for the stars in L1082A P5 and L1041-2 P4.

The submillimetre-to-bolometric luminosity ratio (Fig. 2.7) is also not well suited to separate class 0 sources from class I objects. We caution that the large luminosity ratios $> 0.1$ for some sources are likely not real, but due to an insufficient spectral coverage of our photometry. The original initial observational criterion to identify class 0 sources given by Andre et al. (1993) is a luminosity ratio $\gg 0.005$. Following this criterion, all but one star in our sample would then be regarded as class 0 objects. Then there would also not be any class I source with an envelope mass exceeding that expected for class I sources based on conceptual class definitions. This is because the submillimetre-to-bolometric luminosity ratio roughly measures the envelope-to-stellar mass ratio (Andre et al. 1993). A class definition through luminosity ratios might thus be better suited to derive a self-consistent source classification scheme than one based on bolometric temperatures. The class definition via bolometric temperatures was initially tuned to yield class assignments consistent with those determined from submillimetre data. If bolometric temperatures turn out not to always provide class assignments consistent with new dust emission observations they should not be used to define infrared classes.

The observational properties and the apparent evolution of protostellar envelopes seems to depend on the environment and is not fully consistent with theoretical expectations. The c2d MAMBO survey extends previous work on this subject by showing that class 0 sources have envelope properties similar to those of class I sources. When compared to the $L_{\mathrm{int}}-M_{\mathrm{4200AU}}$ relations for the Taurus and $\varrho$ Ophiuchi star-forming regions the protostars in our sample are more similar to the stars in Taurus. To be precise, in contrast to the class I sources in the $\varrho$ Ophiuchi complex those in our survey do, like those in Taurus, not generally fall short of the conceptual luminosity-dependent mass limit for class 0 sources. This suggests that the stars in our sample reside in regions that are more similar to regions of distributed star formation, like Taurus, than to regions of clustered star formation, like $\varrho$ Ophiuchi.

Independent of the detailed evolution protostellar envelopes must evolve from large aperture masses to lower masses while the envelope is accreted onto the star. Evolved protostars within remnant envelopes not detected in our dust emission maps should have SEDs dominated by photospheric emission at wavelengths of a few $\mu$m and therefore negative spectral indices at wavelengths of $\approx 10$ to $20\,\mu$m. This is consistent with our observations (Table 2.7): All IRAS sources that are undetected with MAMBO are consistent with a negative spectral index. Although some of these IRAS sources may be background galaxies, this observation does support our general view of protostellar evolution.

The protostar associated with L1251A P3 shows a marginally significant offset from its dust emission peak (see Sec. 2.6.5 for details). Present evolutionary scenarios do not explain such offsets. However, an offset could affect the course of protostellar evolution if it grows so large that the protostar is finally left without an envelope from that it could accrete. Higher resolution column density maps, e.g. from extinction observations, would be needed to reliably establish such offsets.

### 2.6.5   Formation and Evolution of VeLLOs

The c2d MAMBO survey provides an opportunity to investigate how VeLLO natal cores are different from starless and protostellar cores. For the first time it allows a direct comparison of the dust emission properties of all three kinds of objects. We here discuss how VeLLO cores differ from starless and protostellar cores.

Figures 2.3 and 2.4 show that VeLLO cores can not be distinguished from starless cores in terms of mass, column density, and total effective radius. This is even more surprising than our failure to distinguish starless cores from protostellar cores in these diagrams since the latter might have significantly evolved since their formation. VeLLOs are, however, thought to be too young (Sec. 2.1.2) and to have too low internal luminosity and accretion rates to have envelopes significantly modified by, e.g., energetic outflows or radiation pressure. The structure of their envelopes should be similar to that at the onset of the protostellar collapse which forms the embedded VeLLOs. Given the small internal luminosities, a comparison of VeLLO and starless cores is also less affected by any systematic biases in the mass estimate, making the analysis more reliable.
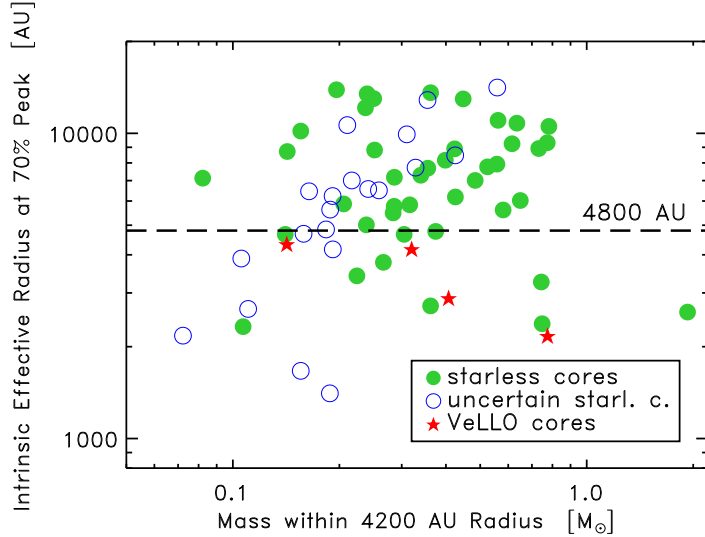
**Figure 2.6:** Relation between the intrinsic radius at 70% peak intensity and the mass within 4 200 AU radius from the peak for VeLLO and starless cores. The plotted effective radii deviate from the ones listed in Table 2.7 in that the beam smearing is removed (7″.2 at 70% peak). See Fig. 2.4 for an explanation of the symbols. The *dashed line* indicates the upper radius limit for evolved dense cores, $\leq 4\,800$ AU, after Crapsi et al. (2005a). The VeLLOs observed all fall below this limit and are, for given aperture mass, smaller than most starless cores. VeLLO cores are thus possibly physically more evolved than starless cores. This appears to distinguish them from starless cores.

We thus find with L1014 C1, L673-7 C1, and L1148 C1 VeLLO subcores that are, at least on the scales probed by our observations, less dense and massive than some starless subcores, like e.g. the dust emission peaks B18-1 P3 and B18-4 P2. This can, e.g., be quantified by column densities, masses with the 4 200 AU aperture, and masses within the 50% intensity contour for the starless cores exceeding those of the above VeLLO cores. Given that a certain density and mass reservoir is required for star formation to be initiated, this observation is in conflict with naive expectations for properties of starless and protostellar cores.

This apparent conflict is a manifestation of the existence of necessary, but not sufficient conditions for active star formation. The properties of the VeLLO and starless cores quoted above are all (with the important exception of the VeLLO in L1148 P1) consistent with being in excess of the critical values from Sec. 2.6.3.2 for active star formation to be possible. The cores thus can, but do not need to form stars. As outlined in Sec. 2.6.3.2, the presence of significant non-thermal pressure in cores like B18-1 and B18-4 might prevent these from actively forming stars.

The VeLLO in L1148 P1 — if confirmed to be a protostar — poses a real challenge to present star formation scenarios. This core does not exceed the stability limits for hydrostatic cores with pure thermal pressure. It is not possible to render this core gravitationally unstable in quasistatic evolutionary schemes. The apparent gravitational collapse onto an embedded star must then be a consequence of a non-quasistatic evolution of this core (Kauffmann et al., in prep., and Sec. 3.6.2.1). If true, this would be one of the first known cases for such evolution to occur.

VeLLO natal cores do, however, have unusually steep dust emission intensity profiles, as e.g. probed by the effective radius of a dust emission peak at its 70% intensity level. For given aperture mass, VeLLO cores do have smaller effective radii than most starless cores (Fig. 2.6). Since their apparent effective radius is (with the exception of the VeLLO in L673-7 P1) significantly larger than the one of a $\varrho \propto r^{-2}$ density profile smeared by a 20″ beam, i.e. 10″.7, their density profile must be flatter than $\varrho \propto r^{-2}$. Then the beam averaged actual mean dust temperatures will be $\lesssim 14$ K, as derived for $p \leq 2$, $d \geq 140$ pc, and $L \leq 0.1\,L_\odot$, and thus heating does not have a significant impact on the appearance of VeLLO dust intensity profiles.

The unusually steep dust intensity profiles of VeLLO natal cores are thus due to unusually steep column density

profiles. This distinguishes them from most starless cores in our sample. Steep radial profiles in the density, and therefore also in the column density, are indeed expected for dense cores temporally near or after the onset of gravitational collapse. This is apparently the case for VeLLO natal cores. Dense cores that become unstable to gravitational collapse evolve by increasing their center-to-surface density contrast until the onset of collapse (e.g., McKee & Holliman 1999). After the onset of collapse their density profile turns into a power-law (see Larson 2003 for a review). Density gradients in VeLLO cores are consistent with this theoretical picture.

The steeper density profiles of VeLLO natal cores suggest that they are temporally closer to the onset of gravitational collapse than most starless cores. *It thus appears that VeLLO cores are structurally different from most starless cores in that their density structure is more evolved.* This was first suggested by Huard et al. (2006), who used infrared extinction maps to derive surface-to-center density contrasts for that L1014 P1 exceed those of previously studied starless cores. Similarly, Crapsi et al. (2005a) suggested that for starless dense cores effective radii at the 70% dust emission peak intensity level below 4 800 AU indicate an advanced evolutionary state. All our VeLLO cores do indeed conform to this criterion. Our survey is thus the first study to reveal systematic differences between VeLLO and starless cores for a comprehensive sample of VeLLO cores.

Huard et al. (2006) found that the VeLLO in L1014 is offset by $10''$ to $15''$ from the apparent natal column density peak, L1014 P1. If L1014-IRS does indeed drift away from its natal core, and therefore away from the mass reservoir available for accretion, this might explain the low rate of accretion onto L1014-IRS inferred by Bourke et al. (2005). Low accretion rates could in turn explain the low luminosities of VeLLOs. They would also suggest low, and possibly substellar, final masses for VeLLOs with low accretion rates (Bourke et al. 2005). Given typical pointing uncertainties of $3''$ for our observations, our data should be sensitive to protostellar offsets of the order observed for L1014-IRS, and we thus search for such offsets in our data. For completeness we extend this analysis to all protostars in our sample.

The protostar positions are taken to be those of Spitzer counterparts listed in Table 2.9. Otherwise the positions of the 2MASS counterparts given in Table 2.8 are used. For B18-4 P1 the protostar position is derived by fitting a Gaussian curve to the Spitzer counterpart in the IRAC images. The dust intensity peak positions are derived as the intensity-weighted mean position of the pixels above 90% peak intensity. The offsets are given in Table 2.10. The uncertainty in the dust emission peak position due to noise is derived from Monte-Carlo experiments with artificial noise, as explained in Sec. 2.4.2. The typical pointing uncertainty of $3''$ is added to the observed offsets to derive the total dust emission position uncertainty. The offsets and their total uncertainties are shown in Fig. 2.7.

Only four sources have significant offsets (i.e., $\geq 2''$ after subtraction of the uncertainty). These are two VeLLOs (associated with L1521F P1 and L1148 P1), and two one class I sources (associated with L1172A P1 and L1251A P3). The pointing corrections before and after observations of L1148 and L1251A were $\leq 4.''3$ and $\leq 5.''9$, respectively, and thus the offsets appear to be significant in these cases. For L1521F the corrections were between $3.''7$ and $8.''8$; the separation of protostar and dust peak is not significant given the pointing uncertainties. For L1172A the protostar position is taken to be the position of a 2MASS source which is the likely counterpart of the IRAS protostar. As this association is not well established, the position offset of L1172A is very uncertain. In summary only the VeLLO in L1148 P1 and the class I protostar related to L1251A P3 have marginally significant offsets from their respective dust emission peaks. These offsets might influence the future stellar evolution, but the significance of these offsets is too low to ultimately establish them beyond doubt.

Given the low precision of the offset measurements, the MAMBO data is thus only partially suited to test whether VeLLOs, and more generally protostars, are offset from their associated dust peaks. Note that, however, the MAMBO data would be sensitive enough to detect the $10''$ to $15''$ offset of the VeLLO in L1014 from the related column density peak inferred from extinction maps (Huard et al. 2006). Our failure to detect this offset in our MAMBO maps of L1014 thus suggests that dust emission maps are perhaps generally not suited to map the density structure near a VeLLO in detail. This might be due to the influence of stellar heating, as already concluded by Huard et al. (2006).

**Table 2.10:** Protostar offsets from dust emission peaks. For each dust emission peak, and related subcore, associated with a protostar listed in Tables 2.8 and 2.9 we give the chosen reference source (preferentially seen by Spitzer) and the observed offset and position angle (i.e., position of star w.r.t. the dust emission peak). The data is plotted in Fig. 2.7.

| Field | Asso. | Position Reference | Offset | | Position Angle |
|---|---|---|---|---|---|
| | | | arcsec | AU | deg |
| L1521F | C1, P1 | SSTc2d J042839.0+265135 | 5.0 ± 0.6 | 701 ± 84 | 289 ± 8 |
| B18-1 | [C2], [P5] | SSTc2d J043215.4+242859 | 1.1 ± 0.6 | 149 ± 80 | 310 ± 41 |
| B18-4 | C1, P1 | SST GO 3584 | 2.2 ± 0.6 | 303 ± 80 | 38 ± 11 |
| TMC1-1C | P3 | SSTc2d J044138.8+255627 | 3.3 ± 2.5 | 457 ± 347 | 36 ± 18 |
| TMC-1 | C2, P2 | SSTc2d J044112.7+254635 | 3.1 ± 0.6 | 429 ± 80 | 288 ± 22 |
| IRAS05413 | C2, P2 | 2MASS J05434630-0104439 | 2.1 ± 0.5 | 837 ± 209 | 214 ± 15 |
| CB188 | C1, P1 | SSTc2d J192014.9+113540 | 2.3 ± 0.7 | 695 ± 203 | 185 ± 148 |
| L673-7 | C1, P1 | SSTc2d J192134.8+112123 | 2.1 ± 0.9 | 643 ± 259 | 16 ± 23 |
| L1148 | C1, P1 | SSTc2d J204056.7+672305 | 7.6 ± 2.7 | 2461 ± 877 | 20 ± 51 |
| L1082A | C1, P1 | 2MASS J20531346+6014425 | 2.7 ± 0.9 | 1195 ± 375 | 212 ± 22 |
| L1228 | C1, P1 | SSTc2d J205712.9+773544 | 0.8 ± 0.1 | 151 ± 12 | 50 ± 29 |
| Bern48 | C1, P1 | SSTc2d J205914.0+782304 | 0.8 ± 0.3 | 165 ± 53 | 134 ± 30 |
| L1172A | C2, P2 | 2MASS J21022122+6754202 | 9.0 ± 1.4 | 2592 ± 414 | 322 ± 10 |
| L1177 | C1, P2 | 2MASS J21173862+6817340 | 4.0 ± 0.0 | 1582 ± 2 | 332 ± 0 |
| L1021 | P1 | 2MASS J21212751+5059475 | 2.5 ± 0.8 | 490 ± 168 | 338 ± 28 |
| L1014 | C1, P1 | SSTc2d J212407.5+495909 | 2.2 ± 1.3 | 440 ± 254 | 10 ± 57 |
| L1251A | C2, P3 | SSTc2d J222959.5+751404 | 8.8 ± 1.3 | 2635 ± 394 | 339 ± 17 |
| | C3, P4 | SSTc2d J223031.8+751409 | 1.2 ± 0.2 | 373 ± 70 | 290 ± 29 |
| | C4, P5 | SSTc2d J223105.6+751337 | 4.3 ± 0.8 | 1295 ± 250 | 353 ± 20 |
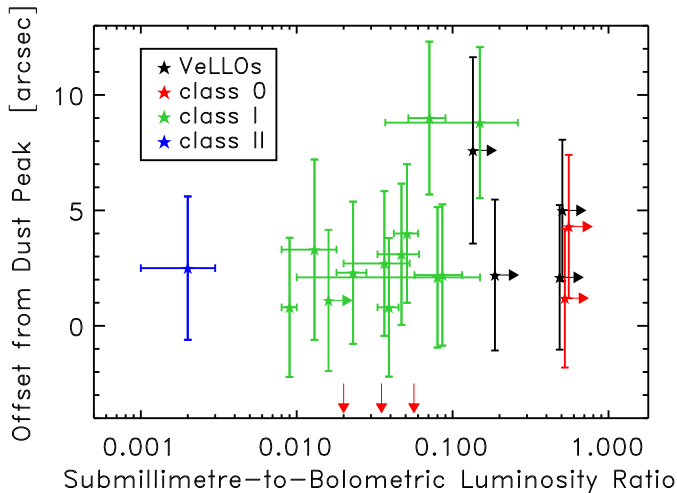
**Figure 2.7:** Offsets of protostars from the related dust emission peaks versus the submillimetre-to-bolometric luminosity ratio. See Fig. 2.5 for an explanation of the symbols. The plotted values are different from those in Table 2.10 in that the typical pointing error of 3″ is added. For completeness *arrows on the luminosity ratio axis* indicate the submillimetre-to-bolometric luminosity ratios for class 0 sources with unknown protostellar offset. Given the individual actual pointing uncertainties estimated from pointing observations marginally significant protostellar offset are found for two sources only (L1148 P1 and L1172A P2).

### 2.6.6   Expected Conditions for Active Star Formation

Crapsi et al. (2005a) give a set of criteria to identify evolved starless dense cores temporally close to the onset of active star formation. Dense cores should be sufficiently massive, dense, and chemically evolved to be able to form stars. As Crapsi et al. (2005b) and Kauffmann et al. (2005) note, the VeLLOs in L1014 and L1148 do not conform to these criteria. Although they are known to actively form stars and have dense cores similar to those at the onset of gravitational collapse (Sec. 2.6.5), they are not evolved according on the Crapsi et al. criteria. This discrepancy between observed and expected initial conditions for star formation means that either the Crapsi et al. criteria miss a significant fraction of cores with physical conditions in favour of gravitational collapse, or that some VeLLOs do form in cores that should not be able to collapse. In the latter case, some VeLLOs pose a challenge to star formation scenarios.

As discussed in Sec. 2.6.5, almost all VeLLO natal cores exceed the stability limits for hydrostatic cores with pure thermal pressure. They thus fulfil a necessary condition to form stars. For given mass within an aperture of 4 200 AU radius, VeLLO natal cores have effective radii at the 70% peak intensity level smaller than those of most starless cores (Sec. 2.6.5). This indicates that most VeLLOs form in dense cores that are evolved enough to collapse.

The Crapsi et al. criteria miss some physically evolved cores, i.e. cores conforming to the necessary conditions for active star formation from Sec. 2.6.3.2. Crapsi et al. (2005a) tuned their criteria to identify starless cores with properties similar to those of the prototypical evolved cores L1544 and L1521F. The latter were shown to be unusually dense (Tafalla et al. 2002 for L1544; for all properties of L1521F see Crapsi et al. 2004), to exhibit inward motions thought to precede the protostellar collapse phase (Tafalla et al. 1998), and to be strongly chemically evolved (Caselli et al. 2002c). These two cores were therefore regarded to be among the best known candidates of starless dense cores just before the onset of active star formation (Crapsi et al. 2004). This reasoning is crowned by the recent discovery of a VeLLO in L1521F (Bourke et al., in prep.). There is, however, no reason to assume that all starless cores just before the onset of active star formation should have properties similar to those of L1544

and L1521F. In particular, there is no obvious need that cores able to actively form stars have sizes and masses comparable to those of L1544 and L1521F. A comparison of the properties of protostar envelopes to those of L1521F actually reveals the contrary (e.g., Fig. 2.4). *The Crapsi et al. criteria should thus not be expected to identify all chemically and physically evolved cores.*

It is therefore desirable to complement the criteria for evolved cores forwarded by Crapsi et al. (2005a) by less biased additional criteria. The necessary condition for active star formation derived in Sec. 2.6.3.2 might serve as an example for such a rule.

## 2.7 Summary

We present a dust continuum emission imaging study of a comprehensive sample of isolated starless and proto-stellar dense molecular cores, the c2d MAMBO survey. This survey is less affected by instrumental biases than previous similar studies. This is made possible by the the large field-of-view of the 117-channel Max-Planck Bolometer (MAMBO-2) array on the IRAM 30m-telescope and by new iterative map reconstruction techniques developed for this survey. Its potential is enhanced by sensitive Spitzer imaging for 2/3 of the cores mapped. The c2d MAMBO sample covers about 1/4 of the isolated dense cores imaged by the Spitzer Legacy Program "From Molecular Cores to Planet Forming Disks" (AKA. "Cores to Disks" or "c2d").

The main result of our study is the identification of necessary conditions for star formation in dense cores (see Sec. 2.6.3.2 and Fig. 2.4): dense cores need to exceed certain critical values for active star formation to be possible. These conditions are, however, not sufficient for star formation to occur; starless and protostellar dense cores have similar properties. The mass distribution probed by our dust emission survey is not the only characteristic controlling the star formation ability of dense cores. The critical values for active star formation to be possible are identical to the critical values for stable hydrostatic equilibria supported by pure thermal pressure. If starless dense cores evolve quasistatically it is possible to understand the existence of such necessary conditions for active star formation: the critical values for gravitational collapse to be initiated depend on the turbulent and magnetic pressure in a particular core, which results in a spectrum of critical values fora sample of dense cores. The assumption of quasistatic evolution is not needed to establish the above conditions observationally. We do not claim that dense cores are indeed hydrostatic equilibria.

We study the relation between the spectral properties of protostars and their envelope characteristics (Sec. 2.6.4 and Fig. 2.5). In our sample the identification of class 0 and class I sources through their bolometric temperature is inconsistent with the conceptual definition of class 0 sources as protostars that accreted less than half of their final stellar mass. This is in disagreement with protostar studies in regions of clustered star formation like $\varrho$ Ophiuchi, where both methods of class assignment agree. The environments probed by our survey are more similar to regions of distributed star formation like Taurus, for which it is already known that different class assignment methods led to inconsistent results. Either the assignment of infrared classes on basis of bolometric temperatures, or the methods to evaluate the conceptual class definition on basis of stellar and dense core masses, or both, need to be revised.

Our VeLLO studies reveal that most VeLLOs form in cores that fulfil the necessary conditions for active star formation derived in Sec. 2.6.3.2 (Sec. 2.6.5 and Fig. 2.4). Thus, it is not surprising that VeLLO natal cores do form stars. Furthermore, they appear to have steeper column density profiles than most starless cores (Fig. 2.6). In this sense they appear to be more physically evolved than starless cores, which distinguishes them from their starless counterparts. VeLLO cores were suggested to be different from usual protostellar cores in that the star is significantly offset from the parental cores' column density peak, which might result in low accretion rates. We can not confirm this finding with our data, but our data may not be suited to establish such offsets.

Based on their dust continuum emission one would classify VeLLO natal cores as physically evolved and suited to form stars. Given that they do form stars, this casts doubt on present criteria to identify "evolved" dense cores that imply that many VeLLO cores are actually not evolved (Sec. 2.6.6). Such criteria apparently need to be revised and extended. In this respect studies like the c2d MAMBO survey have the potential to significantly extent our understanding of the dense core evolution toward the onset of star formation.

# Chapter 3

# The Candidate Very Low Luminosity Protostar L1148-IRS

We report the discovery of L1148-IRS, a candidate Very Low Luminosity Object (VeLLO; $L \leq 0.1 L_\odot$) in the nearby ($\approx$ 325 pc) L1148 dense core. The global spectral energy distribution, the morphology of nebulosity detected at $\approx 1 \mu$m wavelength, the inferred density profile of the dense core, and the tentative detection of inward motions towards L1148-IRS are consistent with those expected for embedded protostars. It is unlikely that L1148-IRS is a galaxy by chance projected onto the L1148 dense core. We do, however, not detect hallmarks of active star formation like molecular outflows or clear bipolar nebulosity conclusively proving a protostellar nature of L1148-IRS. Their lack is consistent with our present view of VeLLOs.

If L1148-IRS is a VeLLO, then it is a very interesting one. Its mass would be presently substellar, and its immediate envelope has a mass of only $\approx 0.15 M_\odot$. Thus L1148-IRS would be the first protostar to definitely have a significantly sub-solar final mass. The collapse of the natal dense core could not be understood in the framework of quasistatically evolving cores. This would make L1148 the first dense core in which non-quasistatic evolution plays a significant role.

## 3.1 Introduction

The sensitivity of the Spitzer Space Telescope allows to search and probe young forming stars that are much less luminous than those studied before. While surveys of star-forming regions on basis of the IRAS satellite data were sensitive to sources with luminosities $\gtrsim 0.1 L_\odot (d/140 \, \text{pc})^2$ (where $d$ is the distance; Myers et al. 1987), Spitzer would even detect objects with luminosities as low as $10^{-3} L_\odot$ at a distance of 350 pc (Evans et al. 2003). Recently Spitzer imaged a large number of isolated dense cores though to be starless, the majority of them (about 60) as part of our Spitzer Legacy Project "From Molecular Cores to Planet Forming Disks", or c2d (Evans et al. 2003). These observations lead to a series of discoveries of Very Low Luminosity Objects (VeLLOs; Kauffmann et al. 2005, Huard et al. 2006, Di Francesco et al. 2006), infrared stars of luminosity $\leq 0.1 L_\odot$ which are embedded in dense cores. The c2d survey revealed about a dozen candidate VeLLOs (Huard et al., in prep.).

VeLLO colours and envelope properties are consistent with those of class 0 or class I protostars (Lada 1987; Andre et al. 1993), young stars in their main accretion phase that are deeply embedded in the dense core from which they form. The first such source was L1014-IRS (Young et al. 2004; Crapsi et al. 2005b; Huard et al. 2006; Bourke et al. 2005). A further discovery discussed in detail was L1521F-IRS (Bourke et al., in prep.). Spitzer recently also detected the VeLLO IRAM04191 (Dunham et al., in prep.), which had been discovered on basis of millimetre radio observations (André et al. 1999). For a further VeLLO candidate in the L1148 dense core we here present a detailed discussion.

The evolutionary status and fate of VeLLOs is presently unclear and likely to be diverse. Given the diversity of accretion rates implied by the CO outflow properties, and their low present mass of order $\lesssim 0.1\,M_\odot$, some VeLLOs have been interpreted as very young (age of order $10^4$ yr) protostars of stellar final mass (e.g., IRAM04191, which has a prominent outflow; André et al. 1999; Belloche et al. 2002), while others might be the first proto brown dwarfs identified (e.g., L1014-IRS, which has a $\approx 3''$ outflow only detected with interferometers; Young et al. 2004; Crapsi et al. 2005b; Bourke et al. 2005; Huard et al. 2006). Some VeLLOs might thus shed light on the not well understood formation of field brown dwarfs (i.e., not in orbit around a stellar mass primary; Whitworth & Goodwin 2005).

The fate of VeLLOs is likely to be controlled by the environment in which they form. While some form in dense and chemically evolved cores (e.g., IRAM04191 and L1521F-IRS; André et al. 1999, Bourke et al., in prep.), others do form in cores previously thought not to be dense and evolved enough to make stars (e.g., L1014-IRS; Crapsi et al. 2005b). For the latter ones it is tempting, though not proven, to make the unusual star formation environment (e.g., low densities) responsible for the unusually low luminosity, accretion rate, and mass.

The above discussion shows that for a comprehensive understanding of a VeLLO its protostellar properties (e.g., luminosity and outflow activity), as well as the properties of the natal dense core (e.g., density, kinematics, and chemistry) need to be studied in detail. We here present such a study for a candidate VeLLO in the dense core L1148.

The dense core L1148 is located in the Cepheus Flare, a large complex of molecular clouds at distances of 200 to 900 pc (Lebrun 1986; Kun 1998). The distance of the clouds roughly increases with decreasing galactic latitude. Those at $b \gtrsim 11°$ are closer than $450 \pm 100$ pc. For these nearby clouds Lebrun derived velocities from his CO spectra spanning across a range of $\approx 15$ km s$^{-1}$, and linewidths of up to 2 km s$^{-1}$. Given the clouds proximity this velocity structure is unlikely to arise from motions of different clouds at different distances, but is likely to reflect the internal motions in the region. The Cepheus Flare region is thus more turbulent than, e.g., the Taurus complex (Ungerechts & Thaddeus 1987). This might have been caused by recent supernovae in this cloud complex (Grenier et al. 1989).

The presence of a low luminosity ($\gtrsim 0.15\,L_\odot$ for the distance adopted then) IRAS Faint Source Catalogue source in L1148 was first noticed by Kun (1998), but this source has never been studied in detail. The core was included in the surveys for inward motions by Lee et al. (1999, 2001, 2004a). No signs of such motions were found, but the observed lines were weak and the position of the IRAS source was not probed. Recently Kirk et al. (2005) observed a small field ($\approx 2'$ diameter) in the L1148 dense core with SCUBA, but again off the IRAS source.

While Kun (1998) gives a distance of 450 pc to L1148, Straizys et al. (1992) derive a distance of $325 \pm 25$ pc for the same field. We here adopt the distance estimate of Straizys et al., as this study in particular concentrates on the L1148 field ($\leq 1° \times 1°$), while Kun studies a large field ($\approx 2° \times 10°$) in which L1148 lies only at the edge.

## 3.2   Observations and Data Reduction

### 3.2.1   Spitzer Space Telescope

L1148 was observed by the Spitzer Space Telescope on 2004 July 3 with the Infrared Array Camera (IRAC; AORKEY 5158144), and on 2004 June 23 with the Multiband Imaging Photometer for Spitzer (MIPS; AORKEY 9440768) as part of the c2d Legacy program (Evans et al. 2003). Details of the observations, post-processing and source extraction are presented in an upcoming paper on the whole c2d dense core sample (Huard et al., in prep.; see also Young et al. 2005 and Harvey et al. 2006), so here we focus on the specific details for L1148. The field-of-view (FOV) covered by the IRAC observations was $900'' \times 610''$ with the long axis at a position angle (P.A.) of 120° (east of north). The IRAC 3.6 and 5.8 $\mu$m arrays covered a slightly different area than the 4.5 and 8.0 $\mu$m arrays. At each position 4 dithers of 12 s each were taken, resulting in a 48 s exposure time for most of the area mapped. With MIPS at 24 $\mu$m a field of $1\,080'' \times 450''$ with the long axis at a P.A. of 130° was observed with a total exposure time 48 s, and at 70 $\mu$m a field of $150'' \times 95''$ with the long axis at a P.A. of 130° with a total exposure time of 126 s was observed. The data were processed by the Spitzer Science Center using their standard

pipeline (version S11.4.0) to produce Basic Calibrated Data images. The c2d team further processed the images to improve their quality (correcting "bad" pixels and other array artifacts) and performed photometry.

### 3.2.2  IRAM 30m-telescope & Effelsberg

Continuum observations of the 1.2 mm thermal dust emission with the IRAM 30m-telescope on Pico Veleta (Spain) were done using the 117-channel MAMBO 2 bolometer camera of the MPIfR (Kreysa et al. 1999). A total of five maps was taken on 2002 November 10, 2003 March 16 and November 1, and 2004 March 11; the zenith optical depths were between 0.2 and 0.4. The beam size on the sky was $11''$. Pointing and focus were checked before and after each map; the pointing corrections in azimuth and elevation were $4''$ and below, and the focus corrections below 0.3 mm. The zenith optical depth was measured with a skydip at least once within an hour from start or end of a map. The source was observed on-the-fly, with the telescope secondary chopping in azimuth by $46''$ to $70''$ at a rate of 2 Hz. The data were co-added and reconstructed using iterative methods (Kauffmann et al., in prep.; see also Sec. 2.3) within the MOPSI[1] software. Our analysis in the following, if not explicitly stated differently, is based on the map smoothed to $20''$ resolution, which significantly reduces the noise level. The intensities given below are always calibrated in mJy per $11''$-beam, independent of additional smoothing. Weight maps, which give the effective observing time at each position, were used to create noise maps, which give the estimated noise level at each position (Kauffmann et al., in prep.). The calibration uncertainty is below 20%.

Spectroscopic observations with the IRAM 30m-telescope were done 2004 December 19 (maps in $^{12}CO$ [2-1], $C^{18}O$ [2-1] and $N_2H^+$ [1-0] with frequency switching) and 2005 July 19 to 21 (pointed observations towards selected positions and HERA map in $^{12}CO$ [2-1] with position switching). We in all cases used the VESPA autocorrelator as the backend. Except for the $^{12}CO$ (2-1) observations with HERA on 2005 July 20/21 the single-pixel facility receivers were used. The pointing corrections in azimuth and elevation were below $3''$, and the focus corrections below 0.45 mm, as checked by regular pointing and focus checks at least once in 3 hours (except for the HERA observations, which ran for 5 hours during stable night conditions without check). Further details on the observational setup and observing conditions are listed in Table 3.1. The intensity scale was converted to the main beam brightness temperature according to the efficiencies reported on the IRAM website[2].

Spectroscopic observations with the Effelsberg 100m-telescope were done 2005 April 13 and April 29 to May 2. We observed with the facility 1.3 cm primary focus spectral line receiver and used the AK90 autocorrelator as the backend. All data was taken in the frequency switching mode. The pointing corrections in azimuth and elevation were mostly below $6''$, but corrections of $9''$ for $HC_3N$ and of $15''$ for CCS each occurred once. The focus corrections were below 0.6 mm. Pointing was checked at least once in 4 hours and the focus corrected at least once in 6 hours. The data is calibrated in the $T_{mb}$-scale using continuum cross-scans on the quasars 3C48 (1.21 Jy), 3C123 (3.14 Jy), 3C147 (1.77 Jy), and 3C286 (2.43 Jy), as well as NGC7027 (5.58 Jy). The fluxes are calculated for the respective observing frequency using the `radiocal.pl` program provided by the telescope team. The elevation dependent gain correction[3] is taken into account. Further details are listed in Table 3.1.

The spectroscopic observations were reduced using the CLASS software package[4]. We removed low-order baselines and partially used Fourier (FFT) filtering to further improve the baseline quality. Further details of the data reduction are given in the respective sections below.

### 3.2.3  KPNO 4m-telescope

As part of a larger program to survey the c2d cores in the near-infrared, we obtained deep $J$, $H$, and $K_s$ observations of L1148 during September of 2004 using FLAMINGOS (Florida Multi-object Imaging Near-IR Grism Observational Spectrometer; Elston 1998) on the 4m-telescope at Kitt Peak National Observatory (KPNO). The

---

[1] MOPSI is a software package developed by R. Zylka.

[2] `http://www.iram.es/IRAMES/`

[3] Calibration parameters for the 1.3 cm receiver are listed at `http://www.mpifr-bonn.mpg.de/div/effelsberg/calibration/1.3cmpf.html`.

[4] `http://www.iram.fr/IRAMFR/GILDAS`

**Table 3.1:** Summary of the spectroscopic observations at the IRAM 30m-telescope and the Effelsberg 100m-telescope. For every probed transition of a molecule the adopted line frequency and its uncertainty in frequency and velocity, the beam size, the frequency trow used for frequency-switched observations, the system temperature in the $T_{mb}$-scale, and the velocity resolution in the spectra (in part including smoothing) are given. References to the adopted line frequencies are listed below.

| Molecule | Transition | Frequency GHz | Freq. Uncert. kHz | Vel. Uncert. km s$^{-1}$ | Beam Size arcsec | Freq. Throw MHz | $T_{sys}$ K | Vel. Resol. km s$^{-1}$ |
|---|---|---|---|---|---|---|---|---|
| *Effelsberg:* | | | | | | | | |
| CCS | $J, F = 2, 1\text{-}1, 0$ | 22.3440308[a] | 1 | 0.013 | 39 | 2.5 | 271 | 0.033 |
| | | | | | | | | |
| *IRAM 30m-telescope:* | | | | | | | | |
| N$_2$H$^+$ | $J, F_1, F =$ | 93.1762608[b] | 6 | 0.019 | 26 | 7.0 | 142[†] | 0.063[†] |
| | $1, 0, 1\text{-}0, 1, 2$ | | | | | | 196[‡] | 0.021[‡] |
| N$_2$D$^+$ | $J, F_1, F =$ | 77.1121180[b] | 6 | 0.023 | 31 | 7.8 | 267 | 0.076 |
| | $1, 0, 1\text{-}0, 1, 2$ | | | | | | | |
| CS | $J = 2\text{-}1$ | 97.980953[c] | 2 | 0.006 | 25 | 7.0 | 145 | 0.020 |
| | $J = 3\text{-}2$ | 146.969029[c] | 1 | 0.002 | 16 | 5.0 | 363 | 0.040 |
| $^{12}$CO | $J = 2\text{-}1$ | 230.538000[d] | 1 | 0.001 | 10 | 15 | 377[†] | 0.051[†] |
| | | | | | | – | 908[★] | 0.51[★] |
| C$^{18}$O | $J = 2\text{-}1$ | 219.560358[e] | 1 | 0.001 | 11 | 15 | 291 | 0.053 |
| HCO$^+$ | $J = 1\text{-}0$ | 89.1884957[a] | 11 | 0.037 | 27 | 7.0 | 132 | 0.023 |
| H$^{13}$CO$^+$ | $J = 1\text{-}0$ "primary" | 86.7542982[f] | 4 | 0.014 | 28 | 7.0 | 111 | 0.045 |
| HCN | $J, F = 1, 1\text{-}0, 1$ | 88.6304157[a] | 1 | 0.003 | 27 | 7.0 | 131 | 0.066 |
| | $J, F = 1, 2\text{-}0, 1$ | 88.6318473[a] | ................................. ditto ................................. | | | | | |
| | $J, F = 1, 0\text{-}0, 1$ | 88.6339360[a] | ................................. ditto ................................. | | | | | |

References: a, Müller et al. (2005); b, Dore et al. (2004); c, Gottlieb et al. (2003); d, F.J. Lovas, `http://physics.nist.gov/cgi-bin/` `micro/table5/start.pl`; e, Cazzoli et al. (2003); f, Schmid-Burgk et al. (2004)

† for mapping observations in December 2004; ‡ for pointed observations in July 2005; ★ for HERA mapping observations in in July 2005

data acquisition and reduction of our c2d FLAMINGOS observations has already been described in Huard et al. (2006) and we here focus on the specific details for our observations of L1148.

The field of view of our observations was $10' \times 10'$ and the seeing was $\approx 1\rlap{.}''3$. The L1148 core was observed for a total of 6 minutes at $J$, 168 minutes at $H$, and 33 minutes at $K_{\mathrm{s}}$. Our final L1148 catalogue contains $\approx 1000$ sources detected at both $H$ and $K_{\mathrm{s}}$, with most of these sources having $H$ and $K_{\mathrm{s}}$ photometric uncertainties of less than 0.15 mag. The seeing was $\approx 1\rlap{.}''0$. We estimate our 90% completeness limits to be $\approx 18.5$, $\approx 19.0$, and 18.0 mag at $J$, $H$, and $K_{\mathrm{s}}$, respectively. Uncertainties in the positions of individual sources are less than $1''$.

## 3.3  Properties of L1148-IRS

### 3.3.1  Association of a Spitzer source with a Dust Emission Peak

Figure 3.1 presents the dust emission of the L1148 dense core as imaged by MAMBO. It reveals two parallel filaments, running northeast to southwest. These have masses and peak equivalent visual extinctions of 3.8 $M_{\odot}$ and 6 mag (northwestern filament), and 8.7 $M_{\odot}$ and 9 mag (southeastern filament), respectively (Sec. 3.5.1 describes the analysis of our MAMBO maps in detail). Spitzer observations of L1148 reveal an unusually bright source in the 24 $\mu$m (59 mJy) and 70 $\mu$m (271 mJy) bands, which dominates the images at these wavelength. This infrared source lies only $7\rlap{.}''6$ away from the dust emission peak of the northwestern filament. This small separation suggests that the infrared source is physically associated with the L1148 dense core. In the following we refer to this object as L1148-IRS.

**Infrared Counterparts**    Spitzer images in the IRAC bands each show one infrared source within the error ellipse of the position of L1148-IRS, SSTc2d J204056.7+672305, as inferred from the Spitzer 24 $\mu$m image. We identify these sources as mid-infrared counterparts of L1148-IRS (which was identified in the far-infrared). The positions from the IRAC bands are more accurate than those from the MIPS bands. We therefore take the average position of the counterparts seen by Spitzer,

$$\alpha = 20^{\mathrm{h}}40^{\mathrm{m}}56\rlap{.}^{\mathrm{s}}6\,, \quad \delta = +67°23'04\rlap{.}''9 \qquad (\mathrm{J2000.0})\,,$$

(this corresponds to the galactic coordinates $l = 102\rlap{.}°2$, $b = 15\rlap{.}°3$) as the position of L1148-IRS. Furthermore, our FLAMINGOS source catalogue, the 2MASS point source catalogue (with 2MASS 20405664+6723047), and the IRAS faint source catalogue (with F20404+6712; see Moshir & et al. 1990) contain each one source consistent with the position of L1148-IRS. For all counterparts in these bands the deviations from the position of L1148-IRS are less than $1''$ and consistent with those expected from measurement errors.

**Separation between L1148-IRS and the Dust Emission Peak**    The dust emission peak position is taken to be the intensity-weighted mean position of the pixels above 90% of the peak intensity. We quantify the significance of the separation between the dense cores dust emission peak and L1148-IRS by analysis of Monte-Carlo experiments. In these we first superpose the observed map with artificial noise of an amplitude identical to the one in the observations, and then measure the separation between the L1148-IRS and the dust emission peak in these maps. The uncertainty of the separation due to noise is then taken to be the standard deviation of the derived figures, which is $2\rlap{.}''7$. An additional uncertainty in the position of the dust emission peak comes from pointing errors of the telescope. These are estimated to be $\lesssim 4''$ for the present observations, as estimated from the regular pointing corrections. The combined uncertainty in the separation from noise and pointing errors is thus $4\rlap{.}''8$. The observed offset of $7\rlap{.}''6$ between L1148-IRS and the dust emission peak is thus marginally significant and has no clear interpretation.

**Excluding Fore- and Background Sources**    The source L1148-IRS is either physically associated with the L1148 dense core, or a galactic background protostar or background galaxy that are by chance projected onto the dense core.
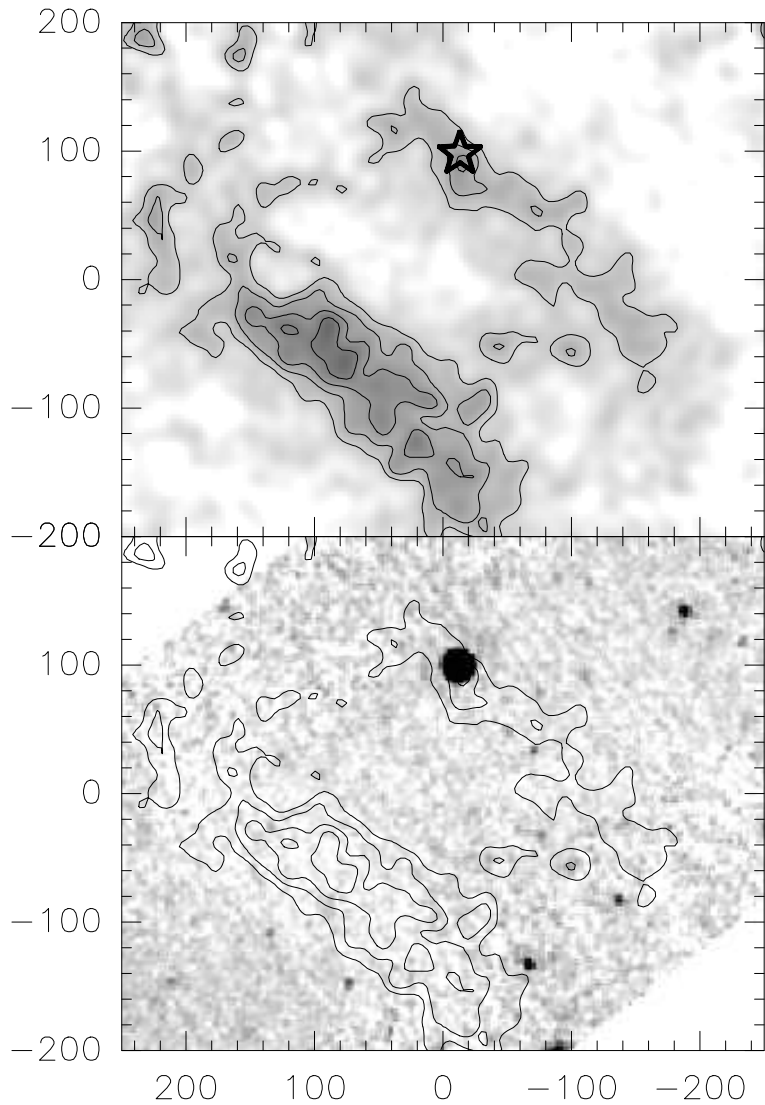
**Figure 3.1:** Association of a dust emission peak position in the MAMBO map (*top*) with the unusually bright source L1148-IRS seen in the 24 $\mu$m Spitzer map of L1148 (*bottom*). The dust emission map is overlayed in *contours*, while the *greyscale* presents the intensities in negative scale. The *star* marks the position of L1148-IRS in the MAMBO map. Offsets are in seconds of arc.

The source L1148-IRS can not be a foreground protostar, as the dense core, in which such a source would be embedded, would have been easily detected in optical images (as an extincting dust core) and by radio observations; no evidence for such a core exists. We can not rule out that L1148-IRS is a galactic background source. However, our $^{12}$CO spectra show no evidence for molecular gas behind the L1148 dense core (Sec. 3.3.4), in which a protostar could be harboured. Furthermore, L1148 has a galactic latitude $b = 15°$ and is thus about $z \approx 80$ pc above the galactic plane. Most of the galactic star-forming sites along the line of sight towards L1148 thus lie in front of it, in particular as at an galactic longitude of $l = 102°$ one looks into the outer galaxy.

Source counts for galaxies in the Spitzer MIPS bands were published by Papovich et al. (2004, for 24 $\mu$m) and Dole et al. (2004, for 70 and 160 $\mu$m). We derive at 24 $\mu$m a number of $\approx 2\,730$ sr$^{-1}$ sources and at 70 $\mu$m a number of $\approx 10^4$ sr$^{-1}$ sources brighter or equally bright as L1148-IRS. The probability to find one source of a brightness comparable or larger than the one of L1148-IRS within a radius of 20″ around the dust core is thus about 1:12 402 at 24 $\mu$m and 1:3 386 at 70 $\mu$m. Given the $\approx 110$ detected dust emission peaks in our c2d MAMBO survey the probability for one chance alignment in our whole survey is thus 1:113 at 24 $\mu$m and 1:31 at 70 $\mu$m. These low probabilities strongly suggests that L1148-IRS is not a background galaxy.

We summarise that out of three options for the nature of L1148-IRS, the option of L1148-IRS being either an unrelated protostar or background galaxy can be excluded with a high confidence level. Thus L1148-IRS is most probably physically associated with the L1148 dense core.

### 3.3.2 Spectral Energy Distribution

The overall features of the spectral energy distribution of L1148-IRS are consistent with those of protostars belonging to the classes 0 or I. Assuming a nature of this kind, we derive internal and bolometric luminosities of $\approx 0.06\,L_\odot$ and 0.1 to 0.2 $L_\odot$. These luminosities would be unusually low for a protostar. Combined with the evidence for being embedded in the dense core L1148-IRS thus qualifies as a candidate VeLLO. Inconsistencies between observations from different instruments might hint at intrinsic variability of L1148-IRS.

**Observations**   We have compiled the spectral energy distribution (SED) of the L1148-IRS dense core from our Spitzer, FLAMINGOS, and MAMBO data, as well the 2MASS point source catalogue and the IRAS faint source catalogue (Table 3.2). For consistency with previous work (André et al. 1999; Motte & André 2001) the MAMBO flux is derived by integration across a circular aperture of 4 200 AU radius (i.e. 12″.9 at 325 pc distance). Note that at wavelengths $\lesssim 100\,\mu$m the compact infrared source L1148-IRS dominates the SED, while at wavelengths $\gg 100\,\mu$m (where only MAMBO data is available) the extended dense core does; different spatial scales are probed in different wavelength regimes.

The IRAS fluxes listed in Table 3.2 include colour corrections. These correct for the differences between the spectrum assumed for the instrument calibration and the actual one. They are derived from those listed[5] by Beichman et al. (1988) by approximating the SED in the IRAS bands by the one of opacity-modified blackbodies matching the Spitzer MIPS observations. This yields corrections of up to 20%. The similarly derived corrections for the Spitzer MIPS observations, e.g. calculated with the Extragalactic Performance Estimation Tool[6], are below 5%. They are neglected as they are much smaller than the calibration uncertainty. No correction is necessary in the other bands.

There are inconsistencies between some datasets. The flux densities derived from $K_s$ band FLAMINGOS and 2MASS observations differ by a factor 1.4, while at 24 $\mu$m wavelength the flux densities from IRAS and Spitzer are different by a factor 2.7. For the $K_s$ band this difference might be due to different data reduction strategies, i.e., point-source fitting for 2MASS and aperture photometry for FLAMINGOS. Point-source fitting has an unclear sensitivity to extended emission that is furthermore different from the one of aperture photometry. Flux density differences are thus not surprising. At 24 $\mu$m wavelength the uncertainty due to noise might be underestimated for IRAS. This is suggested by visual inspection of the IRAS Sky Survey Atlas images, which reveals no source

---

[5]We used the updated and corrected version of the document accessible from `http://irsa.ipac.caltech.edu/IRASdocs/exp.sup/`
[6]http://ssc.spitzer.caltech.edu/tools/expet/index.html
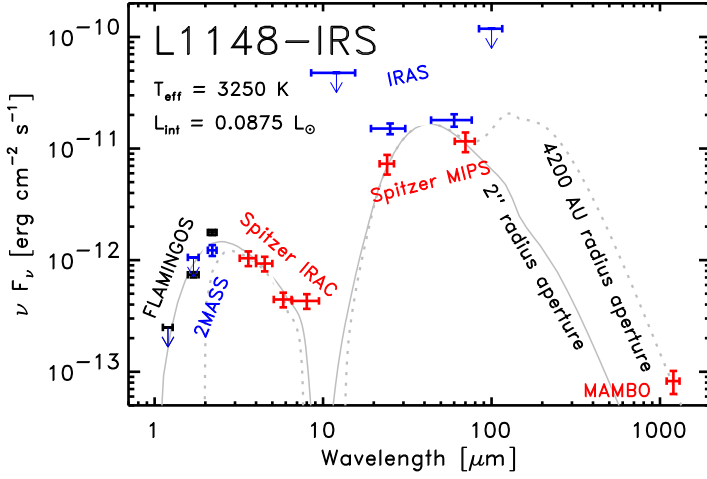
**Figure 3.2:** The spectral energy distribution of L1148-IRS. For every observation the filter width and the uncertainty in the flux density measurement including calibration uncertainties is indicated by bars. Note that the observed flux densities for wavelengths shorter than 100 $\mu$m relate to the compact emission from the infrared source, while for larger wavelengths, where only MAMBO data is available, they refer to the extended emission of the dense core. The model curves for apertures of 2″ (*solid line*) and 4 200 AU radius (*dotted line*) hold for an embedded source with an effective temperature of 3 250 K and an internal luminosity of 0.0875 $L_\odot$. They are described in Sec. 3.4.

**Table 3.2:** The spectral energy distribution of L1148-IRS. For every band the central wavelength and width of the filter, the telescope resolution, the apertures used for photometry, the measured flux density including colour corrections (where necessary) and its uncertainty due to noise, and the calibration uncertainty are given. For most bands photometry is done by point-source fitting. Then the aperture to that the flux density refers is given by the point spread function (PSF) and we mark these bands by listing "PSF" as the used aperture. For the other bands, where we perform aperture photometry, the first number given for the aperture is the diameter across that the intensity is integrated, while the given range indicates the diameter of the inner and outer circle enclosing the area used to obtain an estimate for the background intensity (does not apply to MAMBO).

| Band | Wavelength | Bandwidth | Resolution | Apertures | Flux Density | Calibration Uncertainty |
|---|---|---|---|---|---|---|
| | $\mu$m | $\mu$m | arcsec | arcsec | mJy | |
| 2MASS $J$ | 1.24 | 0.16 | 2.8 | PSF | < 0.1 | 2% |
| FLAMINGOS $J$ | 1.24 | 0.16 | 1.3 | 2.56, 6.4 – 12.8 | < 0.1 | 2% |
| 2MASS $H$ | 1.66 | 0.25 | 2.8 | PSF | < 0.6 | 2% |
| FLAMINGOS $H$ | 1.66 | 0.25 | 1.3 | 2.56, 6.4 – 12.8 | 0.421 ± 0.021 | 2% |
| 2MASS $K_s$ | 2.16 | 0.26 | 2.8 | PSF | 0.9 ± 0.1 | 2% |
| FLAMINGOS $K_s$ | 2.16 | 0.26 | 1.3 | 2.56, 6.4 – 12.8 | 1.304 ± 0.065 | 2% |
| IRAC 1 | 3.6 | 0.8 | 1.7 | PSF | 1.25 ± 0.01 | 15% |
| IRAC 2 | 4.5 | 1.0 | 1.7 | PSF | 1.40 ± 0.02 | 15% |
| IRAC 3 | 5.7 | 1.4 | 1.9 | PSF | 0.86 ± 0.02 | 15% |
| IRAC 4 | 7.9 | 2.9 | 2.0 | PSF | 1.15 ± 0.02 | 15% |
| IRAS 12 | 12 | 7 | 25 | PSF | < 77 | 3% |
| MIPS 1 | 24 | 5 | 6 | PSF | 58.5 ± 0.4 | 15% |
| IRAS 25 | 25 | 11 | 25 | PSF | 156 ± 17 | 6% |
| IRAS 60 | 60 | 33 | 60 | PSF | 283 ± 41 | 6% |
| MIPS 2 | 71 | 19 | 18 | 80, 80 – 160 | 271 ± 4 | 20% |
| IRAS 100 | 100 | 31.5 | 100 | PSF | < 3955 | 10% |
| MAMBO | 1200 | 210 | 11 | 25.8 | 33 ± 4 | 20% |

and is not consistent with the nominal SNR of 9. For these reasons we neglect the 2MASS and IRAS data in the remainder of the analysis.

It is, however, not clear whether differing observational methods alone can explain the flux density differences. Additional intrinsic variability of the source might be required to explain the observations. While the study of variability would be very important for studies of the nature of L1148-IRS, a comprehensive discussion of its presence is not possible on basis of the present data.

**SED Analysis**  The SED is shown in Fig. 3.2. While we defer a detailed discussion of the SED to Sec. 3.4, we note that radiative transfer calculations indicate that for a protostellar nature of L1148-IRS the detected emission can be understood as the superposition of extincted photospheric emission ($\lambda \lesssim 10\,\mu$m), emission from warm dust ($\lesssim 100$ K) in the inner envelope ($10\mu$m $\lesssim \lambda \lesssim 100\,\mu$m), and emission from cold dust ($\approx 10$ K) in the extended envelope ($\lambda \gtrsim 100\,\mu$m). If L1148-IRS is a protostar, then it can be characterised by the bolometric luminosity,

$$L_{\text{bol}} = 4\pi d \int_0^\infty F_\nu \, d\nu \, , \tag{3.1}$$

and the bolometric temperature,

$$T_{\text{bol}} = \frac{\zeta(4)}{4\zeta(5)} \frac{h\langle\nu\rangle}{k_{\text{B}}} \, , \tag{3.2}$$

where $\langle\nu\rangle = \int_0^\infty \nu F_\nu \, d\nu \big/ \int_0^\infty F_\nu \, d\nu$ is the flux-weighted mean frequency, $\zeta$ is the Riemann zeta function, $d$ is the distance, and $h$ and $k_{\text{B}}$ are Planck's and Boltzmann's constant. The bolometric temperature is thus the temperature of a blackbody having the same flux-weighted mean frequency as the observed SED (Myers & Ladd 1993).

To interpolate the flux between the sampled wavelengths we employ a modified version of the method used by Myers & Ladd (1993). We assume the SED to be dominated by a greybody of temperature 10 to 15 K and opacity $\kappa_\nu \propto \nu^2$ at wavelength $\lambda \gg 100\,\mu$m. This is taken to represent the emission from the cold extended envelope seen in the MAMBO maps. We additionally superpose piecewise power-laws on the greybody, $F_\nu \propto \nu^\alpha$, which each hold between two wavelengths with a detection. We neglect the emission for wavelengths shorter than the shortest detected wavelength and assume $F_\nu \propto \nu^2$ for wavelengths longer than 70 $\mu$m (the detection with longest wavelength except for MAMBO).

For the distance of L1148 this method yields $L_{\text{bol}} = 0.09$ to $0.21\,L_\odot$ and $T_{\text{bol}} = 72$ to 142 K, respectively. For protostars these quantities reflect properties of neither the embedded compact source, nor of the extended envelope, but a combination of these. To give an example, the greybody thought to reflect the extended emission seen by MAMBO has a bolometric bolometric luminosity, $L_{\text{bol}}^{\text{extended}}$, of 0.03 to 0.16 $L_\odot$ for the adopted range in greybody temperatures. This emission is due to heating of the dust by the interstellar radiation field and cosmic rays (Goldsmith 2001); for protostars of luminosity $\ll 1\,L_\odot$ it is not related to the properties of the embedded object (Eq. 3 of Motte & André 2001). Then the difference between the total bolometric luminosity and that of the extended emission, $L_{\text{bol}} - L_{\text{bol}}^{\text{extended}}$, is an approximate measure of the internal luminosity due to the infrared source alone. For this we find $0.06\,L_\odot$ in the case of L1148-IRS, independent of the used greybody temperatures in the adopted temperature range. The submillimetre-to-bolometric luminosity ratio, where $L_{\text{submm}}$ is derived by integration of the SED at wavelengths $\geq 350\,\mu$m, is a rough measure of the star-to-envelope mass ratio in protostars. For L1148-IRS we find a figure of 0.05 to 0.07 for the adopted dust temperatures.

**Nature of L1148-IRS**  The bolometric temperatures derived above would imply that L1148-IRS is a class 0 (i.e., $T_{\text{bol}} \leq 70$ K) or class I (70 K $< T_{\text{bol}} \leq 650$ K) protostar (Chen et al. 1995, 1997), i.e., a young star with an age of order $\approx 10^5$ yr (Barsony & Kenyon 1992; Greene et al. 1994; Kenyon & Hartmann 1995) and ongoing accretion that is embedded in a dense core. This agrees well with the evolutionary state and physical nature derived below from our FLAMINGOS images (Sec. 3.3.3). Also the high submillimetre-to-bolometric luminosity ratio $\gg 0.005$ hints at such an early stage (Andre et al. 1993). Infrared stars with a bolometric luminosity as low as the one of L1148-IRS are unusual. To give examples, the catalogues of Andre et al. (2000) and Froebrich (2005) each contain

only one such source, IRAM04191. Given the suggested internal luminosity $\lesssim 0.1\,L_\odot$ and the evidence for being embedded in dense gas, L1148-IRS thus qualifies as a candidate VeLLO. We shall return to this issue in a later section.

### 3.3.3  Nebulosity near L1148-IRS

The FLAMINGOS $H$ and $K_\mathrm{s}$ band images reveal the presence of extended nebulosity around L1148-IRS. It manifests in an arc-like structure about $5''$ to the west of L1148-IRS (Fig. 3.3), and in a broadening of the intensity profile of L1148-IRS compared to neighbouring stars (Fig. 3.4). The extent and spatial distribution of this nebulosity suggests that scattering of light in an outflow cavity is responsible for it. This indicates that L1148-IRS is of protostellar nature and embedded in an envelope dense enough to efficiently scatter radiation. This embeddedness, combined with the low internal luminosity, renders L1148-IRS a candidate VeLLO.

**Evidence for Nebulosity**  The non-symmetric nature of the emission of L1148-IRS in the $H$ and $K_\mathrm{s}$ bands is already obvious then inspecting the images presented in Fig. 3.3. Given the clearer signature of the asymmetry in the $H$ band, we quantify the orientation of the asymmetry by fitting an elongated Gaussian profile to the $H$ band image of L1148-IRS. This yields a position angle (east of north) of $133°$ for the major axis. Figure 3.4 presents cuts through L1148-IRS along the major and minor axis through the $H$ band image. Also shown for comparison are profiles for 7 stars in our image. The selected stars have a brightness reaching from fainter than to brighter as L1148-IRS and do not have intensity profiles affected by close neighbours. Along each cut the peak position is taken to be the center of gravity of the pixels above 30% peak intensity.

The observed width of the profile for L1148-IRS in the $H$ band exceeds the stellar point spread functions by several arc-seconds. At 10% peak intensity L1148-IRS extends from $-1''\!\!.8$ to $2''\!\!.3$ ($-1''\!\!.7$ to $2''\!\!.0$ in the $K_\mathrm{s}$ band) along the major axis, and from $-1''\!\!.7$ to $1''\!\!.8$ ($-1''\!\!.5$ to $1''\!\!.5$) along the minor axis. For comparison, the stellar profiles have a width of only $2''\!\!.5$ ($2''\!\!.7$ for the $K_\mathrm{s}$ band) along the major and minor axis, respectively, at the same intensity level. This suggests an intrinsic extension of order $3''\!\!.2 \times 2''\!\!.4$, as revealed when removing the contribution from the telescope resolution. For the adopted distance this corresponds to an intrinsic size of $1040 \times 780$ AU$^2$. A neighbouring star can not be the cause of the extended features, as these are seen at any position angle.

**Comparison with Protostars**  The structure of L1148-IRS along the major axis is not symmetric to the peak position. While the maximum extension from the peak at the 10% level is $2''\!\!.3$ for positive offsets along the major axis, it is $\approx 1''\!\!.8$ in all other directions. Detailed radiative transfer calculations for an embedded protostar of $1\,M_\odot$, which evolves from the onset of accretion to later stages, were presented by Whitney et al. (2003a). They predict intensity distributions in the $H$ and $K_\mathrm{s}$ bands similar to the one seen for L1148-IRS — i.e., about circular extended emission, but a slightly larger extension into one direction — for their class I and class II models and lines of sight moderately inclined to the axis of an assumed outflow ($\approx 30°$), which is perpendicular to an assumed disk. For all other stages the predicted emission is either circularly symmetric or very elongated. For lines of sight much closer to the plane of the assumed disk the emission is expected to be very elongated along the jet axis, while it is circularly symmetric for views along the outflow axis. In the class II model the extended emission is dominated by radiation scattered by the disk, while in the class I model radiation from the outflow cavity also contributes.

The models thus suggest that L1148-IRS could be a protostar seen at moderate inclination. The extent of the emission from L1148-IRS is, however, not consistent with the predictions of the class II model of Whitney et al. The latter predicts emission on scales smaller than about 300 AU in radius, corresponding to $\lesssim 1''$ at the distance of L1148. One can speculate that for the estimated mass of L1148-IRS ($\ll 1\,M_\odot$ derived in Sec. 3.6.1) the expected size of the nebulosity is even smaller. The observed maximum extent of of 1040 AU is significantly larger than these predictions. It is consistent with the more than 1000 AU radial extent of class I models though. If L1148-IRS is a protostar, models, thus, suggest that it has an outflow-shaped envelope dense and extended enough to reprocess radiation on scales of 1000 AU radius. For the class I model the elongation is predicted to be maximum along the axis of the approaching jet, i.e., for L1148-IRS one would expect an approaching jet at a position angle of $\approx 313°$.
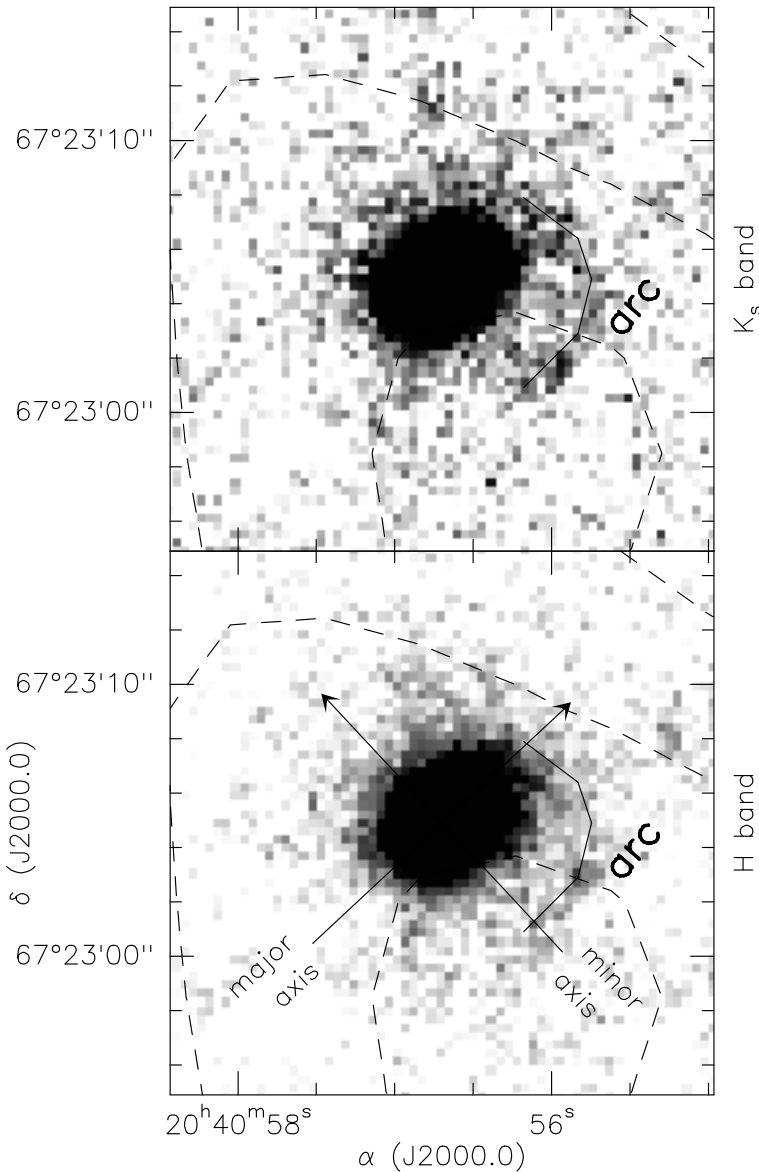
**Figure 3.3:** Images of L1148-IRS in the *H* (*bottom panel*) and $K_s$ bands (*to panel*) as seen by FLAMINGOS, shown as their negative. The overlayed *dashed contours* give the dust intensity distribution as probed by MAMBO (same contours as in Fig. 3.1), while the *arrows* give the position and direction of the cuts through the intensity distribution shown in Fig. 3.4. The images reveal that L1148-IRS is elongated, with the major axis at position angle $\approx 133°$. In addition there is an arc-like extended feature about 5″ to the west of 1148-IRS (*label "arc"*). To facilitate comparison between both images its approximate location is indicated by a *solid line*.
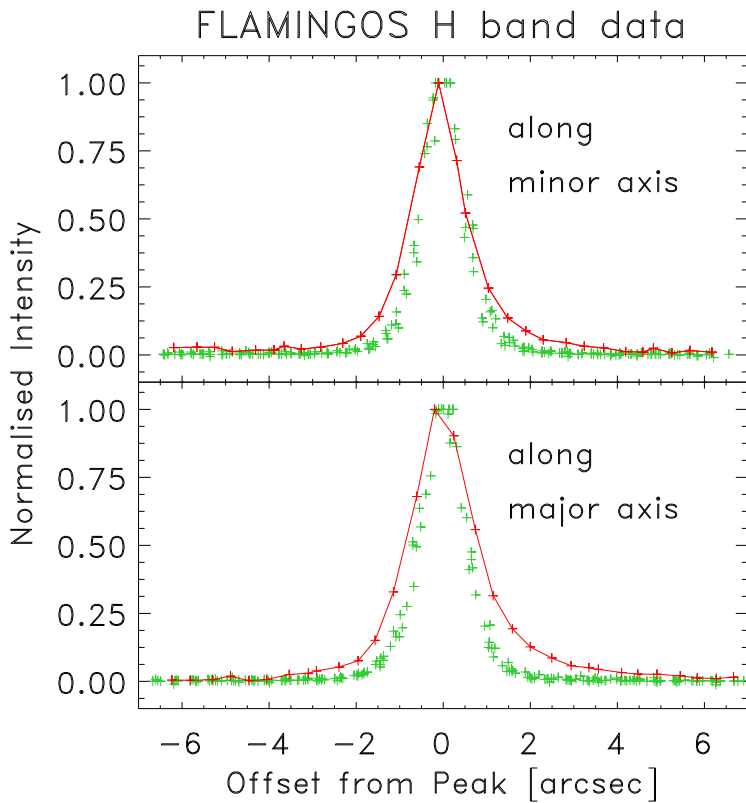
**Figure 3.4:** Cuts through the *H* band emission of L1148-IRS along the major and minor axes of the asymmetry (*solid lines*). *Crosses* show the intensity profiles for 7 comparison stars in our image. The observed width of the profile for L1148-IRS significantly exceeds the stellar point spread functions by up to an arc-second. This implies that L1148-IRS has an intrinsic extension of comparable order.

Similarly, the arc-like structure at about $5''$ or 1600 AU radius seen in our $H$ and $K_s$ band images can not be explained by disks of much smaller expected radius. It could, however, be related to outflows from L1148-IRS. Given its large azimuthal extent of about $90°$ it is not likely to be related to the bow shock of such a flow; these are seen at offsets from protostars much larger than their extent. The arc is more likely to be an inner part of an outflow cavity that, e.g., is illuminated by the central star.

Nebulosity of a similar kind was also observed for the VeLLO L1014-IRS (Huard et al. 2006). However, here the infrared star is not seen in the $H$ band. A fan-shaped nebulosity extending north with an intensity peak offset by $5''$ to $7''$ from L1014-IRS, corresponding to $\approx 1200$ AU, is seen in the $H$ and $K_s$ band. Huard et al. (2006) interpret this as the illuminated wall of an outflow cavity. Given the similar morphology the arc seen towards L1148-IRS could be of a nature similar to the one of the fan-shaped nebulosity in L1014. The infrared star L1014-IRS has a minimum intrinsic diameter at the 10% intensity level of order $2''5$ or $\gtrsim 500$ AU in the $K_s$ band, while L1148-IRS has a maximum extent of 1040 AU. While they differ in details, the nebulosities around L1014-IRS and L1148-IRS are thus similar in their general structure.

### 3.3.4  Outflow Search

We implemented two different strategies to search for an outflow in maps of the CO (2-1) transition obtained with the IRAM 30m-telescope. Because of the lack of a reference position free of CO emission we first used the single pixel heterodyne receivers in frequency switching mode to search for an outflow at about systemic velocity. We then used the HERA array in position switching mode to search for faint outflow emission at higher velocities.

These observations show that L1148-IRS is not driving a prominent outflow detectable by single-dish telescopes. This is surprising, given that, in case of a protostellar nature, L1148-IRS would be in the main accretion phase in which most, if not all, protostars do drive outflows (Andre et al. 2000). We however can not exclude the presence of a small-scale flow like the one seen in L1014-IRS (Bourke et al. 2005).

The frequency switched observations, taken on a $5 \times 5$ point grid with $30''$ spacing, are presented in Fig. 3.5. The baseline quality is improved by Fourier filtering of the spectra and subtraction of polynomials of second order. This filters out faint broad (some km s$^{-1}$) line features; our observations are only sensitive to more narrow features at about systemic velocity. The spectra are contaminated by a telluric CO line at $\approx 7$ km s$^{-1}$ velocity[7] with respect to the local standard of rest (LSR). There are clear spatial variations in the line profiles observed. However, there is no classical signature of an outflow in our spectra; no systematic trend of redshifted emission on one side of L1148-IRS and blueshifted emission on the opposite side is seen. Such structures are also not seen in channel maps (not shown).

The position switched observations (the offset position is $\approx 14'$ to the north-west), taken on a $12 \times 12$ point grid with $24''$ spacing, are summarised in Fig. 3.6. They are sensitive to faint and broad emission features, as only baselines of first order need to be subtracted. The data suffers from platforming though (i.e., discontinuous jumps in the spectra); we exclude scans obviously affected by this. The typical RMS noise level is $\sigma(T_{mb}) = 0.15$ K for smoothing to 0.5 km s$^{-1}$ spectral resolution. Emission at about systemic velocity can not be studied because of artifacts due to emission in the reference position.

Among the approximately 24 000 channels in our spectra of the whole region (they cover the LSR velocity range $-42$ to $+48$ km s$^{-1}$) there are 8 isolated ones (i.e., no neighbours with $> 3\sigma[T_{mb}]$ exist) with an SNR larger than 3 (taking the individual integration time per spectrum into account) at 0.5 km s$^{-1}$ spectral resolution. About 70 channels with an SNR larger 3 are expected for Gaussian noise. The derived number of 8 channels with such SNR is thus not significant. (This however suggests that the noise level is overestimated by the RMS.) We thus can set an upper limit of $3\sigma(T_{mb}) \approx 0.45$ K in the $T_{mb}$-scale to outflow CO emission from L1148-IRS. In order to search for outflow emission with very high sensitivity in the immediate vicinity of L1148-IRS we further improved

---

[7]The LSR velocity of the telescope can, e.g., be found from the calculator provided on the homepage of the *Far Ultraviolet Spectroscopic Explorer* (switched to topocentric coordinates), `http://fuse.pha.jhu.edu/support/tools/vlsr.html`, and using the "source" command within the ASTRO program of the GILDAS software package (`http://www.iram.fr/IRAMFR/GILDAS`). The LSR velocity of telluric lines is the negative of the telescope's LSR velocity.
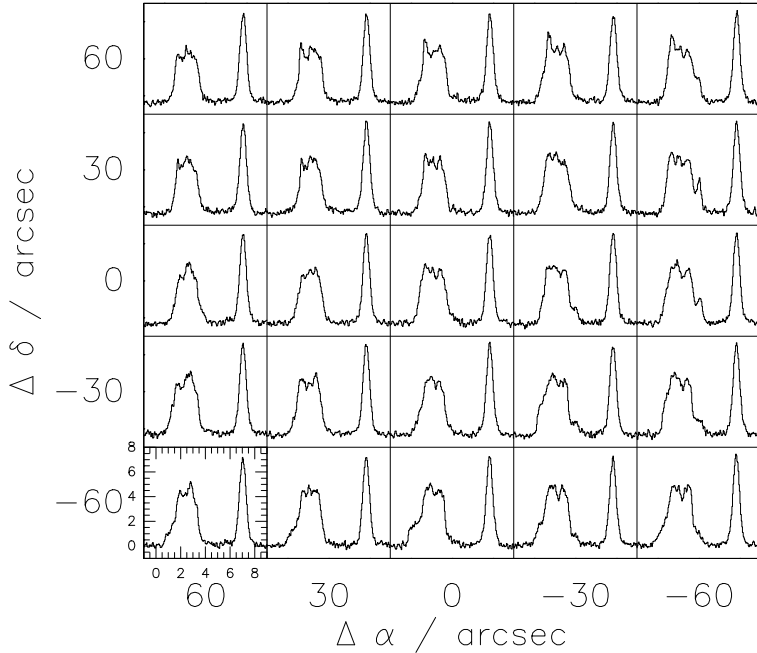
**Figure 3.5:** Spectra in the CO $J = 2$–$1$ transition towards L1148-IRS as observed with frequency switching on a $5 \times 5$ point grid with $30''$ spacing. Offsets are given relative to the approximate dust emission peak position ($\alpha = 20^\mathrm{h}40^\mathrm{m}56\overset{\mathrm{s}}{.}5$, $\delta = +67°22'58\overset{''}{.}0$ [J2000.0]). The LSR velocity and intensity in the $T_\mathrm{mb}$-scale are shown for one spectrum. The spectra are contaminated by a telluric CO line at $\approx 7$ km s$^{-1}$ LSR velocity. No obvious signature of an outflow is seen in the spectra.

the sensitivity by averaging spectra from all 4 positions surrounding it. This again did not reveal any significant emission.

The integrated CO intensity in $T_\mathrm{mb}$-scale is shown in Fig. 3.6. We separately integrated the blue- and redshifted emission across two velocity intervals of each 5 km s$^{-1}$ width offset by $\pm 5.5$ km s$^{-1}$ from the systemic LSR velocity of 2.6 km s$^{-1}$, as inferred from N$_2$H$^+$ (Sec. 3.5.4). This choice of this velocity range was inspired by the range for which an outflow is seen in IRAM04191 (André et al. 1999), a VeLLO with an internal luminosity comparable to the one suggested for L1148-IRS (Dunham et al., in prep.). The RMS noise level is about 0.3 K km s$^{-1}$ in both windows. Emission with a significant SNR larger than 3 is only detected towards one position (which has a short total integration time though) and no systematic spatial differentiation of red- and blueshifted emission is seen at lower intensity levels. Therefore no CO outflow with an integrated intensity exceeding $\approx 0.9$ K km s$^{-1}$ is driven by L1148-IRS.

The lack of an outflow from L1148-IRS is surprising, given the evidence for a protostellar nature from the SED and nebulosity. An outflow like the one driven by IRAM04191 (André et al. 1999), a VeLLO of internal luminosity similar to the one of L1148-IRS (Dunham et al., in prep.), would have been easily detected by our observations. The latter has, at a distance of 140 pc, extended outflow emission on scales of about $1' \times 3'$ at a level of $\geq 5$ K km$^{-1}$ for windows of 5 km s$^{-1}$ width, corresponding to $\geq 1$ K per channel. This significantly exceeds our detection limits. The candidate VeLLO L1148-IRS would, however, not be the first protostar without a prominent outflow detected by single-dish telescopes. The small-scale outflow ($3''$) of the VeLLO L1014-IRS detected by interferometric observations (Bourke et al. 2005) is not seen in single-dish observations (Crapsi et al. 2005b). A similar situation holds for the VeLLO L1521F-IRS (Bourke et al., in prep.). Thus L1148-IRS might still drive an outflow, but on scales smaller than probed by our observations.
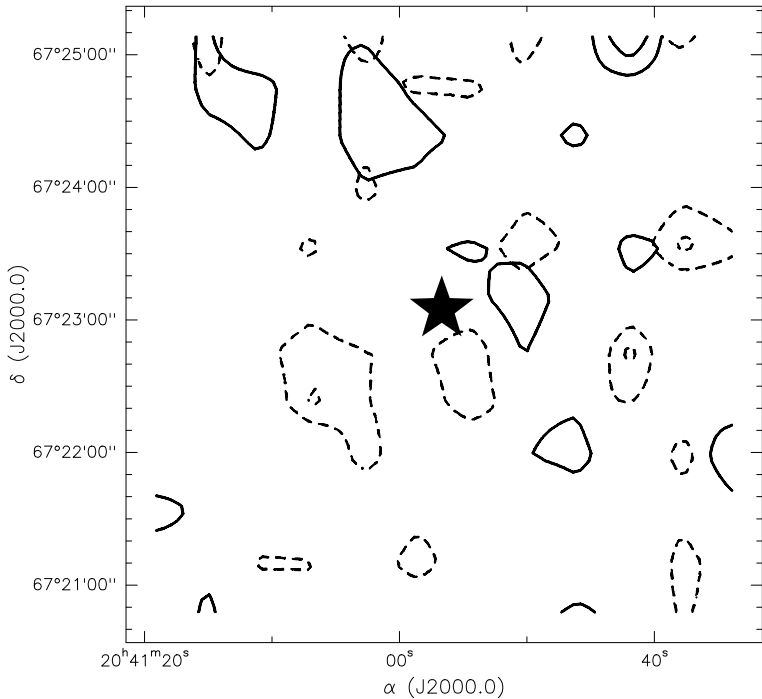
**Figure 3.6:** Integrated intensity map in the CO (2–1) transition for emission blueshifted (*continuous lines*) and redshifted (*dashed lines*) from the L1148 systemic velocity as observed with position switching on a $12 \times 12$ point grid with $24''$ spacing. The integration intervals of each $5 \, \text{km} \, \text{s}^{-1}$ width are spaced by $\pm 5.5 \, \text{km} \, \text{s}^{-1}$ from the systemic velocity. The contours are spaced by the typical RMS noise level of $0.3 \, \text{K} \, \text{km} \, \text{s}^{-1}$. The position of L1148-IRS is indicated by a *star*. Emission at a significant level is not detected and the spatial distribution of emission at lower intensity levels is not indicating any outflow.

## 3.4   SED Modelling of L1148-IRS

Fitting the SED of L1148-IRS by self-consistent radiative transfer models of protostars embedded in a dense core is desirable for several reasons. First, this yields further evidence for L1148-IRS being deeply embedded in, and not only associated with, the L1148 dense core. Second, detailed modelling allows to infer the internal luminosity more reliably then was done heuristically in Sec. 3.3.2. Third, we can learn something about the density structure of the dense core on scales smaller than the beam.

In Sec. 3.4.1 we describe the general layout of our physical model and introduce its free parameters. Details of the numerical scheme are given in Sec. 3.5.1. Results of the calculations are reported in Sec. 3.4.3. Section 3.4.4 discusses processes not well included in our model, their impact on model SEDs, and their influence on parameter estimates. We summarise our modelling of L1148-IRS in Sec. 3.4.5.

As discussed in Sec. 3.3.2, the IRAS and 2MASS $K_s$ band flux densities are not consistent with the higher quality MIPS and FLAMINGOS data, respectively. They are therefore excluded from the present analysis.

### 3.4.1   Boundary Conditions & Model Parameters

We model the observed SED by a spherical dense core with piecewise power-law density profile containing a central point source emitting like a black body of luminosity $L_{int}$ and temperature $T_{eff}$. The dense core is externally heated by the interstellar radiation field (ISRF); we assume the ISRF to be identical to the solar neighbourhood ISRF inferred by Pérault (1987). We refer to $L_{int}$ as the internal luminosity, to distinguish it from the bolometric luminosity of the star-core system. To $T_{eff}$ we refer to as the stellar effective temperature.

The model density drops to zero within the inner radius, $r_{in}$, and outside of the outer radius, $r_{out}$. Three power-law density distributions of the form $\varrho \propto r^{-\alpha}$, which connect continuously at the inner and outer transition radius, $r_{trans}^{in}$ and $r_{trans}^{out}$, are assumed to hold in between $r_{in}$ and $r_{out}$. In between $r_{trans}^{out}$ and $r_{out}$ we adopt $\alpha = 2$, as derived in Sec. 3.5.1 from the dust emission. The density is assumed to be constant in between $r_{trans}^{in}$ and $r_{trans}^{out}$; no good SED fits exist without a region with a flat density (see below). In between $r_{in}$ and $r_{trans}^{in}$ we adopt $\alpha = 2$, as the embedded source should form in dense gas. The absolute value of the density can be parameterised by normalisation to the density at the outer radius, $\varrho_{out}$. We set $r_{out} = 32500$ AU $\approx 0.16$ pc, which corresponds to $100''$ in L1148 and is about the distance out to that the core emission can be tracked. This leaves $r_{out}$, $r_{trans}^{in}$, $r_{trans}^{out}$, and $\varrho_{out}$ as free parameters of the model density structure.

Our model for the density structure is thus complementary to those adopted for other VeLLO models (Young et al. 2004, Bourke et al., in prep., Dunham et al., in prep.). These adopt density profiles with an inwards increasing density in which a star with a circumstellar disk is embedded. As the disk has intrinsic luminosity the internal luminosity in these models is given by the sum of the stellar and the disk luminosity.

The model dust opacity is taken from the "case B" calculations of Weingartner & Draine (2001) for a total-to-selective extinction ratio $R_V = 5.5$. These provide an excellent description to observed extinction curves at wavelengths between 1 and 10 $\mu$m, which are crucial for the modelling below (Indebetouw et al. 2005). These deviate from the Ossenkopf & Henning opacities used for the analysis of the dust emission maps in Sec. 3.5.1, which are believed to hold for longer wavelengths.

### 3.4.2   Model Calculations

Model SEDs are calculated by iteratively improving estimates for the radiation field in the dense core. In each iteration we first calculate the temperature distribution in the dense core resulting from the absorption of the estimated radiation field. A new estimate for the latter is then calculated from the dust emission for the improved estimate of the temperature distribution. (See Appendix A of Pillai et al. 2006 for the computational details.) This procedure is repeated until convergence is reached. The dust grains are assumed to be all of the same size.

The flux densities observed for a wavelength of $\approx 1$ $\mu$m are comparable to those expected from the integration of the ISRF across the apertures used: for an aperture of $5''$ radius the integrated ISRF intensity at 1 $\mu$m is 0.5 mJy,

while L1148-IRS has $\approx 2$ mJy. In real observation the background from the ISRF is removed by subtraction of an intensity estimated from positions off the investigated source. SED models of VeLLOs must take this subtraction into account. This is a crucial difference to previous studies of much brighter protostars, where model flux densities are much lesser affected by an ISRF contamination.

We calculate model flux densities for a small aperture of $2''$ radius, corresponding to the apertures used for observations at wavelengths $\lesssim 20\ \mu$m, and for a larger aperture of 4200 AU, corresponding to the apertures used for the longer wavelength data. At wavelengths $\lesssim 20\ \mu$m the optical depth is so high that the background ISRF varies spatially across the model core because of extinction. Thus the background intensity close to the source is estimated in an annulus with an inner and outer radius of of $5''$ and $10''$, respectively. For longer wavelengths the ISRF is not affected by extinction and it can be removed by subtracting the input ISRF. The 4200 AU radius of the large aperture are matched to the MAMBO observations. As the emission probed by MIPS is not extended, and the method for background subtraction is identical for MIPS and MAMBO, the large aperture can be used to model the data from both instruments.

We quantify the quality of a fit by several criteria. First, we require that a model matches the MAMBO flux density. Then, we require that the model flux densities for both MIPS detections is within the range allowed by the calibration uncertainty. Also, the model flux densities must be below the $J$ band upper limit from 2MASS and FLAMINGOS. Finally, the deviation of model and observation for the other FLAMINGOS bands and the IRAC bands is quantified by the mean squared relative difference between model and observation,

$$\chi^2_{\text{rel}} \;=\; \left\langle \left[ \left( F_\nu^{\text{obs}} - F_\nu^{\text{model}} \right) \middle/ F_\nu^{\text{obs}} \right]^2 \right\rangle \tag{3.3}$$

$$=\; \frac{1}{n_{\text{obs}}} \sum_i \left[ \left( F_\nu^{\text{obs},i} - F_\nu^{\text{model},i} \right) \middle/ F_\nu^{\text{obs},i} \right]^2 \;, \tag{3.4}$$

in which $F_\nu^{\text{obs}}$ and $F_\nu^{\text{model}}$ are the observed and modeled flux density, respectively, the indices $i$ refer to the different observed bands, and $n_{\text{obs}}$ is the number of observations, respectively observed bands. We also calculate for every fit the mean squared uncertainty-normalised difference between model and observation usually adopted to quantify a fit,

$$\chi^2 \;=\; \left\langle \left[ \left( F_\nu^{\text{obs}} - F_\nu^{\text{model}} \right) \middle/ \sigma\left( F_\nu^{\text{obs}} \right) \right]^2 \right\rangle \tag{3.5}$$

$$=\; \frac{1}{n_{\text{obs}}} \sum_i \left[ \left( F_\nu^{\text{obs},i} - F_\nu^{\text{model},i} \right) \middle/ \sigma\left( F_\nu^{\text{obs},i} \right) \right]^2 \;, \tag{3.6}$$

where $\sigma(F_\nu^{\text{obs},i})$ is the uncertainty. However, as we discuss below, our failure to match the observations within their uncertainties makes this a bad quantity to judge the quality of a fit.

### 3.4.3   Results

#### 3.4.3.1   Failure of Pure Power-Law Density Profiles

It is not possible to match the MIPS observations with models having a pure $\varrho \propto r^{-2}$ density profile for any combination of the free parameters internal luminosity, effective temperature, $r_{\text{in}}$, and $\varrho_{\text{out}}$. This would require the presence of warm dust of some dozen K in order to flatten the SED between both MIPS bands. This in turn would demand that dust exists close in to the central source. For a pure $\varrho \propto r^{-2}$ density profile this, however, implies an extinction of several hundred magnitudes towards the embedded source. Then the radiation emitted by hot dust is too much attenuated to match the flux densities in the MIPS bands.

We conclude that no pure power-law density profile can fit the observed SED. However, models with constant density in between $r_{\text{trans}}^{\text{in}}$ and $r_{\text{trans}}^{\text{out}}$ do, as we show below. As the inclusion of this region improves the fits, we choose to make $r_{\text{trans}}^{\text{out}}$ as large as allowed by the dust emission intensity profile discussed in Sec. 3.5.1. To be conservative we set $r_{\text{trans}}^{\text{out}}$ to $2 \cdot 10^{14}$ m $\approx 1340$ AU for the further modelling, corresponding to an angular diameter of $\approx 8''$. This
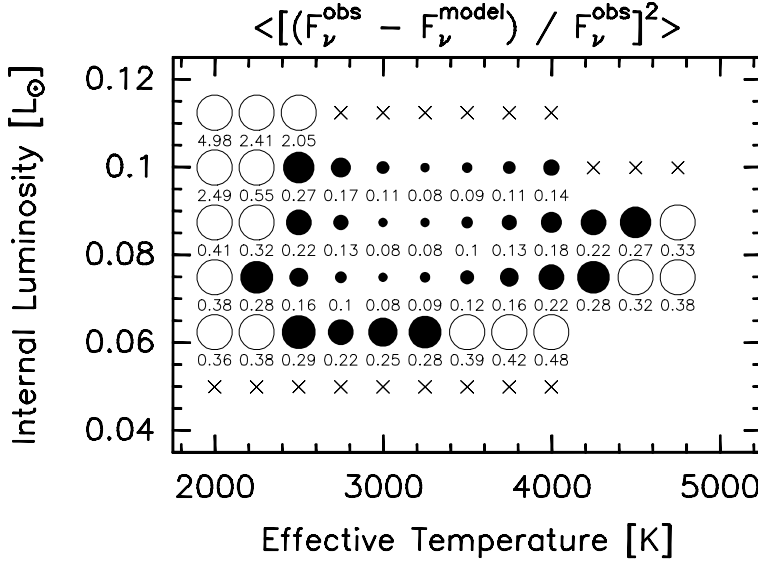
**Figure 3.7:** Quality of SED fits in dependence on the model effective temperature and internal luminosity. *Small numbers* give the minimum mean squared relative difference between model and observations for a given combination of $T_{\text{eff}}$ and $L_{\text{int}}$. For accepted fits, for which $\chi^2_{\text{rel}} \leq 0.3$, this figure is also indicated by the diameter of the *filled circles*. *Empty circles* are drawn for not accepted fits, for which $\chi^2_{\text{rel}} > 0.3$. *Crosses* are drawn if no solution exists. The modelling thus constrains the internal luminosity to $0.06 \lesssim L_{\text{int}}/L_\odot \lesssim 0.11$ and the effective temperature to $2000 \lesssim T_{\text{eff}}/\text{K} \lesssim 4500$.

affects the dust intensity profile on scales much smaller than the MAMBO beam and is therefore in agreement with the profiles in Sec. 3.5.1 from which the density profile is derived.

### 3.4.3.2   Success of Piecewise Power-Law Density Profiles

For given inner and inner transition radius, $r_{\text{in}}$ and $r^{\text{in}}_{\text{trans}}$, respectively, the density at the outer radius is fixed by the requirement that the model matches the dust emission probed by MAMBO. This leaves $r_{\text{in}}$ and $r^{\text{in}}_{\text{trans}}$ as the only remaining free parameters, which we thus vary to minimise $\chi^2_{\text{rel}}$.

Figure 3.2 shows the best model fit to the observations. The differences between the large and small model apertures are apparent; different strategies to remove the ISRF intensity can result in largely different model flux densities. The apertures used in observations need to be taken into account when calculating model SEDs. In our model SEDs the three peaks seen, e.g., in Fig. 3.2 are, in order of decreasing wavelength, dominated by emission from cold dust ($\approx 10$ K) in the extended envelope, emission from warm dust ($\lesssim 100$ K) in the inner envelope that is predominantly radiatively heated by the central source, and by extincted stellar photospheric emission. The latter two make up the bulk of the reprocessed stellar radiation. For good fits the emission from the warm inner envelope must dominate this reprocessed radiation. This requires significant extinction of the photospheric emission. Therefore, if L1148-IRS is associated with the L1148 dense core, it must be deeply embedded in the core.

The minimum values of $\chi^2_{\text{rel}}$ for different internal luminosities and effective temperatures are shown in Fig. 3.7. Solutions to the radiative transfer problem do, however, not exist if $L_{\text{int}} \lesssim 0.06\,L_\odot$, as then it is not possible to match the both MIPS observations at the same time, and not if $L_{\text{int}} \gtrsim 0.11\,L_\odot$, as then is not possible to match both MIPS observations and the $J$ band upper limit at the same time. In other words then the luminosity injected by the central source is different from the power radiated away in the observed bands.

The minimum mean squared uncertainty-normalised difference between model and observation is $\chi^2 \approx 67$. For 6 observations and 2 free parameters this gives a reduced $\chi^2$ of $\chi^2/4 \approx 17$. This is much larger than one and thus

no model is consistent with the short wavelength ($< 10 \, \mu$m) observations within the observational uncertainties. This is a known problem for SED fits to some Spitzer VeLLOs (e.g., $\chi^2 = 121$ for IRAM04191; Dunham et al., in prep.). We defer a discussion of our failure to obtain detailed fits to the next section.

As observational uncertainties alone can not be responsible for the observed departures between model and observations, we use $\chi^2_{\text{rel}}$ to quantify the fit quality. Its minimum is 0.08, implying that the mean relative difference between model and observation is of the order $(\chi^2_{\text{rel}})^{1/2} \approx 28\%$. We only accept fits with about twice this mean relative difference, i.e. we demand $\chi^2_{\text{rel}} \leq 0.3$. This constrains the internal luminosity to be 0.06 to 0.11 $L_\odot$, and the effective temperature to be 2000 to 4500 K. The best-fit model has $L_{\text{int}} = 0.0875 \, L_\odot$ and $T_{\text{eff}} = 3250$ K; the column density corresponds to a visual extinction towards the central source of 30.3 mag. The acceptable range of luminosities is more determined by the existence of solutions than by the quality of fits.

The best-fit inner radii of order $r_{\text{in}} = 10^{12}$ m $\approx 7$ AU imply the absence of hot ($\gg 100$ K) dust in the protostellar envelope. Thus the SED at wavelengths shortward of $\approx 10 \, \mu$m is dominated by extincted photospheric emission of the central source, as the dust temperatures are very low compared to the stellar effective temperature.

All our models reasonably fitting the data exhibit a deep silicate absorption feature at a wavelength of about $10 \, \mu$m, not in agreement with the observations. We discuss this problem in the next section.

### 3.4.4 Physical Interpretation

#### 3.4.4.1 Non-Spherical Models, Internal Luminosity, and Effective Temperature

Our failure to achieve fits to the observed SED within the observational uncertainties implies that our model fails to capture some important aspects of the radiative transfer in the envelope of L1148-IRS. Deviations from spherical symmetry, like the presence of outflow cavities suggested by our $H$ and $K_s$ band images, are one likely candidate for important effects not included in our present model. Such deviations will predominantly affect the predictions for wavelengths shorter than $\approx 10 \, \mu$m (Whitney et al. 2003a,b), where the deviations between model and observations are presently largest. Also, not well included are spectral features of ices, which can have a significant impact on the SED for $\lambda \lesssim 10 \, \mu$m (e.g., Natta et al. 2002). We speculate that the inclusion of these effects into SED models would allow to match the data within the observational uncertainties.

Still, the internal luminosity derived from a spherically symmetric model fit, $L_{\text{int}}^{\text{obs}}$, is usually a good estimate of the actual one. The error in the luminosity estimate made when neglecting the non-spherical protostellar radiation field was gauged by Whitney et al. (2003b). They calculate models of a protostar of a luminosity of 1 $L_\odot$ surrounded by an envelope with central flattening, to that for some models a flared disk and outflow cavities are added. These models are tuned to reflect the properties of class I protostars. On lines-of-sight forming an angle of 18° to 87° with the outflow axis the luminosity correction factor, $L_{\text{int}}/L_{\text{int}}^{\text{obs}}$, which increases with angular distance from the outflow axis, is between 0.5 and 2.1. Models with outflow cavities, which supposedly hold for L1148-IRS because of its nebulosity, have correction factors between 0.5 and 1.5. For the suspected inclination of order 30° with respect to the outflow axis (Sec. 3.3.3), our model fit for L1148-IRS would then overestimate the actual internal luminosity by a factor 1.1 to 1.4.

Similarly, estimates of the stellar effective temperature from fits of spherically symmetric models to emission from non-spherical envelopes do constrain the actual temperature. If the SED close to the peak of the intrinsic SED of the central object is dominated by extincted photospheric emission, as it is apparently the case for L1148-IRS, then the SED to first order depends only on the extincting column density and on the effective temperature, but not on details of the density distribution. Thus, models must yield the same effective temperature and extinction independent from the adopted geometry. If extinction does not dominate, temperature estimates from spherical model fits do set a lower limit to the actual effective temperature: much lower temperatures are usually inconsistent with emission detected at short wavelengths.

### 3.4.4.2  Lack of Hot Dust and Silicate Absorption

The inferred absence of hot dust ($\gg 100$ K) in protostellar models of L1148-IRS would be a surprise for a protostar expected to be accreting. The inflowing dust is supposed to be radiatively heated to temperatures $> 100$ K while approaching the central source, and eventually to evaporate at a temperature of about 1500 K, which marks the upper limit of expected dust temperatures. The actual lack of hot dust in L1148-IRS, and the corresponding lack of inflowing matter, would be a problem for the interpretation of this source as a young and accreting protostar.

Within our model the absence of such dust is very robust. Any attempt to create hot dust by decreasing the inner radius leads to an SED in the IRAC bands too steep and too bright to be consistent with observations, if we require that the model still matches the observations in the MIPS bands. However, spectral slopes in the IRAC bands comparable to those for L1148-IRS are also found for the SED models of Whitney et al. (2003a,b), although dust with temperatures of up to 1600 K exists in these. This suggests that hot dust might be present in L1148-IRS in spite of our model results. Furthermore, the SEDs of L1148-IRS and the VeLLO L1521F-IRS (Bourke et al., in prep.) differ by only a scaling factor in the IRAC and MIPS 1 bands; their colours in these bands are identical within the uncertainties. Given the clear protostellar nature of L1521F-IRS (Bourke et al., in prep.), the SED of L1148-IRS in the IRAC bands is thus consistent with those possible for protostars.

In summary, while the exact implications of the suggested absence of hot dust are not clear yet, it is clear that it would not challenge the protostellar nature of L1148-IRS.

Emission of warm to hot dust ($\gg 10$ K) in the silicate features (e.g., Chiang & Goldreich 1997) could compensate the silicate absorption feature predicted by our model. This would help to explain the discrepancy between the actual and model SED at 8 $\mu$m wavelength. If additional emission in the silicate bands contributes to the observed flux density, such emission is likely to reach us on lines of sight not screened by the cold foregrounds causing the predicted absorption. The emission would otherwise not reach the observer, given the magnitude of predicted extinction in this band. This would supposedly require deviations from spherical symmetry.

## 3.4.5  Modelling Summary

Assuming a protostellar nature for L1148-IRS, the self-consistent radiative transfer modelling in spherical symmetry constrains the internal luminosity and effective temperature to

$$0.06 \lesssim L_{\mathrm{int}}/L_\odot \lesssim 0.11 \quad \text{and} \quad 2000 \lesssim T_{\mathrm{eff}}/\mathrm{K} \lesssim 4500 \,,$$

respectively (Fig. 3.7). If L1148-IRS is associated with the L1148 dense core, then it must be deeply embedded ($\approx 30$ mag) in order to match the flux density ratio between the IRAC and MIPS bands.

The derived luminosity is not likely to differ from the actual one by more than a factor 1.5 in case that L1148-IRS is a protostar with an envelope deviating from spherical symmetry. The presence of such deviations might in part be responsible for our failure to exactly match the observations. We have no ultimate interpretation for the lack of hot dust indicated by our modelling, a feature not expected for an accreting protostar. This possible absence, however, does not challenge the protostellar nature of L1148-IRS, as the related spectral feature is also seen in clear-cut protostars.

The luminosity derived for L1148-IRS is comparable to those derived for other VeLLOs (Table 3.6). These were modeled as stars with circumstellar disks that are embedded in envelopes, while our model lacks a disk. L1148-IRS would thus be the third-faintest embedded protostar known (Andre et al. 2000; Froebrich 2005).

## 3.5  Properties of the Natal Dense Core

After the discussion of the properties of the compact infrared source L1148-IRS we now turn to a study of the dense core from that L1148-IRS appears to form. This on one hand lends further evidence for a physical association of L1148-IRS and the dense core: within L1148 the position of L1148-IRS stands out in its physical and kinematical
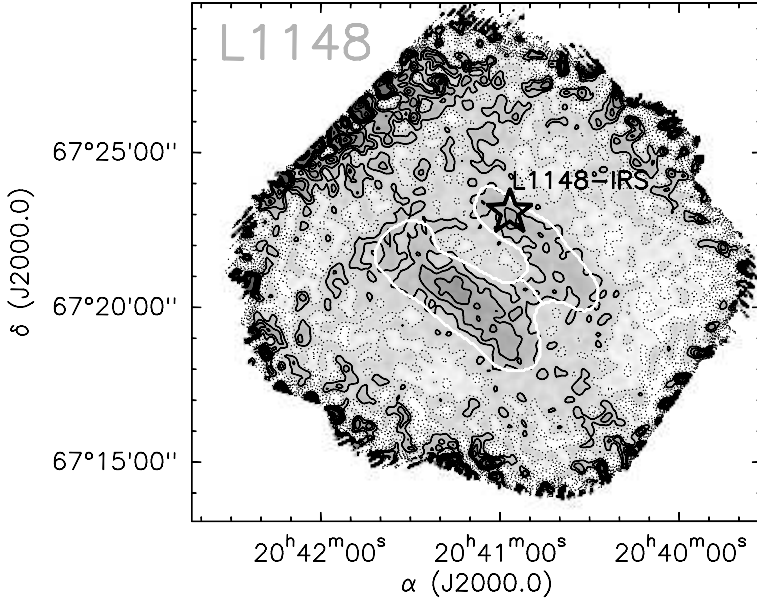
**Figure 3.8:** Thermal dust emission at 1.2 mm wavelength, smoothed to $20''$ resolution, as seen by MAMBO. *Black contours* (*dotted contours* for $\leq 0$ mJy beam$^{-1}$) are drawn in steps of 3 mJy per $11''$ beam. *White contours* delimit the two elongated cores identified in the map. No emission at a significant level is detected outside these cores. The position of L1148-IRS, which resides in the northwestern core, is marked by a *star*.

properties. On the other hand our study of the dense core indicates that L1148 is an unusual region for active star formation, very different from all others studied to date. The inferred properties also set the stage for the general discussion of L1148 as a star-forming region in Sec. 3.6.

We start with a discussion of the dust emission from L1148 in Sec. 3.5.1. This constrains the mass distribution on large and small scales and reveals mass concentrations very low for cores expected to form stars. We then use our CCS spectra to quantify the velocity field across the whole of L1148 in Sec. 3.5.2. Our C$^{18}$O data, presented in Sec. 3.5.3, indicates a complex velocity field in the vicinity of L1148-IRS and suggests a chemical state not different to the one of unevolved starless cores. The subsequent analysis of our N$_2$H$^+$ observations in Sec. 3.5.4 reveals a dense core at the position of L1148-IRS with a low degree of turbulence. Finally, in Sec. 3.5.5, the analysis of deep spectra for several molecular transitions towards selected positions in L1148 suggests the existence of inward motions.

### 3.5.1   Dust Emission: No Indication for very dense Gas

Maps of thermal dust emission allow to map the mass distribution of the dense core harbouring L1148-IRS. Its density, column density, and mass concentration turns out to be low when compared to those of dense cores believed to be in the stage just prior to active star formation. The radial intensity profile of the dust emission peak possibly harbouring L1148-IRS is consistent with the one of an gravitationally unstable equilibrium.

**Overview**   Figure 3.8 shows our complete MAMBO dust emission map of L1148. The RMS noise level is 1.1 mJy per $11''$ beam in the center of the map and increases outwards due to lesser coverage; it is 1.2 mJy beam$^{-1}$ at the position of L1148-IRS. Significant emission with a locally evaluated SNR larger 3 is only detected in two parallel dust filaments in the map center, of which the northwestern one contains L1148-IRS.

We use SNR and intensity maps smoothed to $60''$ resolution to break the emitting regions up into substructures. For this boundaries of regions with a SNR larger 2 are identified first. Within these boundaries cores are identified

by separating them (by eye) at the lowest intensity contour they do not have in common. We find two very elongated cores in our map, which are identical to the two filaments intuitively identified by eye. The peak intensities and the total flux densities within the boundaries thus set for the two filaments are $9 \pm 1$ mJy beam$^{-1}$ and $0.77 \pm 0.06$ Jy for the northwestern filament, and $12 \pm 1$ mJy beam$^{-1}$ and $1.74 \pm 0.10$ Jy for the southeastern filament, where the uncertainty comes from the noise in the map. Both have a length of about $5'$ or $0.5$ pc $\approx 100\,000$ AU.

To quantify the geometry of a filament we fit ellipses to the area above half of the peak flux of the respective filament within the filament boundaries[8]. This way we derive sizes, aspect ratios, and position angles (east of north) of $334'' \times 71''$, $4.7 \pm 0.8$, and $45° \pm 3°$ for the northwestern filament, respectively $291'' \times 82''$, $3.5 \pm 0.4$, and $50° \pm 2°$ for the southeastern filament. The uncertainties are derived in Monte-Carlo experiments in which we first superpose the observed map with artificial noise of an amplitude identical to the one in the observations, and then fitting ellipses to the data. The uncertainties are taken to be the standard deviation of the derived values.

**Dust Emission Properties**   As the thermal dust emission is optically thin, the observed intensities (i.e., flux densities per beam), $S_\nu^{\text{beam}}$, can be converted into $H_2$ column densities,

$$N(H_2) = \frac{S_\nu^{\text{beam}}}{\Omega_{\text{beam}} B_\nu(T_{\text{dust}}) \kappa_\nu \mu} ; \tag{3.7}$$

here $\Omega_{\text{beam}}$ is the area of the beam and $B_\nu(T_{\text{dust}})$ is the Planck function. We assume a dust temperature $T_{\text{dust}} = 10$ K, a mean molecular weight of $\mu = 2.8\, m_H$ per $H_2$ molecule (where $m_H$ is the mass of an hydrogen atom), and a dust opacity of $0.0102$ cm$^2$ per gram of interstellar matter (Ossenkopf & Henning 1994; for $10^5$ yr of coagulation at an H density of $10^6$ cm$^{-3}$, thin ice mantles, and a gas-to-dust mass ratio of 100). This yields estimated peak $H_2$ column densities and total masses of $5.9 \pm 0.8 \cdot 10^{21}$ cm$^{-2}$ and $3.8 \pm 0.3\, M_\odot$ for the northwestern filament, and $7.9 \pm 0.8 \cdot 10^{21}$ cm$^{-2}$ and $8.7 \pm 0.5\, M_\odot$ for the southeastern filament. For a conversion factor of $A_V/N(H_2) = 1.1 \cdot 10^{-21}$ mag cm$^2$ (Bohlin et al. 1978; for a total-to-selective extinction ratio $R_V = 3.1$) this corresponds to a peak visual extinction of $A_V = 6$ mag and 9 mag, respectively. The mass within 4200 AU distance from the dust emission peak, $M_{\text{4200AU}}$ (see Motte & André 2001), is $0.15 \pm 0.01\, M_\odot$ for the northwestern filament and $0.22 \pm 0.01\, M_\odot$ for the southeastern one.

**Dust Emission Peak**   As discussed in Sec. 3.3.1, the dust emission peak of the northwestern filament appears to be physically associated with L1148-IRS. Thus, it is straightforward to assume that this dust emission peak represents the immediate environment from which L1148-IRS aggregates, and the structure of the peak should be relevant for an understanding of L1148-IRS.

The dust filaments are not well enough resolved and detected to allow for detailed modelling of the dust emission peak, but we can gauge the density gradients near L1148-IRS by analysing cuts through the surrounding dust emission. The cuts are shown in Fig. 3.9. Inspection of the maps shows that the dust emission peak near L1148-IRS is about circular, but we only consider cuts perpendicular to the filament major axis in order to minimise the impact of confusion of structures overlying along the filament on our analysis. Given the observational uncertainties the cut through this dust emission peak is about consistent with the beam-smeared intensity profile expected for a spherically symmetric isothermal density profile $\varrho \propto r^{-2}$, where $\varrho$ is the density and $r$ the radius (Fig. 3.9).

This profile is predicted for spherical equilibria supported by isothermal pressure having an infinite center-to-surface density contrast (McKee & Holliman 1999). Such equilibria are unstable to gravitational collapse and it is hypothesised that they represent the density structure of dense cores just before the central formation of a star (Shu 1977). The density structure of the dust emission peak near L1148-IRS is thus consistent with the one expected for environments actively forming stars. The width of the cut through the dust emission peak near L1148-IRS at 50% peak intensity is about $40''$ or 13000 AU. The flux density of $59.2 \pm 1.3$ mJy encircled by an aperture of this diameter corresponds to a mass of $0.29 \pm 0.01\, M_\odot$.

The above analysis would not be much influenced by temperature gradients due to radiative heating by L1148-IRS. As predicted by Eq. (3) of Motte & André (2001) heating by a source of a luminosity similar to the $0.1\, L_\odot$

---

[8]This is implemented by using the IDL routine FitEllipse by David Fanning.
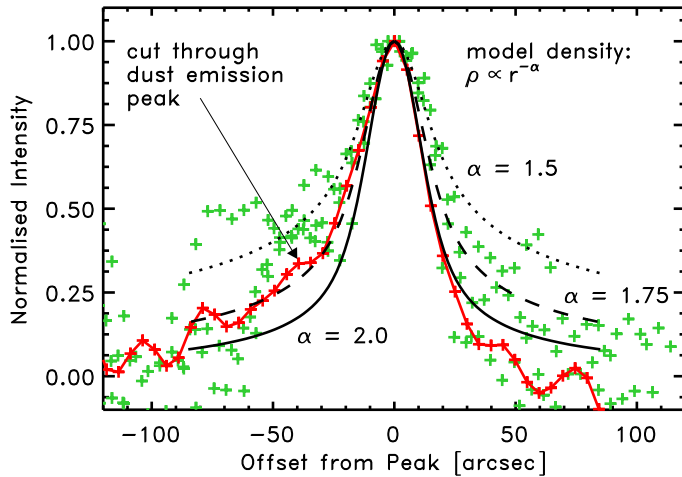
**Figure 3.9:** Cuts through the dust emission of the northwestern filament. The *solid line with crosses* holds for the cut through the dust emission peak near L1148-IRS, while the *crosses* hold for 4 parallel cuts displaced by about ±20″ and ±40″. The cuts have a position angle of 135°, i.e. their orientation is perpendicular to the major axis of the filament. They run from southeast (negative offsets) to northwest (positive offsets). For the cut cut through the dust emission peak near L1148-IRS the uncertainty in the normalised intensity is of order ±15%. Model cuts for beam-folded spherically symmetric isothermal density profiles $\varrho \propto r^{-\alpha}$ are shown as *solid* ($\alpha = 2.0$), *dashed* ($\alpha = 1.75$), and *dotted lines* ($\alpha = 1.5$). The cut trough the dust emission peak is one of the steepest ones. Its slope is about consistent with the $\alpha = 2$ expected for isothermal equilibria.

estimated for L1148-IRS would significantly heat the envelope only in a region of 5″.6 diameter, which is much smaller than the profile width and the beam size.

**Mass Concentration** An estimate for the average density in the filaments can be derived by dividing the observed column density by the depth of the filament. For depths ranging from the minor axis length to the geometrical mean of the major and minor axis length the thus derived densities are 0.8 to $1.7 \cdot 10^4$ cm$^{-3}$ for the northwestern filament, and 1.1 to $2.0 \cdot 10^4$ cm$^{-3}$ for the southeastern one. Similarly, a dense core of mass 0.15 $M_\odot$ within 4200 AU from its peak (the mass inferred for the dust emission peak near L1148-IRS) and a density profile $\varrho \propto r^{-2}$ has a density of order $1.3 \cdot 10^4$ cm$^{-3}$ at 4200 AU radius. These figures are comparable to the similarly derived densities[9] of the starless submillimetre cores studied by Visser et al. (2002), for which the densities are 0.2 to $2.0 \cdot 10^4$ cm$^{-3}$, but much lesser than the 0.3 to $5 \cdot 10^5$ cm$^{-3}$ found by Kirk et al. (2005) for their cores with satellite data[10]

The column density of the parental core of L1148-IRS is rather low when compared to starless cores. Only 2 starless cores in our c2d MAMBO survey (Kauffmann et al., in prep.; see Chapter 2) have column densities significantly smaller than L1148-IRS. Similarly, to have an SNR larger than 3 the starless cores detected by Visser et al. (2002) and Kirk et al. (2005) must have column densities $\gtrsim 8 \cdot 10^{21}$ cm$^{-2}$. Thus, L1148 is among the dense cores with lowest column density studied so far. The low column density might partly be an observational artifact due to the low spatial resolution of 6400 AU = 0.03 pc after smoothing at 325 pc distance. The column density distribution of the nearby ($\lesssim$ 140 pc) 'bright' cores of Kirk et al. have a full width at half maximum (FWHM) comparable to our *resolution*; it is likely that we underestimate the true peak column density because of too poor resolution.

Still, the mass concentrated in the dust emission peak is small. Only three starless cores in our c2d MAMBO

---

[9]We convert published results to our choice of dust opacities and temperatures. While for Visser et al. the scaling factor is of order unity, we have to reduce the densities, column densities, and masses listed by Kirk et al. by a factor 2.

[10]We exclude their results for L1521F from this analysis, as this core contains a VeLLO (Bourke et al., in prep.) and is not starless.

survey (Kauffmann et al., in prep.) have masses within 4200 AU radius significantly smaller than L1148-IRS does; this property is not affected by our low resolution. For a beam size matched to the 15″ of Visser et al. a mass of $0.12\,M_\odot$ is contained in the beam centered on the dust peak. This is only about twice the lowest mass found by Visser et al. for cores closer than L1148 ($\geq 0.05\,M_\odot$ for detected cores at 160 pc distance). Given that for a given core and fixed beam size the mass in the beam decreases when decreasing the distance, the mass concentrated in the dust peak of L1148 is probably comparable to the values in the detected cores of Visser et al. and possibly even smaller.

In particular, the dust emission properties of L1148 are very different from those of the "evolved" cores of Crapsi et al. (2005a). (See also Sec. 3.6.2.2 and Table 3.6 for a summarising discussion.) These are believed to be representative of cores just before the onset of star formation. The two prototypical evolved cores L1544 and L1521F have column densities on the central line of sight $\geq 4.7 \cdot 10^{22}$ cm$^{-2}$ (we converted the values to our choice of dust emission properties), while towards L1148-IRS the column density is lower by a factor 8. Similarly, the average densities derived for L1148 fall short of the $\geq 2.5 \cdot 10^5$ cm$^{-3}$ required for a core to be evolved by more than a magnitude. However, the dust emission peak near L1148-IRS has an effective intrinsic radius at the 70% intensity level, $r_{70\%}$ (i.e., the radius of a circle enclosing an area equal to the area above the 70% intensity level), of 4350 AU, which meets the Crapsi et al. requirement for a core to be evolved, like all other VeLLOs covered by MAMBO (Table 3.6). This radius criterion thus appears to be a good one to select cores close to the onset of star formation.

We conclude that there are no indications from the dust emission for gas densities in L1148 that would be unusual for starless cores. This is likely to some extent a geometrical effect, owing to the low spatial resolution at the cores distance. Geometry alone fails to explain the low concentration of mass in the dust peak though. This would be remarkable for an actively star-forming core in which stars aggregate from dense gas.

### 3.5.2   CCS Map: Large-Scale Velocity Field

The Effelsberg map in the $J, F = 2, 1$–$1, 0$ transition of CCS[11] allows to trace the distribution and kinematics of molecular gas on scales of several arc-minutes. Narrow lines imply low levels of turbulence. The observed radial velocities suggests that the northwestern dust filament on which L1148-IRS is projected is composed of two overlying dense cores.

Figure 3.10 shows that the filaments seen by MAMBO are also seen in CCS emission, though the intensities do not correlate well. For example, there is significant CCS emission at the southwestern end of the northwestern filament where there is no dust emission. However, CCS is known to be a molecule with a complex chemistry. It usually does not correlate well with high density gas (Lai & Crutcher 2000).

The spectra reveal a complex velocity field, suggestive of two overlying velocity components in the northwestern filament (Fig. 3.10). To show this this we fit Gaussian curves to smoothed spectra of 0.066 km s$^{-1}$ resolution with a peak SNR larger 4. We find a kinematical dichotomy in the northwestern filament: the LSR velocity of the northeastern end of the filament (2.63 km s$^{-1}$ from Gaussian fits to an unsmoothed average spectrum) is significantly smaller than the velocity of the southwestern end (2.78 km s$^{-1}$). (The average spectra were calculated from positions with a peak SNR larger 4 after smoothing. The 4 positions near L1148-IRS, and the 7 positions in the southeastern end of the filament are averaged, respectively.) The velocity jumps abruptly from the low to the high velocity along the filament, and is about constant in the respective filaments ends. Such sharp velocity jumps can not exist in single dense cores, as they would soon smoothen out. Also rotation does not manifest in velocity jumps, but smooth gradients. Thus the observed velocity field is indicative of two physically distinct dense cores along the filament, which have different radial speeds. Both ends have a similar average line width (0.17 km s$^{-1}$ and 0.18 km s$^{-1}$, respectively).

The southeastern filament has a radial velocity similar to the one of the northeastern end of the northwestern filament (2.65 km s$^{-1}$ for an average spectrum of 6 positions), which suggests that these both parts of L1148

---

[11]We improve the baseline quality by subtracting polynomials of second order.
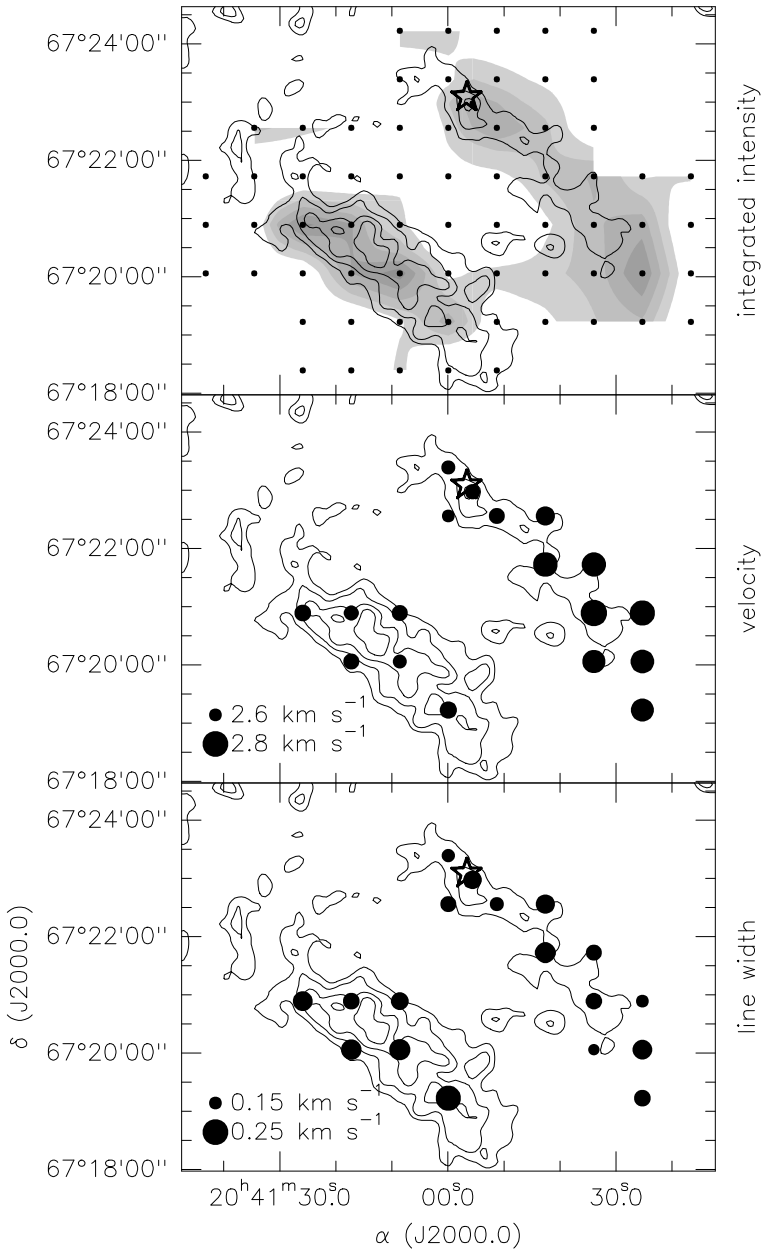
**Figure 3.10:** Effelsberg map of L1148 in the $J, F = 2, 1-1, 0$ transition of CCS. The *top panel* shows the integrated intensity in the $T_{\mathrm{mb}}$ scale for the 1.8 to 3.6 km s$^{-1}$ velocity range in *grey shade*. The shades are drawn in steps of the noise level of 0.085 K km s$^{-1}$, starting with twice the noise level. The MAMBO dust emission map is overlayed in *black contours*; the contours start for 4 mJy beam$^{-1}$ and are spaced by 2 mJy beam$^{-1}$. *Dots* indicate positions observed with Effelsberg. The position of L1148-IRS is indicated by a *star*. The other panels show the LSR velocity (*middle panel*) and the line width (*bottom panel*) for positions with a peak SNR larger 4, as derived from Gaussian fits to data smoothed to 0.066 km s$^{-1}$ resolution. The point diameters indicate the velocity and line width, respectively.

are physically associated. The average linewidth of 0.20 km s$^{-1}$ is slightly higher than those in the northwestern filament.

### 3.5.3   C$^{18}$O Map: Velocity Components and CO Depletion

C$^{18}$O is a very valuable tracer for the study of dense cores, as it probes the spatial distribution of moderately dense gas, the velocity field, and the cloud chemistry. Analysis of these aspects reveals that dense gas traced by C$^{18}$O is associated with L1148-IRS, and that several velocity components exist in the immediate surroundings of L1148-IRS. The C$^{18}$O abundances derived for L1148 are much higher than those expected to hold for starless cores just before the onset of star formation. This would make L1148 an unusual star-forming region.

**Velocity Structure**   Our C$^{18}$O data allows to probe the velocity field near L1148-IRS. Figure 3.11 presents the spectra, overlayed with Gaussian fits to velocity components where their identification is obvious. Baselines are improved by FFT filtering and subtraction of polynomials of fourth order. Simultaneous fitting of several velocity components is performed where required. Two such components are present in the map. One at velocities around $v_{LSR} = 3.05$ km s$^{-1}$, which is detectable towards L1148-IRS and southeast of it. The dominating velocity component is at velocities of about $v_{LSR} = 2.6$ km s$^{-1}$ and extends across the complete mapped area. The radial velocity of the latter component is similar to the velocity derived from CCS for the northeastern end of the filament, which is covered by our C$^{18}$O map, and the systemic velocity derived from N$_2$H$^+$ spectra for the same region (Sec. 3.5.4). This suggests that these velocity components trace the same gas.

The lower velocity C$^{18}$O emission is associated with L1148-IRS (Fig. 3.12); thus not only our MAMBO map alone suggests the presence of dense gas near L1148-IRS. To show this, Gaussian fits to the higher velocity line components are subtracted from the spectra at positions with two velocity components; an integrated intensity map is then calculated from the modified data for the 1.1 to 4.1 km s$^{-1}$ velocity range. Two positions in the map are excluded from this analysis, as the fits to the velocity components are not reliable. The velocity components at offset $\Delta\alpha = 30''$, $\Delta\delta = -30''$ in Fig. 3.11 can not be uniquely separated; the integrated intensity of the higher velocity line component is likely underestimated, as its linewidth is at the lower limit of observed values while the LSR velocity of the fit to the lower velocity line component is at the upper limit of observed values for this velocity component. The integrated intensity plotted for this position is an upper limit. As the C$^{18}$O intensity peaks towards L1148-IRS, dense gas traced by C$^{18}$O appears to be associated with L1148-IRS. Interestingly, there is a further C$^{18}$O intensity peak about 60'' south of L1148-IRS. This peak is similar in intensity to the L1148-IRS position and is free of dust emission at a significant level.

**CO Abundance**   The C$^{18}$O $J = 2$–1 intensity integrated across all velocity components (over the velocity interval 1.1 to 4.1 km s$^{-1}$; Fig. 3.13) does not correlate well with the thermal dust emission. Observed C$^{18}$O-to-dust intensity ratios imply moderate depletion of CO by freeze-out onto dust. The latter property can be quantified by the line-of-sight integrated CO depletion factor, $f_d = [N(CO)/N(H_2)]_0/[N(CO)/N(H_2)]_{obs}$, where $N(CO)$ and $N(H_2)$ are the column densities of CO and molecular hydrogen, respectively. The subscripts indicate the "canonical" CO abundance, $[N(CO)/N(H_2)]_0$, and the observed one. For optically thin C$^{18}$O emission and constant excitation temperature along the line of sight the column densities can be derived from the observed integrated intensities (Eq. A4 of Caselli et al. 2002c; we adopt their dipole moment of 0.11 D). Similarly, the H$_2$ column density follows from the dust emission intensity (Sec. 3.5.1). For consistency with previous work (in particular by Crapsi et al.) we adopt $[N(CO)/N(H_2)]_0 = 9.5 \cdot 10^{-5}$ (Frerking et al. 1982), a $^{16}$O-to-$^{18}$O number ratio of 560 (Wilson & Rood 1994), dust and CO excitation temperatures of 10 K, and — in deviation to all other parts of the paper — $\mu = 2.33\, m_H$ and a opacity at 1.2 mm wavelength of 0.005 cm$^2$ g$^{-1}$ to derive

$$f_d = 0.42 \left( \frac{S_{1.2\,\text{mm}}^{\text{beam}}}{\text{mJy beam}^{-1}} \right) \left( \frac{\int T_{\text{mb}}(\text{C}^{18}\text{O}[2-1])\,\text{d}v}{\text{K km s}^{-1}} \right)^{-1} . \tag{3.8}$$
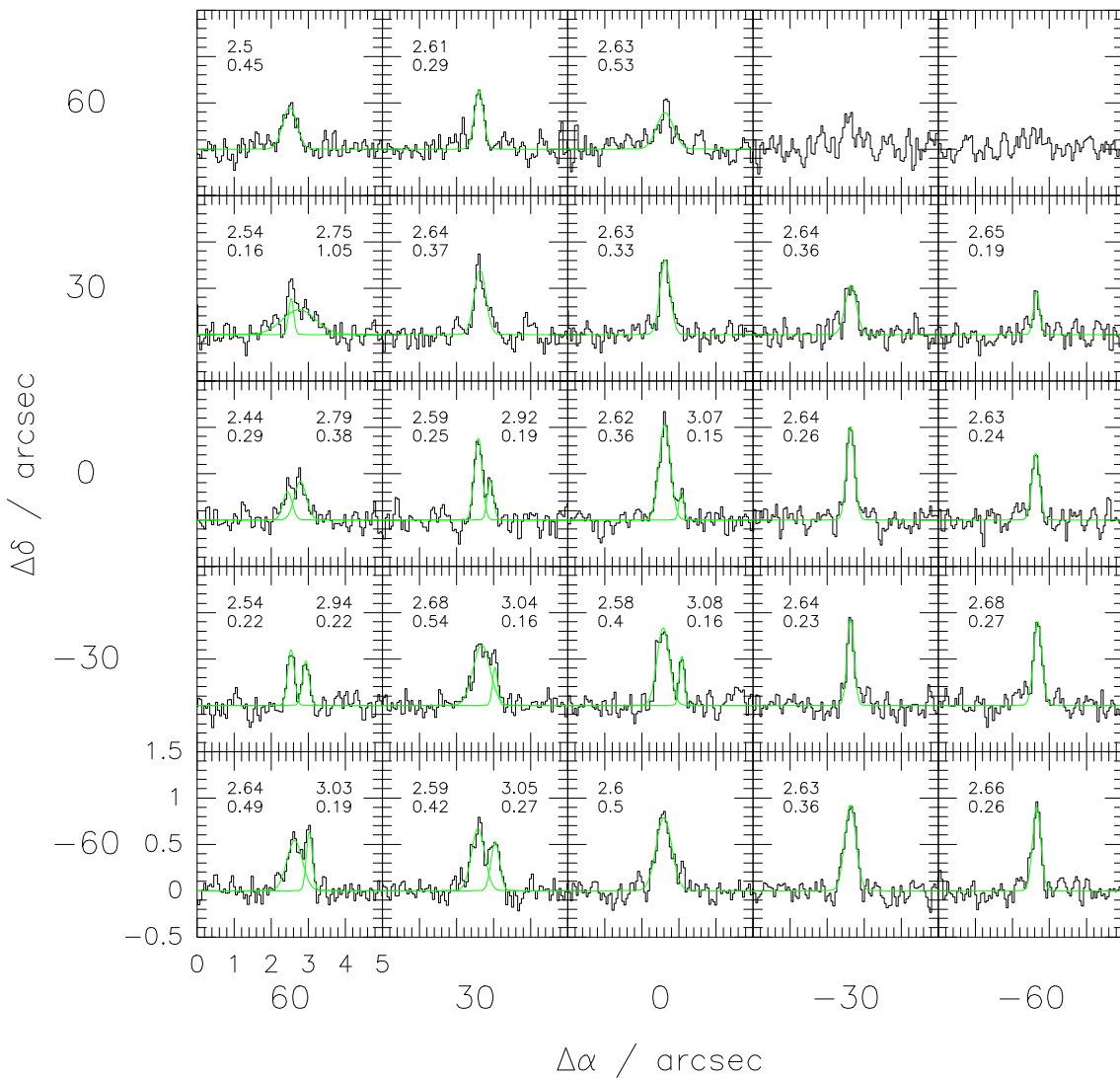
**Figure 3.11:** Spectra in the C$^{18}$O $J = 2$–$1$ transition towards L1148-IRS as observed with frequency switching on a $5 \times 5$ point grid with $30''$ spacing. Offsets are given relative to the approximate dust emission peak position ($\alpha = 20^{\mathrm{h}}40^{\mathrm{m}}56\overset{\mathrm{s}}{.}5$, $\delta = +67\overset{\circ}{.}22\overset{'}{.}58\overset{''}{.}0$ [J2000.0]). The LSR velocity and intensity in the $T_{\mathrm{mb}}$-scale are shown for the spectrum in the lower left corner. Gaussian fits to velocity components are drawn for those positions where the component identification is obvious. *Small numbers* give for every component fitted the derived LSR velocities (*upper lines*) and linewidth (*lower lines*; both in km s$^{-1}$).
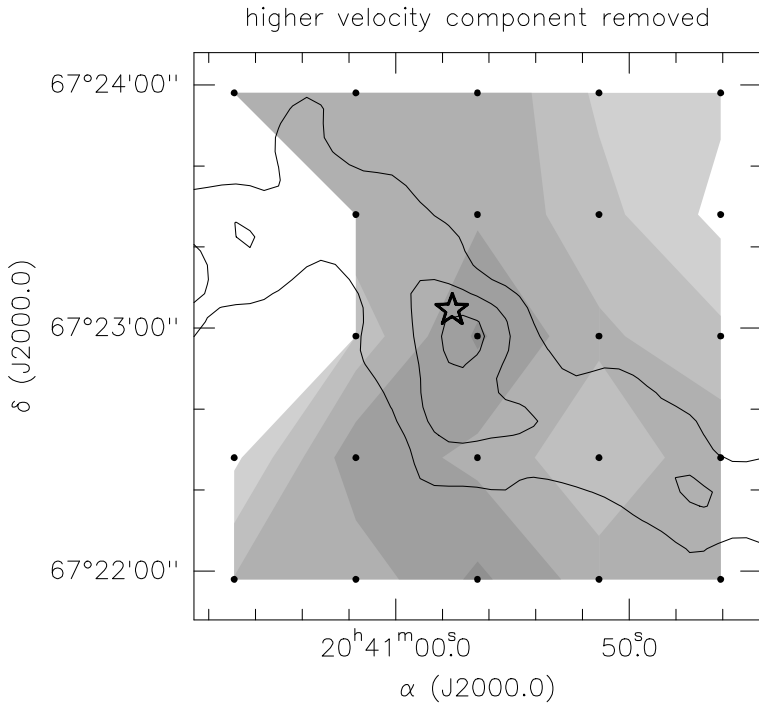
**Figure 3.12:** Integrated intensity map in the $T_{mb}$-scale for the $C^{18}O$ $J = 2–1$ transition near L1148-IRS after removal of the higher velocity line components. Observed positions are marked by *dots*. The *shades* are drawn in steps of twice the noise level of 0.036 K km s$^{-1}$, starting with thrice the noise level. For this map Gaussian fits to the higher velocity line components are subtracted from the observed spectra shown in Fig. 3.11 prior to integration for positions with two velocity components. Two positions (at offsets $\Delta\alpha = 60''$ and $\Delta\delta = 0'', 30''$) are excluded, as the fit quality is not sufficient to allow a separation of velocity components. The MAMBO dust emission map is overlayed in *black contours*; the contours start for 4 mJy beam$^{-1}$ and are spaced by 2 mJy beam$^{-1}$. The position of L1148-IRS is marked by a *star*. As the $C^{18}O$ intensity peaks towards L1148-IRS (the intensity for the position about 40'' southeast of L1148-IRS is an upper limit; see text for details), dense gas traced by $C^{18}O$ appears to be associated with L1148-IRS.
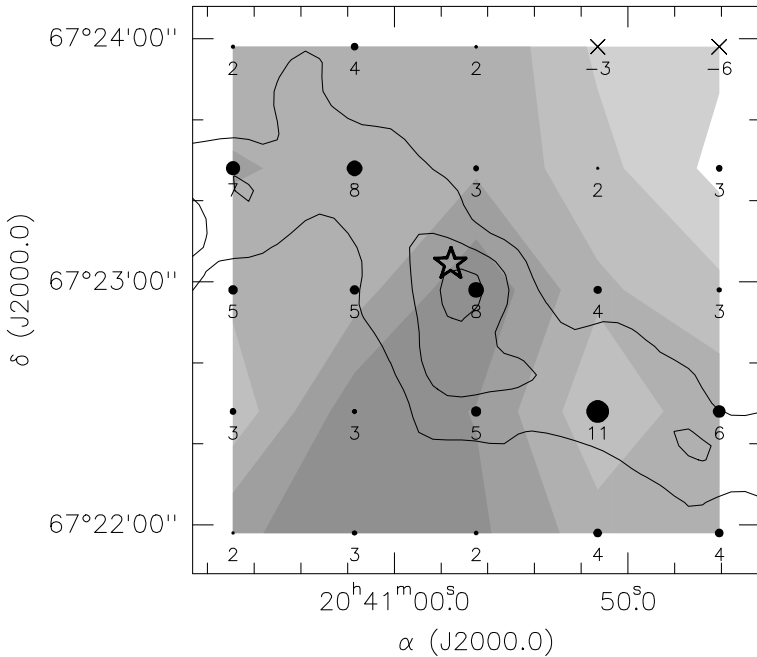
**Figure 3.13:** As Fig. 3.12, but for all velocity components of the $C^{18}O$ $J$ = 2–1 transition. This map traces all $C^{18}O$ along the line of sight, while Fig. 3.12 reflects the distribution of the low velocity emission component only. The noise level is 0.036 K km s$^{-1}$. The *dot diameters and attached numbers* indicate the estimated CO depletion factor, $f_d$ (crosses for $f_d < 0$).

Note that the beam of the $C^{18}O$ observations is only half of the resolution in the smoothed MAMBO map; both observations probe slightly different volumes. This underlines the approximative character of our method to infer $f_d$. The depletion factor is furthermore *an average along the line of sight*. Our method is affected by several sources of uncertainty, like the uncertainty of the canonical CO abundance and of the dust opacity; the actual value of the CO depletion factor can be significantly different from the inferred one. Thus the method it is best suited to compare the properties of cores analysed in the same fashion.

A comparison of depletion factors listed by Crapsi et al. (2005a), which are derived from the $J$ = 1–0 transition, to those derived by us from published $J$ = 2–1 data for a subsample of the Crapsi et al. cores (L183, L492, L694-2, L1498, L1517B, L1521F, and TMC-2; data from Crapsi et al. 2004, Crapsi et al. 2005a, and Tafalla et al. 2004) shows that estimates of $f_d$ from the $J$ = 2–1 transition are in general larger (for the adopted sample on average by a factor 1.6) than those from the $J$ = 1–0 transition. This is most likely due to excitation temperatures below the 10 K adopted here; based on the RADEX[12] online molecular radiative transfer tool (Schöier et al. 2005) the $C^{18}O$ $J$ = 2–1 excitation temperature can be significantly below the adopted gas temperature of 10 K for typical $C^{18}O$ column densities of $10^{15}$ cm$^{-2}$. The $J$ = 1–0 transition is less affected by this problem and should be preferred to estimate $f_d$.

In summary we here, thus, *overestimate* the CO depletion factors derived by the method employed by Crapsi et al. (2005a). The CO depletion factors near L1148-IRS range from 0 to 11 (Fig. 3.13); negative values of $f_d$ are due to negative artifacts in the MAMBO map. These values are small to moderate when compared to those for the dust emission peak positions in the core sample by Crapsi et al. (2005a), especially as we overestimate $f_d$ as used by them. As for the dust emission peak $f_d$ = 7.8 ± 1.3, L1148 misses the CO depletion criterion for "evolved" cores of Crapsi et al. (2005a), $f_d > 10$. (The high depletion factor for the position about 40$''$ southwest of the dust emission peak, $f_d$ = 11.5 ± 3.6, is very uncertain and should not be used to evaluate this criterion.) The

---

[12]http://www.strw.leidenuniv.nl/~moldata/radex.html
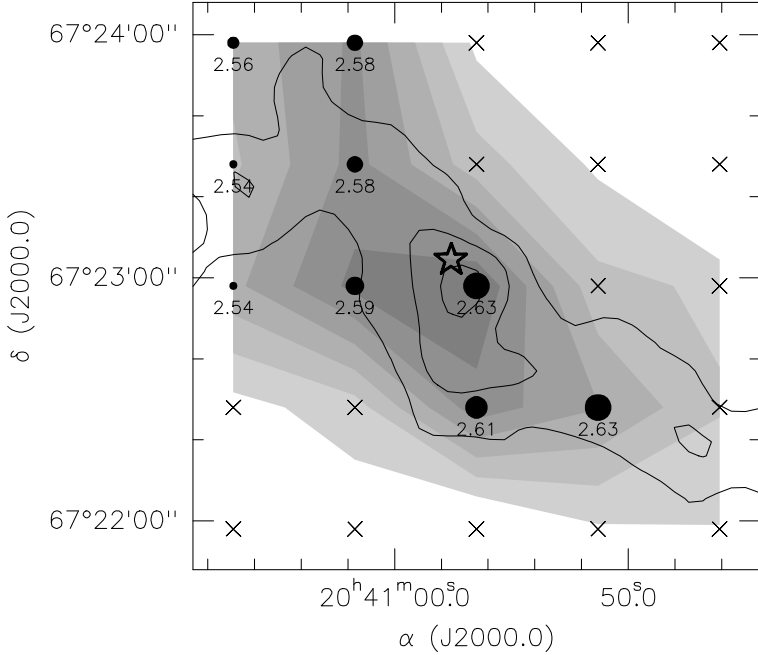
**Figure 3.14:** As Fig. 3.12, but for the $N_2H^+$ $J = 1–0$ transition integrated over all satellites. The noise level is 0.033 K km s$^{-1}$. The intensity distribution peaks towards L1148-IRS. The *dot diameters and attached numbers* indicate radial velocities derived from simultaneous fits to all hyperfine-satellites. As $N_2H^+$ traces dense gas, this again proves the association of L1148-IRS with dense gas.

apparently actively star-forming dense core L1148 thus misses another criterion believed to select cores in a late state of evolution.

### 3.5.4   $N_2H^+$ & $N_2D^+$: Association of L1148-IRS with dense Gas

The integrated intensity in the $N_2H^+$ $J = 1–0$ transition peaks towards L1148-IRS (Fig. 3.14), which shows that L1148-IRS is associated with dense gas. This independently confirms our analysis of the dust emission map. However, the derived column density would be low for a dense core actively forming stars, as is the observed linewidth.

The baseline quality of the $N_2H^+$ data is improved by FFT filtering and subtraction of polynomials of first order. The intensity is integrated over all 7 satellites of the transition (over the $-5.7$ to $-5.1$ km s$^{-1}$, 1.7 to 4.0 km s$^{-1}$, and 7.9 to 9.8 km s$^{-1}$ velocity intervals). As $N_2H^+$ is a well-known dense gas tracer, the derived intensity map reflects the spatial distribution of the dense gas.

The radial velocity of the gas traced by $N_2H^+$ increases from northeast to southwest along the dust filament, as derived from hyperfine structure (HFS) fits to the spectra with a peak SNR $\geq$ 4.5 within CLASS (Fig. 3.14). (The separation between the hyperfine satellites is taken from Caselli et al. 1995, while the line intensities are from Womack et al. 1992.) This trend is not seen in the CCS and C$^{18}$O data presented before. Note however, that the intrinsic beam size of the CCS observations is large (39″) and that the Gaussian fits to the low velocity C$^{18}$O emission are likely corrupted by the high velocity emission; $N_2H^+$ is likely to be the best tracer of the velocity field of the dense gas. Similar velocities suggest that the CCS, low velocity C$^{18}$O, and the $N_2H^+$ emission trace about the same gas.

The high quality $N_2H^+$ spectra towards selected positions acquired in summer 2005 (baselines are improved by subtraction of polynomials of 7th order) allow to infer $N_2H^+$ column densities (Table 3.3). These are derived using

**Table 3.3:** Analysis of high quality $N_2H^+$ and $N_2D^+$ spectra towards selected positions in the L1148 dense core. For easy reference, names are assigned to these positions. The radial velocity, line-width, and total optical depth (i.e., sum of the optical depth of all 7 satellites) for $N_2H^+$ are directly derived from HFS-fits to the $J = 1$–0 transition within CLASS. The quoted uncertainties give the uncertainty of the fit to the data taken. The excitation temperature and column density are calculated from the fit parameters. For $N_2D^+$ $3\sigma$ upper limits to the column density is listed.

| Name | $\alpha$ | $\delta$ | $v_{\text{LSR}}$ | $\Delta v_0$ | $\tau_{\text{tot}}$ | $T_{\text{ex}}$ | $N(N_2H^+)$ | $N(N_2D^+)$ |
|------|----------|----------|------------------|--------------|---------------------|-----------------|-------------|-------------|
|      | J2000.0  | J2000.0  | km s$^{-1}$ | km s$^{-1}$ |          | K | $10^{12}$ cm$^{-1}$ | $10^{11}$ cm$^{-1}$ |
| L1148-IRS | 20:40:56.5 | +67:22:58.0 | $2.621 \pm 0.003$ | $0.203 \pm 0.016$ | $8.5 \pm 1.5$ | $3.2 \pm 0.1$ | $3.1 \pm 0.6$ | $< 4.8$ |
| offset position | 20:41:01.7 | +67:23:28.0 | $2.574 \pm 0.003$ | $0.192 \pm 0.007$ | $6.4 \pm 1.4$ | $3.3 \pm 0.1$ | $2.3 \pm 0.5$ | $< 4.1$ |
| southern peak | 20:41:14.0 | +67:20:31.5 | $2.603 \pm 0.002$ | $0.220 \pm 0.004$ | $2.8 \pm 0.2$ | $4.8 \pm 0.1$ | $1.9 \pm 0.2$ | $< 3.4$ |

Eq. (A1) of Caselli et al. (2002c) for the optically thick lines. The column densities are low when compared to the dense core samples by Crapsi et al. (2005a) and Caselli et al. (2002a). As towards L1148-IRS, where the $N_2H^+$ column density is maximum (Fig. 3.14), $N(N_2H^+) < 8.5 \cdot 10^{12}$ cm$^{-2}$, L1148 misses another criterion of Crapsi et al. (2005a) for "evolved" cores. Note that some of the positions in L1148 have unusually small $N_2H^+$ excitation temperatures, $T_{\text{ex}} \ll 4$ K, which are not found in the surveys by Crapsi et al. (2005a) and Caselli et al. (2002a). The L1148 dense core misses the line-width criterion for evolved cores by Crapsi et al., $\Delta v_0(N_2H^+) > 0.25$ km s$^{-1}$ for $N_2H^+$ intrinsic line-width inferred from HFS-fits.

We do not detect $N_2D^+$ emission in the $J = 1$–0 transition towards any position above an SNR of 1 (intensities integrated over all satellites, i.e. over the $-5.2$ to $-4.4$ km s$^{-1}$, 1.6 to 3.9 km s$^{-1}$, and 7.3 to 9.4 km s$^{-1}$ velocity intervals). Adopting three times the noise level as an upper limit to the integrated intensities, we derive the column densities listed in Table 3.3 (from Eq. [A4] of Caselli et al. 2002c for optically thin lines). These are too high to evaluate the deuteration criterion for evolved cores of Crapsi et al. (2005a).

### 3.5.5 Inward Motions in L1148

Our deep (0.5 to 1 h) spectra taken with the IRAM 30m-telescope in summer of 2005 show blue line shifts of optically thick lines suggestive of inward motions in L1148. The line shifts are largest towards L1148-IRS, where they are of a speed unusual for starless dense cores, suggesting that L1148 might be of a different nature. As these motions are expected to be present in actively star-forming regions, their presence in L1148 supports our interpretation of L1148-IRS as an embedded protostar.

Inward motions manifest in blueshifts (i.e., shifts to lower velocities) of optically thick lines with respect to the systemic velocity as inferred from optically thin lines. This is because a cores' foreground gas will usually appear in absorption in optically thick lines. If inward motions prevail, the receding foreground absorbing material will be redshifted and self-absorption will preferentially affect the red side of a line, resulting in a profile with a blueshifted peak (e.g., Leung & Brown 1977). The line shifts, inferred for each transition from its peak radial velocity, $v_i$, are usually quantified by comparison to the radial velocity of the "isolated" $(J, F_1, F = 1, 0, 1$–$0, 1, 2)$ $N_2H^+$ satellite and normalisation by the linewidth of the same satellite,

$$\delta v_i = \frac{v_i - v_{N_2H^+}}{\Delta v_{N_2H^+}} . \tag{3.9}$$

The latter transition is usually of low $(\tau \lesssim 1)$ optical depth and well suited to infer systemic velocities (Lee et al. 1999). Line peak velocities, width, and normalised lineshifts are listed in Tables 3.4 and 3.5, respectively. Figures 3.15 and 3.16 show the spectra.

**Table 3.4:** Line velocities and widths for several transitions observed towards the positions defined in Table 3.3. If more than one line has to be fitted simultaneously to achieve a good fit to the narrow peak and the broad base of a line the parameters for the component with the lower velocity are listed. No numbers are given for transitions not well detected enough to allow fitting. The lines believed to be optically thick all peak at velocities below the systemic one derived from $N_2H^+$.

| Line | L1148-IRS | | offset position | | southern peak | |
|---|---|---|---|---|---|---|
| | $v_{LSR}/$km s$^{-1}$ | $\Delta v/$km s$^{-1}$ | $v_{LSR}/$km s$^{-1}$ | $\Delta v/$km s$^{-1}$ | $v_{LSR}/$km s$^{-1}$ | $\Delta v/$km s$^{-1}$ |
| $N_2H^+$ $(J, F_1, F = 1, 0, 1\text{--}0, 1, 2)$ | $2.602 \pm 0.015$ | $0.244 \pm 0.030$ | $2.583 \pm 0.023$ | $0.232 \pm 0.048$ | $2.614 \pm 0.013$ | $0.243 \pm 0.029$ |
| CS $(J = 2\text{--}1)$ | $2.418 \pm 0.005$ | $0.149 \pm 0.017$ | $2.488 \pm 0.003$ | $0.118 \pm 0.010$ | $2.509 \pm 0.002$ | $0.119 \pm 0.004$ |
| CS $(J = 3\text{--}2)$ | | | | | $2.513 \pm 0.005$ | $0.106 \pm 0.015$ |
| $HCO^+$ $(J = 1\text{--}0)$ | $2.218 \pm 0.001$ | $0.204 \pm 0.013$ | $2.327 \pm 0.003$ | $0.119 \pm 0.008$ | $2.356 \pm 0.002$ | $0.115 \pm 0.006$ |
| $H^{13}CO^+$ $(J = 1\text{--}0)$ | $2.681 \pm 0.016$ | $0.420 \pm 0.038$ | $2.652 \pm 0.015$ | $0.314 \pm 0.028$ | $2.628 \pm 0.008$ | $0.293 \pm 0.017$ |
| HCN $(J, F = 1, 2\text{--}0, 1)$ | $2.360 \pm 0.013$ | $0.197 \pm 0.048$ | $2.398 \pm 0.006$ | $0.127 \pm 0.018$ | $2.424 \pm 0.008$ | $0.125 \pm 0.021$ |
| HCN $(J, F = 1, 1\text{--}0, 1)$ | | | $2.429 \pm 0.018$ | $0.198 \pm 0.046$ | $2.438 \pm 0.012$ | $0.113 \pm 0.032$ |
| HCN $(J, F = 1, 0\text{--}0, 1)$ | $2.601 \pm 0.041$ | $0.566 \pm 0.086$ | $2.460 \pm 0.016$ | $0.153 \pm 0.033$ | $2.469 \pm 0.010$ | $0.124 \pm 0.034$ |

**Table 3.5:** Dimensionless velocity shifts in several transitions towards the positions defined in Table 3.3. No numbers are given for transitions not well enough detected to allow fitting. The lines believed to be optically thick all do have negative lineshifts indicative of inward motions.

| Line | $\delta v_i = (v_i - v_{N_2H^+})/\Delta v_{N_2H^+}$ | | |
|---|---|---|---|
| | L1148-IRS | offset position | southern peak |
| CS | | | |
| $J = 2\text{--}1$ | $-0.75 \pm 0.09$ | $-0.41 \pm 0.08$ | $-0.43 \pm 0.05$ |
| $J = 3\text{--}2$ | | | $-0.42 \pm 0.05$ |
| $HCO^+$ | | | |
| $J = 1\text{--}0$ | $-1.57 \pm 0.19$ | $-1.10 \pm 0.23$ | $-1.06 \pm 0.13$ |
| $H^{13}CO^+$ | | | |
| $J = 1\text{--}0$ | $0.32 \pm 0.04$ | $0.30 \pm 0.06$ | $0.06 \pm 0.01$ |
| HCN | | | |
| $J, F = 1, 2\text{--}0, 1$ | $-0.99 \pm 0.12$ | $-0.80 \pm 0.16$ | $-0.78 \pm 0.09$ |
| $J, F = 1, 1\text{--}0, 1$ | | $-0.66 \pm 0.14$ | $-0.72 \pm 0.09$ |
| $J, F = 1, 0\text{--}0, 1$ | $0.00 \pm 0.10$ | $-0.53 \pm 0.11$ | $-0.60 \pm 0.07$ |
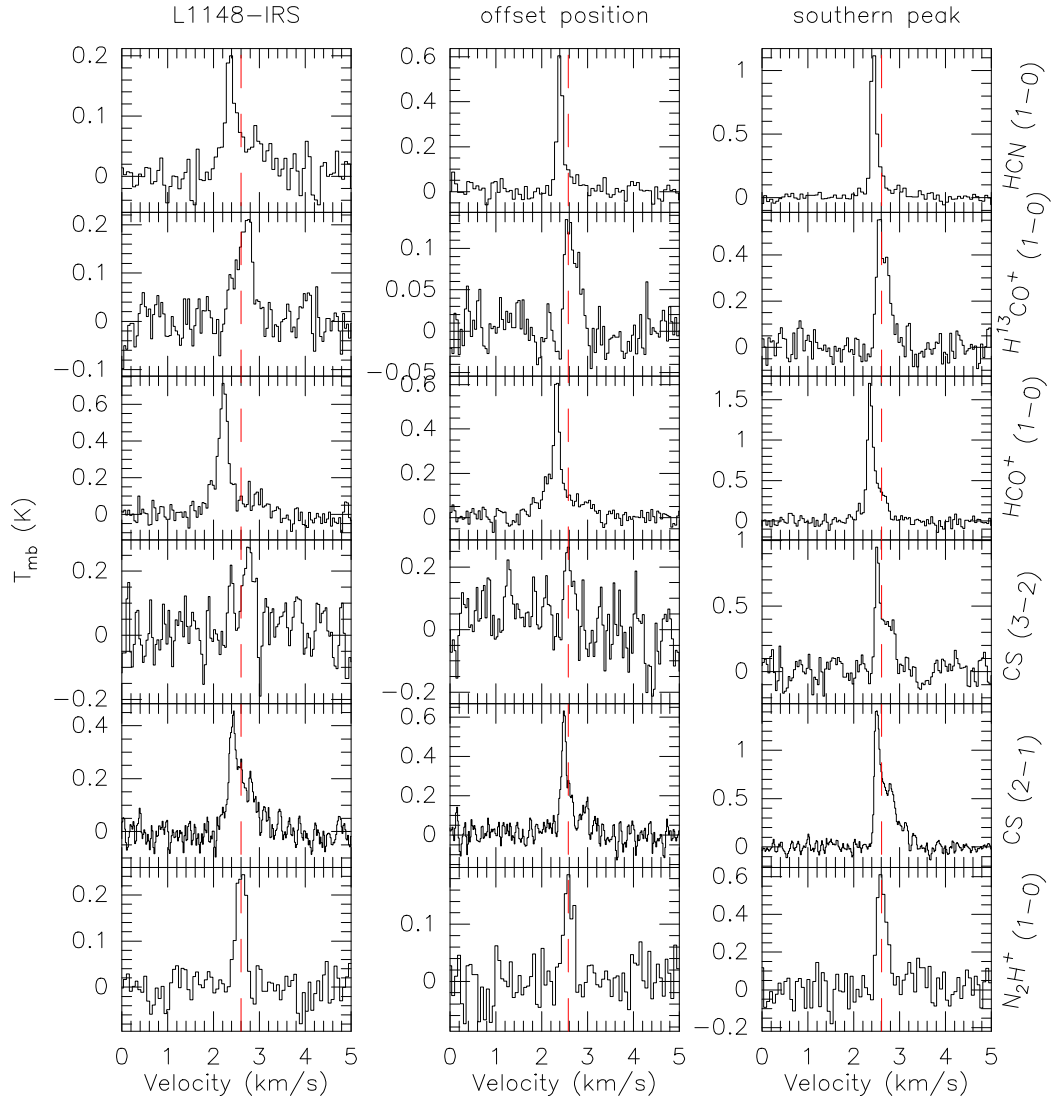
**Figure 3.15:** Spectra towards the positions defined in Table 3.3 (*left to right*) for the transitions listed in Table 3.4 (*top to bottom*; $J, F = 1, 2–0, 1$ for HCN). *Dashed lines* indicate the systemic velocity derived from the N$_2$H$^+$ ($J, F_1, F = 1, 0, 1$–$0, 1, 2$) transition. All well detected lines believed to be good tracers of infall have peaks blueshifted from the systemic velocity, indicating inward motions.
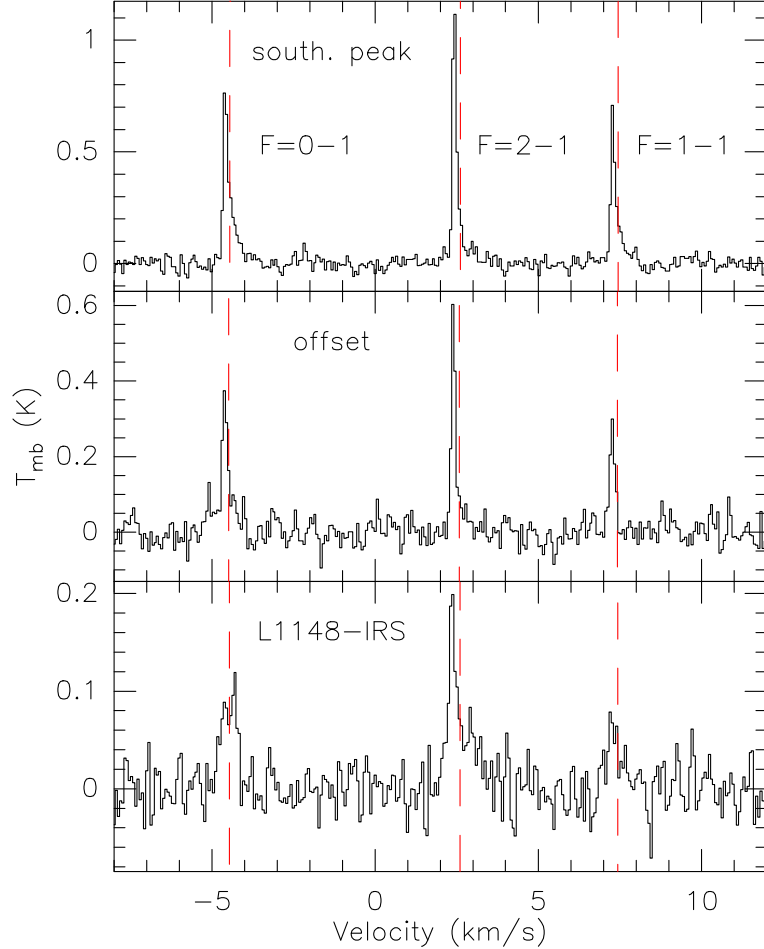
**Figure 3.16:** HCN spectra towards the positions defined in Table 3.3 (*top to bottom*). *Labels* identify the different transitions, while *dashed lines* indicate the systemic velocity of each satellite. The $F = 2$–1 and $F = 1$–1 satellites always peak at velocities lower than the systemic one, indicating inward motions. The $F = 0$–1 satellite peaks at velocities lower than the systemic one towards the southern peak and the offset position, but at about systemic position towards L1148-IRS, where it also has a linewidth exceeding the one of $N_2H^+$. As this satellite has the lowest optical depth it probes deeper layers of the core than the other both satellites. The increased linewidth thus indicates an increased linewidth in the cores' center. This could be a manifestation of mechanical energy input from L1148-IRS.

### 3.5.5.1  Observations and Results

We observed the $J = 2$–1 and 3–2 transitions of CS, and the $J = 1$–0 transitions of $HCO^+$, $H^{13}CO^+$, and HCN to study inward motions in L1148. CS was previously used by Lee et al. (1999, 2001) for such experiments. The $J = 3$–2 transition is only detected towards the southern peak of L1148, though. $HCO^+$ has extensively been used as a kinematic tracer (e.g., Walsh et al. 2005), but to our knowledge no comprehensive survey of dense cores in this molecule exists. The optically thinner $H^{13}CO$ line can be a good velocity reference, as both $HCO^+$ isotopologues are expected to trace the same medium. A survey of velocity shifts in HCN was presented by Sohn et al. (2004).

Accurate line frequencies are a prerequisite for kinematical studies of quiescent cores (Lee et al. 1999, 2001). Our choice of frequencies is summarised in Table 3.1. For the $J = 1$–0 transitions of $N_2H^+$, CS, and HCN the frequency deviations to previous work (Lee et al. 2001; Sohn et al. 2004) are $\leq 2.8$ kHz, equivalent to $\lesssim 0.01$ km s$^{-1}$, and our and their results can thus be compared.

The baseline quality is improved by FFT-filtering and subtraction of polynomials of up to 7th order. The $N_2H^+$ spectra are smoothed to 0.063 km s$^{-1}$ resolution for the analysis of the isolated satellite. Line peak velocities are derived from Gaussian fits to the data within CLASS. Up to two lines were fitted simultaneously, where needed, to obtain appropriate fits to the narrow peak and the broader base of the line. The derived line peak velocities and widths are listed in Table 3.4. Also given are the fit uncertainties. The resulting normalised velocity shifts are given in Table 3.5. Listed uncertainties only include the (dominating) contribution from uncertainties in linewidth.

### 3.5.5.2  Discussion

Figures 3.15 and 3.16 and Table 3.5 show that most lines peak at velocities blueshifted from the $N_2H^+$ reference velocity (when detected). The only exceptions are the optically thin $H^{13}CO^+$ lines and the $F = 0$–1 satellite of HCN towards L1148-IRS. Furthermore, the shifts are largest toward L1148-IRS, suggesting that this position is special within the area probed. The CS $J = 2$–1 spectra taken here also meet the criteria for strong infall candidates by Lee et al. (1999, significantly blueshifted peak in CS, blue peak stronger than red shoulder in CS, but not in $N_2H^+$). *The present data are thus indicative of infall towards L1148-IRS*, with evidence for extended inward motions across the whole region. A better spatial coverage of the region in more lines observed with high SNR is, however, required to unambiguously prove the presence of infall.

Some systematics of the observed line shifts suggest that they are indeed due to optical depth effects, as required for manifestation of kinematics in line shapes. First, the line asymmetry among the HCN satellites (in LTE the optical depth ratio for satellites of different $F$ is 1:5:3 for [0–1]:[2–1]:[1–1]) increases with optical depth towards every position. Second, several peaks have linewidth smaller ($\lesssim 0.12$ km s$^{-1}$) than even the non-thermal linewidth (i.e., with thermal broadening removed) inferred from $N_2H^+$ (even when removing optical depth broadening in HFS fits), $C^{18}O$, and CCS (for all $\geq 0.14$ km s$^{-1}$). This could be caused by absorption of the red linewing, which leaves a narrow blue linewing. Finally, although both lines trace the same gas, the optically thicker $HCO^+$ emission is significantly blueshifted from the $H^{13}CO^+$ emission. Only part of this shift, up to 0.067 km s$^{-1}$, can be due to the $H^{13}CO^+$ hyperfine structure recently confirmed by Schmid-Burgk et al. (2004).

The velocity differences observed in CS and HCN towards L1148-IRS are unusual for starless dense cores. Only 18% of those probed in CS ($J = 2$–1) by Lee et al. (1999, for the reanalysis with new velocities in Lee et al. 2001), and 40% of those probed in HCN ($J, F = 1, 2$–0, 1) by Sohn et al. (2004), have equal or smaller velocity differences in the respective tracer. The line-shifts are thus significant and hint at a nature of the L1148 core different from other ones. Furthermore, the velocity dispersion seen in HCN towards L1148-IRS tentatively increases with decreasing optical depth of the hyperfine satellites, respectively increasing geometrical depth; the $J, F = 1, 0$–0, 1 line is broad at an intensity level where no broad base is seen in the $F = 2$–1 and $F = 1$–1 lines. This is also suggested for the offset position by visual inspection of the spectra, but hard to quantify at the present noise level. If true, this trend suggests an increased velocity dispersion in the cores' center. This could be a manifestation of mechanical energy input from L1148-IRS.

In summary, the L1148-IRS position stands out in its kinematical properties among starless cores in general, and among the positions probed within L1148 in particular. However, the dominance of blueshifts in optically thick

lines across L1148 makes infall claims dubious. These blueshifts could mean that inward motions prevail on scales of several 0.1 pc. They could, however, also mean that the line asymmetries are due to unrelated foregrounds. While the present results strongly hint at inward motions towards L1148-IRS, high SNR mapping of the whole region, especially in higher level transitions insensitive to foregrounds of low density, is needed to unequivocally prove that the L1148-IRS position is indeed remarkable within L1148 and shows infall signatures in even the densest gas.

## 3.6   Discussion

Given that the internal luminosity of L1148-IRS would be unusually low for a protostar, we turn to a detailed discussion of the nature of this source in Sec. 3.6.1. This in particular includes its age and its present and final mass. As, e.g., the densities and column densities in L1148 are much lower than those believed to be required for star formation to occur, we then analyse the star formation ability of L1148 in Sec. 3.6.2, and discuss the implications of this analysis for star formation theories.

### 3.6.1   The Mass and Nature of L1148-IRS

If L1148-IRS is a protostar, it would be very interesting to derive an estimate of its mass. Two indirect mass estimation techniques have already been applied to VeLLOs. We briefly review and extend these methods before we apply them to L1148-IRS.

Age estimates for L1148-IRS are a useful constraint on mass estimates. Estimates for the duration of the protostellar class 0 and I phases, to that L1148-IRS appears to belong, are of order $10^5$ yr (see above). The observed offset of less than $10''$ between L1148-IRS and the apparent natal dust emission peak suggests an age $\lesssim 1.5 \cdot 10^5$ yr, if L1148-IRS drifts away from its birthplace with a speed of order 0.1 km s$^{-1}$ suggested by line-widths and velocity variations seen across L1148, e.g. in N$_2$H$^+$ spectra. If L1148-IRS has a protostellar nature, it must be young.

#### 3.6.1.1   Mass Estimates from Evolutionary Tracks

Masses and ages of young stellar objects can be inferred by comparing observed luminosities with the mass- and age-dependent predictions by models of the pre main sequence evolution of stars. Unfortunately, models for the evolution of stars of very low mass ($\ll 1 \, M_\odot$) suffer severely from uncertainties in the opacities and in the convective energy transport adopted for calculations (Baraffe et al. 2002). For ages $\lesssim 10^6$ yr no reliable predictions at all are possible due to uncertainties in the initial conditions (Baraffe et al. 2002), unless these are modeled in detail (Wuchterl & Tscharnuter 2003).

Models therefore need to be calibrated against observations. Recently Reiners et al. (2005) calibrated the tracks by Baraffe et al. (1998) and Chabrier et al. (2000) against observations of a low-mass binary. The luminosity predicted for the primary of mass 0.32 to 0.40 $M_\odot$ and age 3 to 7 $\cdot 10^6$ yr exceeds the observed one by a factor of up to 3. Young very low mass stars are dimmer than predicted by present models. To obtain upper limits to its mass we thus compare the luminosity of L1148-IRS with the Baraffe et al. and Chabrier et al. model luminosities after reducing these by a factor 3. For an age of $10^6$ yr, the youngest one for that the initial conditions do not matter, the observed luminosity is consistent with that predicted for a mass of $\lesssim 0.35 \, M_\odot$. As L1148-IRS is supposed to be much younger, and the luminosity increases with decreasing age (Wuchterl & Tscharnuter 2003), this comparison in summary yields a very conservative mass estimate of $\ll 0.35 \, M_\odot$.

More appropriate might be a comparison with the tracks of Wuchterl & Tscharnuter (2003). These models are believed to also hold for stars much younger than $\approx 10^6$ yr, as they model the initial conditions self-consistently. However, at present they are entirely uncalibrated. For stars of $\geq 0.1 \, M_\odot$ that are younger than $\approx 3 \cdot 10^5$ yr they predict luminosities of order $\gtrsim 0.2 \, L_\odot$. This implies a mass $< 0.1 \, M_\odot$ for L1148-IRS. The predicted effective temperatures for ages $\gtrsim 10^5$ yr are of order $10^{3.5}$ K $\approx 3000$ K, just as inferred for L1148-IRS.

### 3.6.1.2 Mass Estimates from Accretion Luminosities

The observed internal luminosity of a protostar is the sum of the luminosity inherent to the collapsed and opaque central object, e.g. from nuclear fusion and contraction, and the luminosity due to infall of matter onto the central object: $L_{int} = L_\star + L_{accr}$. For accretion onto the stellar surface

$$L_{accr} = \frac{GM_\star \dot{M}_{accr}}{R_\star} ; \qquad (3.10)$$

here $G$ is the constant of gravity, $R_\star$ and $M_\star$ are the stellar radius and mass, respectively, and $\dot{M}_{accr}$ is the accretion rate. Equation (3.10) holds independent from whether the accretion proceeds via a disk or not, as the total potential energy released when transporting matter down onto the stellar surface needs to be emitted. As $L_{int} > L_{accr}$ it is possible to derive an upper limit for the stellar mass, if the radius and accretion rate are known.

The radius is related to the internal luminosity and effective temperature by

$$R_\star = 1.2 \, R_\odot \, (L_{int}/0.1 \, L_\odot)^{1/2} \, (T_{eff}/3000 \, \mathrm{K})^{-2} , \qquad (3.11)$$

if most of the internal luminosity is emitted by the stellar surface. Substitution of this into Eq. (3.10), application of $L_{int} > L_{accr}$, and subsequent rearrangement yields

$$\begin{aligned} M_\star \quad < \quad & 0.002/\alpha_{accr} \, M_\odot \, (L_{int}/0.1 \, L_\odot)^{3/2} \, (T_{eff}/3000 \, \mathrm{K})^{-2} \\ & \cdot \left( \dot{M}_{in}/2 \cdot 10^{-6} \, M_\odot \, \mathrm{yr}^{-1} \right)^{-1} \end{aligned} \qquad (3.12)$$

as an estimate for the stellar mass. Here we have substituted $\dot{M}_{accr} = \alpha_{accr} \dot{M}_{in}$, where $\alpha_{accr}$ is the accretion efficiency. The mass infall rate from the envelope, $\dot{M}_{in}$, is normalised by the value for the collapse of a singular isothermal sphere of 10 K temperature (Shu 1977), a typical figure for infall rates.

For an accretion efficiency $\alpha_{accr} = 1$ the above discussion yields a mass of $0.002 \, M_\odot$ for L1148-IRS, given that $L_{int} \approx 0.1 \, L_\odot$ and $T_{eff} \approx 3000 \pm 1000$ K. The uncertainty in the temperature results in an uncertainty in the mass estimate of the order of a factor 2. A mass of $0.1 \, M_\odot$ would imply an accretion luminosity of order $1.4 \, L_\odot$. This exceeds the observed luminosity by more than a magnitude and for $\alpha_{accr} = 1$ we can set a very save upper mass limit of $< 0.1 \, M_\odot$ to the mass of L1148-IRS.

However, accretion efficiencies are known to be lesser than unity. Kenyon et al. (1993) find that for their sample of sources in Taurus-Auriga $\alpha_{accr} = 0.1$. They suggest that for most sources $\dot{M}_{accr} < \dot{M}_{in}$ because for most of the time the infalling mass is stored in an accretion disk; significant accretion onto the central object, then at a rate $\dot{M}_{accr} \gg \dot{M}_{in}$, occurs only when the disk becomes unstable. Stars undergoing such accretion events might have been identified in the FU Orionis variables. For this lower accretion efficiency the implied mass of L1148-IRS is $0.02 \, M_\odot$.

It could also be that accretion already ceased in L1148-IRS, rendering mass estimates from accretion luminosities irrelevant. This is suggested by the failure to detect an outflow heralding ongoing accretion. The likelihood to see a very low mass star during its main accretion phase is low, given the short timescale over that such a star accretes to reach its final mass, $M_\star^{final}$:

$$\tau_{accr} = 5 \cdot 10^4 \, \mathrm{yr} \, \left( \frac{M_\star^{final}}{0.1 \, M_\odot} \right) \left( \frac{\dot{M}_{in}}{2 \cdot 10^{-6} \, M_\odot \, \mathrm{yr}^{-1}} \right)^{-1} . \qquad (3.13)$$

However, the observed nebulosity suggests that accretion still prevails. Therefore, the above limits on the mass are likely to be of relevance.

The masses estimated on basis of the Wuchterl & Tscharnuter models are not mass estimates from accretion luminosities derived in a different parameterisation. During accretion the luminosity in these models is exceeding its minimum along the track and is thus not relevant for mass estimates.

### 3.6.1.3    The Mass and Nature of L1148-IRS

It appears very safe to adopt $\ll 0.35\,M_\odot$, as inferred from the Baraffe et al. and Chabrier et al. evolutionary tracks after recalibration by Reiners et al., as a conservative upper limit to the mass of L1148-IRS. The tracks by Wuchterl & Tscharnuter, the most appropriate ones presently available, suggest a mass $< 0.1\,M_\odot$. Given that for $0.1\,M_\odot$ the predicted luminosity exceeds the one observed for L1148-IRS by at least a factor 2 this mass estimate appears to be save too, even when taking the lack of a calibration of these tracks into account. The estimates based on accretion luminosities are of a more uncertain nature. Given the uncertainties in the relevant parameters, it appears to be bold to set an upper mass limit of $\lesssim 0.02\,M_\odot$ to the mass of L1148-IRS, as formally implied for reasonable accretion efficiencies of 0.1 or higher. However, if accretion onto L1148-IRS bears similarities to the one observed in other protostars, then only a mass $< 0.1\,M_\odot$ appears to be consistent with observations.

The final mass might be higher though, as still matter from the surrounding core can be accreted (see also André et al. 1999 and Young et al. 2004). Given the estimated duration of $10^5$ yr for the main protostellar accretion phase (see above), and that the radius of the infalling envelope increases with about the sound speed (Shu 1977), all mater closer than $\approx 4200$ AU to a forming star can be accreted. The observed dust emission of L1148 suggests $M_{4200\mathrm{AU}} = 0.15\,M_\odot$. A mass of this order could in future be accreted onto L1148-IRS.

We thus conclude that the presently available models, combined with our present knowledge of protostellar evolution, suggest a present mass for L1148-IRS that is slightly above the sub-stellar mass limit of $0.08\,M_\odot$, or even below. Up to $\approx 0.15\,M_\odot$ could in future be additionally accreted by L1148-IRS. This yields an upper limit to the final mass of order $\lesssim 0.25\,M_\odot$. If accretion ceases earlier than after $10^5$ yr, proceeds with lesser efficiency as assumed above, or is governed by a combination of both, then the final mass can be as low as the present one.

The uncertainties in the estimate for the final mass would not allow to ultimately infer the nature of L1148-IRS. It could be an object of sub-stellar final mass during or after the end of the main accretion phase. It could also be of a final mass exceeding the sub-stellar limit and then be accreting and younger than a few $10^4$ yr; given the low implied present mass L1148-IRS would then be one of the youngest protostars known. In these respects L1148-IRS is similar to the other well-studied VeLLOs, for which the final mass is unclear while the present mass is supposedly sub-stellar (André et al. 1999; Young et al. 2004; Bourke et al. 2005; Huard et al. 2006, Bourke at al., in prep., Dunham et al., in prep.).

However, L1148-IRS is different from these in that it is expected to definitely have a significantly sub-solar final mass. Except for L1148-IRS, which has $M_{4200\mathrm{AU}} = 0.15\,M_\odot$, all VeLLOs covered by MAMBO (see our c2d MAMBO survey and André et al. 1999) have $M_{4200\mathrm{AU}} > 0.3\,M_\odot$ and thus possible final masses above this. The low upper limit to the final mass makes L1148-IRS unique among the well-studied VeLLOs. Therefore, L1148-IRS is a prime target for studies of the observationally largely unexplored formation of very low mass stars.

## 3.6.2    Implications for Star Formation Theories

### 3.6.2.1    The Physics of Star Formation in L1148

The above discussion suggests that in the dust emission peak near L1148-IRS a low mass star of presently $\lesssim 0.1\,M_\odot$ aggregates via gravitational collapse from a mass of order $0.3\,M_\odot$, the mass encircled by the radius at 50% peak dust intensity inferred in Sec. 3.5.1. However, the overall properties of the surrounding filament on large scales are not consistent with those of unstable equilibria with a mass equal to the observed $3.8\,M_\odot$. Such are, e.g., characterised by masses within 4200 AU exceeding $0.31\,M_\odot$ (Kauffmann & Bertoldi, in prep.). This is much larger than the $0.15\,M_\odot$ observed. Therefore, only a small fraction of mass $< 0.5\,M_\odot$ located within the larger filament appears to be unstable and involved in the formation of L1148-IRS.

In this respect the dust emission peak appears to have decoupled from the filament; the latter only sets the boundary conditions for the matter concentrated in the dust emission peak. Some process appears to have driven a fraction of the northwestern filament of L1148 into gravitational instability without doing the same with the bulk of the filament. Such an evolution appears hardly consistent with what is expected for quasistatic equilibria.

These are predicted to evolve by gradually increasing their center-to-surface density contrast until they become gravitationally unstable as a whole (Shu 1977).

A pressure within L1148 higher than observed is required to render the dust emission peak gravitationally unstable. An isothermal equilibrium of mass $M$ and gas temperature $T_g$ only becomes unstable to collapse if subjected to an external pressure exceeding the critical value,

$$P_{\text{ext,cr}}/k_B = 1.26 \cdot 10^5 \text{ K cm}^{-3} \, (T_g/10 \text{ K})^4 \, (M/M_\odot)^{-2} \, . \qquad (3.14)$$

Additional turbulent or magnetic pressure, or a combination of both, would increase this figure (Kauffmann & Bertoldi). The formation of the unstable $\lesssim 0.5 \, M_\odot$ column density peak near L1148-IRS thus requires an external pressure $\gtrsim 5 \cdot 10^5 \text{ K cm}^{-3}$ if the gas temperature is 10 K. It would reduce by a factor 4 in the unlikely case of a gas temperature as low as 7 K. This pressure exceeds the value of about 1 to $2 \cdot 10^5 \text{ K cm}^{-3}$ implied by our density estimates (Sec. 3.5.1) for an estimated gas temperature of 10 K.

The above two problems to explain the structure and evolution of the northwestern filament of L1148 in the framework of quasistatic models — i.e., the apparent decoupling of the dust emission peak from the filament, and pressures in L1148 too low to trigger collapse — suggest that L1148 did or does evolve non-quasistatically. Turbulence is a likely cause for such evolution. The presence of a non-thermal velocity dispersion, several velocity components, and velocity gradients in our CCS, $C^{18}O$, and $N_2H^+$ spectra indicates the presence of chaotic bulk motions usually referred to as "turbulence".

However, even in non-quasistatic models it is not possible to create gravitationally unstable equilibria of mass $\approx 0.1 \, M_\odot$ in cores like L1148, as this would require an external pressure of order $10^7 \text{ K cm}^{-3}$ or equivalent forces in non-quasistatic models. The latter could in principle be caused within dense cores by the collision of gas flows, but, as the observed non-thermal linewidths and spatial changes in the velocity in L1148 are below the thermal velocity dispersion of $0.2 \text{ km s}^{-1}$ for the mean particle and 10 K gas temperature, these gas flow collisions will not raise the pressure much above the thermal pressure. Therefore, the minimum mass of an equilibrium required for collapse to be triggered is $\gg 0.1 \, M_\odot$. Though L1148-IRS presently appears to have a mass $\lesssim 0.1 \, M_\odot$, it can only attain a final mass of the same order if processes *after* the formation of the unstable equilibrium forming L1148-IRS prevent the accretion of most of the equilibrium matter onto the forming star.

### 3.6.2.2 Diversity in the Initial Conditions of Star Formation

Crapsi et al. (2005a) suggested criteria for properties of starless cores just before the onset of star formation. According to them, such cores must be exceptionally dense and chemically evolved, e.g., they should show high degrees of deuteration and depletion. This reflects our present theoretical understanding of the structure and chemistry of dense cores (e.g., Shu 1977, Lee et al. 2004b). Table 3.6 shows that several VeLLOs meet only a fraction of these criteria. A protostellar core L1148 would, e.g., miss 4 out of the 6 criteria which we can evaluate with our data. The suggested criteria select just a fraction of the cores with actual star formation.

In this respect some VeLLOs appear to form in environments that were never expected to form stars (see also Crapsi et al. 2005b). Since the Crapsi et al. criteria were put forward on the basis of single-dish observations, they may simply be insufficient to probe the VeLLO natal dense cores on scales relevant for the star formation process. Detailed studies of the L1014 and L1148 VeLLO natal cores by Huard et al. (2006) and us (Sec. 3.5.1) support this picture. They do indeed reveal the presence of dense and supposedly gravitationally unstable column density peaks on scales $\lesssim 40''$ while both cores miss the $N_2H^+$ column density criterion by Crapsi et al. (2005a).

The only partial success of the Crapsi et al. criteria suggests that the initial conditions for star formation are more diverse than reflected by these criteria; also cores very different from prototypical "evolved" cores like L1544 (e.g., Tafalla et al. 1998 Caselli et al. 2002b,c) and L1521F (Crapsi et al. 2004), two cores used by Crapsi et al. to "tune" their criteria, can produce stars. It might, however, be that these criteria indeed do select most of the cores capable of forming stars and therefore reflect their average properties.

The broad spectrum in the physical properties of cores near the onset of star formation indicated by the partial failure of the Crapsi et al. criteria implies that there is no common evolutionary path of dense cores towards star

**Table 3.6:** Compilation of the properties of VeLLOs and their natal cores. The dense core properties are compared to the criteria for "evolved" cores by Crapsi et al. (2005a) after conversion of the limiting density to our choice of dust emission properties. A plus indicates that a criterion is met, a minus that it is not, a question mark that the data is insufficient to decide. In deviation to Crapsi et al. inward motions are either inferred from the analysis of line shifts (L1521F, L1014, and L1148), or from detailed modelling of line shapes (IRAM04191). For all sources the uncertainty in the internal luminosity is of order $\pm 0.03\,L_{\odot}$. The VeLLOs in L1014 and in L1148 have a physical and chemical state very different from the one of "evolved" cores identified by Crapsi et al. As star formation is ongoing in all cores listed the initial conditions for stars to form appear to be very diverse.

| Property | L1521F | IRAM04191 | L1014 | L1148 |
|---|---|---|---|---|
| *protostar properties:* | | | | |
| prominent outflow | − | + | − | − |
| $L_{\mathrm{int}}/L_{\odot}$ | $\approx 0.04$ | $\approx 0.07$ | $\approx 0.09$ | $\approx 0.08$ |
| $M_{4200\ \mathrm{AU}}/M_{\odot}$ | 0.87 | 0.60 | 0.36 | 0.15 |
| *dense core properties:* | | | | |
| $N(\mathrm{N_2D^+})$ $> 1.0 \cdot 10^{12}$ cm$^{-2}$ | + | ? | − | − |
| $N(\mathrm{N_2H^+})$ $> 8.5 \cdot 10^{12}$ cm$^{-2}$ | + | + | − | − |
| $N(\mathrm{N_2D^+})/N(\mathrm{N_2H^+})$ $\geq 0.1$ | + | ? | + | ? |
| $f_{\mathrm{d}}(\mathrm{CO}) > 10$ | + | ? | − | − |
| $n(\mathrm{H_2})$ $> 2.5 \cdot 10^5$ cm$^{-3}$ | + | + | − | − |
| $\Delta v(\mathrm{N_2H^+})$ $> 0.25$ km s$^{-1}$ | + | + | + | ? |
| inward motions | + | + | − | + |
| $r_{70\%} < 4\,800$ AU | + | + | + | + |

References: Data are from Lee et al. (1999); André et al. (1999); Motte & André (2001); Belloche et al. (2002); Young et al. (2004); Crapsi et al. (2005a,b), Bourke et al. (in prep.), Dunham et al. (in prep.), our c2d MAMBO survey (Kauffmann et al., in prep.), and this work.

formation. This also hints that additional parameters not yet considered might control the star formation ability of a dense core. Details of the velocity field, which might control the star formation in L1148, are one candidate for such parameters.

## 3.7  Summary

We have presented a detailed study of the protostellar and environmental properties of the candidate VeLLO L1148-IRS. It manifests as an unusually bright Spitzer source (59 mJy and 271 mJy at 24 $\mu$m and 70 $\mu$m wavelengths, respectively) that is associated with a dust emission peak. The physical association between L1148-IRS and the L1148 dense core is suggested by the low probability for a chance alignment between a background source and a dense core seen in several tracers of dense gas (continuum emission from dust and line emission from, e.g., $N_2H^+$ and $C^{18}O$; Secs. 3.3.1, 3.5.3, 3.5.4) which exhibits blue line asymmetries that are unusual for starless cores and apparently increase towards L1148-IRS (Sec. 3.5.5). In case of an association with L1148, L1148-IRS must be a protostar deeply embedded in the dense core. This is indicated by an extinction of order 30 mag required to explain the flux density ratio between the Spitzer IRAC and MIPS bands (Sec. 3.4) and nebulosity on spatial scales requiring scattering in a dense and extended envelope (radius $\gtrsim$ 1000 AU; Sec. 3.3.3). The presence of an embedded protostar of low luminosity is thus the most likely explanation for the observations. However, this evidence remains circumstantial.

If L1148-IRS is of protostellar nature, then its stellar properties are unusual for a protostar. The luminosity would be of order $\lesssim 0.1\,L_\odot$ (Secs. 3.3.2, 3.4). Because of its embedded nature L1148-IRS would thus qualify as a Very Low Luminosity Object (VeLLO). L1148-IRS does not drive a prominent outflow detectable by single-dish telescopes (Sec. 3.3.4), suggestive of a low accretion rate. Only one embedded protostar without a prominent outflow is presently studied well (i.e., L1014-IRS; Bourke et al. 2005). The present and final mass of L1148-IRS is estimated to be of order $\lesssim 0.1\,M_\odot$ and $\lesssim 0.25\,M_\odot$, respectively (Sec. 3.6.1). L1148-IRS would thus be the first VeLLO to definitely have significantly sub-solar final mass.

Also, the environmental properties of L1148-IRS would be very different from those of "evolved" dense cores believed to represent cores just before the onset of star formation (Sec. 3.6.2.2). The dense core properties of L1148 do not challenge the protostellar nature of L1148-IRS, given the detection of a dust emission intensity profile in L1148 that is consistent with those of gravitationally unstable equilibria (Sec. 3.5.1). However, active star formation in L1148 appears not to be consistent with the dense core evolution predicted by quasistatic models (Sec. 3.6.2.1). The diversity in the properties of VeLLO natal cores suggests that stars can form in environments with properties not well reflected by present criteria for "evolved" cores. This hints that additional parameters not considered yet might control the star formation ability of a dense core (Sec. 3.6.2.2).

# Chapter 4

# Summary and Outlook

This chapter summarises work done for my thesis and the scientific conclusions reached during its course. I start with summaries of finished projects that are not suited to be presented here in detail (Sec. 4.1). This section completes the discussion of the other finished research projects presented in Chapters 2 and 3. It is followed by an outlook on projects that I shall pursue in future that is based on unfinished projects (Sec. 4.2). I conclude with an overall summary of the thesis.

## 4.1 Finished Projects not Detailed in this Thesis

One project carried out during the course of my thesis led to too few results to be suited for a separate thesis chapter or publication. In one other project I carried out only a fraction of the work needed to lead this project to completion. I here summarise these efforts in order to give a complete overview of my thesis project.

### 4.1.1 A Dust Emission Survey of the Chamaeleon II Cloud

In fall of 2004 I started to reduce and analyse a dust emission survey of the Chamaeleon II molecular cloud, located at a distance of 180 pc, which had already been acquired in 2001 using the SIMBA bolometer array operated at the SEST. This survey was designed to complement the c2d Spitzer observations of this cloud. Due to the exceptionally bad data quality of the raw data this project was, however, not suited to be published as a separate paper. It thus became part of a Spitzer study of this molecular cloud (Young et al. 2005).

Our map of the Chamaeleon II complex is shown in Fig. 4.1. Most of the surveyed area is devoid of significant emission. Dust emission is only detected towards the regions associated with the IRAS sources 12496−7650 and 12553−7651. The total mass detected is of order $70\,M_\odot$, where previous $^{12}$CO molecular line surveys derived a total mass of order $1\,250\,M_\odot$ for the whole cloud (Boulanger et al. 1998). A low dust-to-total mass recovery fraction of only a few percent is not unusual for such dust emission surveys (e.g., Enoch et al. 2006). Most of the dust emission is either too faint to be detected or so extended that it is filtered away by present bolometer observing techniques. However, given the sensitivity of our observations, still only a small amount of matter in Chamaeleon II appears to be at $H_2$ column densities exceeding $10^{22}$ cm$^{-2}$. This might be the cause for the low star formation efficiency in this cloud.

### 4.1.2 Dust Emission from TMC-1C

In summer of 2004 I began a collaboration with Scott Schnee (Harvard-Smithsonian Center for Astrophysics). He had just finished a multi-wavelength dust emission study of TMC-1C (Schnee & Goodman 2005) when I met him on a conference. We came up with the idea to combine his SCUBA observations acquired at 450 and
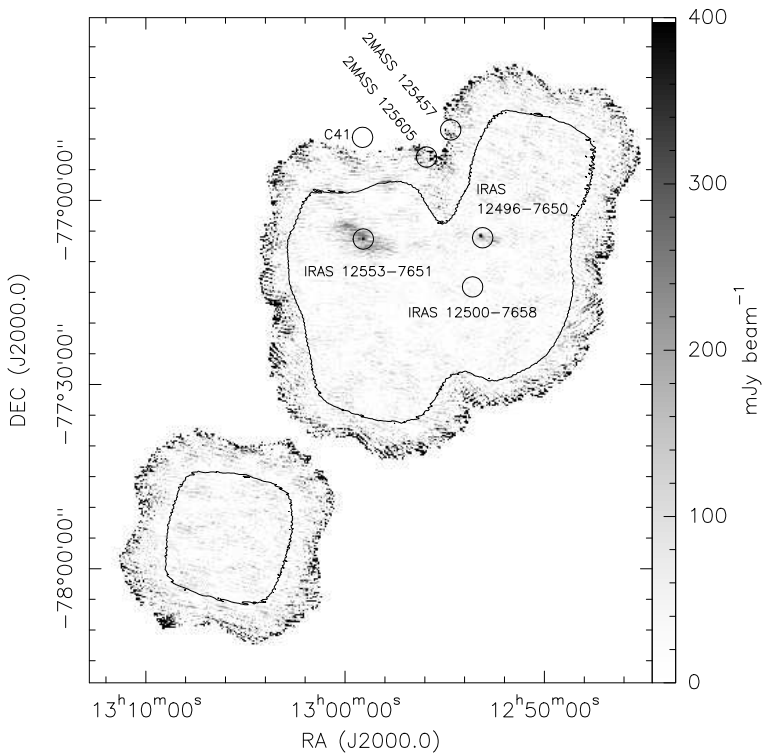
**Figure 4.1:** SIMBA 1.2 mm dust emission map of the Chamaeleon II molecular cloud complex. The *contour* delimits the area mapped with an r.m.s. noise level below 70 mJy per 24″ beam. The *circles* are centered on the positions of the Spitzer MIPS sources discussed by (Young et al. 2005). Emission at a significant level is only detected in the regions associated with IRAS 12496 and IRAS 12553.

850 $\mu$m wavelength with our MAMBO maps taken at 1 200 $\mu$m wavelength. The plan was to derive reliable dust temperature and spectral index maps for the TMC-1C dense core by fitting the spectral energy distributions at each point in the maps with modified blackbody emission spectra. This has lead to a paper soon to be published in the Astrophysical Journal (see also Schnee & Kauffmann 2005).

While Scott performed the actual calculations, I contributed reduced MAMBO data and in particular in-depth knowledge on artifacts affecting bolometer maps to this project. My role in this study thus was only a minor one, and I can not claim this to be a part of my thesis work; this work is listed here for the sake of completeness. Our study reveals the dust temperature in this particular dense core to be of order 10 K, with temperatures as low as 7 K in its densest parts.

## 4.2 Outlook: Ongoing and Upcoming Projects

There is also a set of ongoing projects that can not be presented here in detail. In addition some of my past and present work will lead to new research initiatives, which now start to take shape. This present and future research is outlined below.

### 4.2.1 A systematic Molecular Line Screening of c2d MAMBO Cores

In the winter of 2004/05 we used the IRAM 30m-telescope to screen the molecular line emission of several dense cores covered by the c2d MAMBO survey. The aim was to complement our MAMBO dust emission observations with information on the velocity structure and chemical state of the dense cores. This was suggested by the lack of appropriate emission line data for many cores covered by the c2d MAMBO survey.

We finally acquired usable data towards 22 positions in 17 dense cores. This survey has so far not been exploited for its original purpose, i.e., to create a comprehensive database allowing to put dust emission properties of dense cores into context with their line emission properties. This is yet a project to be realised soon (Sec. 4.2.6). We did, however, use the survey to identify a couple of dense cores with unusual chemical properties, which are further described in Secs. 4.2.2 and 4.2.3.

### 4.2.2 The Chemically Unevolved Core L1521B-2: Clues on the Formation of Dense Cores

Among the starless cores, it is interesting to understand those that are chemically least evolved, and thus represent the earliest phases of core formation. Chemically unevolved cores show a high abundance of carbon bearing molecules such as CO, CS, and CCS — that freeze out on dust grains with time — and a low abundance of "late-time" molecules such as $N_2H^+$ and $NH_3$ — that form only slowly with time. Recently Tafalla & Santiago (2004) showed that the core L1521E has a low CO depletion and is remarkably deficient in $N_2H^+$. This suggests that the gas here is chemically pristine.

We have identified a starless core with properties similar to those of L1521E. It was identified as such during the systematic screening of our sample in pointed line observations outlined in Sec. 4.2.1. The $C^{18}O$ (2-1) to $N_2H^+$ (1-0) intensity ratio $\geq 3.1$ at $3\sigma$ for L1521B-2 is exceptionally large (Fig. 4.2); most other sources in our sample of 16 cores have corresponding intensity ratios < 1. Clearly cores like L1521B-2 and L1521E only represent a small fraction of the known core population (10% or so, Fig. 4.2). Indeed $N_2H^+$ (1-0) was initially not reliably detected in L1521B-2. This suggests a high CO to $N_2H^+$ abundance ratio, indicative of an unevolved core. In this respect, only L1521E (intensity ratio 4.5) is comparable to L1521B-2.

In summer of 2005 we mapped the L1521B-2 dense core in several CO isotopologues in order to be able to derive the CO and $N_2H^+$ abundances across the core. We will in future use this data to carry out a detailed line emission study including a full treatment of line excitation and radiative transfer in molecular lines. This part of the project will be carried out in close collaboration with Mario Tafalla (Observatorio Astronomico Nacional, Madrid).
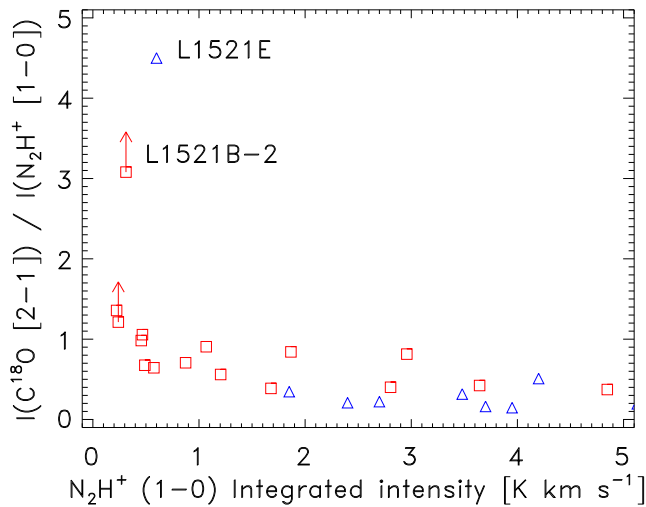
**Figure 4.2:** The $C^{18}O$ (2-1) to $N_2H^+$ (1-0) intensity ratio for starless cores in our c2d MAMBO sample (*squares*) and those taken from published work (*triangles*). As CO depletes onto dust and the $N_2H^+$ abundance increases with time, high intensity ratios are indicative of chemically unevolved cores. Most cores have an intensity ratio ≤ 1, and two sources have ratios between 1 and 1.5. The cores L1521B-2 (our work) and L1521E (Tafalla & Santiago 2004) are thus very exceptional.

### 4.2.3   The Chemically Evolved Core B18-1: Late Stages of Dense Core Evolution

The core B18-1 stands out among the starless cores in the c2d MAMBO survey given its high peak column density. It furthermore shows substructure within the dust emission peak that I initially thought could be disentangled into two close, but separated, dense cores. I proposed to test this scenario by trying to separate these hypothetical cores in velocity chanel maps taken with the IRAM 30m-telescope. This endeavour failed, but the data acquired revealed that B18-1 has a velocity structure unusual for dense molecular cores, and that B18-1 is strongly chemically evolved.

As shown in Fig. 4.3 the $C^{18}O$ (2-1) and the $N_2H^+$ spectra along a cut through the dust emission peak in B18-1 have a very simple velocity structure; there appear to be two or three velocity components at velocities between 5.7 and 5.9 km s$^{-1}$ that overlap in velocity space. The DCO$^+$ (2-1) line, however, has a much more complex structure. The line peaks at velocities between 5.6 and 6.2 km s$^{-1}$, with the peak intensities at the boundaries of this velocity range. Differences in the line shapes of optically thin (i.e., $C^{18}O$ and the "isolated" $N_2H^+$ line in our case) and optically thick lines (DCO$^+$) are not unusual. They are, e.g., systematically used to find cores with inward motions (e.g., Lee et al. 1999, 2001, 2004a) or rotation (Belloche et al. 2002). In these cases differences in line velocities do, however, have radial (for inward notions) or linear trends (for rotation) across cores, with about symmetry with respect to the column density peak. This is not the case in B18-1. DCO$^+$ mapping observations actually suggest that one DCO$^+$ velocity component might be associated with the dust emission peak B18-1 P3 revealed by the c2d MAMBO survey (see Chapter 2). The nature of the velocity structure of B18-1 is presently a riddle.

Observations with the IRAM 30m-telescope and at Effelsberg reveal that B18-1 is also a chemically unusual core. We estimate the deuterium fractionation in the $N_2H^+$ molecule to be 23%, implying that B18-1 is strongly chemically evolved. Furthermore the peak $NH_3$ line temperature in the (1, 1) hyperfine transition is 7 K in the main beam brightness scale, indicating an $NH_3$ column density of order $2.6 \cdot 10^{15}$. Only very few dense cores have such high column densities (Jijina et al. 1999).

In summary B18-1 is a prime target for future studies of evolved cores and research on dense core chemistry. B18-1 might once be regarded as a prototypical evolved core like L1544, once its nature is better understood.
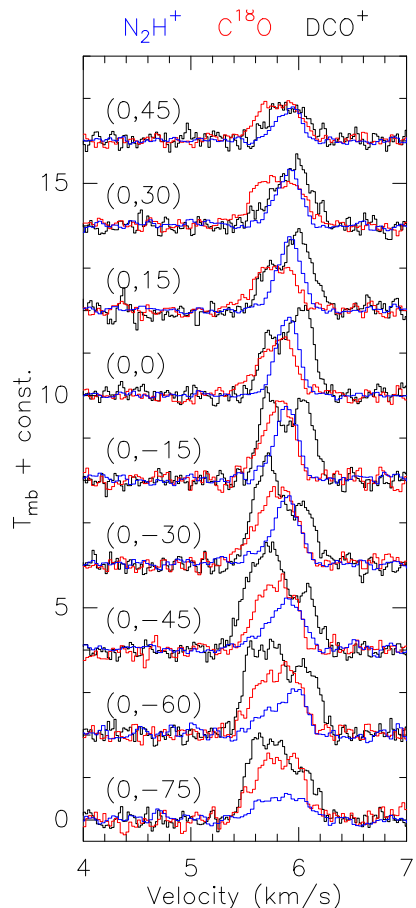
**Figure 4.3:** Spectral lines along a cut through the B18-1 dense core. The *bracketed numbers* give the offset from the dust emission peak B18-1 P3 (see Chapter 2) in right ascension and declination. The *color coding* is used to distinguish different molecules. The transitions shown are the "isolated" satellite of the $N_2H^+$ (1-0) transition, the $C^{18}O$ (2-1) line, and the $DCO^+$ (2-1) line. The velocity structure of the $DCO^+$ line is much more complex than the one of the other two transitions.
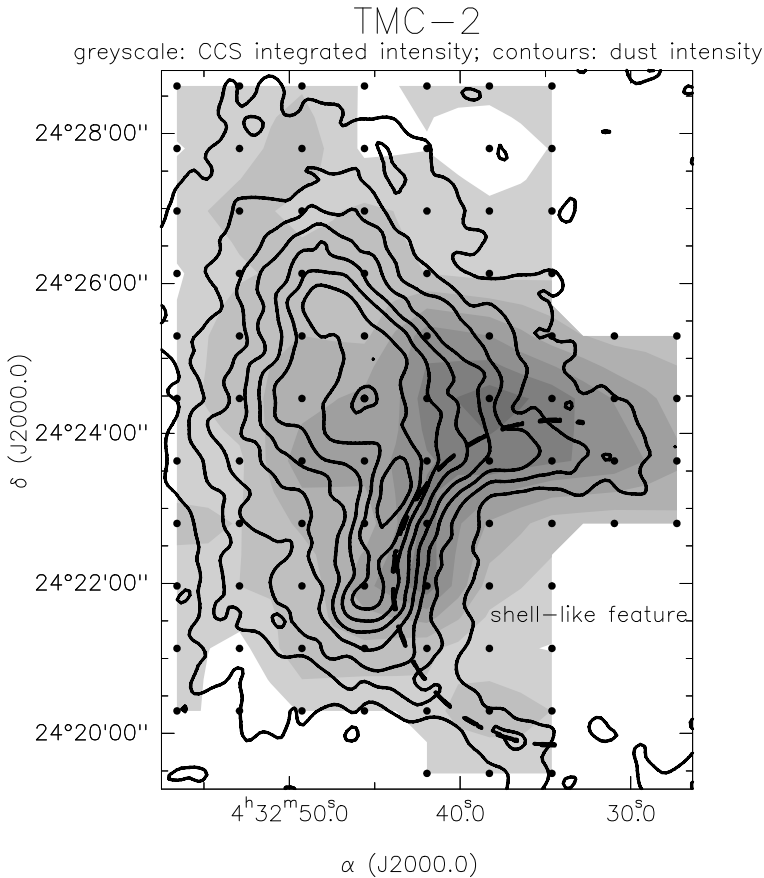
**Figure 4.4:** CCS integrated intensity map (*greyscale*) with MAMBO dust emission intensity *contours* overlayed. *Dots* indicate the positions sampled by the 40″ Effelsberg beam. The *dashed line* indicates the position of the shell-like dust emission feature with that the CCS emission peak appears to be associated.

### 4.2.4   A CCS Mapping Survey of c2d MAMBO Cores

In spring of 2005 I started a mapping survey of several c2d MAMBO cores in the $2_1$-$1_0$ transition of CCS. I used the Effelsberg telescope. I in parallel acquired data on $NH_3$ in its (1, 1) and (2, 2) hyperfine transitions, and on $HC_3N$ in its (2-1) transition towards selected positions. The main purpose of this project was to systematically probe the evolutionary state of our c2d MAMBO cores by comparison of CCS and $NH_3$ column densities (e.g., Suzuki et al. 1992). We also planned to use our $NH_3$ observations to derive the gas temperatures prevailing in these cores.

Part of the $NH_3$ data was finally used to stimulate further research on B18-1 (Sec. 4.2.3), while a fraction of the CCS data is used in the study of L1148 (Sec. 3.5.2). There is, however, still much unexploited potential in these observations. Figure 4.4 compares the spatial distribution of CCS line and dust continuum emission. Both tracers do not correlate well. It is, however, surprising that the CCS emission comes predominantly from a part of the dense core of rather low dust emission intensity. Furthermore, the CCS emitting structure has a shell-like appearance in dust emission, suggesting that the dense core somehow interacts with its surroundings. If this is true the elevated intensity of the CCS emission in this region of the core might be related to this interaction. It would be very interesting to establish such an interaction between a dense core and its surroundings, as this would be the first such case known.

### 4.2.5   Molecular Line Studies of Very Low Luminosity Objects

I am leading studies using molecular line emission to probe the state of some candidate VeLLOs. This includes searches for their outflows in CO lines, research on their chemistry by studying the deuterium fractionation in $N_2H^+$ and depletion in CO, and searches for inward motions in VeLLO natal cores. The part of this project executed at the IRAM 30m-telescope suffered from technical problems during the past semester. It has so far not yielded many results.

Still ongoing is a search for a small-scale outflow from L1148-IRS. In Sec. 3.3.4 I demonstrated that L1148-IRS does not drive a prominent outflow that than be detected by single-dish telescopes. This does, however, not exclude the existence of a low velocity ($\lesssim 2$ km s$^{-1}$) small-scale outflow like the 3″ flow detected towards the VeLLO L1014-IRS (Bourke et al. 2005). The detection of such an outflow at the systemic velocity of L1148 would unambiguously prove that L1148-IRS is indeed physically associated with the L1148 dense core. In that case L1148 would probably become the most extreme star-forming dense core known; no other core with ongoing star formation has densities and column densities as low as those observed for L1148 (Sec. 3.5.1).

This systematic study will once become a crucial element in gauging the state of VeLLO natal cores. No other study has so far been launched to study their properties in a homogenous fashion for a large sample.

### 4.2.6   c2d Core Synthesis Papers

Several c2d dense core surveys in dust continuum and molecular line emission are presently being completed. Each survey in itself brings new insights to star formation physics. However, joint analysis of these surveys will yield insights not possible to derive when analysing each dataset single. To provide such joint analysis is the subject of the future c2d "synthesis papers". It is likely that those for the c2d dense core sample will involve me to some extent, possibly in a leading position.

In particular, it is desirable to combine the c2d bolometer dust emission surveys listed in Table 2.1 in order to derive spectral energy distributions for the individual dense cores. This would allow to infer their dust temperature. In some cases such data might also be complemented by Spitzer observations at 160 $\mu$m. Furthermore the information on the mass distribution of the dense cores should be combined with our knowledge of their velocity fields. This would in particular allow to gauge the turbulent pressure prevailing in these. Such information would constrain the turbulent-to-thermal pressure ratio that at present is a free parameter in the models of core structure and stability outlined in Sec. 2.6.3.1, and would thereby influence the discussion of necessary conditions for active star formation (Sec. 2.6.3.2). For these discussions it is also desirable to combine information on inward motions in the cores with data on their mass distribution: one would expect that gravitationally unstable cores feature contraction motions.

## 4.3   Summary: Thesis Results in broad Context

This thesis summarises the results from an extensive thermal dust continuum emission survey of nearby ($\leq 500$ pc) dense molecular cores with and without ongoing star formation, the c2d MAMBO survey, and from a focused study of a remarkably faint ($\approx 0.1\ L_\odot$) source (L1148-IRS) apparently associated with one of the dense cores. The c2d MAMBO survey has a significant impact on our understanding of how stars form in dense molecular cores. The study of L1148-IRS is to be seen as one element on our way to understand VeLLOs.

The necessary conditions for active star formation to be possible derived in Sec. 2.6.3.2 can turn out to be one key element for a comprehensive understanding of star formation. The properties involved are easily calculated from models of star-forming cores. This permits a direct comparison of models and observations. At present, such analysis often relies on molecular lines, which are much more difficult to interpret (Sec. 1.2.2). The criteria might also turn out to be useful to identify interesting sources in the widefield dust emission surveys at APEX and JCMT. They are one step toward a simple and physical classification scheme of starless dense cores, which is presently lacking.

The constraints on protostar properties discussed in Sec. 2.6.4 are a contribution to the general understanding of protostellar evolution. Combined with many other datasets they are likely to help our understanding of the relation between the age, spectrum, and envelope mass during the embedded phase of star formation. The constraints on the steepness of the column density profiles of VeLLO natal cores (Sec. 2.6.5) does have an immediate impact on this research field. One can, e.g., search the APEX and JCMT dust emission surveys for candidate VeLLO cores by looking for cores with steep column density profiles. The steepness also indicates that some VeLLO cores are more evolved than though, which might put constraints on their formation.

The study of L1148-IRS showed that the properties of this source are consistent with those expected for a protostar (Chapter 3). However, it was not possible to conclusively prove the protostellar nature of L1148-IRS, as no outflow or clear bipolar nebulosity was found. In this sense the study presented here is only a step towards an understanding of L1148-IRS. I could, however, demonstrate that research on such extreme VeLLOs is rewarding. If L1148-IRS is indeed a VeLLO, this would have significant consequences for our understanding of the evolution of dense cores. The formation of a star in L1148 can not be understood in the framework of quasistatic evolution. Thus, in at least some cores non-quasistatic evolution would need to play a significant role (Sec. 3.6.2).

There are obvious extensions of the work presented here. A selection of some projects that have already been started are listed in Sec. 4.2. The research presented in this thesis is the basis for most of these.

# Appendix A

# Dust Emission Properties

This appendix summarises formulas to convert the observed flux density of dust emission into column densities and masses. These are evaluated for the standard assumptions for dust properties made by the c2d collaboration. The discussion presented here is intended to serve as a future reference for the c2d project.

## A.1 Molecular Weight

As one usually wishes to express column densities in terms of particles per area, the molecular weight needs to be introduced into the equations. The molecular weight per hydrogen molecule, $\mu_{H_2}$, is defined via $\mu_{H_2} m_H \mathcal{N}(H_2) = \mathcal{M}$; here $\mathcal{M}$ is the total mass contained in a volume with $\mathcal{N}(H_2)$ hydrogen molecules, and $m_H$ is the H-atom mass. It can be calculated from cosmic abundance ratios. For hydrogen, helium, and metals the mass ratios are $\mathcal{M}(H)/\mathcal{M} \approx 0.71$, $\mathcal{M}(He)/\mathcal{M} \approx 0.27$, and $\mathcal{M}(Z)/\mathcal{M} \approx 0.02$, respectively, where $\mathcal{M} = \mathcal{M}(H) + \mathcal{M}(He) + \mathcal{M}(Z)$ (Cox 2000). As $\mathcal{N}(H) = 2\mathcal{N}(H_2)$, $\mathcal{M}(H) = m_H \mathcal{N}(H)$,

$$\mu_{H_2} = \frac{\mathcal{M}}{m_H \mathcal{N}(H_2)} = \frac{2\mathcal{M}}{m_H \mathcal{N}(H)} = \frac{2\mathcal{M}}{\mathcal{M}(H)} \approx 2.8 \,. \tag{A.1}$$

Note the difference to the mean molecular weight per free particle, $\mu_p$, defined via $\mu_p m_H \mathcal{N} = \mathcal{M}$, where $\mathcal{N} \approx \mathcal{N}(H_2) + \mathcal{N}(He)$ for gas with all H in molecules. As the helium contribution is dominated by $^4$He, and each $H_2$ molecule has a weight of two hydrogen atoms, $\mathcal{N}(H_2) = \mathcal{M}(H)/(2m_H)$ and $\mathcal{N}(He) = \mathcal{M}(He)/(4m_H)$. Thus

$$\mu_p = \frac{\mathcal{M}}{m_H[\mathcal{N}(H_2) + \mathcal{N}(He)]} \tag{A.2}$$

$$= \frac{\mathcal{M}}{m_H[\mathcal{M}(H)/(2m_H) + \mathcal{M}(He)/(4m_H)]} \tag{A.3}$$

$$= \frac{\mathcal{M}/\mathcal{M}(H)}{[1/2 + \mathcal{M}(He)/(4\mathcal{M}(H))]} \tag{A.4}$$

$$\approx 2.37 \,; \tag{A.5}$$

the classical value of $\mu_p = 2.33$ holds for an abundance ratio $\mathcal{N}(H)/\mathcal{N}(He) = 10$ and a negligible admixture of metals.

Both molecular weights are applied in different contexts. The mean molecular weight per free particle, $\mu_p$, is e.g. used to evaluate the thermal gas pressure, $P = \varrho k_B T / \mu_p$, where $T$, $\varrho$, and $k_B$ are the gas temperature, density, and Boltzmanns constant, respectively. The molecular mass per hydrogen molecule, $\mu_{H_2}$, is needed below to derive particle column densities.

## A.2 Radiative Transfer

### A.2.1 Equation of Radiative Transfer

The intensity emitted by a medium of temperature $T$ and of optical depth $\tau_\nu$ at the frequency $\nu$ is given by the equation of radiative transfer, which reads

$$I_\nu = B_\nu(T)\left(1 - e^{-\tau_\nu}\right) \tag{A.6}$$

in the case of local thermal equilibrium. Here $B_\nu$ is the Planck function. For the optical depth,

$$\tau_\nu = \int \kappa_\nu \varrho \, ds, \tag{A.7}$$

where $\kappa_\nu$ is the (specific) absorption coefficient (i.e., per mass) or dust opacity. If most hydrogen is in molecules, the optical depth can be related to the column density of molecular hydrogen,

$$N_{H_2} = \int n_{H_2} \, ds = \int \frac{\varrho}{\mu_{H_2} m_H} \, ds = \frac{1}{\mu_{H_2} m_H \kappa_\nu} \int \kappa_\nu \varrho \, ds, \tag{A.8}$$

and thus

$$N_{H_2} = \frac{\tau_\nu}{\mu_{H_2} m_H \kappa_\nu}, \tag{A.9}$$

where $n_{H_2}$ is the particle density of hydrogen molecules. This reads in a usable form

$$N_{H_2} = 2.14 \cdot 10^{25} \ \text{cm}^{-2} \, \tau_\nu \left(\frac{\kappa_\nu}{0.01 \ \text{cm}^2 \, \text{g}^{-1}}\right)^{-1}, \tag{A.10}$$

where the chosen numerical value of $\kappa_\nu$ is characteristic for wavelength $\lambda \approx 1$ mm. As typical $H_2$ column densities are below $10^{23}$ cm$^2$, $\tau_\nu$ is expected to be by far smaller that 1. Thermal dust emission in the (sub-)millimetre regime is therefore optically thin.

For optically thin conditions the equation of radiative transfer can be simplified:

$$I_\nu \approx B_\nu(T)\,\tau_\nu. \tag{A.11}$$

As the optical depth is related to the column density (Eq. A.10), Eq. (A.11) relates the observed intensity to the column density.

### A.2.2 The Planck Function

The Planck function reads

$$B_\nu(T) = \frac{2h\nu^3}{c^2} \frac{1}{e^{h\nu/(k_B T)} - 1}, \tag{A.12}$$

in which $c$ is the speed of light and $h$ is Planck's constant. In the Rayleigh-Jeans limit, $h\nu \ll k_B T$, this simplifies to

$$B_\nu(T) = \frac{2\nu^2}{c^2} k_B T. \tag{A.13}$$

However, the limiting condition, which reads

$$\lambda \gg 1.44 \ \text{mm} \left(\frac{T}{10 \ \text{K}}\right)^{-1} \tag{A.14}$$

in useful units, is under typical dust temperatures of about 10 K not fulfilled for observations at about 1 mm wavelength. The exact value of the Planck function is

$$
\begin{aligned}
B_\nu(T) \quad = \quad & 1.475 \cdot 10^{-23} \text{ W m}^{-2} \text{ Hz}^{-1}\text{sr}^{-1} \left(\frac{\nu}{\text{GHz}}\right)^3 \\
& \cdot \frac{1}{e^{0.0048(\nu/\text{GHz})(T/10 \text{ K})^{-1}} - 1}
\end{aligned}
\tag{A.15}
$$

in useful units.

## A.3   Observed Quantities

The received flux per beam is related to the intensity by

$$
F_\nu^{\text{beam}} = \int I_\nu \, P \, d\Omega \,,
\tag{A.16}
$$

where $P$ is the normalised power pattern of the telescope (i.e. $\max[P] = 1$). Defining the beam solid angle as the integral

$$
\Omega_{\text{A}} = \int P \, d\Omega \,,
\tag{A.17}
$$

one can derive a beam-averaged intensity,

$$
\langle I_\nu \rangle = F_\nu^{\text{beam}}/\Omega_{\text{A}} \,.
\tag{A.18}
$$

The beam solid angle can be conveniently approximated for telescopes with a beam profile similar to a Gaussian function,

$$
P(\theta) = e^{-\theta^2/(2\theta_0^2)}
\tag{A.19}
$$

(where the angle $\theta$ gives the distance from the beam center). The parameter $\theta_0$ is related to the half power beam width of the telescope, $\theta_{\text{HPBW}}$, via

$$
\theta_0 = \frac{\theta_{\text{HPBW}}}{\sqrt{8 \ln(2)}} \,.
\tag{A.20}
$$

For these idealisations the beam solid angle is

$$
\begin{aligned}
\Omega_{\text{A}} \quad = \quad & 2\pi \int_0^\infty P(\theta) \, \theta \, d\theta = 2\pi \int_0^\infty e^{-\theta^2/(2\theta_0^2)} \theta \, d\theta
\tag{A.21} \\
= \quad & 2\pi\theta_0^2
\tag{A.22} \\
= \quad & \frac{\pi}{4 \ln(2)} \theta_{\text{HPBW}}^2 \,.
\tag{A.23}
\end{aligned}
$$

Using the conversion

$$
1 \text{ arcsec} = 4.85 \cdot 10^{-6} \text{ rad} \,,
\tag{A.24}
$$

one obtains

$$
\Omega_{\text{A}} = 2.665 \cdot 10^{-11} \text{ sr} \left(\frac{\theta_{\text{HPBW}}}{\text{arcsec}}\right)^2 \,.
\tag{A.25}
$$

The parameter $\theta_{\text{HPBW}}$ does not need to be the real telescope beam, but depends on the calibration of the data. To give an example, some software packages (e.g., MOPSIC) apply scaling factors to the data (i.e., $F_\nu^{\text{beam}}$) when spatially smoothing a map, so that the beam width to that the calibration refers is equal to the spatial resolution of the map after smoothing.

   For the idealisations made here the average intensity derived from Eq. (A.18) is a good approximation to the actual intensity only if the source has an extension of the order of the main lobe of the telescope. Otherwise

radiation received via the side lobes may have a significant contribution to $F_\nu^{\text{beam}}$, and the idealisation of the telescope beam by Gaussian functions is too simple. Inclusion of the side lobes increases $\Omega_A$, and thus reduces $\langle I_\nu \rangle$. The nature of the average intensity derived in Eq. (A.18) is therefore comparable to the one of main beam brightness temperatures used in spectroscopic radio observations.

## A.4 Derivation of Conversion Laws

### A.4.1 Flux per Beam and Column Density

Equations (A.9, A.11, A.18) relate optical depth, column density, intensity, and the observed flux per beam with each other. Rearrangement yields

$$N_{H_2} = \frac{F_\nu^{\text{beam}}}{\Omega_A \mu_{H_2} m_H \kappa_\nu B_\nu(T)} \,, \tag{A.26}$$

which reads

$$
\begin{aligned}
N_{H_2} =\ & 2.02 \cdot 10^{20}\ \text{cm}^{-2} \left( e^{1.439(\lambda/\text{mm})^{-1}(T/10\ \text{K})^{-1}} - 1 \right) \left( \frac{\lambda}{\text{mm}} \right)^3 \\
& \cdot \left( \frac{\kappa_\nu}{0.01\ \text{cm}^2\ \text{g}^{-1}} \right)^{-1} \left( \frac{F_\nu^{\text{beam}}}{\text{mJy beam}^{-1}} \right) \left( \frac{\theta_{\text{HPBW}}}{10\ \text{arcsec}} \right)^{-2}
\end{aligned}
\tag{A.27}
$$

in useful units.

### A.4.2 Flux and Mass

The mass is given by the integral of the column densities across the source,

$$M = \mu_{H_2} m_H \int N_{H_2}\ dA \,. \tag{A.28}$$

Substitution of Eqs. (A.9, A.11) yields

$$M = \frac{1}{\kappa_\nu B_\nu(T)} \int I_\nu\ dA \,. \tag{A.29}$$

The surface element $dA$ is related to the solid angle element $d\Omega$ by $dA = d^2\ d\Omega$, where $d$ is the distance of the source. Thus

$$M = \frac{d^2}{\kappa_\nu B_\nu(T)} \int I_\nu\ d\Omega = \frac{d^2 F_\nu}{\kappa_\nu B_\nu(T)} \,, \tag{A.30}$$

where $F_\nu = \int I_\nu\ d\Omega$ is the integrated flux. This reads

$$
\begin{aligned}
M =\ & 0.12\ M_\odot \left( e^{1.439(\lambda/\text{mm})^{-1}(T/10\ \text{K})^{-1}} - 1 \right) \\
& \cdot \left( \frac{\kappa_\nu}{0.01\ \text{cm}^2\ \text{g}^{-1}} \right)^{-1} \left( \frac{F_\nu}{\text{Jy}} \right) \left( \frac{d}{100\ \text{pc}} \right)^2 \left( \frac{\lambda}{\text{mm}} \right)^3
\end{aligned}
\tag{A.31}
$$

in useful units.

## A.5 Conversion Factors

### A.5.1 Conversion from Dust Emission

Table A.1 summarises the c2d standard conversion factors for masses and column densities from dust emission. The wavelength-dependent dust opacities are from Ossenkopf & Henning (1994) and hold for dust with thin ice

**Table A.1:** Standard c2d conversion factors for masses and column densities from dust emission. For each bolometer camera employed by the c2d collaboration we list the effective wavelength, the half power beam width, the dust opacity at the effective wavelength (per gram of ISM), the conversion factors between intensity and column density, and between integrated flux density and mass (this for a distance of 100 pc), respectively.

| Camera | $\lambda$ | $\theta_{\text{HPBW}}$ | $\kappa_\nu$ | $N_{\text{H}_2}/F_\nu^{\text{beam}}$ | $M/F_\nu(d = 100 \text{ pc})$ |
|--------|-----------|------------------------|--------------|--------------------------------------|-------------------------------|
|        | $\mu$m    | arcsec                 | cm$^2$ g$^{-1}$ | cm$^{-2}$ (mJy beam$^{-1}$)$^{-1}$ | $M_\odot$ Jy$^{-1}$ |
| SHARC II | 350  | 8.5 | 0.101  | $7.13 \cdot 10^{19}$ | 0.031 |
| SCUBA    | 450  | 7   | 0.0619 | $1.42 \cdot 10^{19}$ | 0.041 |
|          | 850  | 15  | 0.0182 | $1.34 \cdot 10^{20}$ | 0.18  |
| BOLOCAM  | 1120 | 31  | 0.0114 | $6.77 \cdot 10^{19}$ | 0.39  |
| MAMBO    | 1200 | 11  | 0.0102 | $6.69 \cdot 10^{20}$ | 0.47  |
| SIMBA    | 1200 | 24  | 0.0102 | $1.41 \cdot 10^{20}$ | 0.47  |

mantles coagulating for $10^5$ yr at an H-density of $10^6$ cm$^{-3}$. We adopt a dust temperature of 10 K. This choice for the dust temperature and opacity are the standard assumptions made by the c2d collaboration. The values listed in Table A.1 are thus thought to serve as a standard reference within the collaboration.

## A.5.2  Conversion to Extinction

The c2d standard conversion factor between column densities and visual extinction,

$$N_{\text{H}_2} = 9.4 \cdot 10^{20} \text{ cm}^{-2} \, (A_V/\text{mag}) \,, \tag{A.32}$$

is taken from Bohlin et al. (1978). They combined measurements of $H_2$ and HI from the Copernicus satellite for lightly reddened stars to get

$$\langle [N_{\text{HI}} + 2N_{\text{H}_2}]/E(B - V) \rangle = 5.8 \cdot 10^{21} \text{ cm}^{-2} \text{ mag}^{-1} \,. \tag{A.33}$$

For a standard total-to-selective extinction ratio $R_V = A_V/E(B - V) = 3.1$ this yields the above conversion factor.

# Acknowledgements / Danksagung

This work would not have been possible without the technical, scientific, and moral support by many people, whom I would like to thank here.

There would never have been a thesis project if it had not been offered to me by *Prof. Dr. Frank Bertoldi* (Argelander Institut für Astronomie der Universität Bonn). He was a good, fair, and helpful comrade throughout my thesis. In particular I learned a lot from him about approaching scientific problems ("only dimensionless quantities count"), facing proposals and astro-politics ("sources are always 'enigmatic', studies must be called 'systematic'"), the english language ("always put a comma when using 'which'"), and meat in the oven ("it has to be burned slightly, otherwise it won't taste"). I have to thank him a lot for bearing 'Bandwurm-Sätze' and similar improper use of english language, and last-minute submissions of drafts for talks and proposals.

*Prof. Dr. Karl M. Menten* (Max-Planck-Institut für Radioastronomie in Bonn [MPIfR]) also had to suffer from the latter troubles. I have learned a lot from him about the optimization of scientific output ("I had 6 publications at the end of my thesis!") and the power of passion in science (which made Menten & Melnick 1989 possible). He took over a fatherly position in the background and made it possible for me to visit a couple of schools, conferences, and observatories during my stay in his group. Also, his help was crucial in creating a perspective for my future.

*Prof. Dr. Andreas Heithausen* (now Institut für Physik und ihre Didaktik der Universität Köln) has been one of my supervisors in the beginning of my thesis. Unfortunately, he moved on to a different position during the course of my thesis. I thank him a lot for his expert advice during the start of my thesis, which helped to better focus its aim.

*Prof. Dr. Herbert Hübel* (Helmholtz-Institut für Strahlen- und Kernphysik der Universität Bonn) and *Prof. Dr. Jens Frehse* (Institut für Angewandte Mathematik der Unversität Bonn) were further referees for the PhD exam. I am very gracious to them for helping significantly in expediting the submission process and for taking the effort to deal with an exam in a field of research far off their usual tracks.

*PD Dr. Endrik Krügel* (MPIfR) was crucial in getting the radiative transfer calculations for the modelling of L1148-IRS running. He always had an open ear when I asked for modifications in his radiative transfer code. We had many interesting discussions about radiative transfer and star formation; I benefited a lot from them.

*Prof. Dr. Johannes Schmid-Burgk* (MPIfR) helped to better a theoretical paper not presented here. Unfortunately, this did finally not help in expediting the publication of this work (which is my fault), though the paper itself improved a lot. He also had a thorough look at the evidence for inward motions towards L1148-IRS. Also *Prof. Dr. Malcolm Walmsley* (Osservatorio Astrofisico di Arcetri) tried his best in helping to speed up the submission of the above theory paper. It is also always an extraordinary pleasure to listen when he explains the universe in terms understandable for the common man. I owe him the insight that its the stories behind research projects which make the scientific life so interesting.

The MAMBO mapping results presented here would be of much lesser quality had *Dr. Robert Zylka* (IRAM Grenoble) not dedicated a major fraction of his life to the development of data reduction tools for bolometer observations (i.e., MOPSI and MOPSIC) that actually define the state-of-the-art and were here used to reduce the observations. During several stays at the IRAM 30m-telescope I enjoyed his company and his lectures on principles of bolometer data reduction. Most of the bolometer observing runs for my thesis were coordinated by *Dr. Axel Weiss* (now MPIfR). Only his observation planning and organisation tools made possible the successful completion of many projects presented here. Both gentlemen also took care that the bolometer arrays at the IRAM

30m-telescope were in good shape. Their efforts allowed me to take the first-ever science observation with the rotated secondary mirror of the IRAM 30m-telescope (a map on L1521B-2). The MAMBO bolometers were provided by the *Bolometer Group of the Max-Planck-Institut für Radioastronomie*, which is lead by *Dr. Ernst Kreysa*. In particular the 117-channel incarnation of the MAMBO is an amazing piece of work. To my personal opinion, the combination of the MAMBO bolometers, the IRAM 30m-telescope, and the MOPSI(C) software yields the best bolometer facility presently existing.

My thesis would not have been possible without the help from the c2d collaboration. This project is run by *Prof. Dr. Neal J. Evans II* (University of Texas at Austin). I have to thank him a lot for bearing with the delays in the c2d projects tied to me. He also quickly revised a significant fraction of the drafts which I produced during my thesis and improved them a lot by contributing his expert knowledge. A further help was also the c2d Cores Team, lead by *Prof. Dr. Philip C. Myers* (Harvard-Smithsonian Center for Astrophysics [CfA]). His comments on a meeting in spring of 2006 made me reconsider the relation between necessary conditions for ongoing star formation and quasistatic evolution of dense cores. Also, the discussions with him and *Dr. Chang Won Lee* (Korea Astronomy and Space Science Institute) during the c2d Leiden meeting in summer of 2005 assured me in my discussion of contraction motions towards L1148-IRS, given that both were leading in creating the field of such research. *Dr. Tyler L. Bourke* (CfA) did a great job in keeping the c2d dense core projects coordinated. He was essential in better focusing the MAMBO observations while they were carried out and helped me to better understand the nature of VeLLOs. From *Dr. Tracy L. Huard* (CfA) I learned how near-infrared imaging observations can be used to study protostars. Our nice week in La Palma in summer of 2005 lead to the idea of VeLLOs having low accretion rates when drifting out of dense cores. He provided me with the FLAMINGOS data for L1148-IRS analysed in my thesis. In addition to these few named persons I have to thank many more c2d people who made it possible for me to use Spitzer data.

It is always a feeling of coming home when going to the IRAM 30m-telescope in Granada. This is in particular because of the hospitality of Esther Franzin, Nuria Marcelino, Frederic Damour, Stephane Leon, Enrique Lobato, Sergio Martin, Santiago Navarro, Juan Penalver, Manolo Ruiz, and Albrecht Sievers. I also enjoyed the company of several guest observers at this observatory. This in particular includes *Dr. Philippe André* (CEA Saclay) — I learned from him a lot about star formation research; I also owe him the insight that apparently unevolved VeLLO dense cores might be evolved on scales smaller that the beam, a suggestion which he made during the La Palma conference in summer of 2005 — *Dr. Jean-Francois Lestrade* (Observatoire de Paris-Meudon) — he trained me not to consider debris disks as remnants of protostellar disks and was a good company while being locked in a snowstorm at 3000 m altitude —, and *Dr. Clemens Thum* (IRAM Grenoble) — he can tell many interesting stories about the history of IRAM, gave me an insight to France from a german perspective, and helped to keep the entrance to the control room free of snow.

The people in (and near) the "Kinderzimmer" — *Thushara 'Megaboss' Pillai*, *Arnaud Belloche*, *Jan 'Empfangsdame' Forbrich*, and *Hauke 'Sales Manager' Voß* — were a great company and I am pretty sure that I will miss them a lot in the future years (though this probably does not hold for the frequent paper ball attacks!). In general I enjoyed the climate in the MPIfR Submillimetre Astronomy Division a lot; I would not have wanted to make my PhD in any other group in Bonn. Thanks to all present and past members of this group who made it a nice place to work at!

Und dann sind da noch meine Eltern. Ohne ihre jahrelange Unterstützung bei allen meinen Aktivitäten, ihre Liebe und Aufopferung, hätte ich die letzten Jahre nie gemeistert.

# Bibliography

Altenhoff, W. J., Baars, J. W. M., Wink, J. E., & Downes, D. 1987, A&A, 184, 381

Alves, J. F., Lada, C. J., & Lada, E. A. 2001, Nature, 409, 159

Andre, P. & Montmerle, T. 1994, ApJ, 420, 837

André, P., Motte, F., & Bacmann, A. 1999, ApJ, 513, L57

Andre, P., Ward-Thompson, D., & Barsony, M. 1993, ApJ, 406, 122

—. 2000, Protostars and Planets IV, 59

Ballesteros-Paredes, J., Klessen, R. S., & Vázquez-Semadeni, E. 2003, ApJ, 592, 188

Baraffe, I., Chabrier, G., Allard, F., & Hauschildt, P. H. 1998, A&A, 337, 403

—. 2002, A&A, 382, 563

Barnard, E. E. 1919, ApJ, 49, 1

Barranco, J. A. & Goodman, A. A. 1998, ApJ, 504, 207

Barsony, M. & Kenyon, S. J. 1992, ApJ, 384, L53

Bazell, D. & Desert, F. X. 1988, ApJ, 333, 353

Beichman, C. A., Neugebauer, G., Habing, H. J., Clegg, P. E., & Chester, T. J., eds. 1988, Infrared astronomical satellite (IRAS) catalogs and atlases. Volume 1: Explanatory supplement

Belloche, A., André, P., Despois, D., & Blinder, S. 2002, A&A, 393, 927

Belloche, A., Parise, B., van der Tak, F. F. S., et al. 2006, ArXiv Astrophysics e-prints

Bertoldi, F. & McKee, C. F. 1992, ApJ, 395, 140

Blitz, L. 1993, in Protostars and Planets III, ed. E. H. Levy & J. I. Lunine, 125–161

Blitz, L. & Stark, A. A. 1986, ApJ, 300, L89

Blitz, L. & Thaddeus, P. 1980, ApJ, 241, 676

Bohlin, R. C., Savage, B. D., & Drake, J. F. 1978, ApJ, 224, 132

Bok, B. J. & Reilly, E. F. 1947, ApJ, 105, 255

Bontemps, S., Andre, P., Terebey, S., & Cabrit, S. 1996, A&A, 311, 858

44

Boulanger, F., Bronfman, L., Dame, T. M., & Thaddeus, P. 1998, A&A, 332, 273

Bourke, T. L., Crapsi, A., Myers, P. C., et al. 2005, ApJ, 633, L129

Caselli, P., Benson, P. J., Myers, P. C., & Tafalla, M. 2002a, ApJ, 572, 238

Caselli, P., Myers, P. C., & Thaddeus, P. 1995, ApJ, 455, L77+

Caselli, P., Walmsley, C. M., Zucconi, A., et al. 2002b, ApJ, 565, 331

—. 2002c, ApJ, 565, 344

Cazzoli, G., Puzzarini, C., & Lapinov, A. V. 2003, ApJ, 592, L95

Chabrier, G., Baraffe, I., Allard, F., & Hauschildt, P. 2000, ApJ, 542, 464

Chandler, C. J., Barsony, M., & Moore, T. J. T. 1998, MNRAS, 299, 789

Chen, H., Grenfell, T. G., Myers, P. C., & Hughes, J. D. 1997, ApJ, 478, 295

Chen, H., Myers, P. C., Ladd, E. F., & Wood, D. O. S. 1995, ApJ, 445, 377

Chiang, E. I. & Goldreich, P. 1997, ApJ, 490, 368

Claussen, M. J., Marvel, K. B., Wootten, A., & Wilking, B. A. 1998, ApJ, 507, L79

Clemens, D. P. & Barvainis, R. 1988, ApJS, 68, 257

Cox, A. N. 2000, Allen's astrophysical quantities (Allen's astrophysical quantities, 4th ed. Publisher: New York: AIP Press; Springer, 2000. Editedy by Arthur N. Cox.  ISBN: 0387987460)

Crapsi, A., Caselli, P., Walmsley, C. M., et al. 2005a, ApJ, 619, 379

—. 2004, A&A, 420, 957

Crapsi, A., Devries, C. H., Huard, T. L., et al. 2005b, A&A, 439, 1023

Crutcher, R. M. 1999, ApJ, 520, 706

Dame, T. M., Ungerechts, H., Cohen, R. S., et al. 1987, ApJ, 322, 706

De Vries, C. H., Narayanan, G., & Snell, R. L. 2002, ApJ, 577, 798

Di Francesco, J., Evans, N. J., Caselli, P., et al. 2006, ArXiv Astrophysics e-prints

Dobashi, K., Bernard, J.-P., Yonekura, Y., & Fukui, Y. 1994, ApJS, 95, 419

Dole, H., Le Floc'h, E., Pérez-González, P. G., et al. 2004, ApJS, 154, 87

Dore, L., Caselli, P., Beninati, S., et al. 2004, A&A, 413, 1177

Elston, R. 1998, in Proc. SPIE Vol. 3354, p. 404-413, Infrared Astronomical Instrumentation, Albert M. Fowler; Ed., ed. A. M. Fowler, 404–413

Emerson, D. T., Klein, U., & Haslam, C. G. T. 1979, A&A, 76, 92

Enoch, M. L., Young, K. E., Glenn, J., et al. 2006, ApJ, 638, 293

Evans, N. J., Allen, L. E., Blake, G. A., et al. 2003, PASP, 115, 965

Falgarone, E., Phillips, T. G., & Walker, C. K. 1991, ApJ, 378, 186

Frerking, M. A., Langer, W. D., & Wilson, R. W. 1982, ApJ, 262, 590

Froebrich, D. 2005, ApJS, 156, 169

Goldsmith, P. F. 2001, ApJ, 557, 736

Goodman, A. A., Barranco, J. A., Wilner, D. J., & Heyer, M. H. 1998, ApJ, 504, 223

Gottlieb, C. A., Myers, P. C., & Thaddeus, P. 2003, ApJ, 588, 655

Greene, T. P., Wilking, B. A., Andre, P., Young, E. T., & Lada, C. J. 1994, ApJ, 434, 614

Grenier, I. A., Lebrun, F., Arnaud, M., Dame, T. M., & Thaddeus, P. 1989, ApJ, 347, 231

Harvey, P. M., Chapman, N., Lai, S.-P., et al. 2006, ApJ, 644, 307

Hatchell, J., Richer, J. S., Fuller, G. A., et al. 2005, A&A, 440, 151

Henning, T., Wolf, S., Launhardt, R., & Waters, R. 2001, ApJ, 561, 871

Hotzel, S., Harju, J., & Juvela, M. 2002, A&A, 395, L5

Huard, T. L., Myers, P. C., Murphy, D. C., et al. 2006, ApJ, 640, 391

Indebetouw, R., Mathis, J. S., Babler, B. L., et al. 2005, ApJ, 619, 931

Jijina, J., Myers, P. C., & Adams, F. C. 1999, ApJS, 125, 161

Johnstone, D., Di Francesco, J., & Kirk, H. 2004, ApJ, 611, L45

Johnstone, D., Fich, M., Mitchell, G. F., & Moriarty-Schieven, G. 2001, ApJ, 559, 307

Johnstone, D., Matthews, H., & Mitchell, G. F. 2006, ApJ, 639, 259

Johnstone, D., Wilson, C. D., Moriarty-Schieven, G., et al. 2000, ApJ, 545, 327

Kauffmann, J., Bertoldi, F., Evans, N. J., & the C2D Collaboration. 2005, Astronomische Nachrichten, 326, 878

Kenyon, S. J., Calvet, N., & Hartmann, L. 1993, ApJ, 414, 676

Kenyon, S. J. & Hartmann, L. 1995, ApJS, 101, 117

Kirk, J. M., Ward-Thompson, D., & André, P. 2005, MNRAS, 360, 1506

Kreysa, E., Gemünd, H.-P., Gromke, J., et al. 1999, Infrared Physics and Technology, 40, 191

Kun, M. 1998, ApJS, 115, 59

Kutner, M. L., Tucker, K. D., Chin, G., & Thaddeus, P. 1977, ApJ, 215, 521

Lada, C. J. 1987, in IAU Symp. 115: Star Forming Regions, 1–15

Ladd, E. F., Adams, F. C., Casey, S., et al. 1991a, ApJ, 366, 203

Ladd, E. F., Adams, F. C., Fuller, G. A., et al. 1991b, ApJ, 382, 555

Lai, S.-P. & Crutcher, R. M. 2000, ApJS, 128, 271

Langer, W. D. & Willacy, K. 2001, ApJ, 557, 714

Larson, R. B. 1969, MNRAS, 145, 271

—. 1981, MNRAS, 194, 809

—. 2003, Reports of Progress in Physics, 66, 1651

Lebrun, F. 1986, ApJ, 306, 16

Lee, C. W., Myers, P. C., & Plume, R. 2004a, ArXiv Astrophysics e-prints

Lee, C. W., Myers, P. C., & Tafalla, M. 1999, ApJ, 526, 788

—. 2001, ApJS, 136, 703

Lee, J.-E., Bergin, E. A., & Evans, N. J. 2004b, ApJ, 617, 360

Leung, C. M. & Brown, R. L. 1977, ApJ, 214, L73

Levin, S. M., Langer, W. D., Velusamy, T., Kuiper, T. B. H., & Crutcher, R. M. 2001, ApJ, 555, 850

Müller, H. S. P., Schlöder, F., Stutzki, J., & Winnewisser, G. 2005, JMoSt, 742, 215

Maddalena, R. J., Morris, M., Moscowitz, J., & Thaddeus, P. 1986, ApJ, 303, 375

Magnani, L., Caillault, J.-P., Buchalter, A., & Beichman, C. A. 1995, ApJS, 96, 159

Mardones, D., Myers, P. C., Tafalla, M., et al. 1997, ApJ, 489, 719

McKee, C. F. & Holliman, J. H. 1999, ApJ, 522, 313

Menten, K. M. & Melnick, G. J. 1989, ApJ, 341, L91

Moshir, M. & et al. 1990, in IRAS Faint Source Catalogue, version 2.0 (1990)

Motte, F. & André, P. 2001, A&A, 365, 440

Motte, F., Andre, P., & Neri, R. 1998, A&A, 336, 150

Myers, P. C. & Benson, P. J. 1983, ApJ, 266, 309

Myers, P. C., Fuller, G. A., Mathieu, R. D., et al. 1987, ApJ, 319, 340

Myers, P. C. & Ladd, E. F. 1993, ApJ, 413, L47

Myers, P. C., Linke, R. A., & Benson, P. J. 1983, ApJ, 264, 517

Natta, A., Testi, L., Comerón, F., et al. 2002, A&A, 393, 597

Neufeld, D. A., Green, J. D., Hollenbach, D. J., et al. 2006, ArXiv Astrophysics e-prints

Ossenkopf, V. & Henning, T. 1994, A&A, 291, 943

Papovich, C., Dickinson, M., Ferguson, H. C., et al. 2004, ApJ, 600, L111

Pérault, M. 1987, Ph.D. Thesis

Pillai, T., Wyrowski, F., Menten, K. M., & Krügel, E. 2006, A&A, 447, 929

Pudritz, R. E. 2002, Science, 295, 68

Reiners, A., Basri, G., & Mohanty, S. 2005, ApJ, 634, 1346

Scalo, J. 1990, in ASSL Vol. 162: Physical Processes in Fragmentation and Star Formation, ed. R. Capuzzo-Dolcetta, C. Chiosi, & A. di Fazio, 151–176

Schmid-Burgk, J., Muders, D., Müller, H. S. P., & Brupbacher-Gatehouse, B. 2004, A&A, 419, 949

Schnee, S. & Goodman, A. 2005, ApJ, 624, 254

Schnee, S. & Kauffmann, J. 2005, in Protostars and Planets V, 8275–+

Schöier, F. L., van der Tak, F. F. S., van Dishoeck, E. F., & Black, J. H. 2005, A&A, 432, 369

Shirley, Y. L., Evans, N. J., Rawlings, J. M. C., & Gregersen, E. M. 2000, ApJS, 131, 249

Shu, F. H. 1977, ApJ, 214, 488

Sohn, J., Lee, C. W., Lee, H. M., et al. 2004, Journal of Korean Astronomical Society, 37, 261

Stanke, T., Smith, M. D., Gredel, R., & Khanzadyan, T. 2006, A&A, 447, 609

Straizys, V., Cernis, K., Kazlauskas, A., & Meistas, E. 1992, Baltic Astronomy, 1, 149

Suzuki, H., Yamamoto, S., Ohishi, M., et al. 1992, ApJ, 392, 551

Tafalla, M., Mardones, D., Myers, P. C., et al. 1998, ApJ, 504, 900

Tafalla, M., Myers, P. C., Caselli, P., & Walmsley, C. M. 2004, A&A, 416, 191

Tafalla, M., Myers, P. C., Caselli, P., Walmsley, C. M., & Comito, C. 2002, ApJ, 569, 815

Tafalla, M. & Santiago, J. 2004, A&A, 414, L53

Terebey, S., Chandler, C. J., & Andre, P. 1993, ApJ, 414, 759

Trumpler, R. J. 1930a, PASP, 42, 214

—. 1930b, PASP, 42, 267

Uchida, K. I., Fiebig, D., & Güsten, R. 2001, A&A, 371, 274

Ungerechts, H. & Thaddeus, P. 1987, ApJS, 63, 645

Visser, A. E., Richer, J. S., & Chandler, C. J. 2001, MNRAS, 323, 257

—. 2002, AJ, 124, 2756

Walker, C. K., Adams, F. C., & Lada, C. J. 1990, ApJ, 349, 515

Walmsley, M. 2003, in SFChem 2002: Chemistry as a Diagnostic of Star Formation, proceedings of a conference held August 21-23, 2002 at University of Waterloo, Waterloo, Ontario, Canada N2L 3G1. Edited by Charles L. Curry and Michel Fich. NRC Press, Ottawa, Canada, 2003, p. 221., ed. C. L. Curry & M. Fich, 221–+

Walsh, A. J., Bourke, T. L., & Myers, P. C. 2005, ArXiv Astrophysics e-prints

Ward-Thompson, D. 2002, Science, 295, 76

Ward-Thompson, D., André, P., Crutcher, R., et al. 2007, in Protostars and Planets V, ed. B. Reipurth, D. Jewitt, & K. Keil, 33–46

Ward-Thompson, D., Kirk, J. M., Crutcher, R. M., et al. 2000, ApJ, 537, L135

Ward-Thompson, D., Motte, F., & Andre, P. 1999, MNRAS, 305, 143

Ward-Thompson, D., Scott, P. F., Hills, R. E., & Andre, P. 1994, MNRAS, 268, 276

Weingartner, J. C. & Draine, B. T. 2001, ApJ, 548, 296

Whitney, B. A., Wood, K., Bjorkman, J. E., & Cohen, M. 2003a, ApJ, 598, 1079

Whitney, B. A., Wood, K., Bjorkman, J. E., & Wolff, M. J. 2003b, ApJ, 591, 1049

Whitworth, A. P. & Goodwin, S. P. 2005, Memorie della Societa Astronomica Italiana, 76, 211

Williams, J. P., Blitz, L., & McKee, C. F. 2000, Protostars and Planets IV, 97

Williams, J. P., de Geus, E. J., & Blitz, L. 1994, ApJ, 428, 693

Wilson, T. L. & Rood, R. 1994, ARA&A, 32, 191

Womack, M., Ziurys, L. M., & Wyckoff, S. 1992, ApJ, 387, 417

Wuchterl, G. & Tscharnuter, W. M. 2003, A&A, 398, 1081

Yonekura, Y., Dobashi, K., Mizuno, A., Ogawa, H., & Fukui, Y. 1997, ApJS, 110, 21

Young, C. H., Jørgensen, J. K., Shirley, Y. L., et al. 2004, ApJS, 154, 396

Young, K. E., Enoch, M. L., Evans, II, N. J., et al. 2006, ApJ, 644, 326

Young, K. E., Harvey, P. M., Brooke, T. Y., et al. 2005, ApJ, 628, 283

Yun, J. L. & Clemens, D. P. 1994, ApJS, 92, 145